

INFORMATION TO USERS

This manuscript has been reproduced from the microfilm master. UMI films the text directly from the original or copy submitted. Thus, some thesis and dissertation copies are in typewriter face, while others may be from any type of computer printer.

The quality of this reproduction is dependent upon the quality of the copy submitted. Broken or indistinct print, colored or poor quality illustrations and photographs, print bleedthrough, substandard margins, and improper alignment can adversely affect reproduction.

In the unlikely event that the author did not send UMI a complete manuscript and there are missing pages, these will be noted. Also, if unauthorized copyright material had to be removed, a note will indicate the deletion.

Oversize materials (e.g., maps, drawings, charts) are reproduced by sectioning the original, beginning at the upper left-hand corner and continuing from left to right in equal sections with small overlaps.

Photographs included in the original manuscript have been reproduced xerographically in this copy. Higher quality 6" x 9" black and white photographic prints are available for any photographs or illustrations appearing in this copy for an additional charge. Contact UMI directly to order.

ProQuest Information and Learning
300 North Zeeb Road, Ann Arbor, MI 48106-1346 USA
800-521-0600

UMI[®]

**GAS MIXING AND FLOW DYNAMICS IN CIRCULATING FLUIDIZED BEDS
WITH SECONDARY AIR INJECTION**

by

Murat Koksal

**Submitted
in partial fulfillment of the requirements
for the degree of**

DOCTOR OF PHILOSOPHY

Major Subject: Mechanical Engineering

at

DALHOUSIE UNIVERSITY

Halifax, Nova Scotia

June, 2001

© Copyright by Murat Koksal, 2001



**National Library
of Canada**

**Acquisitions and
Bibliographic Services**

**395 Wellington Street
Ottawa ON K1A 0N4
Canada**

**Bibliothèque nationale
du Canada**

**Acquisitions et
services bibliographiques**

**395, rue Wellington
Ottawa ON K1A 0N4
Canada**

Your file Votre référence

Our file Notre référence

The author has granted a non-exclusive licence allowing the National Library of Canada to reproduce, loan, distribute or sell copies of this thesis in microform, paper or electronic formats.

The author retains ownership of the copyright in this thesis. Neither the thesis nor substantial extracts from it may be printed or otherwise reproduced without the author's permission.

L'auteur a accordé une licence non exclusive permettant à la Bibliothèque nationale du Canada de reproduire, prêter, distribuer ou vendre des copies de cette thèse sous la forme de microfiche/film, de reproduction sur papier ou sur format électronique.

L'auteur conserve la propriété du droit d'auteur qui protège cette thèse. Ni la thèse ni des extraits substantiels de celle-ci ne doivent être imprimés ou autrement reproduits sans son autorisation.

0-612-63479-5

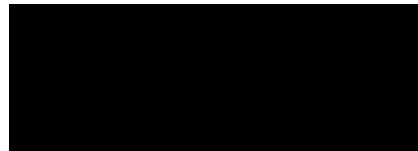
Canada

Dalhousie University
Faculty of Engineering

The undersigned hereby certify that they have examined, and recommended to the Faculty of Graduate Studies for acceptance, the thesis entitled "Gas Mixing and Flow Dynamics in Circulating Fluidized Beds with Secondary Air Injection" by Murat Koksal in partial fulfillment of the requirements for the degree of Doctor of Philosophy.

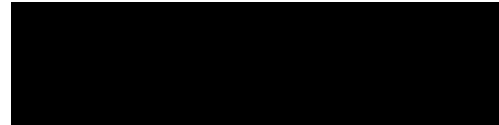
Dated: JUNE 4, 2001

Supervisor:



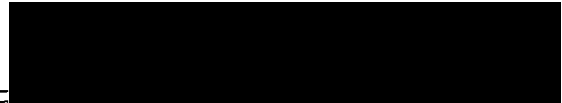
Dr. Feridun Hamdullahpur

External Examiner:

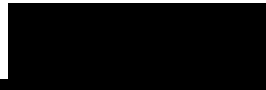


~~Dr. Tarhal~~ Chaouki,
Ecole Polytechnique de Montreal

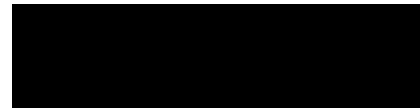
Examiners:



Dr. Adel M. Al Taweel



~~Dr. Indio~~ Militzer



Dr. Prabir Basu

Dalhousie University
Faculty of Engineering

DATE: JUNE 18, 2001

AUTHOR: Murat Koksal
TITLE: Gas Mixing and Flow Dynamics in Circulating Fluidized Beds
with Secondary Air Injection
MAJOR SUBJECT: Mechanical Engineering
DEGREE: Doctor of Philosophy
CONVOCATION: June 2001

Permission is herewith granted to Dalhousie University to circulate and to have copied for non-commercial purposes, at its discretion, the above thesis upon the request of individuals or institutions.


Signature of Author

The author reserves other publication rights, and neither the thesis nor extensive extracts from it may be printed or otherwise reproduced without the author's written permission.

The author attests that permission has been obtained for the use of any copyrighted material appearing in this thesis (other than brief excerpts requiring only proper acknowledgements in scholarly writing), and that all such use is clearly acknowledged.

To my uncle, Servet Koksal

TABLE OF CONTENTS

List of Tables	viii
List of Figures	ix
List of Abbreviations and Symbols	xiv
Acknowledgements	xviii
Abstract	xix
Chapter 1- Introduction and Literature Review	1
1. Problem Statement	1
2. An Overview of CFBs.....	2
3. Secondary Air Injection in CFBs	7
3.1. Introduction	7
3.2. Effects of SA injection on Gas-Solid Hydrodynamics.....	12
4. Gas Mixing in CFBs.....	14
4.1. Introduction	14
4.2. Quantification of the Quality of Mixing in Fluidized Beds: Dispersion Coefficients.....	16
4.3. Overall Axial Gas Mixing Studies in CFBs	19
4.4. Backmixing Studies in CFBs.....	20
4.5. Lateral Gas Mixing Studies in CFB Risers	21
4.5.1. Gas Mixing in CFBs with SA injection.....	26
5. Significance of the Study	28
6. Objectives of the Study	28
7. Methodology	29
8. Scope of the Study.....	29
9. Structure of the Thesis.....	29
Chapter 2- Theory	31
1. Introduction	31
2. Eddy Dispersion Concept for Gas Mixing	32
3. Radial Dispersion Coefficients.....	34
3.1. Dispersed Plug Flow Model (DPFM).....	34
3.2. Mean Square Displacement Model (MSDM).....	37
3.2.1. Axi-Symmetric Pipe Flow	42
4. Conclusions	43
Chapter 3- Experimental Set-up, Instrumentation, and Procedure	44
1. Outline of the Chapter	44
2. The Tracer Gas Technique	44
3. The Experimental Set-Up.....	45
3.1. The CFB Assembly	45
3.2. SA Injection Port	46
4. Gas Injection and Sampling System.....	49
5. Instrumentation.....	50
5.1. Air Flow Rate Measurements	50
5.2. Time Averaged Differential Pressure Measurements.....	51
5.3. Solids Circulation Rate Measurements.....	52

5.4. Sampled and Injected Gas Flow Rates	52
5.5. CO ₂ Concentration in the Sample Gas	52
5.6. Data Acquisition System	53
6. Experimental Procedure and Description.....	54
6.1. Tracer Gas Flowrate	57
6.2. Radial Gas Mixing Experiments	59
6.3. Gas Backmixing Experiments	62
6.4. Mixing of SA with Rising Gas-Solid Suspension	63
7. Conclusion.....	63
Chapter 4- Experimental Results and Discussion	64
1. Introduction	64
2. Time Averaged Axial Static Pressure Measurements	64
3. Radial Gas Mixing Experiments	72
3.1. Measurements without solids and secondary air injection ($G_s = 0 \text{ kg/m}^2\text{s}$, SA/PA=0).	72
3.2. The Radial Dispersion Coefficients.....	75
3.3. Measurements with solids and without secondary air injection (SA/PA=0).....	80
3.3.1. A Discussion on the Effects of the Solids on Radial Gas Mixing.....	87
3.4. Measurements with Secondary Air Injection	90
3.4.1. Effects of SA Injection Design on Radial Gas Mixing	93
3.4.2. Effects of the Solids Circulation Rate on Radial Gas Mixing with SA Injection	101
3.4.3. Effects of the SA/PA Ratio on Radial Gas Mixing with SA Injection..	103
3.4.4. Comparison of the Results of this Study with Zheng <i>et al.</i> (1992) and Namkung and Kim (2000).....	106
3.5. Radial Gas Mixing Predictions with DPFM.....	107
4. Backmixing Experiments	109
5. Mixing of SA with Rising Gas-Solid Suspension.....	110
6. Uncertainty in Experimental Results.....	112
7. Conclusions	113
Chapter 5- Two Fluid Modeling of CFBs.....	117
1. Introduction	117
2. A Simple Classification of Gas-Solid Two Phase Flows	118
3. CFB Hydrodynamic Models	123
4. Numerical Models (Type III models) for Gas-Solid Two-Phase Flows	124
5. The Two-Fluid (Eulerian-Eulerian) Model	125
5.1. Continuum Assumption for Solids Phase.....	125
5.2. Governing Conservation Equations.....	126
5.2.1. Introduction	126
5.2.2. Conservation Equations.....	129
5.3. Closure Laws	130
5.3.1. Gas and Solid Phase Stress Tensors, τ_g and τ_s	130
5.3.2. Gas and Solids Phase Pressures, p and p_s	131
5.3.3. Gas-Solid Interphase Exchange Coefficient, β	131

5.3.4. Solid Phase Closures: Solids Phase Viscosity and Pressure.....	134
5.3.4.1. The Physical Significance of the Solids Phase Viscosity and Pressure	134
5.3.4.2. Kinetic Theory of Granular Solids	137
5.3.5. Gas and Solid Phase Turbulence	145
5.3.5.1. The $k-\epsilon$ Eddy Viscosity Turbulence Model.....	145
5.3.5.2. Near Wall Turbulence Modeling.....	147
5.4. Numerical Solution of the Model Equations	150
5.5. Wall Boundary Conditions	150
6. Conclusion	152
Chapter 6- Simulation Results and Discussion.....	154
1. Introduction	154
2. Riser Flow Simulation without SA Injection	154
3. Riser Flow Simulation with SA Injection.....	169
4. Modeling of Mixing of SA with Rising Gas-Solid Suspension	191
5. Conclusions	196
Chapter 7- Overall Conclusions and Recommendations.....	198
1. Conclusions	198
2. Recommendations for Future Work	199
References.....	201
Appendices	215
Appendix A: Gas-Solid Fluidization Regimes	216
Appendix B: Properties of the Bed Material Used in the Experiments	220
Appendix C: Calibration of the Pressure Transducers and Flow Meters	223
Appendix D: Kinetic theory Expressions in the Literature	227
Appendix E: Fluent V4.5.....	229

LIST OF TABLES

Table 1.1. Comparison of FCC reactors and CFB combustors (compiled from Zhu and Bi, 1993; Werther, 1993 ; Berruti <i>et al.</i> , 1995).....	7
Table 1.2. Major studies on effects of SA injection on gas-solid hydrodynamics in CFBs.....	14
Table 1.3. Major overall axial gas mixing studies in CFBs.....	20
Table 1.4. Major gas backmixing studies in CFBs.....	21
Table 1.5. Major lateral gas mixing studies in CFBs.....	25
Table 1.6. Studies on the gas mixing in CFB risers with SA injection.....	27
Table 3.1. Distance of the pressure ports from the distributor plate.....	51
Table 3.2. Values of the operational parameters used in the experiments.....	55
Table 3.3. Variables used in gas mixing experiments.....	62
Table 4.1. Approximate radial dispersion coefficients and Peclet numbers including the single phase values obtained in other studies.....	86
Table 6.1. Properties of the gas and solid phase for the simulation of riser data of Miller and Gidaspow (1992).....	156
Table 6.2. Properties of the gas and solids phase for the simulation of riser data of Ersoy (1998).....	169

LIST OF FIGURES

Figure 1.1. Typical configuration of a CFB	4
Figure 1.2. Types of SA injection devices investigated in laboratory scale risers.....	9
Figure 1.3. The optimization problem of fluidized bed combustion (Lyngfelt <i>et al.</i> , 1998).....	10
Figure 1.4. Contributions of different mechanisms to gas mixing in a gas-solid flow	17
Figure 1.5. The procedures of the gas radial and backmixing experiments.....	18
Figure 1.6. Summary of the work carried out in this study.....	30
Figure 2.1. The parameters used in dispersed plug flow model.....	36
Figure 2.2. Mean square displacement model.....	38
Figure 3.1. DalTech CFB riser	47
Figure 3.2. Modular SA injection port (Ersoy, 1998)	48
Figure 3.3. Types of SA injectors used in this study.....	48
Figure 3.4. The layout of the gas injection and sampling apparatus used in the experiments	49
Figure 3.5. Injection and sampling probes used in the experiments	50
Figure 3.6. The measurement principle of IR gas analyzer.....	53
Figure 3.7. The circumferential position of the gas sampling plane on the riser cross- section.....	56
Figure 3.8. Variation of the measured tracer concentration with mean mixed concentration at different solids circulation rates, $U_o = 5$ m/s	58
Figure 3.9. The locations of the tracer injection and gas sampling probes along the riser height in radial mixing experiments.....	61
Figure 4.1. Axial variation of the bed suspension density for different solids circulation rates, $U_o = 5$ m/s, SA/PA = 0.0.....	68
Figure 4.2. Average suspension density in the riser for different solids circulation rates, $U_o = 5$ m/s, SA/PA = 0.0.....	68
Figure 4.3. Axial variation of the bed suspension density with SA/PA for tangential SA injection, $U_o = 5$ m/s, $G_s = 8$ kg/m ² s.	69
Figure 4.4. Axial variation of the bed suspension density with SA/PA for radial SA injection, $U_o = 5$ m/s, $G_s = 8$ kg/m ² s.	69
Figure 4.5. Axial variation of the bed suspension density with SA/PA for mixed SA injection, $U_o = 5$ m/s, $G_s = 8$ kg/m ² s.	70
Figure 4.6. Effect of SA injection design on axial suspension density, $U_o = 5$ m/s, G_s $= 8$ kg/m ² s, SA/PA = 0.2.	70
Figure 4.7. Effect of SA injection design on axial suspension density, $U_o = 5$ m/s, G_s $= 8$ kg/m ² s, SA/PA = 0.4.	71
Figure 4.8. Effect of SA injection design on axial suspension density, $U_o = 5$ m/s, G_s $= 15$ kg/m ² s, SA/PA = 0.2.	71
Figure 4.9. Radial distribution of the tracer gas at different heights above the tracer injection plane, no solids, $U_o = 5$ m/s, $C_o = 0.3$ %.	73
Figure 4.10 Radial distribution of the tracer gas at different heights above the tracer injection plane, no solids, $U_o = 3$ m/s, $C_o = 0.3$ %.....	74

Figure 4.11. Radial distribution of the tracer gas at different heights above the tracer injection plane, no solids, $U_o = 5$ m/s, $C_o = 0.25$ %.	74
Figure 4.12. The variation of the radial dispersion coefficient with the distance from the tracer injection point, no solids, no secondary air.	76
Figure 4.13. Average radial Peclet number for single phase flow in the riser, no secondary air.	77
Figure 4.14. Application of the dispersed plug flow model, $U_o = 5$ m/s, no secondary air, no solids, $z_i = 0.44$ m, 1.19m, 2.34m.	79
Figure 4.15. Radial distribution of the tracer gas at different heights above the tracer injection plane, $U_o = 5$ m/s, $G_s = 8$ kg/m ² s, SA/PA = 0.0, $C_o = 0.25$ %.	81
Figure 4.16. Radial distribution of the tracer gas at different heights above the tracer injection plane, $U_o = 5$ m/s, $G_s = 15$ kg/m ² s, SA/PA = 0.0, $C_o = 0.25$ %.	81
Figure 4.17. Effect of the solids circulation rate on radial distribution of the tracer gas at $z = 0.44$ m, $U_o = 5$ m/s, $C_o = 0.25$ %.	82
Figure 4.18. Effect of the solids circulation rate on radial distribution of the tracer gas at $z = 1.19$ m, $U_o = 5$ m/s, $C_o = 0.25$ %.	82
Figure 4.19. Effect of the solids circulation rate on radial distribution of the tracer gas at $z = 2.34$ m, $U_o = 5$ m/s, $C_o = 0.25$ %.	83
Figure 4.20. The variation of the radial dispersion coefficient with the distance from the tracer injection point for different solids circulation rates, $U_o = 5$ m/s, SA/PA = 0.0.	84
Figure 4.21. The variation of the radial Peclet number with solids circulation rate, $U_o = 5$ m/s, SA/PA = 0.0.	85
Figure 4.22. The variation of the radial dispersion coefficient with axially averaged solids volume fraction at the sampling probe location, $U_o = 5$ m/s, SA/PA = 0.0.	87
Figure 4.23. Radial distribution of the tracer gas at different heights above the tracer injection plane, tangential SA injection, $C_o = 0.25$ %.	91
Figure 4.24. Radial distribution of the tracer gas at different heights above the tracer injection plane, radial SA injection, $C_o = 0.25$ %.	92
Figure 4.25. Radial distribution of the tracer gas at different heights above the tracer injection plane, mixed SA injection, $C_o = 0.25$ %.	92
Figure 4.26. Effect of SA injector design on radial gas mixing at 0.44 m above the tracer gas injection plane, $U_o = 5$ m/s, $G_s = 8$ kg/m ² s, $C_o = 0.25$ %.	93
Figure 4.27. Effect of SA injector design on radial gas mixing at 1.19 m above the tracer gas injection plane, $U_o = 5$ m/s, $G_s = 8$ kg/m ² s, $C_o = 0.25$ %.	94
Figure 4.28. Effect of SA injector design on radial gas mixing at 2.34 m above the tracer gas injection plane, $U_o = 5$ m/s, $G_s = 8$ kg/m ² s, $C_o = 0.25$ %.	94
Figure 4.29. The variation of the radial dispersion coefficients with the distance from SA injector, $U_o = 5$ m/s, $G_s = 8$ kg/m ² s.	95
Figure 4.30. The effect of the radial SA injection on radial tracer dispersion for single phase flow, $U_o = 5$ m/s, $z_i = 0.44$ m, $C_o = 0.25$ %.	98
Figure 4.31. The variation of the axial gas velocity in the riser, two-dimensional single phase simulation with Fluent V4.5.	99

Figure 4.32. The variation of the turbulent kinetic energy in the riser, two-dimensional single phase simulation with Fluent V4.5	100
Figure 4.33. The effect of solids circulation rate on radial gas dispersion for radial SA injection, $U_o = 5$ m/s, SA/PA=0.2, $z_i = 0.44$ m, $C_o = 0.25\%$	102
Figure 4.34. The effect of solids circulation rate on radial gas dispersion for tangential SA injection, $U_o = 5$ m/s, SA/PA=0.2, $z_i = 0.44$ m, $C_o = 0.25\%$	102
Figure 4.35. The effect of solids circulation rate on radial gas dispersion for mixed SA injection, $U_o = 5$ m/s, SA/PA=0.2, $z_i = 0.44$ m, $C_o = 0.25\%$	103
Figure 4.36. The effect of SA/PA ratio on radial gas dispersion for tangential SA injection, $U_o = 5$ m/s, $G_s = 8$ kg/m ² s, $z_i = 0.44$ m, $C_o = 0.25\%$	104
Figure 4.37. The effect of SA/PA ratio on radial gas dispersion for mixed SA injection, $U_o = 5$ m/s, $G_s = 8$ kg/m ² s, $z_i = 0.44$ m, $C_o = 0.25\%$	105
Figure 4.38. The effect of SA/PA ratio on radial gas dispersion for radial SA injection, $U_o = 5$ m/s, $G_s = 8$ kg/m ² s, $z_i = 0.44$ m, $C_o = 0.25\%$	105
Figure 4.39. The effect of solids circulation rate on radial gas dispersion coefficient, $U_o = 5$ m/s, $z_i = 0.44$ m, $C_o = 0.25\%$	106
Figure 4.40. Prediction of the radial distribution of the tracer gas at different heights above the tracer injection probe, $U_o=5$ m/s, $G_s= 8$ kg/m ² s, SA/PA=0.0, $C_o = 0.25\%$	108
Figure 4.41. Prediction of the radial distribution of the tracer gas for different SA injection modes at $z = 0.44$ m, $U_o=5$ m/s, $G_s= 8$ kg/m ² s, SA/PA=0.4, $C_o = 0.25\%$	109
Figure 4.42. Radial distribution of the tracer gas at 5 cm below the tracer gas injection plane, $U_o = 5$ m/s, $G_s = 15$ kg/m ² s, SA/PA = 0.2, $C_o = 0.4$ %	110
Figure 4.43. Radial distribution of the tracer gas at 0.15 m above the SA injection port, $U_o = 5$ m/s, $G_s = 8$ kg/m ² s, SA/PA = 0.2, $C_o = 0.25$ %	111
Figure 4.44. Radial distribution of the tracer gas at 0.76 m above the SA injection port, $U_o = 5$ m/s, $G_s = 8$ kg/m ² s, SA/PA = 0.2, $C_o = 0.25$ %	112
Figure 4.45. The repeatability in axial pressure measurements, $U_o = 5$ m/s, $G_s = 8$ kg/m ² s and SA/PA = 0.4, tangential SA injector	113
Figure 5.1. A classification of gas-solid two phase flows	122
Figure 5.2. Concept of two-fluid approach in gas-solid flows	128
Figure 5.3. Comparison of the drag laws for gas-solid flows	134
Figure 5.4. Sketch of the particle measurements of Campbell and Wang (1991).	137
Figure 5.5. The concept of granular temperature in gas-solid flows based on kinetic theory of granular flow (based on Campbell, 1990)	138
Figure 5.6. Effect of near wall turbulence modeling on solids volume fraction in a 2-D gas-solid flow in a vertical channel (Koksal, 1998)	149
Figure 5.7. Effect of near wall turbulence modeling on solids axial velocity in a 2-D gas-solid flow in a vertical channel (Koksal, 1998)	149
Figure 6.1. 2-D grid for riser simulation of Miller and Gidaspow (1992)	162
Figure 6.2. The contours of solids volume fraction for the riser simulation of Miller and Gidaspow (1992)	163
Figure 6.3. Comparison of the simulation and the experimental results at a height of 5.52 m above the distributor plate for solids axial velocity.	164

Figure 6.4. Comparison of the simulation and the experimental results at a height of 5.52 m above the distributor plate for solids volume fraction.	164
Figure 6.5. The contours of solids volume fraction for the riser simulation of Miller and Gidaspow (1992).	165
Figure 6.6. The contours of solids volume fraction for the riser simulation of Miller and Gidaspow (1992) at $t = 5.5$ s, 12 s, 18.5 s, 28 s and 35 s based on the kinetic theory expressions of Sylamlal <i>et al.</i> (1993).....	166
Figure 6.7. Comparison of the granular temperature profiles at a height of 5.52 m above the distributor plate for different kinetic theory formulations.....	167
Figure 6.8. The variation of the granular temperature, solids turbulent kinetic energy and air turbulent kinetic energy in the riser at a height of 5.52 m.	167
Figure 6.9. The solids phase laminar and turbulent shear viscosity at a height of 5.52 m above the distributor plate.....	168
Figure 6.10. The solids phase pressure at a height of 5.52 m above the distributor plate.....	168
Figure 6.11. 2-D Cartesian grid for the riser simulation with SA injection.....	178
Figure 6.12. Solids volume fraction contours in the riser for two cases, SA/PA = 0 and SA/PA =0.5, $U_o = 3$ m/s, $G_s = 18$ kg/m ² s	179
Figure 6.13. Solids volume fraction contours in the riser for two cases, SA/PA = 0 and SA/PA =0.5, $U_o = 5$ m/s, $G_s = 33$ kg/m ² s	180
Figure 6.14. Solids distribution in a 2-D riser with SA injection, $U_o = 6$ m/s, $G_s = 35$ kg/m ² s, SA jet velocity = 30 m/s, bed material: ballatoni ($d_p = 89$ μ m, $\rho_s = 2540$ kg/m ³), photograph from Marzochella <i>et al.</i> , 1996, white: solids, black: gas,	181
Figure 6.15. Riser pressure drop, simulation vs experiment, $U_o = 3$ m/s, $G_s = 18$ kg/m ² s and $U_o = 5$ m/s, $G_s = 33$ kg/m ² s, SA/PA = 0	182
Figure 6.16. Riser pressure drop, simulation vs experiment, $U_o = 5$ m/s, $G_s = 33$ kg/m ² s, SA/PA = 0.5.....	182
Figure 6.17. Riser pressure drop, simulation vs experiment, $U_o = 3$ m/s, $G_s = 18$ kg/m ² s, SA/PA = 0.5.....	183
Figure 6.18. Axial Particle Velocity, Simulation vs Experiment, $U_o = 3$ m/s, $G_s = 18$ kg/m ² s, 0.52 m above the distributor plate.	183
Figure 6.19. Axial Particle Velocity, Simulation vs Experiment, $U_o = 3$ m/s, $G_s = 18$ kg/m ² s, 0.93 m above the distributor plate.	184
Figure 6.20. Axial Particle Velocity, Simulation vs Experiment, $U_o = 3$ m/s, $G_s = 18$ kg/m ² s, 1.26 m above the distributor plate.	184
Figure 6.21. Axial Particle Velocity, Simulation vs Experiment, $U_o = 3$ m/s, $G_s = 18$ kg/m ² s, 1.82 m above the distributor plate.	185
Figure 6.22. The effect of constant, m, defined in Equation 6.4 on the granular temperature, $U_o = 3$ m/s, $G_s = 18$ kg/m ² s, SA/PA = 0.....	185
Figure 6.23. The effect of constant, m, defined in Equation 6.4 on the suspension density, $U_o = 3$ m/s, $G_s = 18$ kg/m ² s, SA/PA = 0.....	186
Figure 6.24. The effect of constant, m, defined in Equation 6.4 on the solids axial velocity, $U_o = 3$ m/s, $G_s = 18$ kg/m ² s, SA/PA = 0.	186

Figure 6.25. The effect of the particle-particle coefficient of restitution on the solids distribution in the riser, $U_o = 3$ m/s, $G_s = 18$ kg/m ² s, SA/PA = 0.....	187
Figure 6.26. The effect of SA injection on granular temperature, $U_o = 3$ m/s, $G_s = 18$ kg/m ² s, SA/PA = 0 and 0.5.....	188
Figure 6. 27. The effect of SA injection on air turbulent kinetic energy, $U_o = 3$ m/s, $G_s = 18$ kg/m ² s, SA/PA = 0 and 0.5.....	189
Figure 6.28. The effect of the discretization scheme on the solids distribution in the riser, $U_o = 3$ m/s, $G_s = 18$ kg/m ² s, SA/PA = 0.....	190
Figure 6.29. Grid geometry for SA mixing study	192
Figure 6.30. Non-dimensional tracer concentration for SA/TA = 0.5 (0.46 m and 1.3 above SA port).....	194
Figure 6.31. Effect of SA/TA on radial gas mixing ($G = 10$ kg/m ² s).....	195
Figure 6.31. Effect of SA injection on gas phase turbulent kinetic energy	195

LIST OF ABBREVIATIONS AND SYMBOLS

Abbreviations

CFB	circulating fluidized bed
CFD	computational fluid dynamics
CO	carbon monoxide
CO ₂	carbon dioxide
DEM	discrete element method
DPFM	dispersed plug flow model
DNS	direct numerical simulation
DSU	dense suspension upflow
FCC	fluid catalytic cracking
He	helium
ID	inner diameter
IIT	Illinois Institute of Technology
IR	infrared
LDV	laser Doppler velocimeter
LES	large eddy simulation
MSDM	mean square displacement model
N ₂	nitrogen
N ₂ O	nitrous oxide
NaCl	sodium chloride
NO _x	nitrogen dioxide
PA	primary air
RTD	residence time distribution
SO ₂	sulfur dioxide
SA	secondary air
TA	total air
SA/PA	secondary-to-primary air volumetric air flow ratio
SA/TA	secondary-to-total air volumetric air flow ratio

Greek Letters

α	volume fraction (-)
β	gas-solid momentum exchange coefficient (kg/m ³ s)
ρ	density (kg/m ³)
ξ	Bulk viscosity (Pa.s)
ε	dissipation rate of the turbulent kinetic energy (m ² /s ³)
λ_p	mean interparticle distance (m)
μ	absolute viscosity (Pa.s)
μ_{eff}	effective shear viscosity (Pa.s)
$\mu_{g,t}$	turbulent eddy viscosity of the gas phase (Pa.s)
$\mu_{s,t}$	turbulent eddy viscosity of the particle phase (Pa.s).

κ	von Karman's constant (= 0.42)
Θ_s	pseudo or granular temperature (m^2/s^2)
Γ_{eff}	effective mass dispersion coefficient (m^2/s)
τ	stress tensor
τ_c	interparticle collision time (s)
τ_f	fluid integral turbulent time scale (time scale of the most energetic eddies or eddy turnover time) (s)
τ_L	lagrangian integral time scale (s)
τ_{pr}	particle relaxation time (aerodynamic response time) (s)
τ_w	shear stress at the wall (N/m^2)
v_{dr}	particle drift velocity (m/s)
ω_{av}	average velocity (gas or solid) (m/s)

Symbols

c_m	measured concentration of the tracer gas (kmol/m^3), (% volume)
C	concentration of the species under consideration (kmol/m^3), (% volume)
C_{air}	CO_2 concentration in atmospheric air (% volume)
C_D, C_d	single particle drag coefficient
C_o	mean-mixed concentration (kmol/m^3), (% volume)
C_μ	empirical constant used in k- ϵ turbulence model (= 0.09)
d_p	particle diameter based on sieve analysis (μm)
d_r, d_t	riser diameter (m)
d_{sv}	surface/volume diameter (μm)
d_v	volume diameter (μm)
D	dispersion coefficient (m^2/s)
D_b	gas backmixing coefficient (m^2/s)
D_g	overall axial dispersion coefficient (m^2/s)
D_r	radial gas dispersion coefficient (m^2/s)
e	coefficient of restitution (-)
e_w	coefficient of restitution for particle-wall collisions (-)
F_{gw}	gas-wall friction force per unit volume (N/m^3)
F_{sw}	solid-wall friction force per unit volume (N/m^3)
g	vector representing the acceleration due to gravitational field (m/s^2)
g_o	radial distribution function (-)
G_s	solids circulation rate (solids mass flux) ($\text{kg}/\text{m}^2\text{s}$)
h_r	height of the riser (m)
I	turbulence intensity (-)
I_{gs}	average interphase force per unit volume (N/m^3).
J	molar flux of a species ($\text{kmol}/\text{m}^2\text{s}$)

k_i	turbulent kinetic energy (m^2/s^2)
$k_{s,avg}$	cross-sectionally averaged solids fluctuating kinetic energy (m^2/s^2)
l	mean free path of the particles (m)
L, l_e	characteristic length of the most energetic eddies (m)
n	direction normal to the mean flow
p	gas pressure (N/m^2)
p_s	solid pressure (N/m^2)
Pe	radial Peclet number ($U_0 d_t / D_r$) (-)
Q	volumetric flow rate (m^3/s)
r	radial distance from the riser axis, cylindrical coordinate (m)
r_m	measurements radius (m)
R	riser radius (m)
$\overline{R^2}$	mean square displacement in radial direction (m^2)
R_c	core radius (m)
Re	Reynolds number (-)
R_L	lagrangian correlation coefficient (-)
S	specularity coefficient (-)
Sc	Schmidt number (-)
t	time (s)
T_d	total dispersion time (s)
u'	fluctuating component of the instantaneous gas velocity in the direction normal to the mean flow (m/s)
$\overline{u'^2}$	time averaged value of the square of the fluctuating component of the instantaneous gas velocity in the direction normal to the mean flow (m^2/s^2)
u_{rms}	root mean square velocity, ($\sqrt{\overline{u'^2}}$) (m/s)
U_0	superficial gas velocity (m/s)
U_c	core velocity (m/s)
U_s	solids velocity (m/s)
U_{slip}	average slip velocity (m/s)
$\overline{X^2}$	mean square displacement (m^2)
Y_i	mass fraction of i^{th} species (-)
z, z_i	distance between injection and sampling ports (m)

Subscripts

θ	circumferential
ave	average
ax	axial
col	collisional

<i>g</i>	gas phase
<i>kin</i>	kinetic
<i>max</i>	maximum
<i>mb</i>	minimum bubbling
<i>mf</i>	minimum fluidization
<i>min</i>	minimum
<i>mix</i>	gas-solid mixture
<i>p</i>	particle
<i>r</i>	radial
<i>s</i>	solids phase
<i>tr</i>	transport

ACKNOWLEDGEMENTS

I would first like to thank my supervisor Dr. Feridun Hamdullahpur, for all his support and encouragement with his genuine kindness and warm personality since the day I came to Canada to pursue a Ph.D. degree. His guidance was crucial and invaluable in bringing this thesis to its fruition.

I owe much thanks to Dr. Julio Militzer for carefully reviewing the manuscript and making the text more readable. I also would like to thank to Dr. Prabir Basu, Dr. Adel M. Al Taweel and Dr. Jamal Chaouki for their valuable suggestions and constructive criticisms.

I would like to extent my deep gratitude to my close friend and colleague Dr. Levent Ersoy for his constant support and lively companionship throughout the time we spent sharing the same office.

I would like to acknowledge the support and help of the following individuals:

Dr. Ismet Ugursal, Mr. Michel Hamelin, Mr. Burak Guler, Ms. Nirmla Singh, Mr. Alan Fung, Dr. Bulent Belibagli, Ms. Pamela Griffin-Hody, Mr. Stewart Carr, Mr. Ray Dubai, Ms. Diane Davis and Ms. Cathy Wood.

I am indebted to my parents for their constant support and dedication to my education.

Finally, my beloved, Merih, who soon will become Dr. Merih Aydinalp, deserves the highest praise for her constant inspiration and love.

ABSTRACT

In circulating fluidized bed (CFB) boilers, secondary air (SA) injection is obtained by splitting the total fluidization air into primary and secondary streams, the latter being injected usually laterally at a certain height above the distributor plate. The main motivation of the SA injection lies in its effectiveness in controlling the nitrogen oxide formation, especially in combustion of highly volatile fuels. Despite its common utilization, information on the effects of SA injection on riser hydrodynamics is scarce.

This thesis investigates the flow dynamics and gas mixing in CFB risers with SA injection. In the experimental part of this thesis, axial static pressure measurements are carried out to find the axial solids distribution along the riser and tracer gas experiments are performed to investigate the effects of the SA on gas mixing. Experiments are performed in a laboratory scale (0.23m ID, 7.6 m high) Plexiglas CFB riser with sand particles. Three different types of SA injectors are used in the experiments, radial, mixed and tangential injectors. In the numerical part of this study, a two-dimensional gas-solid flow model is proposed to describe the gas-solid hydrodynamics in the riser section of a CFB with SA injection. The model uses an Eulerian-Eulerian (two-fluid) approach based on the kinetic theory of model of Hrenya and Sinclair (1997) for solids phase closures and is implemented using FLUENT V4.5, the commercial computational fluid dynamics (CFD) package.

The axial pressure measurements show that the SA injection significantly alters the axial solids distribution in the riser compared to the case without SA injection at the same superficial gas velocity and solids circulation rate. The tangential secondary air injector results in the highest increase in the overall solids hold up in the riser compared to other two modes of injections.

The mean square displacement model which fundamentally depends on classical Taylor's theory of turbulence dispersion is used to calculate the radial dispersion coefficients under SA injection conditions. The tracer gas measurements and the calculated dispersion coefficients indicate that SA injection can be used as a promising tool to enhance the observed poor radial gas mixing in CFB risers. Significant improvement is obtained in radial gas dispersion especially when radial SA injector is used. This is attributed to the large scale unsteady gas motion caused by the two impinging SA jets. The effects of the design of the SA injector on the radial and gas backmixing are also shown and discussed.

The CFD model is tested against the experimental data of Ersoy (1998) for the simulation of a laboratory scale CFB riser with SA injection. The model results for the axial solids velocity and the pressure drop along the riser are compared to experimental measurements with FCC particles and reasonable agreement is reached between the measured and computed parameters. The model has also been able to capture some of the measured and observed characteristic aspects of the SA injection successfully.

Chapter 1

Introduction and Literature Review

1. Problem Statement

In a circulating fluidized bed (CFB) combustor, secondary air (SA) injection or the so-called air staging is obtained by splitting the fluidization air into primary and secondary streams. While the primary air (PA) is fed into the riser through the distributor plate in a conventional way, the SA is injected usually laterally at a certain height above the distributor plate in the form of one or more high momentum jets. The main motivation of the SA injection lies in its effectiveness in controlling the nitrogen oxide (NO_x) formation, especially in combustion of highly volatile fuels.

The emissions from a CFB combustor are closely linked with how the gas and the solids are distributed in the riser, i.e., the riser hydrodynamics. Despite its common utilization in fossil fuel combustion, the effects of SA injection on the riser hydrodynamics are still not very well known, due to the fact that most of the studies in CFBs have been carried out without considering the air staging. A limited number of studies with SA injection have concentrated mostly on its effects on the axial and radial solids distribution; the available information on its effects on gas mixing is even more scarce. However, it has been observed that gas mixing in CFB combustors is generally poor and the incomplete mixing of the air and the fuel can be a major problem. The information on the effects of the

design and the utilization of the SA injection system on gas mixing becomes crucial for the combustor performance. Thus, one part of this study investigates the effects of the SA injection on gas mixing in CFB risers.

The gas-solid flow modeling efforts in CFB risers have always excluded the presence of the SA injection. This partly comes from the complex nature of the problem, i.e., one or more high momentum jets are injected into the medium of a flowing gas-solid mixture and the resulting flow pattern strongly depends on the geometrical scale and design of the injection system. In recent years, with remarkable developments in computer technology, computational fluid dynamics (CFD) techniques have found increasing number of applications in gas-solids flows. In this study, such an approach is taken and a model based on solving the fundamental equations of fluid mechanics is proposed to describe the effects of the SA injection on riser hydrodynamics.

2. An Overview of CFBs

A CFB can be defined as a fluid bed with a steady recirculation of solids through a gas-solid separator (Kunii and Levenspiel, 1991). The solid circulation rate should be sufficiently high to ensure uniformity all through the bed. A typical CFB configuration is shown in Figure 1.1. The primary fluidization gas is fed from the bottom part of the riser through a distributor plate. At a certain height above the distributor plate, the secondary fluidization gas is introduced. The gas and particles flow co-currently up in the riser, where the most critical reactions take place. In a cyclone, gas and particles are separated; particles flow down in downcomer section, and are fed to the riser again. A CFB shows spatial heterogeneity in terms of fluidization regimes¹. The bottom part (dense part) is usually in turbulent fluidization regime and can be even in bubbling regime as in the case of CFB combustors (Leckner, 1998). The apparent bed density decreases with height and fast fluidization regime usually prevail in the upper part (dilute part) of the riser.

1. Appendix A gives a brief review of fluidization regimes.

Numerous processes in chemical, petrochemical, power generation, pharmaceutical, and mineral processing industries employ CFBs as gas-solid reactors. The applications of CFB technology in these industries can be classified in two broad groups depending on the conversion of either gas or solid (Werther, 1994; Grace and Bi, 1997; Horio, 1997). The so-called solid conversion reactions include combustion of coal, wood or shale, incineration of solid waste, calcination reactions, roasting of sulphidic ores, and cement production. The second group of applications is called gas conversion reactions; fluid catalytic cracking (FCC) and Fischer-Tropsch synthesis can be counted as the major examples of this group.

The CFB reactors offer improved gas-solid contacting with shorter residence times, operational flexibility, ability to have staged processes more easily, good turndown capability, and decreased NO_x emission in fossil fuel combustion (Berruti *et al.*, 1995; Grace and Bi, 1997). The main disadvantages of CFB reactors are increased overall reactor height, higher capital cost, decreased suspension-to-wall heat transfer coefficients for given particles, erosion of in-bed surfaces, increased particle attrition, added complexity in designing, and higher nitrous oxide (N₂O) emission in fossil fuel combustion (Grace and Bi, 1997).

Quantitative understanding of the hydrodynamics of CFBs is essential for the scale-up and design of the processes taking place in a CFB. The yield in a gas conversion reaction, the combustion efficiency and emissions in fossil fuel combustion, heat and mass transfer between gas and solids, wall-to-bed heat transfer coefficients all depend on to a lesser and greater extent how gas and solids are distributed and mixed in the riser.

The two main operational parameters in CFBs are superficial gas velocity, U_o , and solids circulation rate (solids mass flux), G_s . The former is an independent operating variable defined as the volumetric flow rate of the total fluidization gas divided by the riser cross-sectional area. The latter can be either independent or dependent based on the design of the solids inventory and is defined as the mass of the solids passing through a unit riser cross-sectional area per unit time (Berruti *et al.*, 1995). Other design and operating

parameters which affect the gas-solid flow pattern in a CFB are geometry of the riser (size, shape, inlet/exit configurations), riser wall roughness, particle properties and size distribution, and SA injection (Arena *et al.*, 1992; Brereton and Grace, 1993; Kunii and Levenspiel, 1995; Zhou *et al.*, 1996; Pugsley *et al.*, 1997; Arena, 1997).

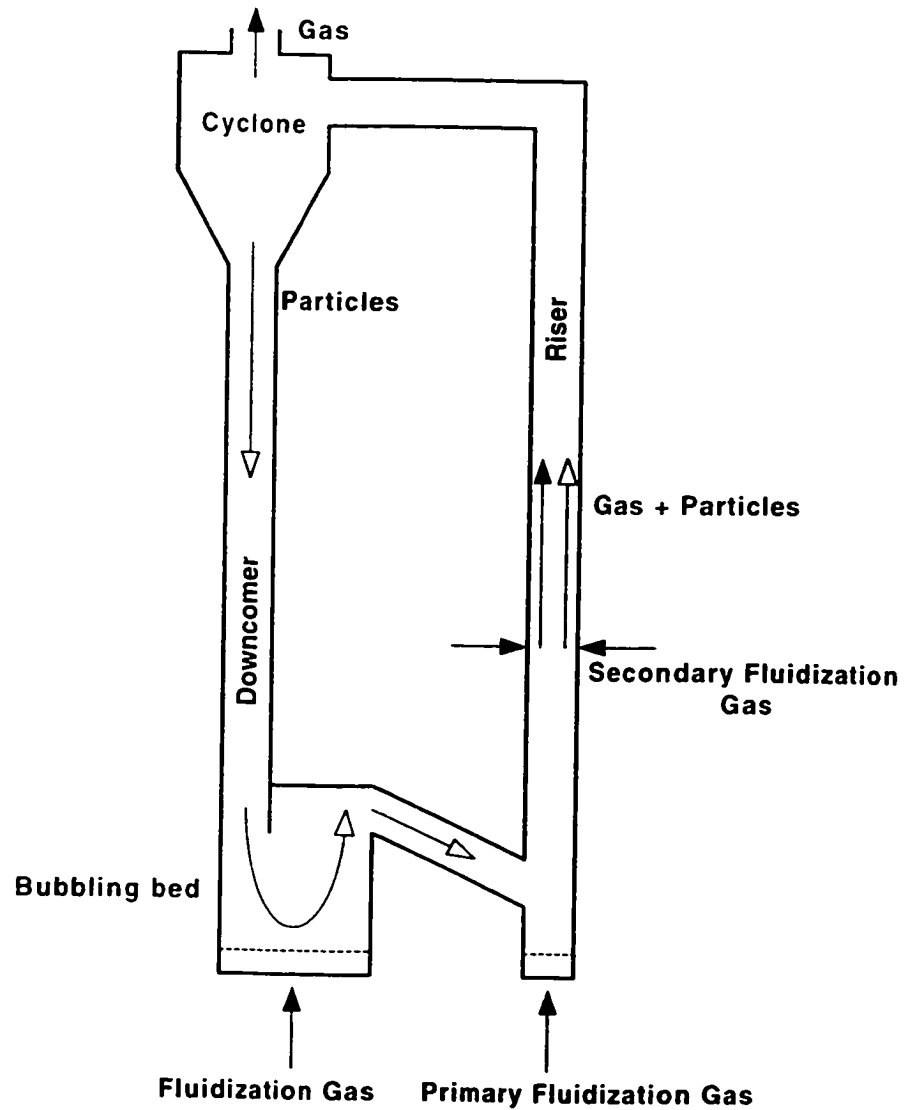


Figure 1.1. Typical configuration of a CFB

The gas-solid hydrodynamics inside the riser of a CFB is inherently complex. From purely fluid mechanical point of view, the problem can be seen as the flow of a turbulent gas-solid two-phase mixture in a vertical pipe or channel. The particles are neither small enough to follow the gas motion faithfully nor course enough to be unaffected by the gas. In addition to the effects of the gas, the particle motion is equally affected by particle-particle and particle-wall collisions. The gas flow dynamics, in turn, is also altered by the presence of the particles. The interactions between gas and particles via viscous drag and between particles themselves via collisions produce complex solids congregation forms at different length scales such as clusters, streamers, swarms, and sheets (Lim *et al.*, 1995). These solids congregations form and disintegrate continuously. A cluster has a slip velocity (relative velocity between the particles and the surrounding gas) of an order of magnitude larger than the terminal velocity of a single particle (Yerushalmi, 1986). This unique feature is the main cause of the improved heat and mass transfer between the particles and the gas in fast fluidization regime where clustering effects are dominant.

Although, the above dynamic and microscopic fluid dynamics characteristics form the core of the problem, engineers are more interested in the average behavior of the CFBs at different operating conditions. A time-averaged picture of a fast fluidization regime shows a dilute center (core) region with dispersed particles predominantly moving up and a descending particle flow in a relatively dense wall layer (annulus). This lateral solids segregation is usually attributed to particle-particle interactions (Sinclair and Jackson, 1989).

Depending on the nature of the application, a CFB may show different characteristics in terms of geometry, operating conditions, and mixing requirements. This can be demonstrated by comparing the CFB combustors to FCC reactors, being two characteristic examples of solid and gas conversion reactions, respectively. In a CFB combustor, the pressure drop limits the height of the lower dense region because of the fan power requirements (Horio, 1997; Leckner, 1998). This makes atmospheric CFB combustors different in geometry from FCC reactors, which have circular risers with a height-to-diameter ratio of over 20. On the other hand, the riser of a CFB combustor is a

larger size combustion chamber mostly of rectangular or square cross-section, with a height-to-hydraulic diameter ratio around 5 (Werther, 1993).

In FCC reactors, high reaction rates require very short contact times between gas and catalyst. So, higher superficial gas velocities are needed to promote plug flow in the riser. In addition, the quick deactivation of the catalyst also requires that catalyst be regenerated in the regenerator and fed back to the riser as quickly as possible. Thus, higher solid circulation rates are also employed (Zhu and Bi, 1993). In CFB combustors, however, back mixing is not very critical, even in some cases, internal circulation of gas is desirable. The solid circulation rate is an order of magnitude smaller than that of FCC reactors, which in turn, results in higher solids residence times increasing the combustion efficiency.

The mean solids volume fraction in the upper dilute zone of the riser is also different in FCC reactors and CFB combustors. In FCC reactors, concentrations of 1 to 10% are very typical whereas in CFB combustors, the upper dilute part is comparatively empty with a solids volume fraction below 1% (Werther, 1994). Table 1.1 presents the comparison of FCC reactors and CFB combustors compiled from different studies. A typical FCC unit is operated at a gas velocity ranging from 5-28 m/s and a solids flux higher than 300 kg/m².s, whereas a typical CFB combustor is operated at a gas velocity from 2 m/s to 9 m/s and a much lower solids flux in the range of 5-40 kg/m².s.

Table 1.1. Comparison of FCC reactors and CFB combustors (compiled from Zhu and Bi, 1993; Werther, 1994; Berruti *et al.*, 1995)

Characteristic	FCC Reactors	CFB Combustors
Geometry	Circular	Mostly rectangular
Height to Diameter Ratio	> 20	< 5
Wall of the Riser	Flat	Vertical tubes/fins
Superficial Gas Velocity	5-28 m/s (increases with height)	2-9 m/s
Solids Circulation Rate	> 250 kg/m ² .s	5-40 kg/m ² .s
Particle Density	1100-1700 kg/m ³	1800-2600 kg/m ³
Particle Diameter	40-80 μm	100-300 μm
Geldart's Classification	A	B
Temperature	250-650 °C	> 800 °C
Riser Diameter	0.7-2 m	8-10 m
Solids Mixing	Short residence time is desired (typically 1.5 s)	High residence time is desired (typically 10 s)
Gas Mixing	Backmixing is not desirable, plug flow is needed.	Backmixing is not critical. Lateral dispersion of gas is poor.
Exit Geometry	Smooth, abrupt	Abrupt

3. Secondary Air Injection in CFBs

3.1. Introduction

Secondary air injection (air staging) is obtained by splitting the total fluidization air into primary and secondary streams, the latter being injected at a certain height above the distributor plate. The region below the SA injection port is usually referred as *primary zone* whereas the region above is called as *secondary zone*. Three main parameters can be considered associated with SA injection problem:

1. **Secondary-to-primary air volumetric flow ratio (SA/PA):** In industrial CFB boilers, approximately 30-50% of the total fluidization air enters the riser as secondary air (Thermax Babcock and Wilcox Limited, 2001). This corresponds to a SA/PA value of 0.4-1.0. In laboratory scale CFB risers, experiments have been conducted with SA/PA values changing between 0.2-1.27 (Table 1.2).

2. Ratio of the height of the injection level and total riser height: The height of the injection level and total bed height ratio also shows difference among the industrial boilers and lab scale CFBs varying between 12-29% for the former (Ersoy, 1998) and 12-70% for the latter.
3. Design and orientation of the injector: Figure 1.2 illustrates the different designs of SA injectors used by different researchers in laboratory scale risers. In industrial boilers and in most of the lab scale risers, SA is injected laterally (normal to the rising gas-solid stream). However, it can also be injected in co-current (in the same direction of rising gas-solid stream) or counter current (in the opposite direction of rising gas-solid stream) modes.

SA injection or air staging is one of the effective ways of controlling the fuel based NO_x emission in combustion of highly volatile coals (Basu and Fraser, 1991; Talukdar, 1996; Brereton, 1997; Leckner, 1998). When the fluidization air is staged, insufficient combustion air passing through the bottom of the riser suppresses the volatile nitrogen oxidation to NO_x by creating a fuel-rich zone in the primary zone. Since the fuel nitrogen is already transformed into molecular nitrogen, formation of NO_x above this zone is controlled.

The common utilization of SA injection makes it an important design parameter in CFB combustors. The width of the primary zone is usually designed with respect to the penetration depth of the SA jets for which a complete understanding is still lacking. (Basu and Fraser, 1991). The secondary air injection is also used in CFB combustors for load control and turndown (Brereton, 1997).

While reducing the NO_x emission from CFB combustors, air staging may have different effects on emissions of other major pollutants. Lyngfelt *et al.* (1998) proposed that emission control in CFB boilers can be treated as an optimization problem; the temperature and the air supply being the two controlling parameters as shown in Figure 1.3.

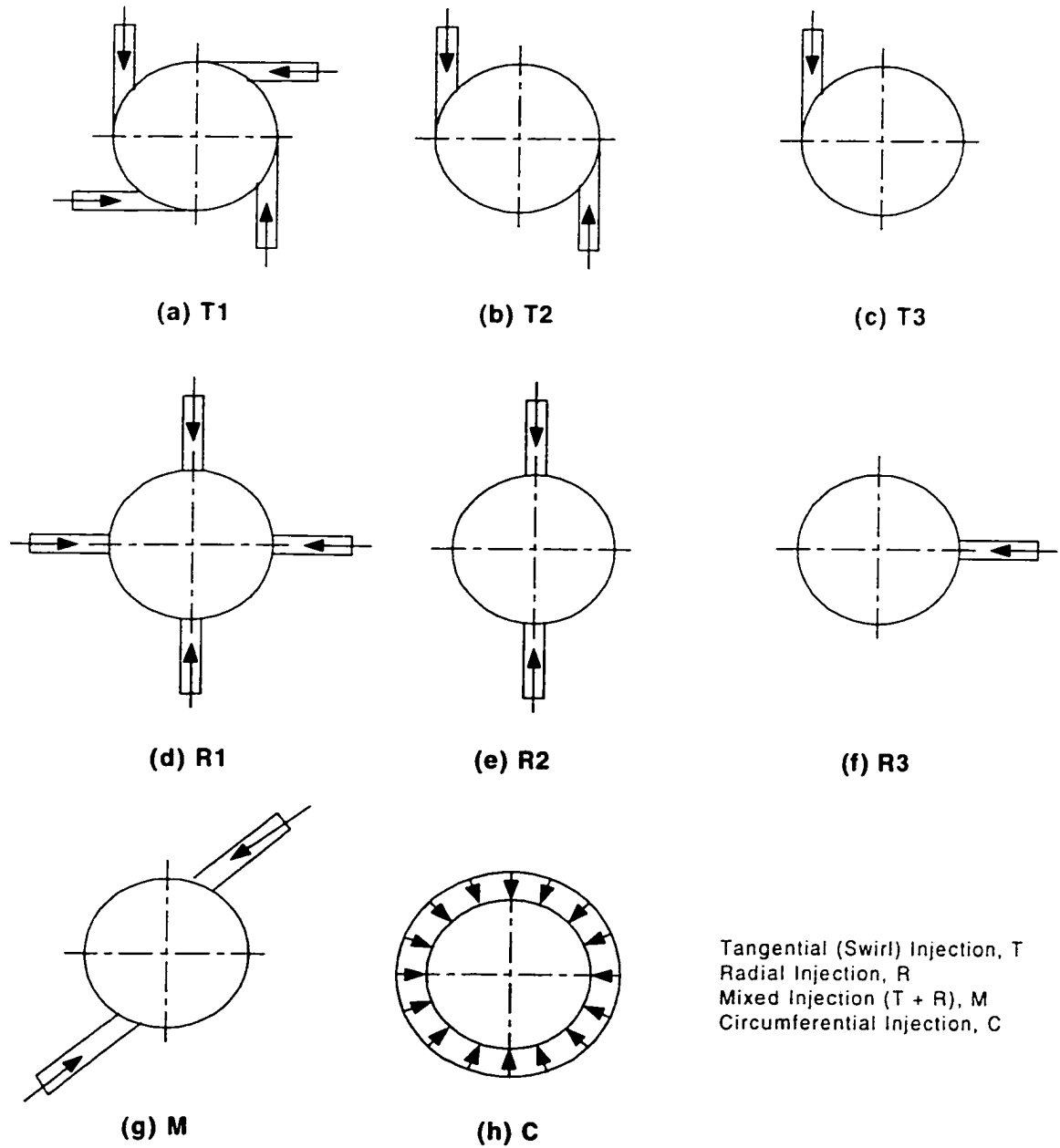


Figure 1.2. Types of SA injection devices investigated in laboratory scale risers.

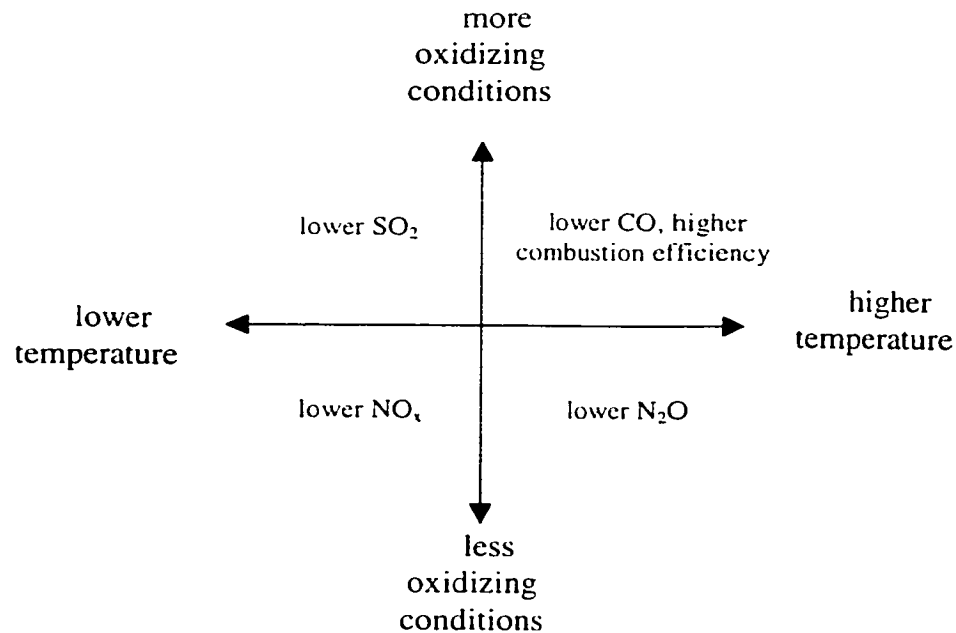


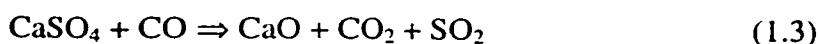
Figure 1.3. The optimization problem of fluidized bed combustion (Lyngfelt *et al.*, 1998)

The effect of air staging on N_2O emissions is not yet well established. Some researchers found no significant change whereas some reported a decrease in N_2O emissions with air staging (Lyngfelt and Leckner, 1993; Diego *et al.*, 1996). The amount of N_2O emission was also found to be dependent on the vertical distance between the distributor plate and the injection device (Diego *et al.*, 1996).

One of the characteristic features of fluidized bed combustion systems is to provide *in situ* sulfur capture by utilizing a low-cost sorbent which is usually limestone or dolomite. At atmospheric pressure, limestone calcines and captures the sulfur from SO_2 producing calcium sulfate according to following reactions (Brereton, 1997):



As can be seen from Equations 1.1 and 1.2, the sulfation reaction is favored at oxidizing conditions. When the air is staged in CFB combustors, the sulfur capture may deteriorate at the bottom zone as the limestone is exposed to oxygen-deficient conditions as expressed by the overall reaction (Leckner, 1998):



This phenomena is also known as *reverse sulfation*.

Hydrocarbon and CO emissions depend on the oxidizing conditions in the bed. Air staging may slightly increase the hydrocarbon and CO emissions, decreasing the combustion efficiency in the bottom zone (Leckner, 1998). Also, incomplete mixing of the SA jets with the rising gas-solid suspension may yield high hydrocarbon emissions. (Arena, 1997).

Another important design and performance parameter in a CFB is the wall-to-bed heat transfer coefficient. There are only a few studies available on the effects of SA injection on heat transfer in CFBs. Baskakov *et al.* (1993) found a decrease in the wall-to-bed heat transfer coefficient with SA injection relating it to the decrease in suspension density at the same superficial gas velocity. Cho *et al.* (1996) also reported a decrease in the heat transfer coefficient with increasing SA/PA using radial secondary air injection attributing this to the decrease in the particle down flow near the walls.

As can be deduced from previous studies, both the emission and the heat transfer aspects of SA injection problem involve complex interactions between gas and solids which depend on gas-solid hydrodynamics. Thus, understanding the underlying mechanisms of these two important phenomena depends on the extent of the information on the hydrodynamics of gas-solid flow in CFBs with SA injection. In the following sections, the state of knowledge about the effects of the SA injection on gas-solid hydrodynamics in CFBs will be reviewed.

3.2. Effects of SA injection on Gas-Solid Hydrodynamics

Depending on the type of the injection device, height of the SA injection port from the distributor plate and SA/PA, SA injection can cause significant differences in suspension density and solids motion compared to riser flow without SA. It is now accepted that the SA injection divides the riser into two regions. The region below the SA injection shows an increase in overall suspension density whereas the suspension density above the SA injection is slightly reduced or remains constant compared to non-SA operation only *when the bed is operated at the same solids mass flux and superficial gas velocity*. (Wang and Gibbs, 1991; Brereton and Grace, 1993; Cho *et al.*, 1994; Ersoy, 1998; Pecora and Goldstein, 1996; Kang *et al.*, 2000). The significant increase of the suspension density below the SA injection level has been attributed to decreased primary region flow rate and the “cutting” or “barrier” effects of SA streams, simultaneously.

The effects of the SA injection on the average solids residence time were investigated by Ilias *et al.* (1988) and Weinell *et al.* (1997). Ilias *et al.* (1988) performed experiments with dyed particles in a so-called swirling CFB combustor. The results of the experiments showed an increase in the average residence time of particles with increasing secondary-to-total air ratio (SA/TA). Based on their findings, they concluded that tangential SA injection increases the slip velocity, gas turbulence hence mixing in CFBs. However, the diameter of the particles used in the experiments was larger, and the superficial gas velocity and solids mass flux values were significantly lower than those employed in a typical CFB operation (Table 1.2). Weinell *et al.* (1997) also reported a slight increase in mean residence time of the particles above the SA injection ports with increasing SA/TA using radioactive particles.

Wang and Gibbs (1991) measured the pressure drop along the riser of a laboratory scale CFB operated with two different types of SA injectors; T1 and R3 according to the classification of Figure 1.3. They showed that the total solids holdup in the riser increases with increasing the distance between the distributor plate and the SA injection level. This finding is also supported by the experimental studies of Cho *et al.* (1994) and Ersoy

(1998). Their swirling injector provided the similar trends as the radial injector, except for the solids concentration above the injection port. Contrary to the radial injection case, they noted an increase in solids concentration above the SA injection level attributing it to the helical motion of the solids imposed by the swirling SA. The same trend for the solids concentration with the tangential SA injection was also obtained by Brereton and Grace (1993), Ersoy (1998) and Kang *et al.* (2000).

Marzocchella and Arena (1996a) measured the radial profiles of upward and downward solids mass fluxes using an isokinetic sampling with two modes of SA injection; circumferential and radial (C and R1). Their experiments showed that the solids downflow near the wall completely vanishes in case of circumferential SA injection at the downstream of the injection port at least up to a distance of 1.2 m. For radial injection, they observed a gradual reduction in solids downflow. They concluded that the two injection devices lead to substantially different solids mass flux profiles at the same operating conditions.

Ersoy (1998) and Ersoy *et al.* (1997) performed experiments to study the effects SA injection with three different types of injection devices; radial, tangential and mixed (T2, R2 and M). The axial particle velocity measurements showed that different SA injectors result in different type of axial velocity profiles across the riser cross-section. In case of tangential injection, the particles are accelerated upwards while passing through the injection plane resulting in a more parabolic velocity profile. The radial secondary air injection, on the other hand, produced flatter axial particle velocity profiles compared to tangential SA injection.

Recently, Kang *et al.* (2000) correlated the solids volume fraction in the riser as a function of the superficial gas velocity, SA/PA and the solids circulation rate under SA injection conditions based on their experimental measurements. However, their correlations have not been tested against the experimental data from previous studies.

Table 1.2. Major studies on effects of SA injection on gas-solid hydrodynamics in CFBs

Study	Riser	Bed Material	Injector	Operational Parameters
Ilias <i>et al.</i> (1988)	$d_r = 0.076$ m $h_r = 3.66$ m	Styro foam beads $d_p = 2$ mm $\rho_p = 2000$ kg/m ³	T1	SA/PA = 0 - 0.81 $U_o = 1.24 - 1.61$ m/s $G_s = 0.31 - 0.6$ kg/m ² s
Wang and Gibbs (1991)	$d_r = 0.08$ m $h_r = 4$ m	Sand $d_p = 245$ μ m $\rho_p = 1640$ kg/m ³	T1, R3	SA/PA = 0 - 0.43 $U_o = 7 - 9$ m/s $G_s = 10 - 60$ kg/m ² s
Brereton and Grace (1993)	$d_r = 0.152$ m $h_r = 9.3$ m	Ottawa Sand $d_p = 148$ μ m $\rho_p = 2650$ kg/m ³	T1, R1	SA/PA = 0.72, 1.27 $U_o = 8.6$ m/s $G_s = 45$ kg/m ² s
Cho <i>et al.</i> (1994)	$d_r = 0.1$ m $h_r = 5.3$ m	FCC $d_p = 65$ μ m $\rho_p = 1720$ kg/m ³	T3, R3	SA/PA = 0 - 1 $U_o = 1.5 - 3.5$ m/s $G_s = 5 - 50$ kg/m ² s
Pecora and Goldstein (1996)	$d_r = 0.1$ m $h_r = 4$ m	Sand $d_p = 200, 548, 920$ μ m $\rho_p = 2600$ kg/m ³	R2	SA/PA = 0 - 0.81 $U_o = 3.2-8.5$ m/s $G_s = 0-18$ kg/m ² s
Marzocchella and Arena (1996a)	$d_r = 0.12$ m $h_r = 5.75$ m	Ballotini $d_p = 89$ μ m $\rho_p = 2540$ kg/m ³	C, R1	SA/PA = 1 $U_o = 6$ m/s $G_s = 35- 55$ kg/m ² s
Ersoy (1998)	$d_r = 0.23$ m $h_r = 7.6$ m	FCC $d_p = 60$ μ m $\rho_p = 1600$ kg/m ³	T2, R2, M	SA/PA = 0 - 0.5 $U_o = 3 - 5$ m/s $G_s = 5 - 33$ kg/m ² s
Kang <i>et al.</i> (2000)	$d_r = 0.102$ m $h_r = 3.5$ m	Sand $d_p = 300$ μ m $\rho_p = 2650$ kg/m ³ FCC $d_p = 74$ μ m $\rho_p = 1840$ kg/m ³	T3, R3	SA/PA = 0 - 0.5 $U_o = 2.7$ m/s $G_s = 20, 30$ kg/m ² s

4. Gas Mixing in CFBs

4.1. Introduction

Mixing in fluidized beds, as in any other type of reactors, is the major concern of a designer. In the early stages of fluidized bed research, the fluidized beds were assumed to be well-mixed reactors having good contact between the particles and the gas. Based on this thought, large full-scale fluid catalytic crackers were designed which resulted in very poor conversions. However, later, as laboratory and full-scale experimental studies were carried out, it was shown that the completely mixed model assumption was too simplistic for most cases (van Deemter, 1985). In a fluidized bed reactor, one ideally wants to

achieve (van Deemter, 1980):

1. Rapid mixing of solids in order to obtain uniform temperature and a chemical composition throughout the bed.
2. Efficient contact between gas molecules and particles.

In a fluidized bed, whether it operates in a bubbling, turbulent or fast fluidization regime, it is very difficult to set general guidelines apart from the two points mentioned above for the mixing requirement as it depends on the specific needs of each application. For instance in a CFB combustor, gas back mixing is highly desirable whereas in a FCC reactor, it significantly reduces the yield (Werther, 1994; Zhu and Bi, 1993).

The words *mixing*, *dispersion* and *diffusion*, are often used interchangeably in the literature which can lead to confusion. The word *diffusion* is restricted to mixing process taking place at the molecular scale. *Dispersion*, on the other hand, is usually used to refer to the total transport of the gas due large scale gas motion, i.e., turbulent eddy motion and bulk convective motion. The combination of all the mechanisms present in the system including the diffusion and dispersion is best described by the term *mixing*. In this thesis the terms dispersion and mixing are used interchangeably to refer to the overall spread or motion of a species or a reactant in a fluidized bed.

The mixing phenomenon in a CFB occurs at different length scales. (van Deemter, 1980; Arena, 1997; Leckner, 1988). As seen in Figure 1.4, the total gas mixing in a CFB riser can be thought as the sum of the several mechanisms;

- the dispersion due to convective motion of gas (occurring at a scale comparable to riser characteristic length).
- the dispersion due to turbulent motion of gas (occurring at a scale roughly 10% of the riser characteristic length)
- contributions due to the modification of the gas mean and turbulent flow fields due to the presence of the particles, i.e., turbulence modulation effects.
- Mechanisms directly caused by the particles themselves, i.e, solids downflow near the wall.

- Fluctuations caused by the erupting bubbles at the bottom dense bed.
- molecular diffusion

The first five are usually referred as macro scale mixing, whereas the molecular diffusion represents the micro scale mixing. The molecular diffusion becomes of interest in fast chemical reactions such as volatile combustion. For instance, in order to describe the combustion phenomena properly, the small scale details of the transport of oxygen and volatiles should be introduced (van Deemter, 1980). In this study, only macro scale gas mixing is considered, however, in the case of a chemical reaction, molecular diffusion can be very important to smoothen out the small scale concentration gradients.

Mixing phenomenon in a fluidized bed depends on the fluidization regime (Geldart, 1986). Depending on the regime, one of the above mechanisms might dominate over the others. Even in the same system, such as a CFB, one may observe different mixing patterns due to the presence of different fluidization regimes, i.e., bubbling or turbulent fluidization regime at the bottom section, fast fluidization regime at higher sections.

4.2. Quantification of the Quality of Mixing in Fluidized Beds: Dispersion Coefficients

The traditional way of obtaining information on gas mixing in fluidized beds is the tracer gas experiments. Based on the results of the tracer gas experiments, the quality of mixing is quantified by a coefficient known as mixing or dispersion coefficient. Although, the techniques for tracer injection and detection, the location of the injection and sampling probes along the axial and lateral direction may differ depending on the scope of the study, two types of gas tracer experiments are usually carried out (Arena, 1997):

1. Transient (stimulus-response) gas tracer experiments
2. Steady-state (continuous) gas tracer experiments.

In transient gas experiments, a given amount of tracer gas is injected at the bottom of the bed with a pulse or a step input in concentration as the continuous samples are taken at a downstream position.

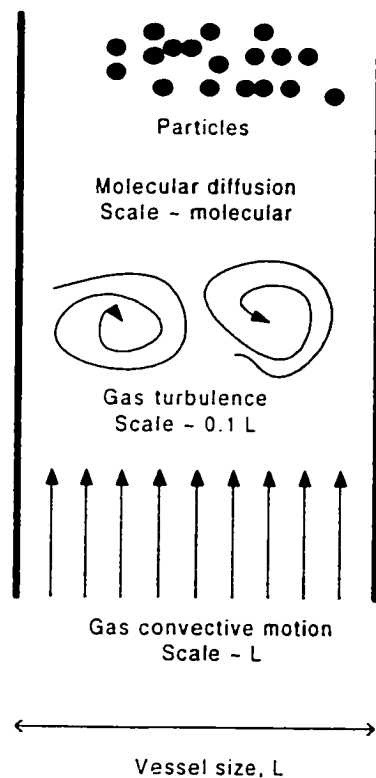


Figure 1.4. Contributions of different mechanisms to gas mixing in a gas-solid flow

Transient gas experiments provide the information about the gas residence time distribution (RTD) inside the bed and show the extent of the deviation from the ideal plug flow or well-mixed flow (Levenspiel, 1964). It is customary to obtain the overall, effective gas mixing or dispersion coefficient, D_g from the spread of the RTD curves. D_g represents the measure of the intensity of the overall gas mixing in the direction of the flow. In steady-state gas tracer experiments, on the other hand, the tracer gas is injected continuously at a single point by a traversing probe that can be located at several positions. For information on lateral/radial mixing, samples are taken downstream of the injection point at different lateral/radial locations (Figure 1.5a). The lateral/radial dispersion coefficient, D_r , which characterizes the intensity gas mixing in the direction normal to the flow is obtained from the spread of the tracer gas. To obtain information on

gas backmixing, the tracer concentration is measured at different radial/lateral positions at several elevations upstream of the tracer injection point (Figure 1.5b). Similar to lateral mixing, gas backmixing coefficient, D_b , which represents the intensity of the gas mixing in the direction opposite to the bulk flow can then be evaluated from the spread of the tracer gas (Schugerl, 1967; van Deemter, 1985; Arena, 1997).

It is important to note that if the injection and the sampling points are located at the inlet and exit of the bed respectively, the results will reflect the overall behavior of the bed as they are affected by the mixing characteristics of various regions established along the bed. If information relating to a specific fluidization condition is sought, the test section should be set such that the flow inside matches the fluidization regime of interest. The next two sections are devoted to the major experimental gas mixing studies that have been carried out in CFB risers.

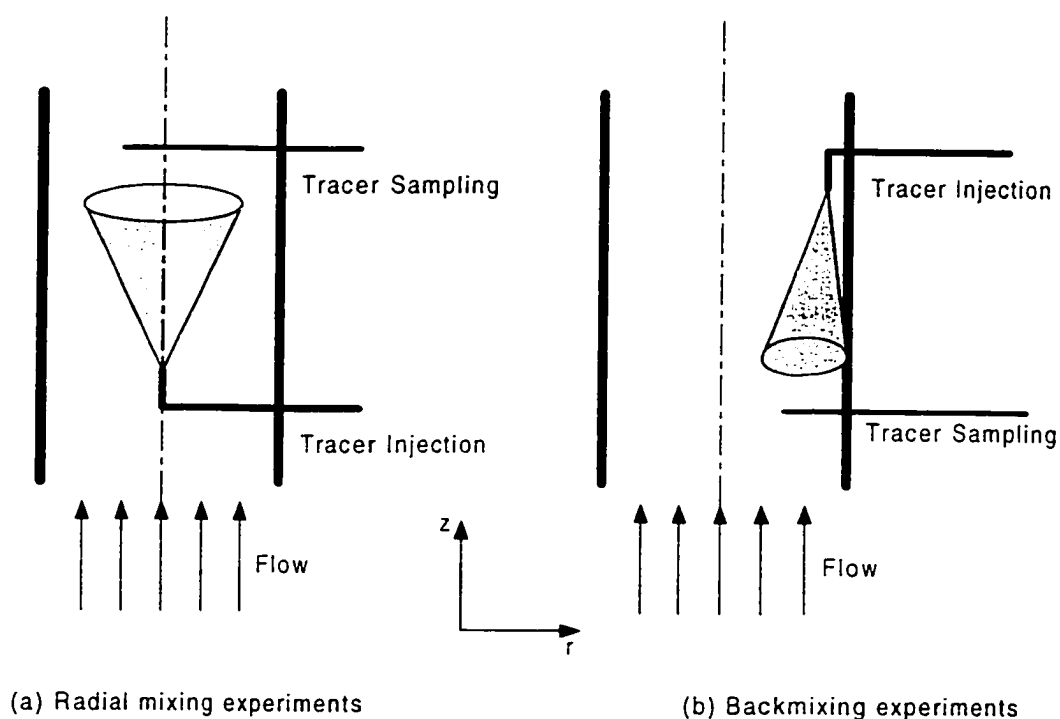


Figure 1.5. The procedures of the gas radial and backmixing experiments

4.3. Overall Axial Gas Mixing Studies in CFBs

Table 1.3 summarizes the major overall axial gas mixing studies carried out in CFB risers using the stimulus-response technique. With the recent experimental information (Liu *et al.*, 1999), it can be concluded that the variation of the overall gas mixing with solids hold up in the riser is not monotonic. At low solids circulation rates where a typical fast fluidization condition is obtained with a core-annular structure, the overall axial gas dispersion increases with increasing bed solids hold-up due to increasing solids downflow (Brereton *et al.*, 1988; Li and Wu, 1991; Bai *et al.*, 1992). For this case, Li and Wu (1991) proposed a correlation for the overall gas dispersion coefficient based on experimental data:

$$D_g = 0.1953\alpha_g^{-4.1197} \text{ (m}^2\text{/s)} \quad (1.4)$$

where α_g is the voidage (gas volume fraction).

The above correlation is valid for turbulent, fast and pneumatic transport regimes. As can be inferred from Equation 1.4, D_g increases with increasing solids holdup (i.e., increasing G_s at a fixed superficial gas velocity or decreasing U_o at a fixed G_s).

As the loading is increased, the overall axial gas dispersion coefficient reaches a maximum and then begins to decrease (Liu *et al.*, 1999). The point at which the local maximum is obtained corresponds to the onset of “dense suspension upflow” regime, a new regime identified by Grace *et al.* (1999). This regime is characterized by a dense annulus moving upwards in the riser contrary to what is observed in fast fluidization regime. In the absence of the solids downflow, the gas backmixing diminishes decreasing the overall axial gas mixing (Liu *et al.*, 1999).

There is still a need for new experimental data from risers with different sizes to verify and support the above arguments.

Table 1.3. Major overall axial gas mixing studies in CFBs

Researcher(s)	Tracer Gas	Riser Size	Particle	Operating Conditions
Brereton <i>et al.</i> (1988)	Helium	0.152 m ID 9.3 m high	Sand $d_p = 148 \mu\text{m}$ $\rho_s = 2650 \text{ kg/m}^3$	$U_o = 7.1 \text{ m/s}$ $G_s = 0-65 \text{ kg/m}^2\text{s}$
Dry and White (1989)	Argon	0.09 m ID 7.2 m high	FCC Catalyst $d_p = 71 \mu\text{m}$ $\rho_s = 1370 \text{ kg/m}^3$	$U_o = 2-8 \text{ m/s}$ $G_s = 36-232 \text{ kg/m}^2\text{s}$
Li and Wu (1991)	Hydrogen	0.09 m ID 8 m high	FCC Catalyst $d_p = 58 \mu\text{m}$ $\rho_s = 1575 \text{ kg/m}^3$	$U_o = 1-2 \text{ m/s}$ $G_s = 0-30 \text{ kg/m}^2\text{s}$
Bai <i>et al.</i> (1992)	Organic Substance	0.14 m ID 10 m high	Silica Gel $d_p = 99.6 \mu\text{m}$ $\rho_s = 710 \text{ kg/m}^3$	$U_o = 2-10 \text{ m/s}$ $G_s = 10-100 \text{ kg/m}^2\text{s}$
Liu <i>et al.</i> (1999)	Helium	0.076 m ID 5.6 m high	FCC $d_p = 70 \mu\text{m}$ $\rho_s = 1600 \text{ kg/m}^3$	$U_o = 4.8-7.0 \text{ m/s}$ $G_s = 21-486 \text{ kg/m}^2\text{s}$

4.4. Backmixing Studies in CFBs

Table 1.4 summarizes the gas backmixing studies carried out in CFB risers using continuous tracer injection. The initial studies concluded that the gas backmixing is practically negligible in fast fluidization regime (Cankurt and Yerushalmi 1978; Guilin *et al.*, 1984; Bader *et al.*, 1988). One of the most extensive and fruitful studies on gas backmixing were carried out by City University of New York researchers (Li and Weinstein, 1989; Weinstein *et al.*, 1989). The experiments were performed spanning the whole fluidization regime; from bubbling to dilute transport regimes in a 0.152 m ID and 8 m high fluidization facility with FCC particles. Their experiments showed that considerable backmixing exists in fast fluidization regime, especially in the annulus part, unlike the previous findings of Cankurt and Yerushalmi (1978), Guilin (1984) and Bader *et al.* (1988). They pointed out that in the previous studies the locations of the tracer injection and sampling probes were not determined based on the local flow structure. They also stated that increasing the superficial gas velocity increases the backmixing in captive regimes (bubbling, turbulent) whereas an opposite trend exists in fast fluidization regime.

Recently, Namkung and Kim (1998) investigated the gas backmixing characteristics in dilute, transition, and dense regions of a laboratory scale CFB. Similar to the findings of Li and Weinstein (1989) and Weinstein *et al.* (1989), they also reported some gas backmixing near the wall due to downflow of solids. They showed that the gas backmixing coefficients calculated from a core-annular type of model increases with increasing ratio of the average particle to gas velocity ratio. One of their significant findings is the difference in the dispersion coefficients obtained using two different tracer gases; helium (He) and carbon dioxide (CO₂). The gas backmixing coefficients, D_b , obtained using CO₂ as the tracer gas, were larger than those obtained using He by 60% in the dense region, 49-62% in the transition region and 2.4-19% in the dilute region. They attributed this discrepancy to the adsorption characteristics of CO₂ on FCC particles.

Table 1.4. Major gas backmixing studies in CFBs

Researcher(s)	Tracer Gas	Riser Size	Particle	Operating Conditions
Cankurt and Yerushalmi (1978)	Methane	0.0152 m ID 8.5 m high	FCC Catalyst, $d_{sv} = 55 \mu\text{m}$ $\rho_s = 1074 \text{ kg/m}^3$	$U_0 = 0.2\text{-}5.6 \text{ m/s}$ $G_s = 25\text{-}145 \text{ kg/m}^2\text{s}$
Guilin <i>et al.</i> (1984)	Helium	0.115 m ID 8 m high	Silica Gel $d_p = 220 \mu\text{m}$ $\rho_s = \text{not mentioned}$	$U_0 = 2.8\text{-}5.5 \text{ m/s}$ $G_s = 32\text{-}160 \text{ kg/m}^2\text{s}$
Bader (1988)	Helium	0.305 m ID 12.2 m high	FCC Catalyst $d_p = 76 \mu\text{m}$ $\rho_s = 1714 \text{ kg/m}^3$	$U_0 = 3.7\text{-}6.1 \text{ m/s}$ $G_s = 98\text{-}195 \text{ kg/m}^2\text{s}$
Li and Weinstein (1989), Weinstein <i>et al.</i> (1989)	Helium	0.152 m ID 8 m high	FCC Catalyst $d_p = 59 \mu\text{m}$ $\rho_s = 1450 \text{ kg/m}^3$	$U_0 = 0.03\text{-}4 \text{ m/s}$ $G_s = 0\text{-}271 \text{ kg/m}^2\text{s}$
Namkung and Kim (1998)	Helium and Carbon dioxide	0.1 m ID 5.3 m high	FCC Catalyst $d_p = 65 \mu\text{m}$ $\rho_p = 1720 \text{ kg/m}^3$	$U_0 = 1.5\text{-}4.5 \text{ m/s}$ $G_s = 14\text{-}62 \text{ kg/m}^2\text{s}$

4.5. Lateral Gas Mixing Studies in CFB Risers

Table 1.5 lists the major studies on lateral gas mixing in literature. Generally, the lateral dispersion of gas in CFB risers is thought to be caused by the gas turbulence and it has been considered to be poor, especially in industrial scale risers (Couturier *et al.*, 1991, Leckner, 1998). In a gas conversion reaction where plug flow is often desired, this may not be a problem but in the case of a CFB combustor, the deficiency of lateral mixing

may lead to the incomplete mixing of air and fuel (Arena, 1997).

Guilin *et al.* (1984) studied the lateral gas mixing in the fast fluidization regime using helium as the tracer gas. They found out that the radial gas dispersion coefficient increases with solid circulation rate, G_s , in the range of 2.6–7 cm²/s at constant superficial gas velocity and decreases with superficial gas velocity at constant solids circulation rate. They measured the voidage in the bed using capacitance probes and proposed the following empirical correlation for radial gas dispersion coefficient, D_r (cm²/s):

$$D_r = \left[43.4 \frac{U_o}{\left(\frac{U_s}{\alpha_g} - U_s \right)} \cdot \frac{1 - \alpha_g}{\alpha_g} \right] + 0.7 \quad (1.5)$$

where U_s is average solids velocity, U_o is superficial gas velocity and α_g is the voidage. Thus, their correlation clearly indicates an increase in dispersion coefficient with increasing solids volume fraction.

Adams' (1988) study in a rectangular column (0.3 m × 0.4 m) of 4 m high with dolomite and sand particles in the fast fluidization regime showed opposite trends for the variation of the radial dispersion coefficients with the solids circulation rate, G_s , and superficial gas velocity, U_o compared to the findings of Guilin *et al.* (1984). His results indicated that the presence of the particles greatly reduces the lateral dispersion coefficient. He concluded that the dispersion coefficient increases with superficial gas velocity, U_o at constant solids circulation rate and decreases with solid circulation rate, G_s , at constant superficial gas velocity. This indicates a decrease in radial gas dispersion coefficient with solids volume fraction. The lateral dispersion coefficients found were an order of magnitude greater than the ones found by Guilin *et al.* (1984).

Werther and his co-workers (Werther *et al.*, 1991; Werther *et al.*, 1992a) carried out radial mixing studies in the core region of a laboratory scale CFB riser. To characterize

the intensity of the radial mixing, they relied on the radial Peclet number ($Pe = 2U_c R_c / D_r$) based on the average core velocity, U_c , and radius, R_c . They found out an average radial Peclet number value of 465 from the tracer gas experiments. This value was independent of the solids circulation rate in the core region at constant superficial gas velocity. Thus, they concluded that the concentration of the particles was not high enough to have an effect on the radial dispersion of the gas.

Zheng *et al.* (1992) showed that the variation of the radial dispersion coefficient with the solids volume fraction or the solids circulation rate at constant superficial gas velocity is not monotonous. They demonstrated that at constant superficial gas velocity there is a certain value of solids circulation rate acting as a threshold below which D_r decreases with increasing solids circulation rate. Above that threshold, however, the opposite trend is observed. This trend also holds true for the solids volume fraction. Arena (1997) explained the inconsistencies in the data presented by Guilin *et al.* (1994), Adams (1988), Werther *et al.* (1992a), Martin *et al.* (1992) based on the findings of Zheng *et al.* (1992).

Amos *et al.* (1993) studied the radial gas dispersion in gas-solid risers. They pointed out that the discrepancies between the findings of the previous researchers may be due to the different experimental equipment and operating conditions and the models used to interpret the tracer gas measurements to find the values of the radial dispersion coefficient. Depending on their experiments, they correlated the radial Peclet number ($Pe = UR/D_r$) to the apparent suspension Reynolds number in the core region as follows:

$$Pe = 3.23 Re_m^{0.297} \quad (1.6)$$

where radial Peclet number is defined based on the riser radius, R , and interstitial gas velocity (i.e., $U = U_o/\alpha_g$) and the suspension Reynolds number, Re_m , given as:

$$Re_m = \frac{(G_s + \rho_g U_o) d_t}{\mu_g} \quad (1.7)$$

where d_t is riser diameter. This relation shows an increase in Peclet number (decrease in

radial dispersion coefficient) with solids circulation rate at constant superficial gas velocity which is contrary to the findings of Werther *et al.* (1992a).

Gayan *et al.* (1997) studied the radial dispersion in fast fluidized beds. They proposed that the radial gas dispersion coefficient, D_r , is small and dependent on gas velocity and solids circulation rate in the dilute region, whereas, in dense region it is very high due to the vigorous motion of the solids. They correlated their gas dispersion coefficient values in the dilute region with an apparent suspension Reynolds number, Re_m , using the following equation, which is similar to the one proposed by Amos *et al.* (1993):

$$D_r = c_1 Re_m^{c_2} (G_s + 1) \left(\frac{d_p}{\rho_s} \right)^{c_3} d_t^{c_4} \quad (1.8)$$

where Re_m is given in Equation 1.7 and the constants c_1 , c_2 , c_3 and c_4 were found by fitting the above equations to their own experimental results as well as to the results of other researchers. (Adams *et al.*, 1988; Bader *et al.*, 1988; Martin *et al.*, 1992; Werther *et al.*, 1992a; Guilin *et al.*, 1984; van Zoonen, 1962). The best values of the constants are:

$$c_1 = 1.4 \times 10^{-6}, \quad c_2 = -1.14, \quad c_3 = -1.3, \quad c_4 = 1.85$$

Equation 1.8 gives a reasonable prediction of radial dispersion coefficient over a wide variety operating conditions.

Mastellone and Arena (1999) investigated the effects of the particle size and density on the radial gas mixing in CFBs. They found out that the radial dispersion coefficient decreases with increasing particle density and diameter.

Recently, Namkung and Kim (2000) proposed the following correlation for the radial gas mixing coefficient based the isotropic turbulence theory:

$$Pe_{r,d_p} = 153.10 \left(\frac{d_p}{d_t} \right)^{0.96} \left(\frac{U_o}{U_{slip}} \right)^{3.73} \quad (1.9)$$

where $Pe_{r,dp}$ is the radial Peclet number based on the particle diameter and superficial gas velocity and U_{slip} is the average slip velocity, i.e., $U_{slip} = U_o/\alpha_g - U_s$. The correlation depends on their own experimental data as well as the data from the previous studies covering a range of:

$$2.5 \times 10^{-4} \leq d_p/d_t \leq 6.9 \times 10^{-3} \quad \text{and} \quad 1.3 \leq U_o/U_s \leq 4.1$$

Table 1.5. Major lateral gas mixing studies in CFBs

Researchers	Tracer Gas	Riser Size	Particle Properties	Operating Conditions
Guilin <i>et al.</i> (1984)	He	0.115 m ID 8 m high	Silica Gel $d_p = 220 \mu\text{m}$ $\rho_s =$ not mentioned	$U_o = 2.8\text{-}5.5 \text{ m/s}$ $G_s = 32\text{-}160 \text{ kg/m}^2\text{s}$
Adams (1988)	CH ₄	0.3 m \times 0.4 m 4 m high	Dolomite $d_{sv} = 200 \mu\text{m}$ $\rho_s =$ not mentioned Sand $d_{sv} = 250 \mu\text{m}$ $\rho_s = 3300 \text{ kg/m}^3$	$U_o = 3.8\text{-}4.5 \text{ m/s}$ $G_s = 30\text{-}45 \text{ kg/m}^2\text{s}$
Werther <i>et al.</i> (1992a)	CO ₂	0.4 m ID 8.5 m high	Sand $d_s = 130 \mu\text{m}$ $\rho_s = 2300 \text{ kg/m}^3$	$U_o = 3\text{-}6.2 \text{ m/s}$ $G_s = 0\text{-}70 \text{ kg/m}^2\text{s}$
Martin <i>et al.</i> (1992)	He	0.19 m ID 11.7 m high	FCC Catalyst $d_p = 62 \mu\text{m}$ $\rho_s = 1560 \text{ kg/m}^3$	$U_o = 3.8\text{-}6.8 \text{ m/s}$ $G_s = 40\text{-}225 \text{ kg/m}^2\text{s}$
Zheng <i>et al.</i> (1992)	CO ₂	0.102 m ID 5.25 m high	Resin, Sand Sand $d_p = 701 \mu\text{m}$ (Resin) $d_p = 570 \mu\text{m}$ (Sand) $\rho_s = 1392 \text{ kg/m}^3$ (Resin) $\rho_s = 2560 \text{ kg/m}^3$ (Sand)	$U_o = 2\text{-}10 \text{ m/s}$ $G_s = 0\text{-}30 \text{ kg/m}^2\text{s}$
Amos <i>et al.</i> (1993)	Sulphur hexafluoride	0.305 m ID 6.6 m high	Alumina $d_p = 71 \mu\text{m}$ $\rho_s = 2450 \text{ kg/m}^3$	$U_o = 2.6\text{-}5.0 \text{ m/s}$ $G_s = 20\text{-}120 \text{ kg/m}^2\text{s}$
Gayan <i>et al.</i> (1997)	CO ₂	0.1 m ID 4 m high	Sand $d_p = 380$ and $710 \mu\text{m}$ $\rho_p = 2600 \text{ kg/m}^3$	$U_o = 5\text{-}8 \text{ m/s}$ $G_s = 0\text{-}115 \text{ kg/m}^2\text{s}$
Mastellone and Arena (1999)	CO ₂	0.120 m ID 5.75 m high	FCC, Ballotoni and Sand $d_p = 70, 89, 310 \mu\text{m}$ $\rho_p = 1770, 2540, 2600 \text{ kg/m}^3$	$U_o = 6 \text{ m/s}$ $G_s = 16\text{-}55 \text{ kg/m}^2\text{s}$
Namkung and Kim (2000)	CO ₂	0.1 m ID 5.3 m high	Sand $d_p = 125 \mu\text{m}$ $\rho_p = 3055 \text{ kg/m}^3$	$U_o = 2.5\text{-}4.5 \text{ m/s}$ $G_s = 0\text{-}53 \text{ kg/m}^2\text{s}$
Sterneus <i>et al.</i> (2000)	He	Boiler 1.7 \times 1.4 m 13 m high Cold model 0.12 \times 0.7 m 8.5 m high	Boiler, Cold Model Sand $d_p = 320 \mu\text{m}$ $\rho_p = 2600 \text{ kg/m}^3$	Boiler $U_o = 1.2\text{-}4.3 \text{ m/s}$ Cold Model $U_o = 1\text{-}6 \text{ m/s}$ $G_s = 0\text{-}35 \text{ kg/m}^2\text{s}$

Sterneus *et al.*, (2000) carried out lateral gas mixing experiments using helium as the tracer gas in a small scale CFB boiler and a cold model CFB riser, both having a rectangular cross-section. They obtained lateral dispersion coefficients ranging between 100-230 cm²/s in the boiler and 20-90 cm²/s in the cold unit, which are high compared to the values of the previous studies in circular risers with high aspect ratios. It should be mentioned that Adams (1988) also obtained lateral dispersion coefficient values close to that of Sterneus *et al.* (2000) around 50 cm²/s in a rectangular riser and there is a tendency for the radial gas dispersion coefficients to increase with riser diameter (Namkung and Kim, 2000). In the cold unit, with increasing solids loading (solids circulation rate), Sterneus *et al.* (2000) observed an increase in the value of the lateral dispersion coefficient up to plateau value after which it almost remains constant which is in contradiction with the findings of Zheng *et al.*, (1992). They attributed this difference to the large scale motions caused by the bubble eruptions observed in the cold model².

4.5.1. Gas Mixing in CFBs with SA injection

There are only a few studies in the literature on the effects of the SA injection on gas mixing in CFBs. Table 1.6 summarizes these studies.

Zheng *et al.* (1992) carried out experiments to investigate the radial mixing with SA injection using CO₂ as a tracer gas. Utilizing a secondary-to-primary air ratio of 2.3, collecting data at a height of 0.6 m to 2 m above the SA injection ports, they found out that the gas dispersion in the riser is enhanced by the SA injection jets. They also stated that the effect of SA injection quickly dissipates with increasing solids concentration. However, there was no information about the type of the injector that they used in their study.

² Leckner (1998) presents a discussion on the fluidization regime observed in the bottom section of CFB risers with low height-to-diameter ratio. He argues that the bottom bed remains in bubbling fluidization mode even at high velocities contrary to turbulent and/or fast fluidization regimes observed in laboratory scale risers with high height-to-diameter ratio.

Marzochella and Arena (1996a) studied the mixing of lateral air injection with the rising gas-solid suspension. The tracer gas, CO₂, was first mixed with the SA stream and injected into the riser with two types of injectors, C and R1 according to the classification given in Figure 1.2. They measured the concentration at the downstream and upstream of the injection location. The tracer concentration profiles revealed that both injection modes resulted in completely different patterns of gas mixing. With the circumferential gas injection (type C), no gas backmixing was detected below the injection port. With the radial injection (type R1), the mixing of the injected gas with the gas-solid flow took place at a shorter axial distance than the case with the circumferential (R1) injection.

Recently, Namkung and Kim (2000) investigated the effects of the SA injection on gas mixing with radial and tangential injectors (T3 and R3). They obtained an increase in the radial gas dispersion coefficient with SA which is more pronounced with tangential injection. This was attributed to the increase in solids holdup with tangential injection since their measurements showed an increase in radial dispersion with solids loading without SA injection.

Table 1.6. Studies on the gas mixing in CFB risers with SA injection

Researcher (s)	Tracer Gas	Riser Size	Particle Properties	SA Injector	Operating Conditions	Aspect Studied
Zheng <i>et al.</i> (1992)	CO ₂	0.102 m ID 5.25 m high	Sand $d_p=570 \mu\text{m}$ $\rho_s = 2560 \text{ kg/m}^3$	No information	$U_0 = 4-6 \text{ m/s}$ $G_s = 0-30 \text{ kg/m}^2\text{s}$	Radial gas mixing
Marzochella and Arena (1996a)	CO ₂	0.12 m ID 5.75 m high	Ballotoni $d_p=89 \mu\text{m}$ $\rho_s = 2540 \text{ kg/m}^3$	C, R1	$U_0 = 6 \text{ m/s}$ $G_s = 35-55 \text{ kg/m}^2\text{s}$	Mixing of SA with rising suspension
Namkung and Kim (2000)	CO ₂	0.1 m ID 5.3 m high	Sand $d_p=125 \mu\text{m}$ $\rho_p = 3055 \text{ kg/m}^3$	T3, R3	$U_0 = 2.5 - 4.5 \text{ m/s}$ $G_s = 0-53 \text{ kg/m}^2\text{s}$	Radial gas mixing

5. Significance of the Study

Most of the studies on various aspects of CFBs were carried out by feeding the fluidizing gas through the bottom of the riser only (Arena, 1997). The existing studies with SA injection have mostly addressed the effects of SA on the emissions from CFB combustors and the solid phase hydrodynamics, i.e., the axial pressure drop, suspension density and particle velocity profiles. There are only a few studies on gas phase hydrodynamics with SA injection, i.e., dispersion of gas with SA injection and the mixing phenomena of SA with the rising gas-solid suspension. As shown in this chapter, gas mixing is an important design consideration in the design of CFB reactors.

On the modeling side, to the author's knowledge, there is not a hydrodynamic model for CFB risers operated with air staging except that of Ersoy (1998), which is an extension of core-annular type models. Thus, there is a need for a study which will provide further information on the effects of SA injection on gas mixing and a modeling approach applicable to CFB risers with SA injection.

6. Objectives of the Study

The objectives of the work carried out in this thesis are:

- a) To carry out an experimental study to quantify and provide a better understanding of the effects of SA injection on gas mixing in CFB risers.
- b) To determine the radial dispersion coefficients which are used in reactor design calculations in CFBs with SA injection.
- c) To determine the mixing patterns of the SA with rising gas-solid flow for different SA injection devices.
- d) To propose a mathematical model which will describe the hydrodynamics of gas-solid flow in CFBs with SA injection and be able to predict the available experimental data.

7. Methodology

The tracer gas technique is used to study the gas mixing in a laboratory scale CFB riser with three different SA injectors. A computational fluid dynamics (CFD) model is implemented with Fluent 4.5, Fluent Inc., to simulate the riser flow in CFBs with SA injection.

8. Scope of the Study

This study is limited by the operating conditions of the CFB boilers. The superficial gas velocity and solids circulation rate are chosen such that they match their typical values in a CFB boiler. Thus, dense gas-solid flow regimes observed in FCC reactors are not considered.

9. Structure of the Thesis

The summary of the work carried out to form this thesis is outlined in Figure 1.6. The contents of the individual chapters are as follows:

Chapter 2: The radial/lateral gas dispersion theory is reviewed and the mean square displacement model (MSDM) used to calculate the dispersion coefficients is explained.

Chapter 3: The experimental set up, procedure, measurement system are discussed in detail.

Chapter 4: The results of the experiments are presented with a detailed discussion.

Chapter 5: The two-fluid gas-solid flow model is presented with underlying assumptions.

Chapter 6: The application of the two-fluid model to CFB riser flow is given.

Chapter 7: The general conclusions are presented.

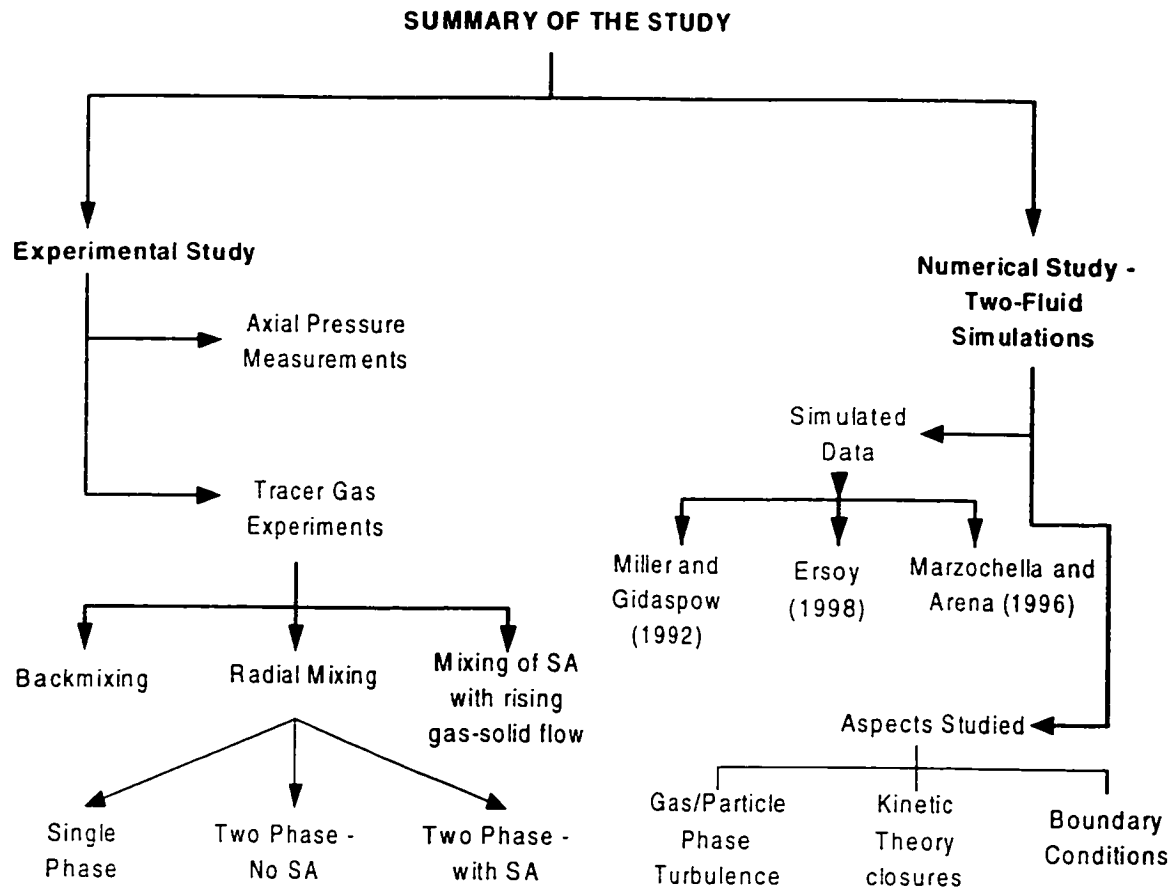


Figure 1.6. Summary of the work carried out in this study.

Chapter 2

Theory

1. Introduction

As presented in Chapter 1, the quality of mixing is often described by dispersion coefficients in fluidized beds. The dispersion coefficients, radial, backmixing or axial, are calculated from corresponding tracer gas experiments. The common procedure for finding the dispersion coefficients can be outlined as follows: First, an adequate mixing model that can describe the relevant mixing phenomenon is proposed or described. Then, the results of the tracer gas experiments are fitted to the model in order to find the adjustable parameter(s) which are usually the dispersion coefficients. Once the dispersion coefficients are found, the available model can be used as a predictive tool with the known (calculated) dispersion coefficients. One major and inevitable disadvantage of this approach is the dependency of the dispersion coefficients on the model that they are derived from as argued by Amos *et al.* (1995). The calculated dispersion coefficients can also be used in more sophisticated models as shown by Kruse *et al.* (1995).

In this chapter, two methods to calculate the radial dispersion coefficients in pipe flows which can also be applied to circulating fluidized risers are presented. As both of the methods depend on the eddy dispersion concept, first an introduction about it is given. Then, the methods are presented. The chapter ends with a conclusion.

2. Eddy Dispersion Concept for Gas Mixing

The basic mechanisms of gas dispersion in CFB risers were described in Chapter 1. In the direction normal to the mean gas flow in CFB risers, the gas transport or dispersion is mainly due to the mixing and blending of the turbulent eddies. Turbulence is characterized by rapid and highly irregular motion of the fluid when a threshold Reynolds number is exceeded. Contrary to laminar flow in which the molecular diffusion being the only mechanism for heat, mass, and momentum transfer, in turbulent flows, three-dimensional vortices or eddies with different sizes continually form, mix, stretch, and fragment at different frequencies. The vigorous motion of these eddies increase the transfer of mass, momentum, and heat transfer between the fluid layers to such a degree that the molecular diffusion is often neglected. The transport of the mass, heat, and momentum via eddies in a turbulent flow is known as turbulent dispersion.

A complete understanding of turbulent dispersion depends on a complete description of the gas phase turbulence, covering all eddies with different sizes. There is no general mathematical theory yet, which provides that information even in single phase flows.

The statistical theory of turbulence tries to simplify this complex picture by introducing the concept of "scale" and represents the spectrum of eddy sizes and energies by a single characteristic or average eddy size. It can be shown that the largest scale eddies, whose sizes are comparable to the size of the vessel, are responsible for most of the turbulent transport. They are the eddies which continually extract kinetic energy from the mean motion by shear and transferring it to smaller eddies by vortex stretching (Tennekes and Lumley, 1972; Hinze, 1975). Thus, most of the turbulent energy is associated with those large scale eddies. On the other hand, the smaller scale eddies (still larger than the molecular scale) are responsible for dissipating this energy into heat.

In the light of the arguments given in the previous paragraph, the eddy dispersion concept is used to model the transport of momentum, heat, and mass by the large scale and most energetic eddies. The transport mechanism is assumed to be similar to molecular diffusion, albeit at a larger scale. The turbulent momentum transport at a direction normal

to the mean flow is expressed as:

$$\tau_n = -\rho v_t \left(\frac{\partial U}{\partial n} \right) \quad (2.1)$$

where U is the mean flow velocity, n is the direction normal to the mean flow, ρ is fluid density, and v_t (m^2/s) is turbulent eddy momentum dispersion coefficient or the so-called eddy viscosity. Unlike the molecular kinematic viscosity, the turbulent viscosity is a function of the size and the velocity of the large scale eddies, mean velocity, and its gradient, geometry of the vessel, etc., i.e., the flow conditions. It can be seen as a coefficient of momentum transport.

The turbulent mass transfer or dispersion can be also described with the same analogy. The total molar flux of species, A , in the direction normal to the mean gas flow is expressed by the product of a turbulent eddy mass dispersion coefficient and the concentration gradient:

$$J_A = -D \frac{\partial C_A}{\partial n} \quad (2.2)$$

where J_A is molar flux of species A ($\text{kmol}/\text{m}^2\text{s}$), D is dispersion coefficient (m^2/s) and C_A is the molar concentration of species A (kmol/m^3). Equation 2.2 is the same as the Fick's law of molecular diffusion if D is replaced by binary molecular diffusion coefficient. Similar to eddy viscosity, the turbulent eddy mass dispersion coefficient is also a function of the flow properties.

Both mass and momentum turbulent dispersion coefficients can be related to each other with a non-dimensional turbulent Schmidt number:

$$Sc = \frac{v_t}{D} \quad (2.3)$$

For single phase pipe flows, the Schmidt number lies between 0.7 to 1.0 for a wide range of Reynolds number (Sherwood *et al.*, 1975). For two-phase gas solid flows in pipes, such data do not exist, thus, Equation 2.3 can not be used to estimate one of the

dispersion coefficients once the other one is known. The real challenge is actually to find the eddy dispersion coefficients since they implicitly contain the effects of the particles.

In the next section, two methods to calculate the turbulent eddy mass dispersion coefficient based on the experimental tracer gas measurements are presented.

3. Radial Dispersion Coefficients

There are basically two approaches to calculate the radial gas dispersion coefficients and interpret the radial mixing data in fluidized beds:

1. Dispersed plug flow model (DPFM) (Adams, 1988; Werther *et al.*, 1992a, b; Gayan *et al.*, 1997; Mastellone and Arena, 1999; Namkung and Kim, 2000)
2. Mean square displacement model (MSDM) (Jovanovic *et al.*, 1980; Streneus *et al.*, 2000)

Generally speaking, both of these models depend on the eddy dispersion concept of turbulent flows. The difference between them lies in the underlying assumptions in the model development stage.

3.1. Dispersed Plug Flow Model (DPFM)

DPFM is derived from the general convection-diffusion equation. The transport of the tracer in the medium in which it is injected into, assuming constant density, can be written as (Bischoff and Levenspiel, 1962; Naumann and Buffham, 1983):

$$\frac{\partial C}{\partial t} + \mathbf{V} \cdot \nabla C = \nabla \cdot (D \nabla C) \quad (2.4)$$

where C is the concentration of the species under consideration, \mathbf{V} is a three-dimensional velocity vector of the carrier phase and D is a dispersion coefficient. The second term on the left hand side of the equation represents the transport of the tracer gas with mean gas flow, whereas the term on the right hand side is the dispersion term.

The dispersion coefficient, in its most general form, is a function of concentration, position, and time. As explained above, for a laminar flow, Equation 2.4 can be a

transport equation if D is a molecular diffusivity. If one defines an eddy dispersion, Equation 2.4 can well represent the transport in turbulent flows (Naumann and Buffham, 1983).

To solve Equation 2.4, the velocity field of the carrier phase and the dispersion coefficients at every point in the domain should be known *a priori*. However, in almost all cases, the flow is turbulent, neither the carrier phase hydrodynamics is known completely nor the dispersion coefficients are available. Paradoxically, they are the parameters which are sought. Thus, assumptions are to be made to simplify the problem and derive a simpler equation from Equation 2.4, which has an analytical solution.

In radial gas mixing experiments in CFB risers, the tracer gas is introduced as a point source on the riser axis. Using cylindrical coordinates as shown in Figure 2.1, the following assumptions are made to simplify Equation 2.4 for the spread of the tracer:

1. The flow is steady.
2. The mean gas flow is upwards (z direction) and uniform across the cross-section. There are no components of gas velocity in radial and circumferential direction (i.e., $V_r = V_\theta = 0$)
3. The axial and circumferential dispersion of the tracer gas is ignored (i.e., $D_{ax} = D_\theta = 0$)
4. The radial dispersion coefficient is not a function of time, concentration and position; hence constant (homogenous dispersion)
5. The gas flow field, hence the spread of the tracer gas, is axi-symmetric.

With the above assumptions, Equation 2.4 can be simplified to:

$$0 = -\frac{U_o}{\alpha_g} \frac{\partial C}{\partial z} + D_r \frac{\partial}{\partial r} \left(r \frac{\partial C}{\partial r} \right) \quad (2.5)$$

where U_o/α_g is the average interstitial gas velocity and the D_r is average radial dispersion coefficient.

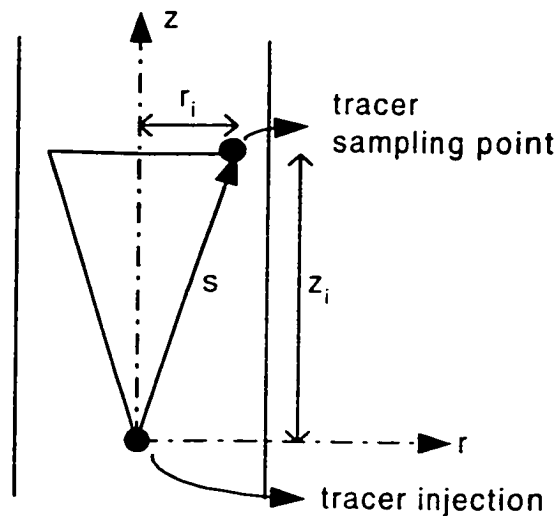


Figure 2.1. The parameters used in dispersed plug flow model

The boundary conditions can be expressed as:

$z \rightarrow -\infty, C = 0$; no gas backmixing

$z \rightarrow \infty, C = C_o = \frac{\dot{Q}_t}{\dot{Q}_{gas}}$; uniform distribution of the tracer gas

$r = R, \frac{\partial C}{\partial r} = 0$; zero flux at the wall (2.6)

$r = 0, \frac{\partial C}{\partial r} = 0$; symmetry

$z = 0, r = 0, C = C_i$; C_i is the injection concentration of the tracer

In Equation 2.6, Q_t and Q_{gas} are the flowrates of the tracer and the fluidization gas, respectively. C_o is called the mean-mixed concentration and represents the uniform concentration that would be measured far from the tracer injection point when the tracer gas is completely and uniformly dispersed. A more detailed discussion on C_o is given in the next chapter.

Due to the low solids volume fraction, the interstitial gas velocity term (U_o/α_g) can be approximated by the superficial gas velocity, U_o (Adams, 1988; Gayan *et al.*, 1997; Mastellone and Arena, 1999; Namkung and Kim, 2000). Werther *et al.* (1992a, b), on the

other hand, defined a core radius and a uniform core velocity (instead of the superficial gas velocity) based on this radius and used it in their dispersed plug flow model.

The exact analytical solution of Equation 2.5 was originally derived by Klinkenberg *et al.* (1953) based on Bessel functions. An approximate solution of Equation 2.5 based on Wilson's equation of heat conduction was presented by Towle and Sherwood (1939) for the cases of large z_i / r_i where z_i is the distance between injection and sampling ports as (Figure 2.1):

$$C(r, z) = \frac{C}{C_i} = \frac{\dot{Q}_t}{4\pi s D_r} \exp\left(-\frac{U_o(s-z)}{2D_r}\right) \quad (2.7)$$

Thus, the radial distribution of the concentration of the tracer gas at a certain distance above the injection point can be obtained from Equation 2.7 provided that D_r is known. On the other hand, if the tracer concentration distribution is known, then the radial dispersion coefficient can be obtained by fitting Equation 2.7 to the available distribution. This can be easily done by taking the natural logarithm of each side of Equation 2.7 and plotting $\ln(sC/C_i)$ with respect to $(s-z)$. The resulting best fit straight line will have a slope of $-U_o/2D_r$ from which the average value of the radial dispersion coefficient can be calculated (Davies, 1972).

3.2. Mean Square Displacement Model (MSDM)

The MSDM is the solution of the classical molecular diffusion problem which dates back to the beginning of 20th century. Based on the studies of Scottish botanist Robert Brown, the molecular diffusion was found to be a purely stochastic phenomena where the motion of the diffusing fluid particles are random and can be assumed to be independent of each other (Rage, 1996). If an event is random, the statistical properties such as the variance can be easily calculated and the variance of the displacement of the diffusing particles from a source along a line is called the mean square displacement. Einstein (1905) was the first who related the mean square displacement to the molecular diffusion coefficient using Fick's law of diffusion. The application of this theory to turbulent dispersion came with G. I. Taylor (Hinze, 1975). Taylor (1960) showed that using an eddy dispersion

concept, the mean square displacement can be related to the turbulent dispersion coefficient in an isotropic turbulence field. Taylor's theory (Taylor, 1960) is summarized below.

Referring to Figure 2.2, it is assumed that a particle¹ starts moving along a line (x direction) at $t = 0$. After a time step of Δt , the particle stops and remains at some distance away from the origin (shown by station numbers from 1 to i). If a large number of particles behave randomly in the same way, without affecting the progress of the others, a distribution will be obtained on each side of the origin along the line. If the line is assumed to move with the uniform mean flow velocity in the streamwise direction (z direction), the dispersion along the line with time corresponds to dispersion normal to the flow with downstream distance. Thus, the dispersion of a tracer from a continuous point source can be analyzed (Sherwood *et al.*, 1975).

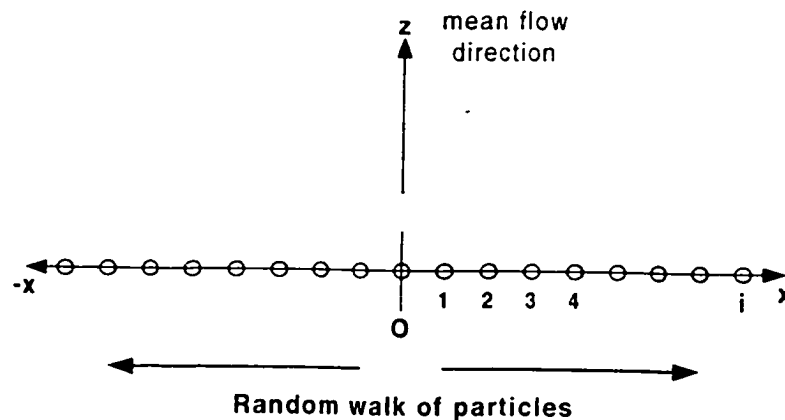


Figure 2.2. Mean square displacement model

Referring to Figure 2.2, the variance of the distribution of all of the particles along a line can be described by the variance of the displacement of the particles, a simple statistical

¹ At this point, the particle is an entity having the same properties as the fluid.

measure, the mean square displacement, $\overline{X^2}$ as:

$$\overline{X^2} = \frac{l}{\sum n_i} \left[\sum_{j=1}^i (n_i (x_i - x_o)^2) \right] \quad (2.8)$$

where n_i is the number of particles accumulated at station i and $x_i - x_o$ is the distance of i^{th} station from the origin. Thus, the distribution with a larger mean square displacement indicates a larger variance, i.e., more particles are able to reach the stations located away from the origin. It should be noted that Equation 2.8 represents a 1-D variance along a line.

The problem now is to relate the mean square displacement to a turbulent dispersion coefficient along the same direction. If u is a point instantaneous velocity in a turbulence field, the instantaneous velocity can be written as the sum of the time averaged mean velocity and the instantaneous fluctuating velocity:

$$u = \bar{u} + u' \quad (2.9)$$

Taylor (1960) related the mean square displacement to the properties of the fluid turbulence through two parameters; the intensity of the velocity fluctuations in the direction normal to the bulk flow (x direction), $\overline{u'^2}$ and the lagrangian integral time scale, τ_L .

The lagrangian integral time scale can be viewed as the time that a particle stays in a large scale eddy before passing to another one and is defined as:

$$\tau_L = \int_0^{\infty} R_L d(\Delta t) \quad (2.10)$$

where R_L is lagrangian correlation coefficient describing the correlation between fluctuating velocities of the same particle at different times, i.e., t and $t + \Delta t$. It is defined as:

$$R_L = \frac{\overline{u'_t u'_{t+\Delta t}}}{u'^2} \quad (2.11)$$

The overbar shows the time averaging.

Taylor (1960) showed that the variation of the mean square displacement in the direction normal to the mean flow as a function of time can be expressed as:

$$\frac{d \overline{X^2}}{dt} = 2 \overline{u'^2} \int_0^{T_d} R_L(\Delta t) d(\Delta t) \quad (2.12)$$

where T_d is the total dispersion time for all the particles to disperse, i.e., for a total of n discrete particles, $T_d = n \times \Delta t$. It should be noted that Equation 2.12 is based on the assumption of a homogeneous turbulence field.

For very short dispersion times, $T_d \ll \tau_L$ (i.e., when the sampling plane is very close to the injection plane), the lagrangian correlation coefficient approaches to unity and the mean square displacement value becomes proportional to the square of the total dispersion time (Brodkey, 1967):

$$\overline{X^2} = \overline{u'^2} T_d^2 \quad (2.13)$$

On the other hand, for very large dispersion times, $T_d \gg \tau_L$ (i.e., when the sampling plane is far away from the injection plane), the mean square displacement value becomes proportional to the total dispersion time (Brodkey, 1967):

$$\overline{X^2} = 2 \overline{u'^2} \tau_L T_d \quad (2.14)$$

For the dispersion occurring at intermediate times, the variation of R_L should be known to carry out the integration in Equation 2.12.

For large dispersion times, Fick's law of diffusion holds and it can be employed for turbulent dispersion analogous to molecular diffusion (Sherwood *et al.*, 1974). Hence, the

turbulent mass dispersion coefficient in the direction normal to the mean flow can now be defined as the product of the lagrangian integral time scale and the intensity of the velocity fluctuations:

$$D_x = \overline{u'^2} \tau_L \quad (2.15)$$

Combining Equations 2.14 and 2.15, the desired relation between the mean square displacement and the turbulent mass dispersion coefficient is obtained:

$$\overline{X^2} = 2 D_x T_d \quad (2.16)$$

The total dispersion time can be estimated as:

$$T_d = \frac{z_i}{U_o} \quad (2.17)$$

Then, the turbulent eddy mass dispersion coefficient can be expressed as:

$$D_x = \frac{U_o \overline{X^2}}{2 z_i} \quad (2.18)$$

For one-dimensional spread along a line, Equation 2.8 can be used to calculate the mean square displacement value. For a pipe flow, the calculation procure is given in the next section.

An estimate of the ratio of the dispersion time, T_d , and the lagrangian integral time scale, τ_L , can be made by considering the corresponding length scales. It is known that the integral length scale of turbulence² is of the order of the characteristic length of the riser. Based on the findings of Hutchinson *et al.* (1971) in a single phase flow, the ratio of the integral length scale of turbulence to the pipe diameter, l_e/d_t , can be taken as 0.1. On the

² The distinction between the Eulerian and Lagrangian length scales is not considered for this simple analysis.

other hand, the characteristic length for the dispersion is the distance between the injection and sampling planes, z_i . In order to have a large dispersion time, if a highly conservative criterion is set such that:

$$\frac{z_i}{l_e} = 10 \quad (2.19)$$

the minimum axial distance at which the sampling probe should be located can be found from the following relation:

$$\frac{l_e}{d_t} = \frac{(z_i / 10)}{d_t} = 0.1 \Rightarrow \frac{z_i}{d_t} = 1 \quad (2.20)$$

Thus, the sampling plane should be at least one pipe or riser diameter away from the injection plane.

3.2.1. Axi-Symmetric Pipe Flow

In case of a pipe flow with a point tracer source on the axis, the spread of the tracer gas can be assumed to be axi-symmetric. Also, the flow area is proportional to r^2 , where r is the radial distance from the pipe axis. In order to find the amount of the tracer gas (number of particles) at any point r , a differential area of $2\pi r dr$ is taken and Equation 2.8 is applied. Then, the mean square displacement in the radial direction, $\overline{R^2}$ can be expressed in integral form as (Flint *et al.*, 1960):

$$\overline{R^2} = \frac{\int_0^{r_m} (2\pi r)(r^2) U(r) c_m(r) dr}{\int_0^{r_m} (2\pi r) U(r) c_m(r) dr} \quad (2.21)$$

where c_m is the measured concentration of the tracer gas and r_m is the radial distance up to which the measurements are carried out. The numerator of Equation 2.21 represents the amount of tracer at any radial location multiplied by the square of the radial distance. The

denominator, on the other hand, is the total volumetric flow rate of the tracer. Thus, Equation 2.21 complies with Equation 2.8.

In an axi-symmetric flow, the mean square displacement in x direction will be equal to the mean square displacement in y direction, hence the following relation can be obtained:

$$\overline{X^2} + \overline{Y^2} = 2\overline{X^2} = \overline{R^2} \Rightarrow \overline{X^2} = \frac{\overline{R^2}}{2} \quad (2.22)$$

Combining Equations 2.21 and 2.22 and assuming uniform flow in radial direction, i.e., $U(r) = U_0$, the mean square displacement value can be expressed as:

$$\overline{X^2} = \frac{\overline{R^2}}{2} = \frac{l}{2} \frac{\int_0^{r_m} r^3 c_m(r) dr}{\int_0^{r_m} r c_m(r) dr} \quad (2.23)$$

Thus, Equations 2.18 and 2.23 can be used to obtain the average radial dispersion coefficient in the riser under axi-symmetric flow conditions.

4. Conclusions

In this chapter, two models to calculate the radial dispersion coefficients from experimental measurements are presented. Both models depend on the eddy dispersion concept. The DPFM is a simplified version of the general convection diffusion equation whereas the MSDM depends on the Taylor's theory of turbulent dispersion. The tracer gas data from the experiments is applied to both of models and the relevant results and discussions are presented in Chapter 4.

Chapter 3

Experimental Set-up, Instrumentation, and Procedure

1. Outline of the Chapter

This chapter describes the experimental set-up, instrumentation, and methodology used in this study. The tracer gas technique is used to study the gas mixing phenomena in a laboratory scale CFB riser with SA injection. Hence, the tracer gas technique is first introduced. Then, the experimental set-up (riser and SA ports) is described. Finally, the instrumentation and the experimental procedures are presented.

2. The Tracer Gas Technique

Tracers are often used to obtain information on the mixing characteristics or residence time distribution of a reactor (Louge, 1997). By definition, a tracer is a material used to represent the flow properties of the substance into which it is injected. Ideally, a perfect tracer should have exactly the same flow properties as the substance it represents but at the same time should bear a non-flow characteristic which can be easily detected by an analytical instrument (Nauman and Buffham, 1983).

For solids and gas mixing studies in fluidized beds, different types of solid and gas tracers have been used. The substances such as sodium chloride (NaCl), ferromagnetic particles,

fluorescent dye and irradiated sand have been utilized successfully as solid tracers in CFB risers (Werther and Hirschberg, 1998). Similarly, gases such as argon, helium, CO₂, hydrogen, methane, and ozone have been very commonly employed in gas mixing studies in CFB risers as mentioned in Chapter 1.

To study the hydrodynamics of gas motion in fluidized beds, almost any gas or volatile liquid can be used as a tracer if there is a suitable detector. Linearity, detectability, and adsorption characteristics of the tracer gas on the solids particles are the aspects that should be considered while selecting a tracer gas. Adsorption is the phenomenon of binding of gas molecules to the surfaces of the solid particles. When this happens, the tracer gas travels with the solid particles as well as the gas that it is supposed to represent, which is, of course, not desirable. Namkung and Kim (1998) showed the effects of the adsorption on gas backmixing in a lab scale CFB when CO₂ was used as the tracer gas with FCC particles.

In this study, CO₂ was chosen as the tracer gas because of its low cost, safety of operation and ease of analysis. The concentration of CO₂ can be accurately measured with an infrared gas analyzer. As far as its adsorption characteristic is concerned, it was shown that the adsorption effects of CO₂ are negligible for sand fluidized beds (Yates and Simmons, 1994).

3. The Experimental Set-Up

3.1. The CFB Assembly

The experiments were carried out in a cold model CFB assembly as shown in Figure 3.1. Both the riser and the downcomer are made of plexiglass. The riser has an ID of 0.23 m and a height of 7.6 m. The fluidization air is supplied by a Roots type blower (Universal Rai - frame size 56) operating at 2850 rpm. The maximum flow rate obtained from the blower is approximately 0.3 m³/s, corresponding to a superficial gas velocity of approximately 5.0 m/s in the riser.

The fluidization air is fed to the CFB assembly with a 0.1 m ID PVC pipe, branched into four streams; the primary air, the secondary air, the loop seal aeration, and the bypass pipe. The primary air and the loop seal aeration flow rates are controlled by a 10-position butterfly valve. The secondary air flow rate is adjusted with two slider valves and the bypass line is controlled with a ball valve. Extra horizontal aeration can also be supplied to the loop seal as shown in Figure 3.1.

The solids are recycled to the riser via 0.152 m ID horizontal return leg connecting the loop seal and the riser. The solids circulation rate is controlled by adjusting the amount of aeration in the loop seal. At the top, a 0.32 m ID and 1.33 m high vertical cyclone separates the solids and the gas. The connection between the cyclone and the riser is established with a flexible hose that provides a smooth exit from the riser. Fine particles, which can not be captured by the cyclone, are transported to the bag filters housed in a box with dimensions 0.5 m \times 0.5 m \times 1 m, and returned to the downcomer via a PVC pipe.

3.2. SA Injection Port

The modular secondary injection port used in the experiments was designed by Ersoy (1998). It consists of a steel body (0.23 m ID, 0.14 m high) and two identical and symmetrically placed injector openings around the periphery to assemble the injector heads as shown in Figure 3.2. When the injector heads are assembled, the SA can be injected laterally into the riser from two points. Each injector head is welded to a 0.0397m ID and 0.4 m long steel pipe connected to the main supply line via flexible tubing, and a 0.0397 m ID and 0.5 long PVC pipe. The injector opening was designed to host three different types of injector heads that provide different air injection modes to the riser; tangential (swirl), radial, and mixed. The orientations of the three different injectors with respect to the riser cross-section are given in Figure 3.3. In tangential injection, the SA enters the riser with a circumferential velocity component. In case of radial injection, two SA jets impinge on each other. With the mixed injector, the SA gains both tangential and radial velocity component before entering the riser.

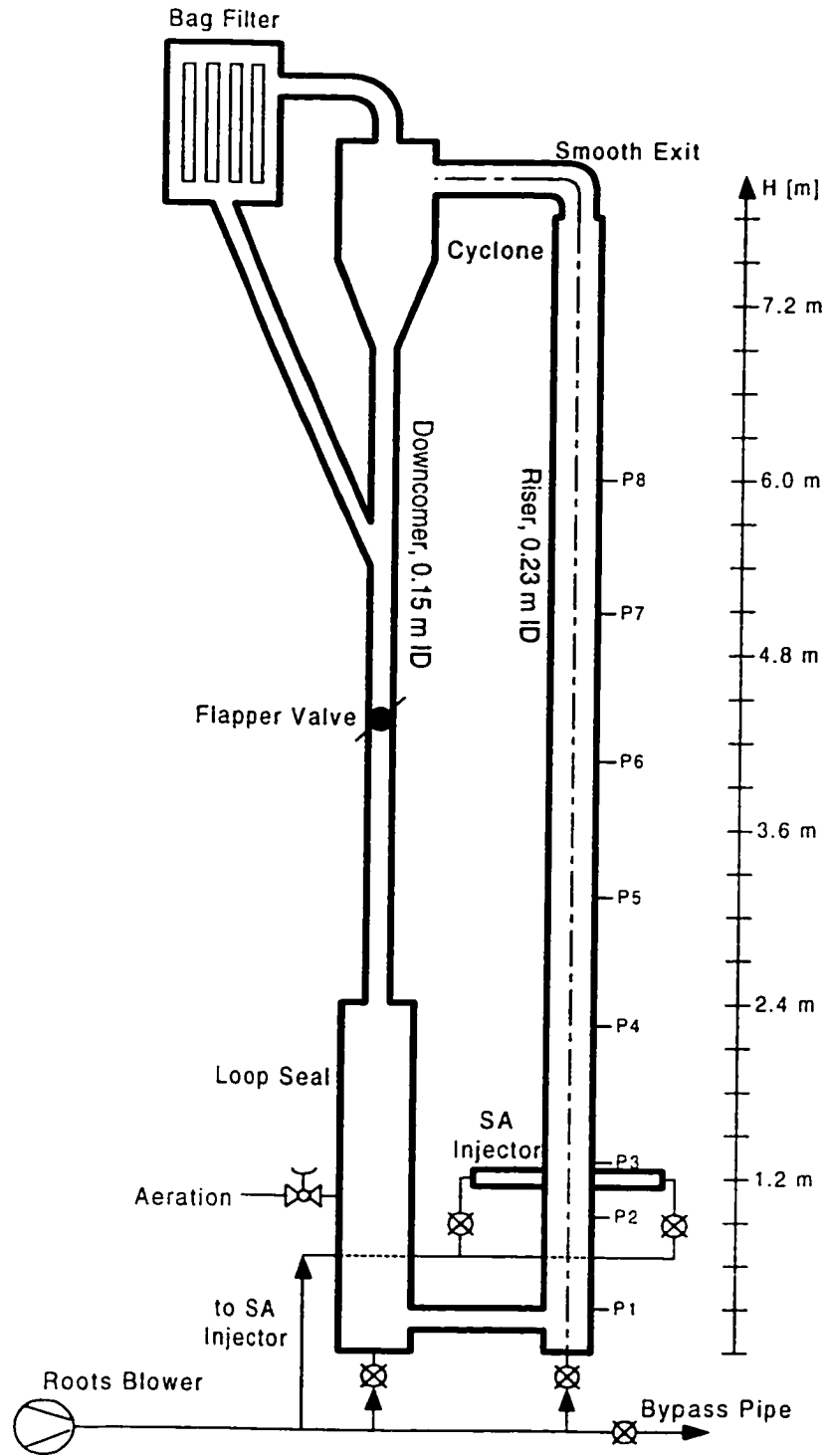


Figure 3.1. DalTech CFB riser

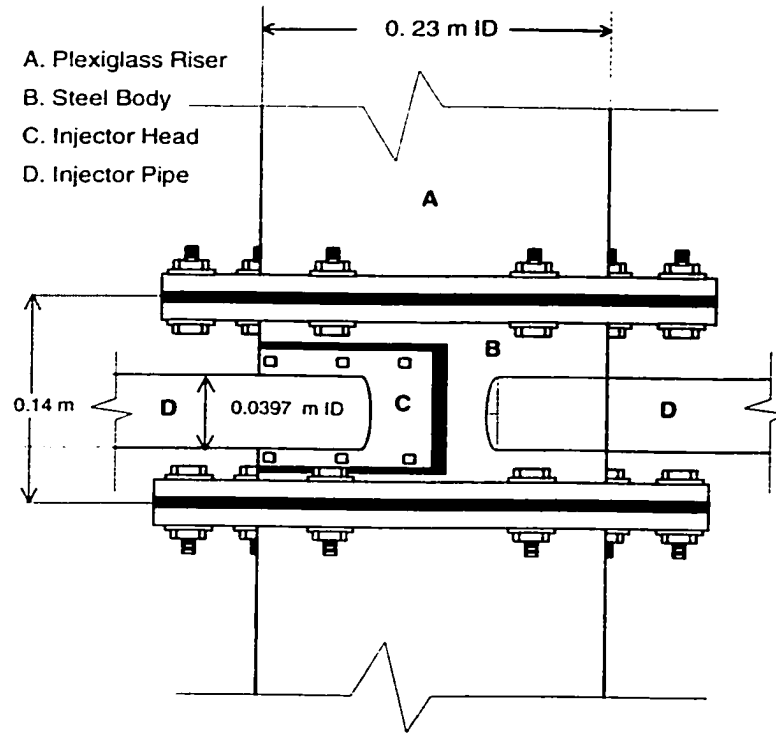


Figure 3.2. Modular SA injection port (Ersoy, 1998)

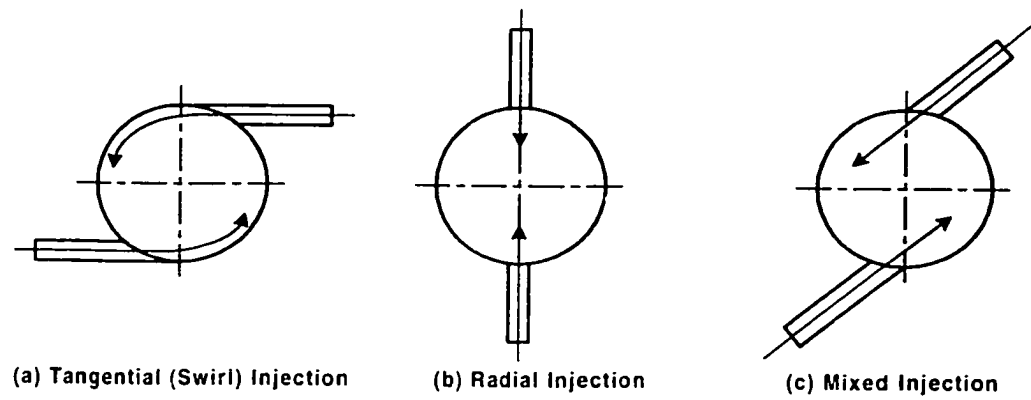


Figure 3.3. Types of SA injectors used in this study

4. Gas Injection and Sampling System

The schematic view of the tracer gas injection and sampling system is given in Figure 3.4. The tracer gas injection apparatus consists of a cylinder in which CO_2 is stored in liquid form, a flow meter to measure its flow rate, and an injection probe. The sampling line consists of a sampling probe, a flow meter to measure the flow rate of the sampled gas, a vacuum pump to suck the gas, a filter to prevent the fine particles from entering the gas analyzer, an infrared gas analyzer, and a personal computer (PC). Nylon tubing with a negligible permeability is used all throughout the injection and sampling system. The injection probe is made of copper and is composed of two welded tubes of ID of 8 mm and 14 mm, respectively, (Figure 3.5). A stainless steel filter with a pore size of $60\ \mu\text{m}$ is welded to the tip of the injection probe to avoid jet formation and prevent the solids entering the injection line. The sampling probe is also made of a copper tube with an ID of 5 mm. Its tip is covered with a cloth filter.

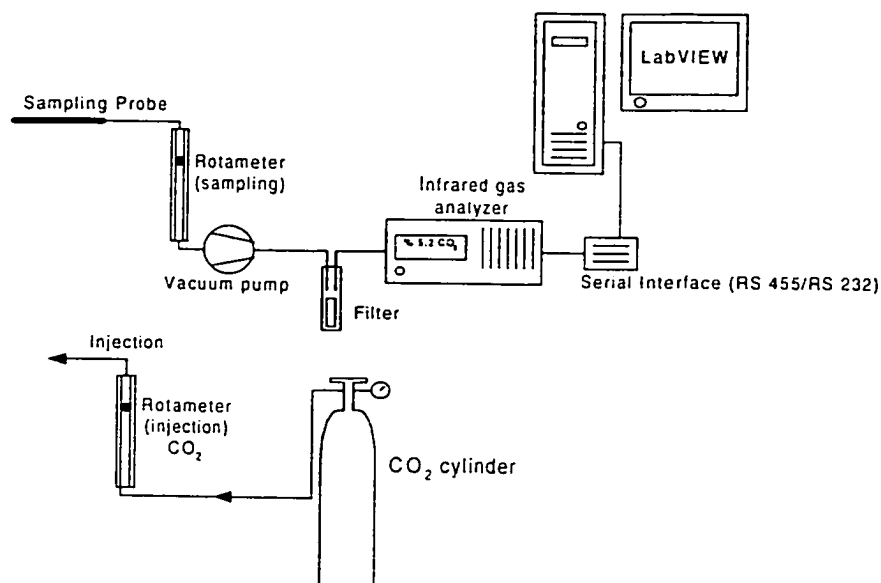


Figure 3.4. The layout of the gas injection and sampling apparatus used in the experiments

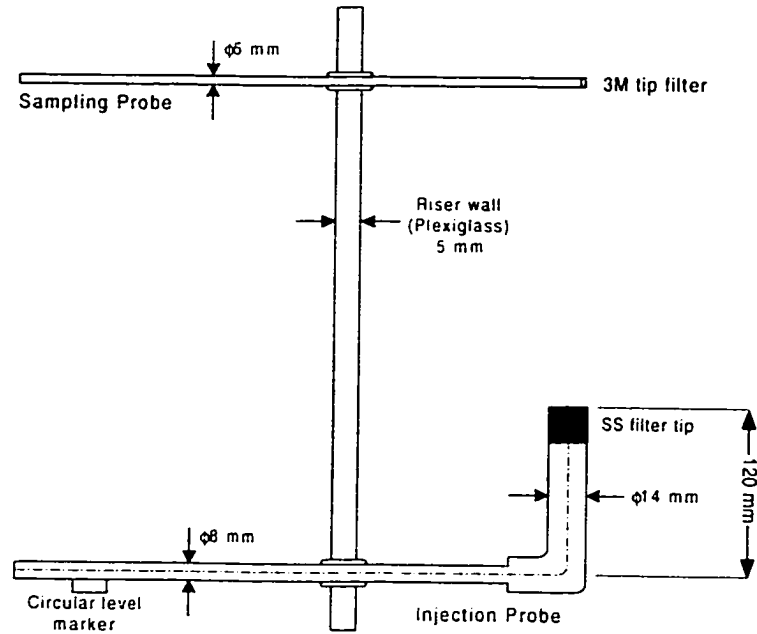


Figure 3.5. Injection and sampling probes used in the experiments

5. Instrumentation

During experiments, the following parameters were continuously recorded, controlled, and measured:

1. Primary and SA flow rates,
2. Differential pressure measurements from eight successive, axially located pressure ports,
3. Solids circulation rate,
4. Flow rate of the sampling gas and the injected tracer,
5. CO₂ concentration in the sampling gas

In the following sections, each of the above items is discussed in detail.

5.1. Air Flow Rate Measurements

The primary and SA flow rates were measured by three pitot tubes by Dwyer Instruments, Inc. The differential pressure from each of the pitot tube was measured by a differential

pressure transducer having a range of 0-5 inches water column (Omega PX164 – 005D5V). The calibration of the pressure transducer is given in Appendix C. The average air velocity in each of the corresponding pipe was found from the correlation suggested by the manufacturer as:

$$V = 1096.2 \sqrt{\frac{\Delta P}{\rho_{air}}} \quad (3.1)$$

where V is the velocity in ft/sec, ΔP is the differential pressure in inches of water and ρ_{air} is the air density in lb/ft³. The flow rates were then obtained by multiplying the average velocity with the pipe cross-sectional area.

5.2. Time Averaged Differential Pressure Measurements

Static gas pressure is an easily measurable quantity in lab scale CFBs. By having consecutive pressure ports along the height of the riser, one can both measure the absolute gas pressure with respect to the atmosphere or the differential pressure difference between each port. Usually, a cloth filter or a wire mesh screen is used at the entrance of each port to prevent solids entering the pressure line connected to a pressure transducer or a manometer. Table 3.1, as well as Figure 3.1, shows the placement of the eight pressure ports along the riser.

In this study, the differential pressure between each port was measured by a differential pressure transducer having a range of 0-5 inches water column (Omega PX164 – 005D5V). The calibration curve for this transducer is given in Appendix C.

Table 3.1. Distance of the pressure ports from the distributor plate

Pressure Port	Height (m)
1	0.31
2	0.95
3	1.30
4	2.21
5	3.13
6	4.09
7	5.07
8	5.97

5.3. Solids Circulation Rate

The solids circulation rate was measured by a flapper valve in the return line as shown in Figure 3.1. A stop watch was activated with the manual closing of the flapper valve. The flapper valve was kept closed until the solids filled up the desired volume, while the elapsed time was being recorded. The mass flow rate was then calculated by dividing the mass of the accumulated solids with the elapsed time. This procedure was repeated several times during an experimental run to ensure accuracy.

5.4. Sampled and Injected Gas Flow Rates

The flow rates of the injected tracer gas, CO₂, and the sampling gas from the bed were measured by two different flow meters by Cole and Parmer. The flow meters are simply variable area rotameters with floats each having an accuracy of 1% of the full-scale reading. Both flow meters were calibrated by the manufacturer for CO₂ and air. The calibration curves are provided in Appendix C.

5.5. CO₂ Concentration in the Sample Gas

The CO₂ concentration in the sample gas was measured by an infrared red (IR) gas analyzer (Siemens Ultramat 23) produced by Siemens. The gas analyzer measures one infrared gas component, CO₂. It has a measuring range of 0-10% by volume and a resolution of 0.01% by volume which corresponds to 0.1% of the output signal span.

The analyzer uses a spectroscopic method based on the absorption of non-dispersive IR radiation. The working principle of the gas analyzer is given schematically in Figure 3.6. The IR radiation is passed through a continuously flowing sample gas and then measured by three different detectors. The attenuation in the radiation which depends on the wavelength is a measure of the respective concentration of CO₂ in the sample gas. The calibration of the analyzer was carried out with a zero and a span gas. For the zero gas, pure nitrogen gas (N₂) was used and for the span gas a mixture of 5% CO₂ by volume and a 95% N₂ by volume was utilized. The linearization error is given as being less than 1%

of the full-scale by the manufacturer.

According to manufacturer's manual, the sample gas pressure and flow rate should be in the ranges of 0.5 to 1.5 bar and 1.1 to 2 l/min, respectively. The sample gas flow rate puts a constraint on the diameter of the sampling probe as the probe suction velocity affects the measurements. This aspect will be discussed in section 6.

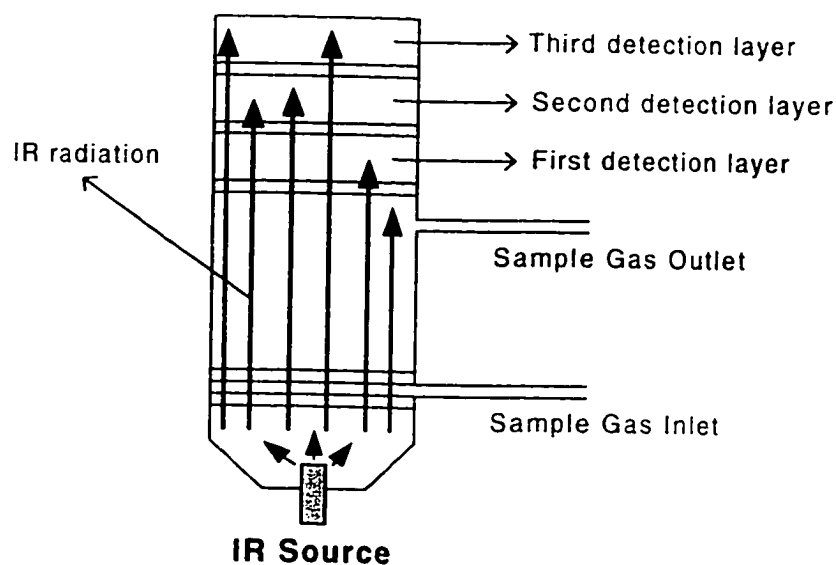


Figure 3.6. The measurement principle of IR gas analyzer

5.6. Data Acquisition System

A data acquisition board, AT-MIO-64E-3 from National Instruments was used to digitize the pressure signals from the two pressure transducers. The data acquisition board has a resolution of 12 bits, can measure 64 single-ended or 32 differential signals with a maximum sampling rate of 500 kHz when only one channel is being used. The control of the data acquisition board and the analysis of the digitized signals were carried out using LabVIEW software by National Instruments.

In air flow rate measurements, the sampling rate was set to be 400 Hz and data was taken for 2 seconds, and this was repeated several times during an experimental run. In differential pressure measurements, the sampling rate and time was set as 400 Hz and 10 seconds, respectively. In this way, almost 4000 data from a port were processed which allowed to capture the steady state behavior of the system. The pressure measurements were also repeated several times during a run.

The need for three transducers for the air flow rates (two for secondary air and one for primary air) and eight transducers (for eight pressure ports) for the static pressure measurements were eliminated by using a multiplexer board consisting of 32 solenoid valves. A LabVIEW program was written to control the solenoid valves; the valves were opened and closed with a specified sequence such that the pressure signals from the pressure ports and the pitot tubes were measured by the same transducer. This method does not, of course, allow simultaneous measurements from all the ports, however, the calibration discrepancies are avoided as all pressure lines are brought to the same transducer.

The CO₂ measurements were carried out on-line. The gas analyzer has a RS-485 serial output. This output was first converted to a conventional RS-232 signal by using an interface converter and then was directly connected to the serial port of a PC as seen in Figure 3.4. A LabVIEW program was written to control the serial port of the PC and analyze the data. The on-line measurement of the concentration of the tracer gas was essential, since in this way the average value at a particular point could be decided easily by monitoring the variation of the instantaneous measurements.

6. Experimental Procedure and Description

Three different types of gas mixing experiments were performed in this study:

1. Radial gas mixing experiments,
2. Gas backmixing experiments,
3. Mixing of SA with rising gas-solid suspension experiments.

Each experimental group differ in the way the tracer gas is injected. For all of them, the gas sampling is performed along the radial direction at different heights with respect to tracer gas injection point. In this section, an overview of the experimental procedure is presented. Aspects specific to each experimental group are discussed in the subsequent sections.

In all of the above experiments, the SA air was injected at a height of 1.2 m above the distributor plate. The bed material used in this study was OO grade Nova Scotia silica sand which has an average sieve diameter of 251 μm and a particle density of 2664 kg/m^3 . The properties of the bed material (size distribution, terminal velocity etc..) can be found in Appendix B. The variation of the operational parameters in the experiments is given in Table 3.2.

Table 3.2. Values of the operational parameters used in the experiments

Parameter	Values
U_o (m/s)	3, 5
G_s ($\text{kg/m}^2\text{s}$)	0, 8, 15, 25
SA/PA	0, 0.2, 0.4
U_{primary} (m/s)	3 – 5
$U_{\text{secondary}}$ (m/s)	0.49 -1.41
$U_{\text{secondary, jet}}$ (m/s)	13.8 – 23.7

With these conditions and the silica sand being used as the bed material, the gas-solid flow structure becomes typical of a CFB combustor; an average suspension density corresponding to a value less than 10 kg/m^3 is obtained along the riser.

A typical experimental run starts with running the bed for 25-30 minutes to ensure steady-state operation. During this period, the solids circulation rate and the air velocities are measured several times. Then, the tracer gas is injected. At every point, the gas is sampled for approximately 2-5 minutes. For the SA operation where the steady-state operation is difficult to achieve, this duration can reach up to 10 minutes. The gas analyzer is able to send two concentration data per second through the serial interface.

Thus, approximately 300-600 data points are averaged at every point to measure the corresponding tracer concentration. For each run, the corresponding static pressure measurements are also carried out.

At any cross-section, to find the radial variation of the tracer concentration, data are taken at 17 radial locations; $r/R = -0.87, -0.7, -0.52, -0.43, -0.35, -0.26, -0.17, -0.09, 0, 0.09, 0.17, 0.26, 0.35, 0.43, 0.52, 0.7, \text{ and } 0.87$ where the centerline is assumed to be the origin (R is the radius of the riser). Thus, the riser radius is traversed from 0.1 m to -0.1 m.

The two point injection of the SA with radial, tangential, and mixed injectors used in this study do not necessarily lead to an axisymmetric flow pattern in the riser. Thus, any measurement such as velocity, solids volume fraction or tracer concentration in the radial direction at any cross-section may depend on the circumferential position. In this study, the gas sampling plane was chosen such that it makes an angle of 45° with the axis of the radial injector as shown in Figure 3.7. This plane was assumed to represent the average behavior of the flow in riser at that cross-section.

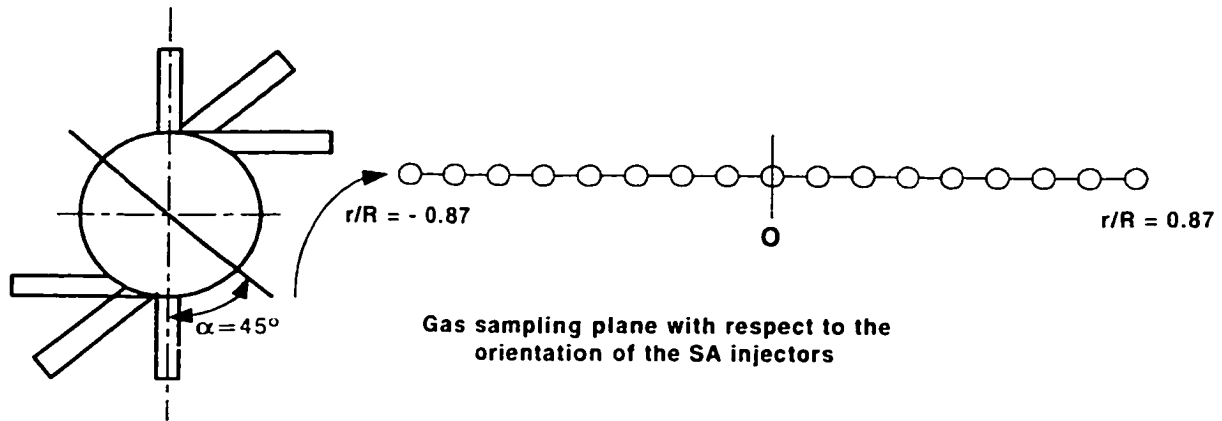


Figure 3.7. The circumferential position of the gas sampling plane on the riser cross-section

6.1. Tracer Gas Flowrate

The amount of the tracer gas injected is an important parameter that should be set *prior* to the experiments. On the design side, as discussed in the subsequent sections, the diameter of the tracer gas injection probe is chosen by considering the total tracer gas flowrate, such that the tracer gas is introduced into the riser at a velocity smaller than the local gas velocity in the riser. On the measurement side, the linearity and the detectability of the measurements are the two factors that should be considered.

The atmospheric air contains CO₂ at an average concentration of 0.04% by volume. Thus, the volumetric flow rate of CO₂ should be adjusted such that it gives a mean mixed concentration that is well above the normal CO₂ composition of air. If the amount of CO₂ in the atmospheric air is taken into account not to introduce error even at low concentrations, the mean mixed concentration, C_o (% volume), can be defined as:

$$C_o = 100 \times \frac{\dot{Q}_{CO_2} + C_{air} \dot{Q}_{air}}{\dot{Q}_{air}} \quad (3.2)$$

where \dot{Q}_{tracer} and \dot{Q}_{air} are the tracer and total fluidization air flow rates and where C_{air} (% volume) is the concentration of CO₂ in atmospheric air. From a physical point of view, C_o is the uniform concentration that would be attained if the tracer were instantaneously mixed with the air inside the riser at the moment of injection. As far as the detection is concerned, C_o should be well above the normal concentration of CO₂ in atmospheric air.

The linearity of the measurements also imposes a constraint on the mean mixed concentration. In order to find out the response of the system with changing tracer injection flow rate, a series of experiments were conducted. In these experiments the tracer gas was injected at the riser axis and its concentration was measured at a distance of 0.4 m above the injection level, again at the riser axis. Figure 3.8 shows the results of these experiments.

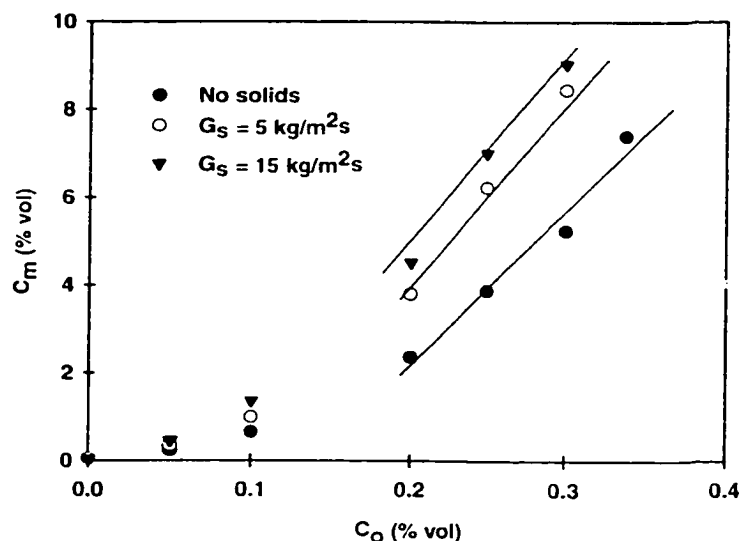


Figure 3.8. Variation of the measured tracer concentration with mean mixed concentration at different solids circulation rates, $U_o = 5 \text{ m/s}$

As can be seen from the figure above, as the mean mixed concentration varies from 0 to 0.35 % vol, the measured tracer gas concentration increases almost exponentially for all of the solids circulation rates at a superficial gas velocity of 5 m/s. Thus, there is a non-linear input-response relationship in the measurement system. For very low values of C_o , (less than 0.05 % vol), linearity exists, however, it is not possible to detect the tracer gas at those low values of C_o because of the presence of CO_2 in the atmospheric air. Figure 3.8 also shows that, if C_o , is chosen between 0.2 to 0.35, the input-response relation is almost linear in that range for all of the cases. This is also a detectable range as far as the CO_2 in atmospheric air is concerned. Thus, in all experiments of this study, the mean mixed concentration was set in this range.

In their gas backmixing experiments, Weinstein *et al.* (1989) used a value of 0.7% vol for C_o whereas Namkung *et al.* (1998) limited it to a value of 0.45% vol. In none of the radial mixing studies reviewed in Chapter 1, C_o was stated explicitly, but from the given

information on the tracer gas flowrates, its value can be calculated as 0.3% vol for Werther *et al.* (1992 a, b) as an example.

Once the mean mixed concentration is set, the required tracer gas flow rate can be calculated for a given superficial gas velocity, U_o , in a bed of diameter d_t , from Equation 3.3 as:

$$\dot{Q}_{CO_2} = \frac{I}{100} \times \left(\frac{\pi d_t^2}{4} U_o \right) (C_o - C_{air}) \quad (3.3)$$

In the above analysis, the contribution of the tracer gas flow rate to the superficial gas velocity is neglected.

6.2. Radial Gas Mixing Experiments

As described in Chapter 1, to obtain information about the dispersion of the tracer gas in the direction normal to the bulk flow, the tracer is continuously injected at a certain height along the riser axis and then gas samples are taken at different radial locations downstream. The resulting tracer concentration curves represent how the tracer gas is dispersed in the radial direction. The location of the injection and the sampling probes along the riser height with respect to axial solids distribution is important since the resulting gas dispersion will depend on the gas-solid regime between the two probes. For instance, if the probes are located in the fully developed region where the axial solids distribution is relatively constant, the information will be specific to that dilute region.

There are several pitfalls that have to be avoided in radial mixing experiments; the tracer gas injection and gas sampling velocities may affect the gas dispersion. For tracer gas injection, the tracer gas velocity at the tip of the injection probe should be less than the local gas velocity since injection at a velocity greater than the maximum gas velocity at the centerline can produce jet formation which in turn increases gas dispersion (Werther *et al.*, 1992). In this study, the injection probe tip diameter was chosen as 14 mm. This ensures a tracer gas velocity which is less than the local gas velocity for all the tracer gas

flow rates and superficial gas velocities used during the experiments. For instance, for a typical tracer gas flowrate of $1.6 \text{ m}^3/\text{hr}$ at a superficial gas velocity of 5 m/s , the tracer injection velocity becomes 2.5 m/s , which is well below the average gas velocity in the riser. Furthermore, a porous stainless steel filter was welded to the tip of the injection probe so that the tracer gas has a uniform entrance to the riser without a jet formation (Figure 3.5).

For gas sampling, in their experiments, Amos *et al.* (1993) did not see any effect of the sampling gas velocity on the radial dispersion coefficients when it was kept smaller than the local gas velocity. The sampling flow rate in this study was determined by the limitations of the gas analyzer; the specifications dictated it to be in the range of $1.1 - 2.0 \text{ l/min}$ and it was set to be between $1.6 - 2.0 \text{ l/min}$ during the experiments. With a sampling probe of 5 mm ID as described in Figure 3.5, the suction velocity at the tip varied between 1.35 and 1.7 m/s with varying suction flow rate. This is a fairly low velocity compared to the superficial gas velocities (3 and 5 m/s) used in this study. Preliminary tests showed no difference in tracer gas concentration as the suction flow rate changed between $1.6 - 2.0 \text{ l/min}$.

As far as the design of the sampling probe was concerned, two different sampling probes were tested, one with a cross-section facing towards the rising flow (similar to injection probe but facing down) and the other one with a cross-section facing parallel to the flow (as described in Figure 3.5). No significant difference was found between two designs in terms of the resulting tracer concentration. However, the latter one is easier to use since one has to make sure that the former one faces down all the time.

In radial gas mixing experiments, the tracer gas was injected at a height of 1.52 m above the distributor plate, or 0.32 m above the SA injection port as can be seen in Figure 3.9. The gas was sampled at three different heights along the riser axis; 1.96 m above the distributor plate (0.44 m above the tracer gas injection probe), 2.71 m above the distributor plate (1.19 m above the tracer gas injection probe), and 3.86 m above the distributor plate (2.34 m above the tracer gas injection probe).

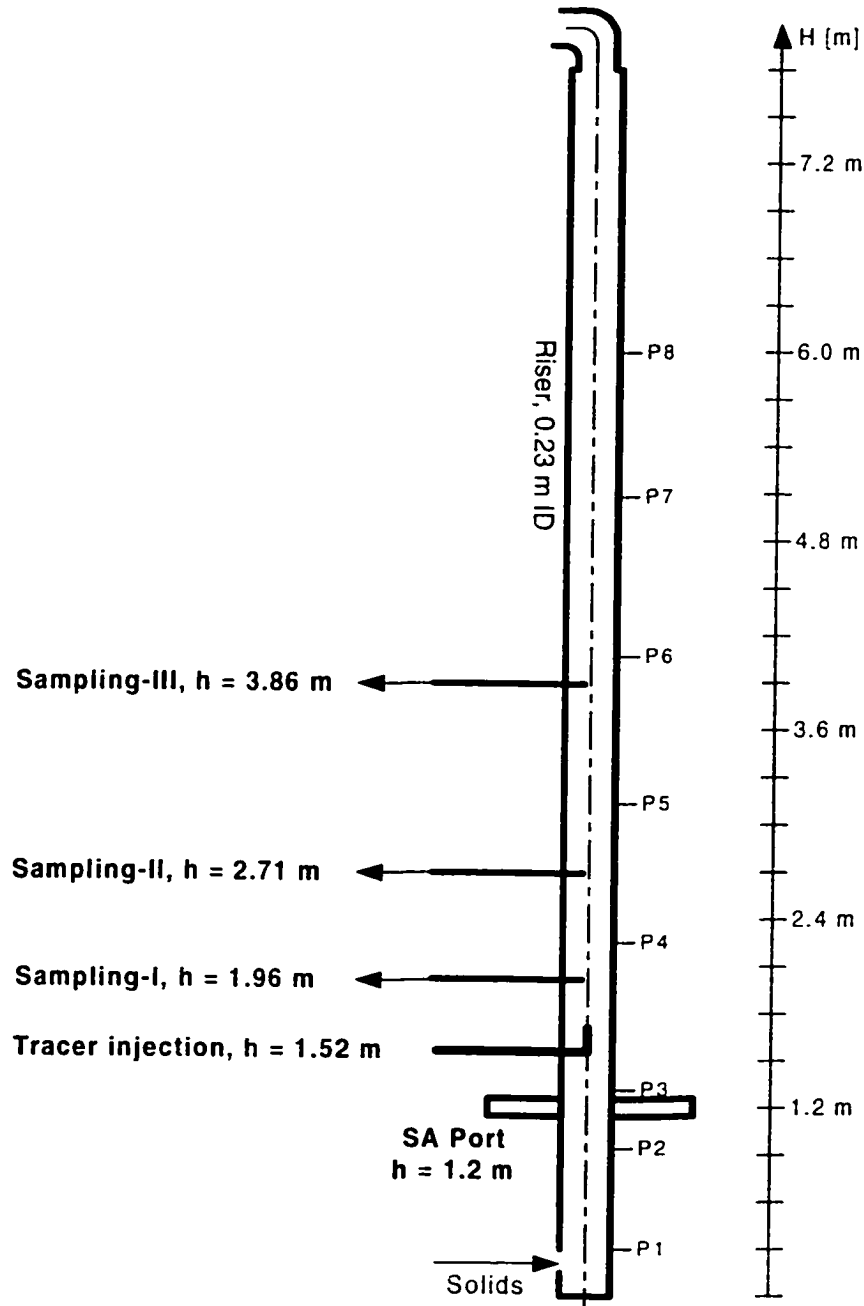


Figure 3.9. The locations of the tracer injection and gas sampling probes along the riser height in radial mixing experiments

Table 3.3. Variables used in gas mixing experiments (SA is injected at 1.2 m above the distributor plate).

#	EXP	U_o (m/s)	G_s (kg/m ² s)	SA/PA	Distance from the tracer gas injection plane, m (Distance from the SA injection port, m)	Type
1	R	3	0	0.0	0.44 (0.76), 1.19(1.51), 2.34(2.66)	N/A
2	R	5	0	0.0	0.44 (0.76), 1.19(1.51), 2.34(2.66)	N/A
3	R	5	8	0.0	0.44 (0.76), 1.19(1.51), 2.34(2.66)	N/A
4	R	5	15	0.0	0.44 (0.76), 1.19(1.51), 2.34(2.66)	N/A
5	R	5	25	0.0	1.19(1.51), 2.34(2.66)	N/A
6	R	5	8	0.4	0.44 (0.76), 1.19(1.51), 2.34(2.66)	Swirl
7	R	5	8	0.4	0.44 (0.76), 1.19(1.51), 2.34(2.66)	Radial
8	R	5	8	0.4	0.44 (0.76), 1.19(1.51), 2.34(2.66)	Mixed
9	R	5	0	0.2	0.44 (0.76)	Radial
10	R	5	8	0.2	0.44 (0.76)	Radial
11	R	5	15	0.2	0.44 (0.76)	Radial
12	R	5	0	0.2	0.44 (0.76)	Swirl
13	R	5	8	0.2	0.44 (0.76)	Swirl
14	R	5	15	0.2	0.44 (0.76)	Swirl
15	R	5	8	0.2	0.44 (0.76)	Mixed
16	R	5	15	0.2	0.44 (0.76)	Mixed
17	B	5	15	0.0	-0.05 (0.15)	N/A
18	B	5	15	0.2	-0.05 (0.15)	Swirl
19	B	5	15	0.2	-0.05 (0.15)	Radial
20	B	5	15	0.2	-0.05 (0.15)	Mixed
21	SAM	5	8	0.2	0.15 (0.15), 0.76 (0.76)	Swirl
22	SAM	5	8	0.2	0.15 (0.15), 0.76 (0.76)	Radial
23	SAM	5	8	0.2	0.15 (0.15), 0.76 (0.76)	Mixed

R: Radial mixing, B: Backmixing, SAM: Secondary air mixing with the gas-solid suspension

Table 3.3 above presents the variables used in the gas mixing experiments with the measurement locations of the tracer gas both with respect to the tracer gas injection plane and the secondary air injection port.

6.3. Gas Backmixing Experiments

As presented in Chapter 1, the local gas backmixing experiments are performed by injecting the tracer gas near the wall and then taking samples upstream at different radial

positions. Similar to radial gas mixing, the results reflect the backmixing behavior of the region bounded between the planes of the injection and the sampling probes.

In gas backmixing experiments, the tracer gas should be introduced isokinetically, i.e., the injection velocity should be equal to the gas velocity in the riser (Bader, 1989). In this study, a copper tube of 14 mm ID is used to inject the tracer gas at a height of 1.4 m from the distributor plate (0.2 m above the SA injection port) near the wall ($r/R = 0.9$). in the direction normal to the bulk flow. The mean mixed concentration, C_m , was chosen as 0.4% vol. which set the tracer gas injection velocity at the probe tip to be equal to 4.9 m/s. A quick calculation using classical $1/7^{\text{th}}$ power law with a mean velocity of 5 m/s in a pipe of 0.23 m ID yields a local gas velocity of 4.8 m/s at $r/R = 0.9$ (Schlichting, 1979). This ensures the isokinetic tracer gas introduction. The gas samples were taken radially at an upstream position of 0.05 m below the tracer injection plane. Table 3.3 gives the list of the values of the operational parameters used in backmixing experiments.

6.4. Mixing of SA with Rising Gas-Solid Suspension

In this group of experiments, the tracer gas was directly mixed with SA from only one side before being fed into the riser. The purpose was to find out the mixing pattern of each injector with the rising gas solid suspension. The tracer gas injection was straightforward in this case, and samples were taken at two different heights; 0.15 m and 0.76 m above the SA injection port. Table 3.3 presents the list of the values of the operational parameters used in this group of experiments.

7. Conclusion

In this chapter, the experimental procedure, method and set-up are presented. Each different set of mixing experiments are described in detail marking the major pitfalls. Next chapter is devoted to the results of the experiments.

Chapter 4

Experimental Results and Discussion

1. Introduction

In this chapter, the experimental results obtained from pressure measurements and tracer gas experiments are discussed. The chapter starts with the presentation of the results of the static pressure measurements (section 2) and continues with the results of the gas mixing experiments (sections 3, 4, 5). The radial gas mixing, gas backmixing and mixing of SA jets with rising gas-solid suspension are discussed separately. The chapter ends with a general conclusion.

2. Time Averaged Axial Static Pressure Measurements

In this section, the results of the time averaged axial static pressure measurements are presented. In a CFB riser, the axial solids distribution can be obtained from the time averaged differential static pressure measurements under certain simplifying assumptions. The static pressure drop for a gas-solid flow mixture in a section of a vertical pipe can be obtained by rearranging the 1-D axial momentum balance of a gas-solid mixture:

$$\Delta P = \frac{1}{2} \rho_g \alpha_g U_g^2 + \frac{1}{2} \rho_p \alpha_s U_s^2 + F_{gw}L + F_{sw}L + \rho_p \alpha_s gL + \rho_g \alpha_g gL \quad (4.1)$$

where U_g and U_s are gas and solid velocities, F_{sw} and F_{gw} are solid-wall and gas-wall friction forces per unit volume and L is the length of the section in question. The first two terms on the right hand side of the equation represent the gas and solid acceleration forces per unit cross-sectional area whereas the last two terms are the static heads of solids and gas. In Equation 3.1, the solids volume fraction, hence the gas voidage, is assumed to be constant along the section where the pressure is sought.

The pressure drop is, thus, due to the acceleration of the gas and the solids, gas-wall and gas-solid friction and the static heads of the gas and the particles. In a CFB, the gas and solid velocities are low enough to neglect the corresponding friction interactions at the wall. In the fully developed region, the acceleration terms vanish, hence, for the case of $\alpha_s \gg \alpha_g$, the following simplified relation is obtained:

$$\frac{\Delta P}{L} = -g\rho_p\alpha_s \quad (4.2)$$

Equation 4.2 is called the manometer formula. The right hand side of the equation comes from the time averaged differential static pressure measurements. The resulting volume fraction of solids (or the suspension density, $\rho_p\alpha_s$) represents the average value between the planes of the two consecutive pressure ports. The dependability of Equation 4.2 was proved for CFBs operating without SA injection (Arena *et al.*, 1988).

In case of CFBs with SA injection, the gas and particle acceleration terms can be significant, especially around the SA injection zone. Thus, the interpretation of the axial static pressure measurements around the SA injection port may not be that straightforward as in the case of non-SA operation as indicated by Marzochella *et al.* (1996a). However, since in this study there was insufficient information to calculate the acceleration effects, Equation 4.2 was utilized to calculate the axial variation of the suspension density for SA operation.

Figures 4.1 shows the pressure drop profiles along the riser height at different solids circulation rates when the bed is operated without SA injection. Figure 4.2 presents the

variation of the average suspension density with solids circulation rate as calculated from Equation 4.2. As expected, the total solids holdup in the riser increases with increasing solids circulation rate at a constant superficial gas velocity. The increase in solids holdup is more pronounced with increasing solids circulation rate, possibly due to clustering effects and increased backmixing of solids.

When the secondary air is introduced at a height of 1.2 m above the distributor plate, the axial suspension density profiles change considerably compared to non-SA operation as can be seen from Figures 4.3, 4.4 and 4.5 for tangential, radial and mixed injectors, respectively. The bed was operated at a superficial gas velocity of 5 m/s and a solids circulation rate of 8 kg/m²s. For all three injectors used the suspension density increases significantly in the primary region (region below the SA injection port). This behavior becomes more pronounced with increasing SA/PA and is very typical for a riser with SA injection. The same trends were also obtained by different researchers as already discussed in Chapter 1.

The increase in the suspension density in the primary region can be attributed to the cumulative effect of two phenomena; the decrease in the total gas flow passing through the primary region and the “cut off” or “barrier” effect of SA jets. When the total fluidization air is staged, less air passes through the primary zone leading to a higher solids concentration. As well as that, the secondary air jets partially block the flow of the rising gas solid suspension which also contributes to the increase of the solids concentration in the primary region.

In the secondary region (region above SA injection port), on the other hand, the suspension density does not change significantly in case of radial and mixed injectors when compared to non-SA operation. As can be seen from the figures, the departure from the non-SA operation occurs just at the SA injection plane for radial and mixed injectors. Thus, SA injection determines the extent of the bottom dense zone in these cases. On the contrary, for tangential injection, the suspension density continues to be higher than that of non-SA operation even above the SA injection plane. This is most probably due to the

helical motion imposed on the particles by the SA jets. Because of this circumferential velocity component, the solids take a longer path on their way to the cyclone. the net solids residence time increases, increasing the total solids hold-up both below and above the SA injection ports.

Figures 4.6, 4.7 and 4.8 are plotted to compare the axial suspension density obtained by three injectors and the non-SA operation at SA/PA=0.2 and 0.4. When the whole riser is considered, the tangential injection results in the highest solids concentration, the mixed injection lies between the radial and tangential injections. The difference between the radial and mixed injection in the primary region can be explained by the fact that the blockage or cut-off effect is more pronounced for the mixed injection since the SA jets cover a wider proportion of the riser cross section in this case compared to radial injection. The increase in the total solids holdup in the riser with tangential SA injection is quite significant. For instance, for SA/PA = 0.4, $U_o = 5$ m/s and $G_s = 8$ kg/m²s, an average solids suspension density of 9.2 kg/m³ is obtained in the riser which is almost equivalent to its non-SA operation counterpart at the same superficial gas velocity but with a solids circulation rate of 15 kg/m²s (Figure 4.2).

The axial distribution of the solids and total solids hold-up are very important as far as the radial gas mixing is concerned as shown in the next section. Thus, axial static pressure measurements are vital to understanding the complex interactions of gas and particles.

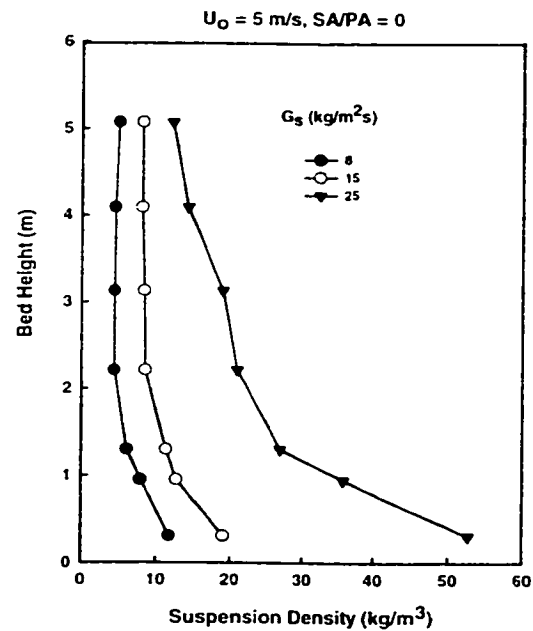


Figure 4.1. Axial variation of the bed suspension density for different solids circulation rates, $U_0 = 5 \text{ m/s}$, $SA/PA = 0.0$

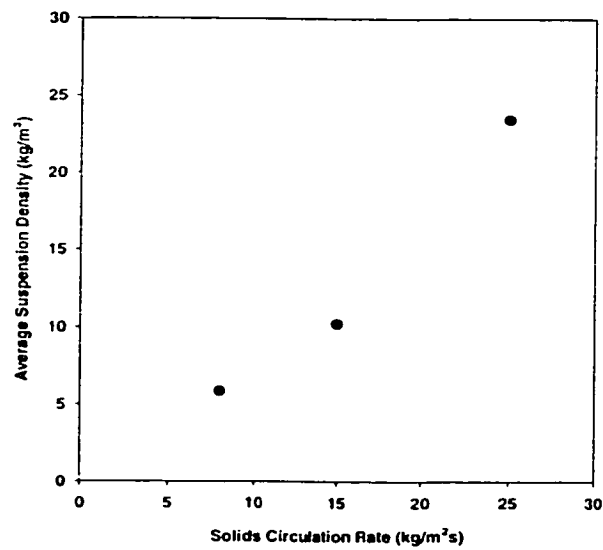


Figure 4.2. Average suspension density in the riser for different solids circulation rates, $U_0 = 5 \text{ m/s}$, $SA/PA = 0.0$

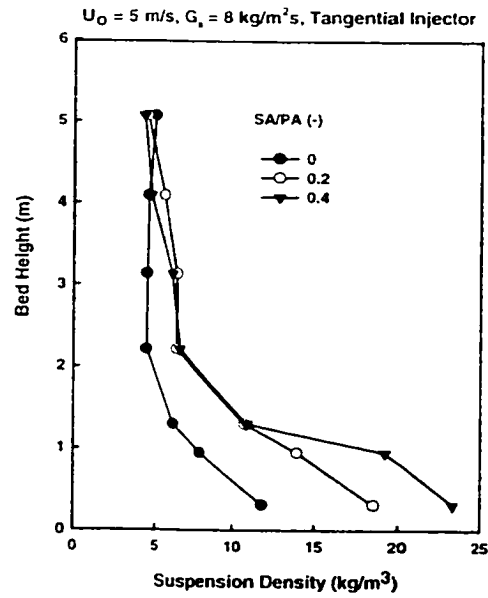


Figure 4.3. Axial variation of the bed suspension density with SA/PA for tangential SA injection, $U_o = 5 \text{ m/s}$, $G_s = 8 \text{ kg/m}^2\text{s}$.

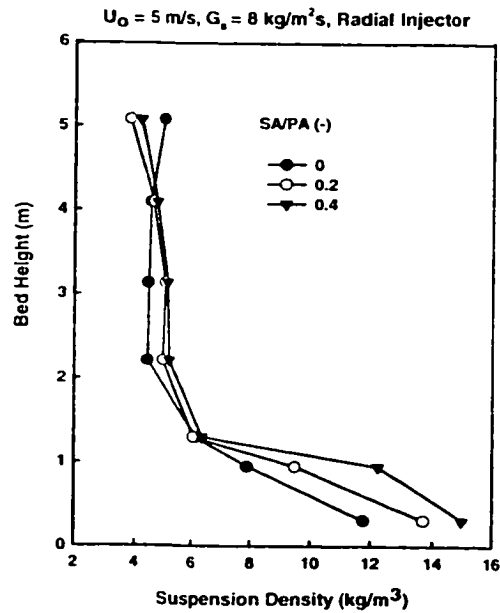


Figure 4.4. Axial variation of the bed suspension density with SA/PA for radial SA injection, $U_o = 5 \text{ m/s}$, $G_s = 8 \text{ kg/m}^2\text{s}$.

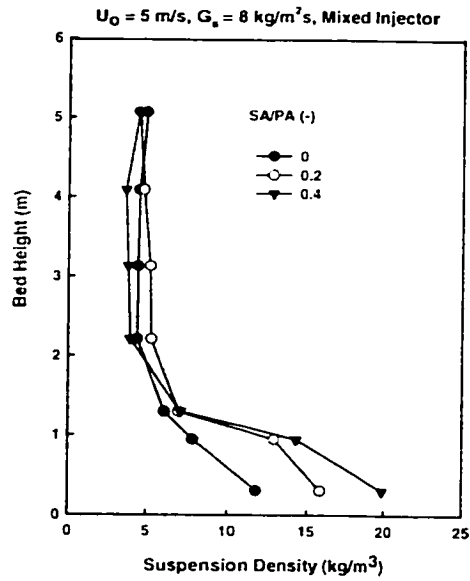


Figure 4.5. Axial variation of the bed suspension density with SA/PA for mixed SA injection, $U_o = 5 \text{ m/s}$, $G_s = 8 \text{ kg/m}^2\text{s}$.

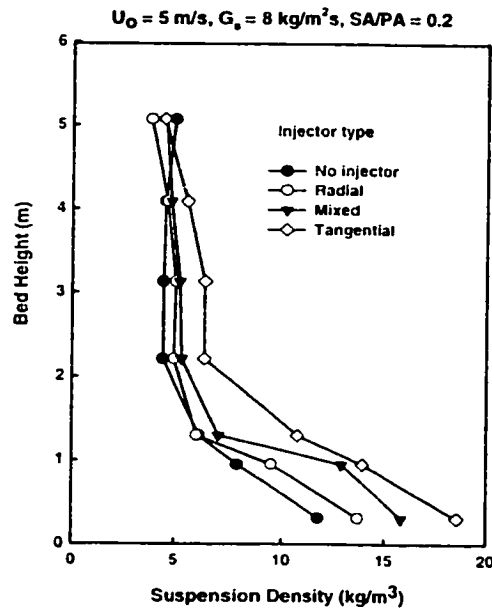


Figure 4.6. Effect of SA injector design on axial suspension density, $U_o = 5 \text{ m/s}$, $G_s = 8 \text{ kg/m}^2\text{s}$, SA/PA = 0.2.

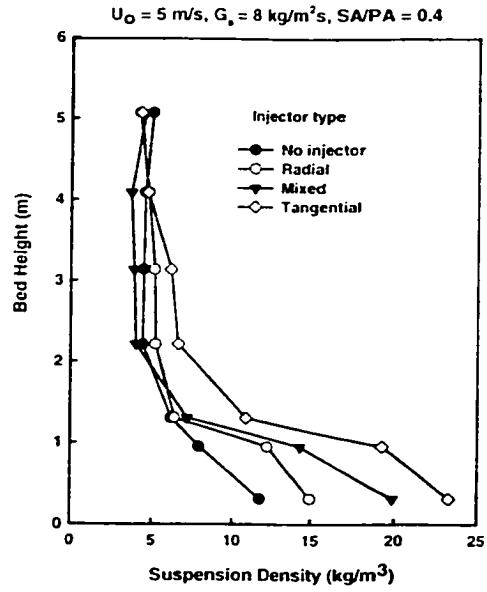


Figure 4.7. Effect of SA injection design on axial suspension density, $U_0 = 5 \text{ m/s}$, $G_s = 8 \text{ kg/m}^2\text{s}$, $SA/PA = 0.4$.

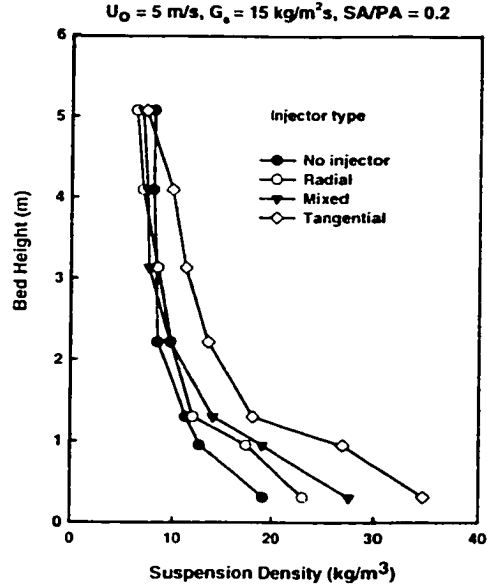


Figure 4.8. Effect of SA injection design on axial suspension density, $U_0 = 5 \text{ m/s}$, $G_s = 15 \text{ kg/m}^2\text{s}$, $SA/PA = 0.2$.

3. Radial Gas Mixing Experiments

3.1. Measurements without solids and secondary air injection ($G_s = 0 \text{ kg/m}^2\text{s}$, $SA/PA=0$).

Before the pilot CFB riser was operated with solids and SA injection, several radial mixing runs were performed without the solids. These runs:

1. provide a basis for comparison with the runs with solids and SA injection
2. are used to check the tracer mass balance and the measurement system since the flow pattern is not as complex as that of the runs with solids and SA injection.

Figures 4.9 - 4.11 show the radial variation of the tracer concentration at three different axial locations above the tracer injection port for two different superficial gas velocities ($U_o = 3, 5 \text{ m/s}$) and mean mixed concentrations ($C_o = 0.25 \%, 0.3 \%$). As expected, the concentration profiles flatten as the distance from the injection point increases. Ideally, the perfect mixing would be indicated by a flat line with $C/C_o = 1.0$. Even 2.34 m above the injection point, which corresponds to a distance of approximately 10 times the riser diameter, the perfect mixing condition is not obtained as can be seen from the figures. The flattening of the tracer concentration curves moving from 0.44 m to 1.19 m is more pronounced than that obtained when moving from 1.19 m to 2.34 m as can be seen from the figures. As the tracer gas is dispersed, the concentration gradients decrease leading to less mass transfer in radial direction if the dispersion coefficient is assumed to be constant. This complies with the eddy diffusion concept presented in Chapter 2 and the solution of DPFM (Equation 2.7) which shows an exponential variation of the tracer concentration with height.

The ordinate, C/C_o , in Figures 4.9-4.11 varies with the value of the mean mixed concentration, hence with the amount of tracer injected. The effect of the mean mixed concentration on the radial dispersion coefficient is discussed in the next section.

Based on the discussion in section 3.2.1 of Chapter 2, in order to find the tracer gas

volumetric flow rate from the measurements to check with the amount of the injected tracer gas, the following integral is carried out numerically:

$$\dot{Q}_t = \int_0^{r_m} U_o 2\pi r c_m dr \quad (4.3)$$

where c_m is the measured concentration of the tracer gas and r_m is the measurement radius which was set as 0.1 m during the experiments.

For single phase runs, all the tracer concentration curves were checked using Equation 4.3, and the maximum discrepancy between the injected and measured tracer gas flow rates were found to be approximately 10%. The analysis neglects the gas backmixing, assumes that the flow is perfectly axi-symmetric and a constant uniform velocity of U_o prevails along the measurement line, i.e., $-0.1 \text{ m} < r_m < 0.1 \text{ m}$.

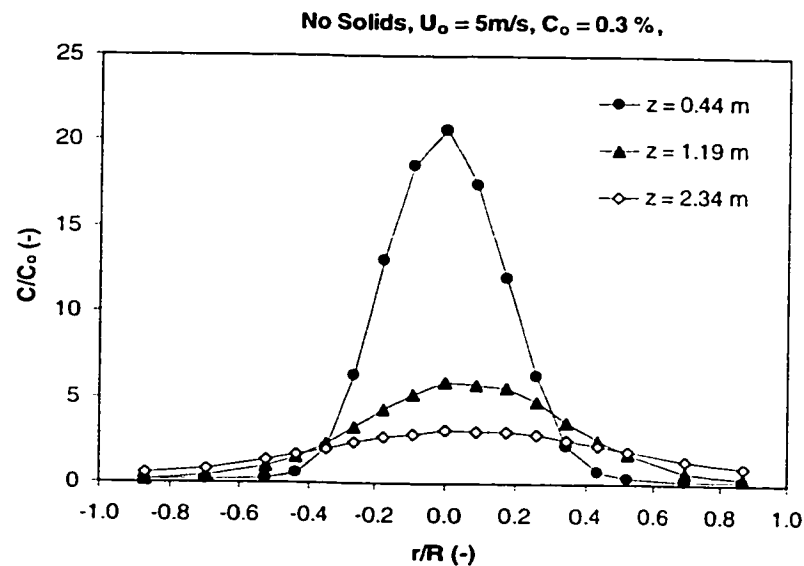


Figure 4.9. Radial distribution of the tracer gas at different heights above the tracer injection plane, no solids, $U_o = 5 \text{ m/s}$, $C_o = 0.3 \%$.

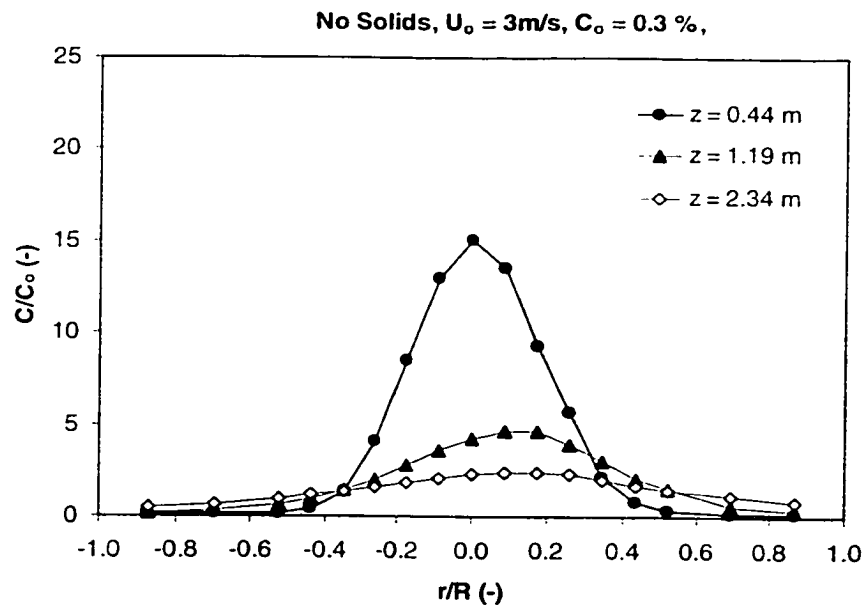


Figure 4.10 Radial distribution of the tracer gas at different heights above the tracer injection plane, no solids, $U_o = 3\text{ m/s}$, $C_o = 0.3\%$.

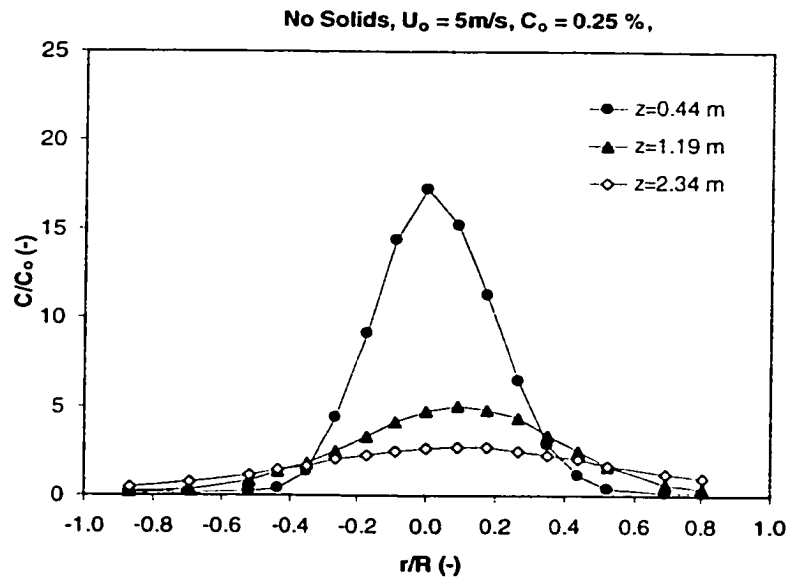


Figure 4.11. Radial distribution of the tracer gas at different heights above the tracer injection plane, no solids, $U_o = 5\text{ m/s}$, $C_o = 0.25\%$.

3.2. The Radial Dispersion Coefficients

The MSDM, presented in Chapter 2, is used to calculate the average dispersion coefficients in the riser. First, Equation 2.23 was employed to find the mean square displacement of the particles, $\overline{X^2}$, and then, using Equation 2.22, the average radial dispersion coefficient was calculated. The integrations in the equations were carried out numerically.

Figure 4.12 shows the variation of the radial dispersion coefficients with the distance from the tracer injection point for single phase runs. Regardless of the velocity, the radial dispersion coefficients remain almost constant at three different measurement levels. For $U_o = 3$ m/s and $U_o = 5$ m/s, the average radial dispersion coefficients are 13.5 cm²/s and 22 cm²/s, respectively. As presented in Chapter 2, the radial dispersion coefficient is a function of the turbulent velocity fluctuations in the spanwise direction (direction normal to the mean flow) and the size of the largest scale eddies. The former can be described quantitatively by the turbulent intensity whereas the latter can be related to the riser diameter. Since the riser diameter does not change, once the flow is fully developed, the turbulence intensity becomes invariant of the streamwise direction, producing almost constant dispersion coefficients.

Figure 4.12 also compares the radial dispersion coefficients obtained with different mean mixed concentration, C_o , values, 0.25 % and 0.3 %, at the same superficial gas velocity. There is no significant difference in radial dispersion coefficients for these cases as inferred from the figure. Thus, the assumption of linearity, between C_o range of 0.2 %-0.3% is also verified as discussed in Chapter 3.

In order to check the measurement system and the gas analyzer, one single phase run is carried out with gas chromatography as shown in Figure 4.12. Gas is sampled into the vacuum bags and then analyzed with HP gas chromatograph. An almost identical dispersion coefficient is obtained in the experiment with infrared gas analyzer at the same operating conditions.

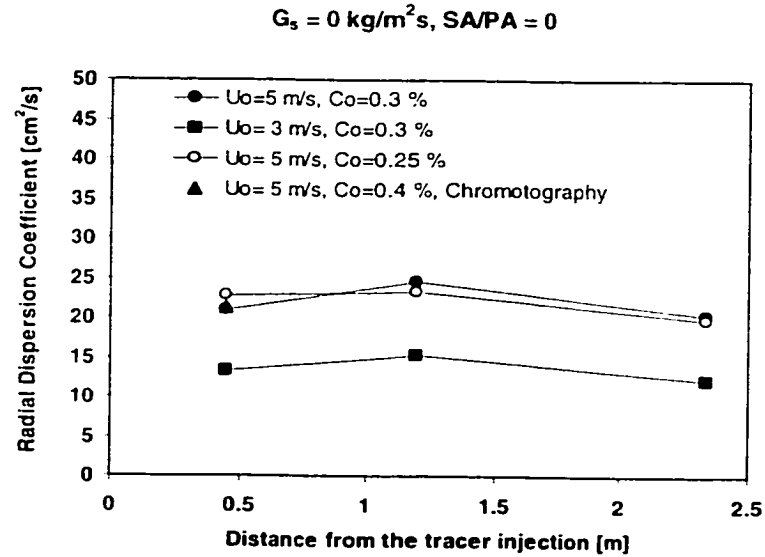


Figure 4.12. The variation of the radial dispersion coefficient with the distance from the tracer injection plane, no solids, no secondary air.

To express the calculated dispersion coefficients in non-dimensional form, a radial Peclet number, Pe_r , can be defined as the ratio of the convective gas transport and the gas dispersion normal to the mean flow:

$$Pe_r = \frac{U_0 d_t}{D_r} \quad (4.4)$$

where d_t is the riser diameter. Figure 4.13 shows the values of the average radial Peclet number for two superficial gas velocities, 3 m/s and 5 m/s, obtained from the single phase runs. It is interesting to note that Peclet number does not change with velocity as noted by Sherwood *et al.* (1975). As the superficial gas velocity increases from 3 m/s to 5 m/s, the radial dispersion coefficient also increases at the same ratio leading to an average Peclet number of 520 for single phase runs. If D_r is expressed in terms of the mean square displacement using Equation 2.18, Equation 4.4 can be rewritten as:

$$Pe_r = \frac{2z_i d_t}{X^2} \quad (4.5)$$

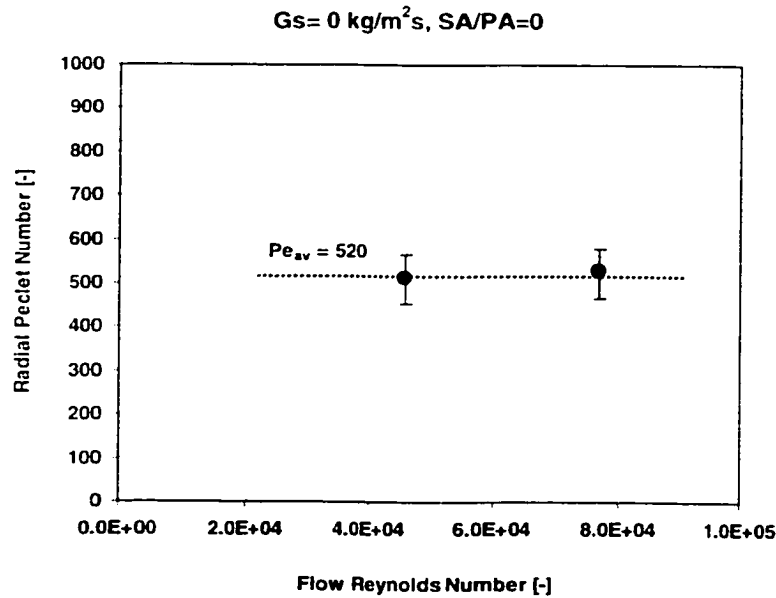


Figure 4.13. Average radial Peclet number for single phase flow in the riser, no secondary air.

Thus, for a constant riser diameter and injection and sampling plane distance, z_i , a constant Peclet number with increasing velocity indicates also a constant mean square displacement value. When the velocity is increased to 5 m/s, more gas (tracer) is mixed at the same degree as in the case of 3 m/s, but the quality of the mixing¹ remains the same (Sherwood *et al.*, 1975). From the gas phase turbulence point of view, with increasing velocity, hence Reynolds number, more turbulence is generated, the velocity fluctuations in the spanwise direction increases which leads to an increase in the dispersion coefficient more or less at the same ratio as the increase in the velocity. Thus, the ratio of the convective gas transport to radial dispersion remains the same for a given unit for single phase flows.

¹ Mixing at this points refers to macro scale mixing which occurs at the scale of the largest eddies. One still needs the molecular diffusion to smoothen out the concentration gradients occurring over distances less than the eddy size.

In Figure 4.14, the application of the dispersed plug flow model to the single phase tracer data (curves are given in Figure 4.8) is presented as outlined in Chapter 1. All the data from three measurement levels (0.44m, 1.19m, 2.34 m above the tracer injection plane) are used to construct the figure shown to find the average radial dispersion coefficient. As explained in Chapter 2, the slope of the fitted line is equal to $-U_c/2D_r$, from which the radial dispersion coefficient can be calculated. In this case, the slope is calculated as -10.7 which gives an average dispersion coefficient of 23.4 cm²/s. This value is almost the same as the value (22 cm²/s) obtained from the MSDM.

The solution of the DPFM, Equation 2.7, is a normal (Gaussian) distribution. If the measured tracer concentration curves are Gaussian, DPFM can be applied to the tracer data with a high value of coefficient of correlation, R^2 , (close to 1.0) as shown in Figure 4.14. In this case, MSDM and DPFM will give identical values of radial dispersion coefficient. On the other hand, if the tracer concentration curves are non-Gaussian, the fit to the tracer data will have a low value of R^2 , showing that DPFM is not suitable to describe the gas mixing phenomena. However, MSDM, can be applied to any kind of tracer distribution and will yield an average dispersion coefficient in any case (Flint *et al.*, 1960).

Sherwood *et al.* (1975) states that the average radial Peclet number based on the average gas velocity and the pipe diameter lies in the range of 250-1000 as obtained from the experiments of different researchers with different carrier fluids and tracer techniques. The data that is reported in Sherwood *et al.* (1975) is for a vertical pipe flow, rather than data obtained from CFB risers operated without solids. Werther *et al.* (1992a) reports an average radial Peclet number² of 482 to describe their single phase experiments in a riser of 0.4 m ID and 9 m height. Amos *et al.* (1993) obtained a value of approximately 190. Recently, Mastellone and Arena (1999) and Namkung and Kim (2000) reported single phase Peclet number values of 225 and 190, respectively, from their riser experiments.

² Werther *et al.* (1992) defines a Peclet number based on the average core gas velocity and core radius.

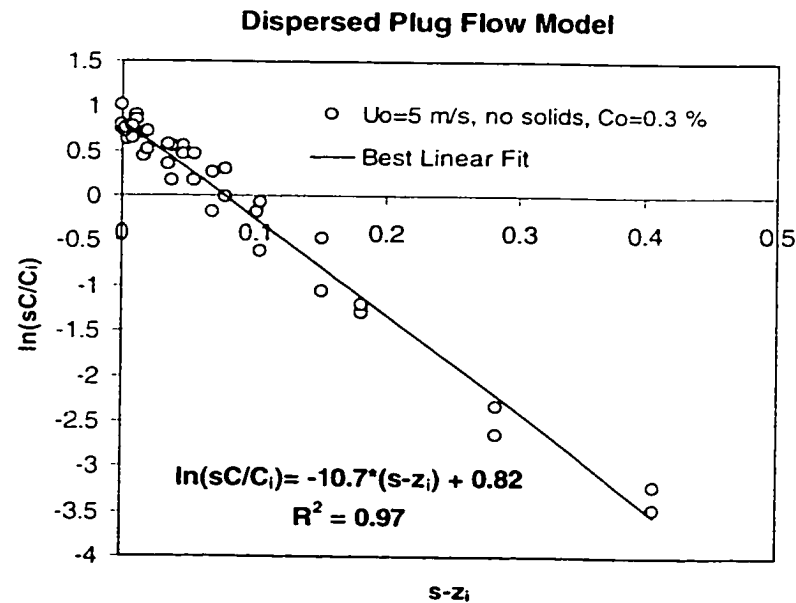


Figure 4.14. Application of the dispersed plug flow model, $U_o = 5$ m/s, no secondary air, no solids, $z_i = 0.44$ m, 1.19m, 2.34m.

So far there is no reliable correlation to estimate the radial Peclet number, even for single phase flows. One can get quite different Peclet numbers in two different units having the same diameter and operated at the same average velocity (Sterneus *et al.*, 2000). This shows that average gas velocity (related to turbulence intensity, hence turbulent velocity fluctuations) and riser diameter (related to length scale of the large eddies) are only approximate indicators of gas mixing. The geometry of the riser, inlet effects, gas distributor, wall roughness can all have significant effects on radial gas mixing even when the average gas velocity and the riser diameter remain unchanged (Sterneus *et al.*, 2000).

3.3. Measurements with solids and without secondary air injection (SA/PA=0).

In this section, the results of the experiments without the secondary air injection are presented. Also, the effects of solids circulation rate on gas mixing is investigated without the presence of SA injection.

Figures 4.15 and 4.16 show the radial distribution of the tracer gas at different axial distances from the tracer injection point for solids circulation rates of $8 \text{ kg/m}^2\text{s}$ and $15 \text{ kg/m}^2\text{s}$, respectively. Similar to single phase experiments, the tracer concentration curves flatten with distance from the injection point. The tracer gas concentration curves were integrated using Equation 4.3 to check the injected volumetric flow rate of the tracer.

Figures 4.17–4.19 compare the radial distribution of the tracer gas at different solids circulation rates for $z = 0.44 \text{ m}$, 1.19 m and 2.34 m . These figures clearly show that the highest gas dispersion is achieved without the solids present in the riser. For instance, as can be seen from Figure 4.17, at $z = 0.44 \text{ m}$, a concentration of almost 40 times larger than the ideal concentration is obtained on the riser axis for $G_s = 8 \text{ kg/m}^2\text{s}$ indicating poor gas mixing. Also, even 2.44 m above the tracer gas injection plane which is more than 10 times the riser diameter, the tracer gas has not been able to reach to the riser wall.

As the solids circulation rate is increased at constant velocity, the dispersion of tracer gas also decreases in radial direction. The decrease in dispersion is more pronounced at low solids circulating rates, i.e., when moving from 0 to $8 \text{ kg/m}^2\text{s}$ than moving from 8 to $15 \text{ kg/m}^2\text{s}$ or 15 to $25 \text{ kg/m}^2\text{s}$.

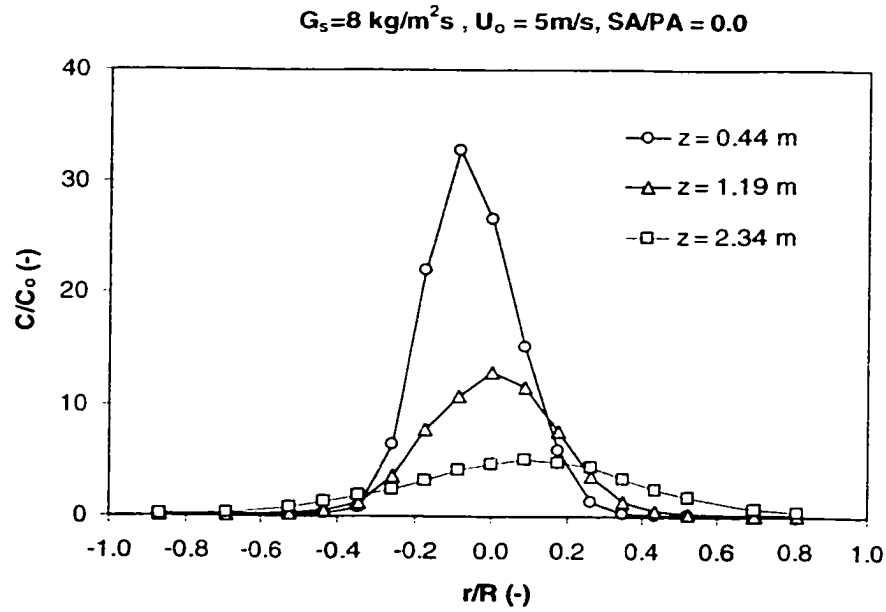


Figure 4.15. Radial distribution of the tracer gas at different heights above the tracer injection plane, $U_o = 5 \text{ m/s}$, $G_s = 8 \text{ kg/m}^2\text{s}$, $SA/PA = 0.0$, $C_0 = 0.25 \%$.

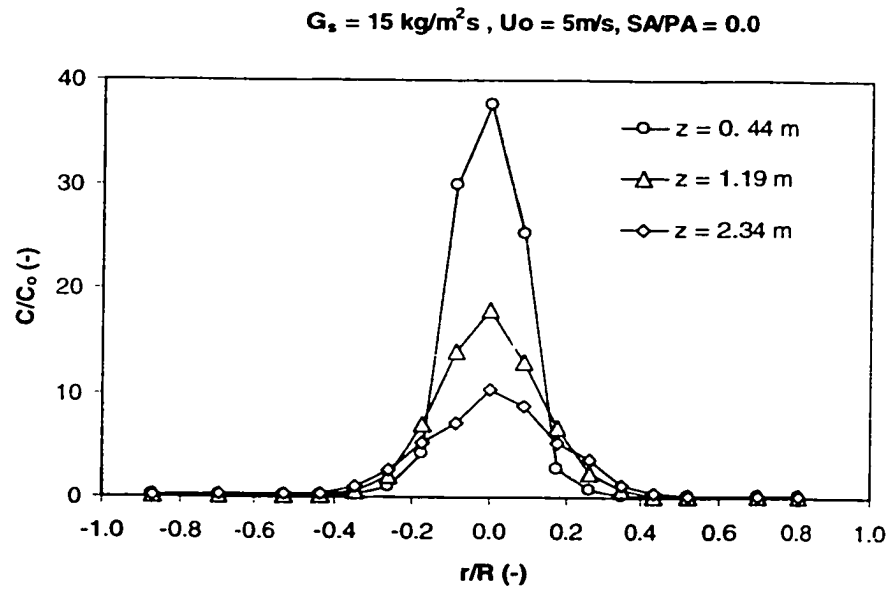


Figure 4.16. Radial distribution of the tracer gas at different heights above the tracer injection plane, $U_o = 5 \text{ m/s}$, $G_s = 15 \text{ kg/m}^2\text{s}$, $SA/PA = 0.0$, $C_0 = 0.25 \%$.

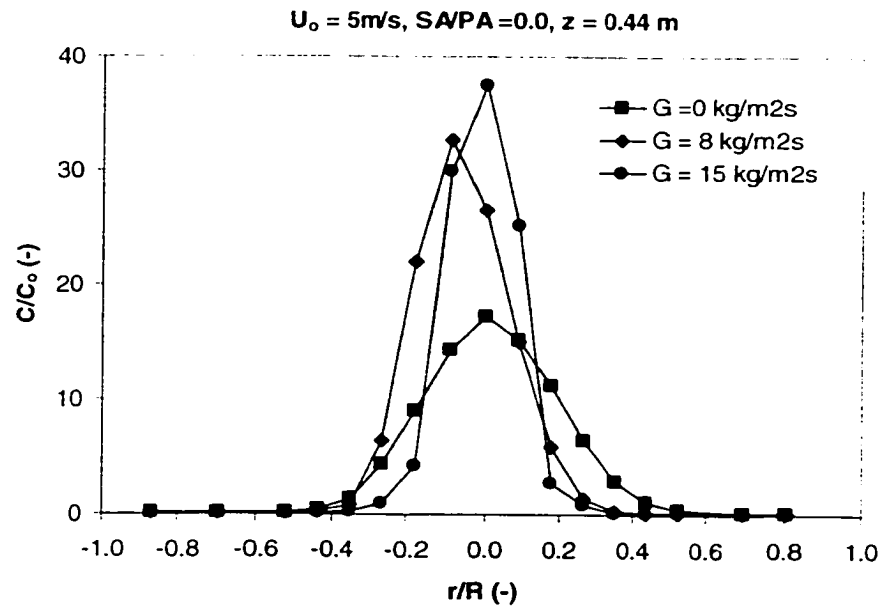


Figure 4.17. Effect of the solids circulation rate on radial distribution of the tracer gas at $z = 0.44\text{ m}$, $U_o = 5\text{ m/s}$, $C_0 = 0.25\%$.

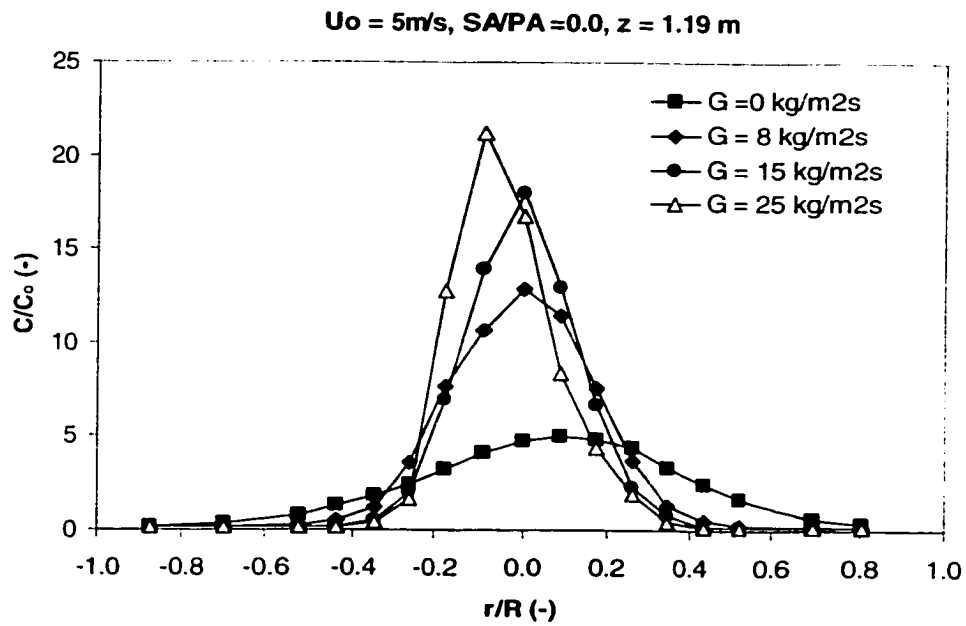


Figure 4.18. Effect of the solids circulation rate on radial distribution of the tracer gas at $z = 1.19\text{ m}$, $U_o = 5\text{ m/s}$, $C_0 = 0.25\%$.

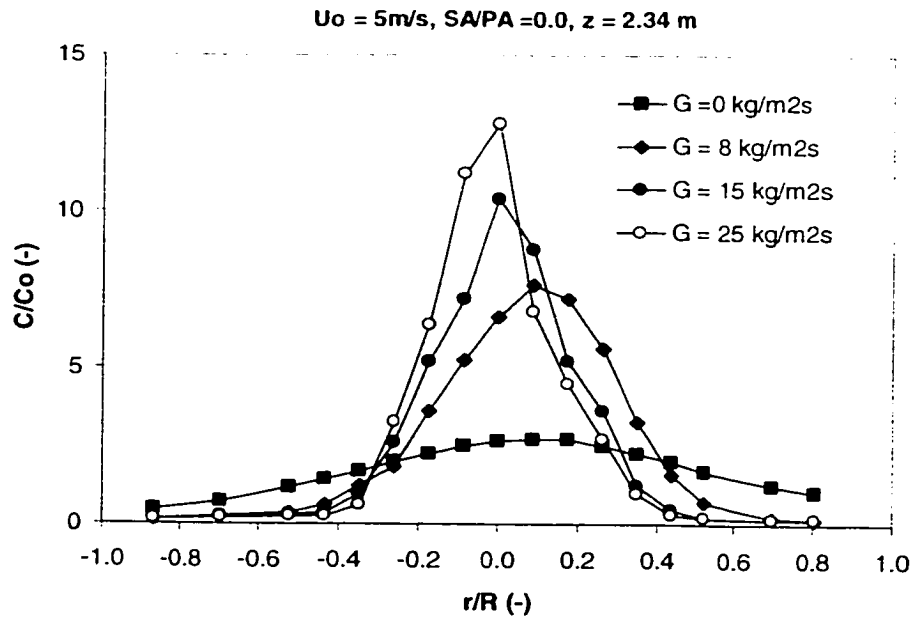


Figure 4.19. Effect of the solids circulation rate on radial distribution of the tracer gas at $z = 2.34 \text{ m}$, $U_o = 5 \text{ m/s}$, $C_o = 0.25 \%$.

To quantify the quality of mixing, as in the case of single phase experiments, the MSDM is used. Figure 4.20 gives the variation of the radial dispersion coefficient with the distance from the tracer injection point for solid circulation rates of 0, 8, 15 and 25 kg/m²s at a superficial gas velocity of 5 m/s. Similar to single phase experiments, no significant variation of the dispersion coefficients with height is found. Thus, the flow should be fairly fully developed between the tracer injection and the third sampling location which corresponds to the heights of 1.96 m and 3.86 m from the distributor plate. Figure 4.1 also confirms this point showing that the bed suspension density is almost constant between these two aforementioned heights.

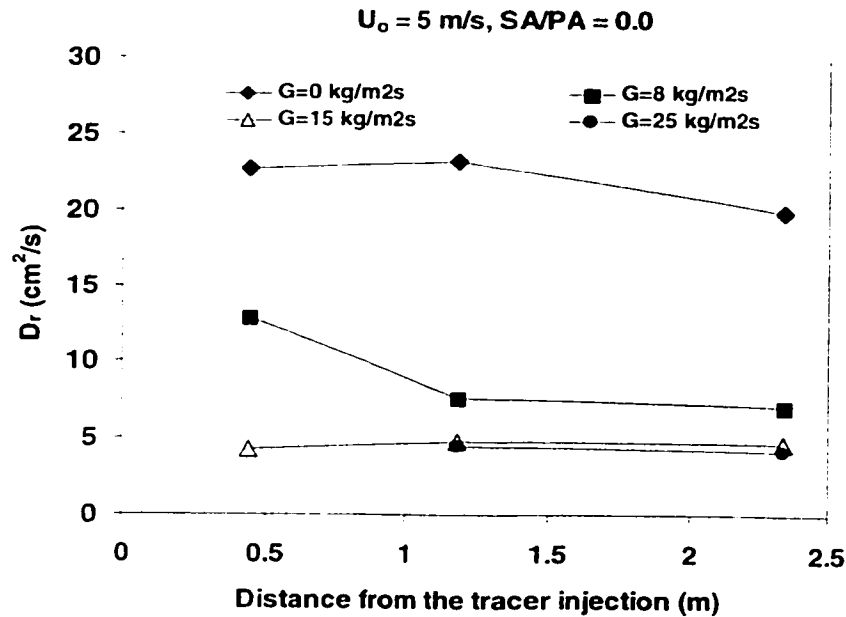


Figure 4.20. The variation of the radial dispersion coefficient with the distance from the tracer injection point for different solids circulation rates, $U_o = 5$ m/s, $SA/PA = 0.0$.

Compared to other studies in the literature (Werther *et al.*, 1992a; Mastellone and Arena, 1999), the gas injection and sampling planes are set closer to the bottom of the riser rather than in the upper dilute zone so that the results of experiments without SA injection can be compared to those with SA injection. However, at the bottom of the riser a turbulent and/or fast fluidization regime was observed during the experiments and the bottom dense region had no effect on the radial gas mixing, as can be seen from Figure 4.20.

The average radial dispersion coefficient drops to 9.2 cm²/s at $G_s = 8$ kg/m²s from 22 cm²/s which is the single phase value. Further increase in the solids circulation rate decreases the radial dispersion coefficient to 4.6 cm²/s at 15 kg/m²s after which the dispersion coefficient is almost unchanged (4.3 cm²/s at $G_s = 25$ kg/m²s). Figure 4.21 shows the same data plotted in terms of the radial Peclet number. As can be inferred from the figure, the Peclet number increases sharply between 0 to 15 kg/m²s and then it remains almost constant.

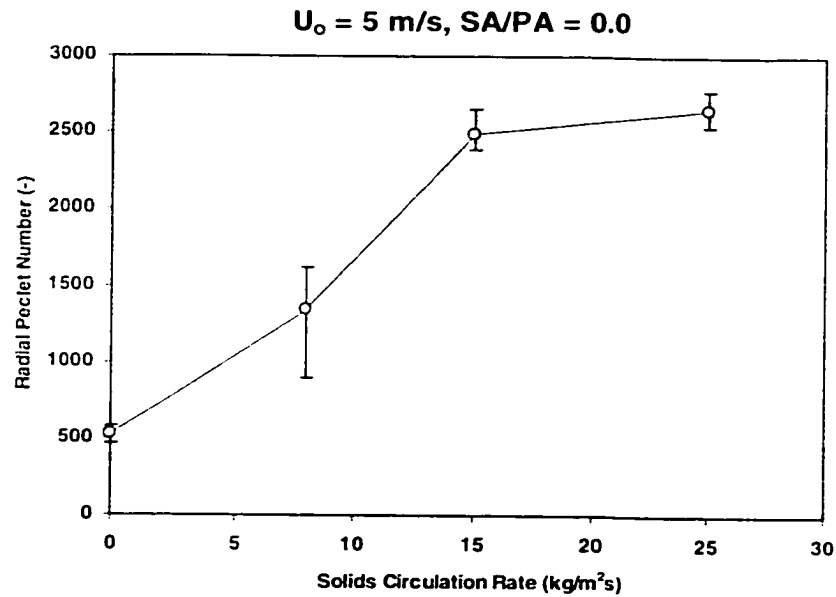


Figure 4.21. The variation of the radial Peclet number with solids circulation rate, $U_o = 5 \text{ m/s}$, $SA/PA = 0.0$.

The radial dispersion coefficients and Peclet numbers obtained from the experiments performed in CFB risers by different researchers are presented in Table 4.1. As can be seen, both the radial dispersion coefficients and Peclet numbers vary significantly. Excluding Sterneous *et al.* (2000), Table 1.4 covers the experimental studies with a range of 0.1-0.4 m for riser diameter, 4-8.5 m for riser height, 2.8-10 m/s for superficial gas velocity and 0-160 $\text{kg/m}^2\text{s}$ for solids circulation rate³. Finding an empirical correlation to express the Peclet number as a function of the operational and design parameters such as superficial gas velocity, solids circulation rate, riser size and geometry, and bed material properties is an ongoing work (Namkung and Kim, 2000).

³ See Table 1.5 for the detailed information on each study.

Table 4.1. Approximate radial dispersion coefficients and Peclet numbers including the single phase values obtained in other studies (See Table 1.5 of Chapter 1 for the detailed information about the particular study).

Researchers	D_r (cm ² /s)	Pe_r
Guilin <i>et al.</i> (1984)	2.5-7.8	500-2300 ¹
Werther <i>et al.</i> (1992a)	26-54 ²	465 ³
Zheng <i>et al.</i> (1992)	6-28	273-780 ¹
Amos <i>et al.</i> (1993)	N/A	320-500
Gayan <i>et al.</i> (1997)	2-6	500-2000
Mastellone and Arena (1999)	2-44	260-1900
Sterneus <i>et al.</i> (2000)	100-235 (boiler), 20-90 (cold unit)	170-205(boiler)
Namkung and Kim (2000)	7-29	139-496
Present study	4.1-23.2	496-2778

1. Calculated from D_r .
2. Calculated from Pe_r .
3. Based on core velocity and diameter.
4. N/A: Sufficient information is not available.

Increasing the external solids circulation rate in a CFB at constant superficial gas velocity increases the net solids hold up in the riser. In Figure 4.22, the radial dispersion data obtained from the experiments are plotted with respect to the corresponding average solids volume fraction values⁴ at each level of sampling plane. As can be seen from the figure, the relation between the radial dispersion coefficient and the solids volume fraction is not monotonic; the dispersion coefficient drops very sharply up to the average solids volume fraction value of 0.004-0.005 (the suspension density is ≈ 13 kg/m³) and then remains almost unchanged in the range of experimental conditions. This is important since in most of CFB boilers, the external solids circulation rate is typically 10 kg/m²s, leading to a suspension density of less than 10 kg/m³ in the upper dilute region (Leckner, 1998; Arena, 1997). Thus, the gas mixing will be always poorer than the single phase case and will deteriorate with increasing suspension density, or at the most remain constant (Arena, 1997).

⁴ Obtained from time averaged differential pressure measurements

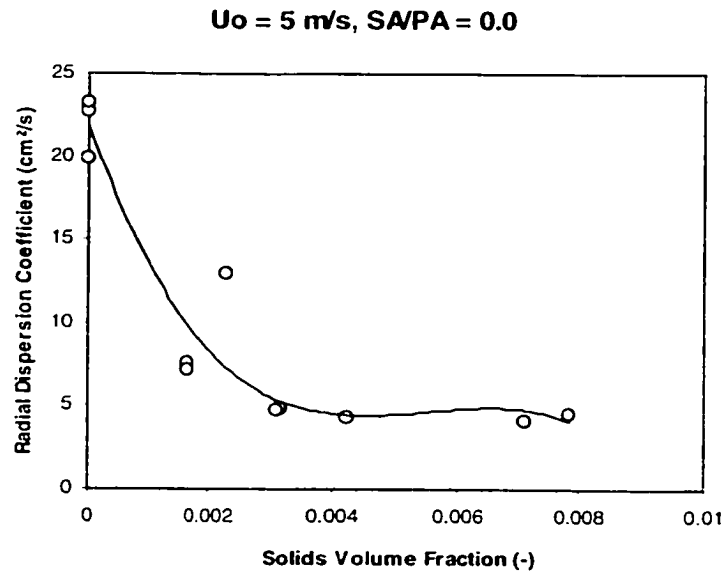


Figure 4.22. The variation of the radial dispersion coefficient with axially averaged solids volume fraction at the sampling probe location, $U_o = 5 \text{ m/s}$, $SA/PA = 0.0$.

3.3.1. A Discussion on the Effects of the Solids on Radial Gas Mixing

The result presented in Figure 4.22 can be analyzed in the context of particle-turbulence interaction in gas-solid flows. As the carrier phase turbulence is thought to be the main mechanism in dispersion of gas in radial direction, any change in the turbulence structure due to particle presence also affects the gas dispersion. Generally, the problem in which the changes in the carrier phase turbulence due to the effect of the dispersed phase is analyzed, is known as *turbulence modulation*.

It is now accepted that for dilute two-phase flows, the presence of the particles can either dampen or augment the gas phase turbulence depending on the gas and particle properties (Tsuji *et al.*, 1984; Hetsroni, 1989; Gore and Crowe, 1989; Elgobashi, 1994; Kulick *et al.*, 1994) However, there is no general consensus about the criterion which determines the borderline and extent of the suppression and augmentation of gas phase turbulence with the addition of particles. Some experimental data suggest an increase in turbulence with addition of particles (Tsuji and Morikawa, 1982; Yokuda, 1990) whereas some results indicate the opposite trend (Schreck and Kleis, 1993). It should also be noted the

fluctuations in one direction can be more affected by the presence of the particles than the fluctuations in the other direction (Tsuji *et al.*, 1984).

Gore and Crowe (1989) gathered data from variety of researchers in order to find a trend for turbulence modulation. They suggested that the ratio of the particle diameter to length scale of the largest eddy, l_e , (scale of the most energetic eddy) could be used as the key parameter determining the turbulence modulation. When this ratio is smaller than 0.1, the data show that the turbulence level decreases with the addition of particles whereas an increase is observed for ratios greater than 0.1. The physical explanation is as follows: the small particles which are much smaller than the large scale eddies responsible for the turbulent transport follow the eddies they interact for at least part of their life time. Part of eddy's energy is imparted to the particles since the eddy, through the drag force, is moving the particle. The turbulent energy of the eddy is therefore transformed in to the kinetic energy of the particle and the turbulent intensity is reduced. Large particles ($d_p/l_e > 0.1$), on the other hand, tend to create turbulence in their wake near the scale of the large scale eddies, thus increasing the turbulent intensity of the gas.

Hestroni (1989) postulated a similar theory by performing an order of magnitude analysis, stating that the particles with Reynolds numbers greater than 400 would augment the turbulence due the generation of turbulence by vortex shedding at their wakes and those with Reynolds numbers less than 400 would attenuate it.

When both criteria of Gore and Crowe (1989) and Hestroni (1989) are applied to the operating conditions of this study, they predict a decrease or suppression in gas phase turbulence with solids (calculated $d_p/l_e \approx 0.01$ and calculated $Re_p \approx 88$) similar to the experimental measurements. The decrease in the radial dispersion coefficient at the transition when moving from single phase to two-phase flow found in this study is also supported by the experimental measurements of Adams (1988), Zheng *et al.* (1992), Amos *et al.* (1993), Gayan *et al.* (1997), Mastellone and Arena (1999) and Namkung and Kim (2000).

The second aspect, apart from the transition, is the variation of the radial dispersion coefficient with solids volume fraction. In a CFB riser, the solids holdup can be increased in two ways; by increasing the solids circulation rate at constant superficial gas velocity or by decreasing the superficial gas velocity at constant solids circulation rate. Zheng *et al.* (1992) also obtained a similar trend to the one presented in Figure 4.22; their radial dispersion coefficients decreased to a minimum value at a solids volume fraction of 0.02 and then increased slightly up to a solids volume fraction value of 0.04. Arena (1997) suggests that for higher solids volume fraction values, clustering effects become significant and a cluster having an effective diameter larger than a single particle might increase the turbulence due to the wake effects. The recent studies of Gayan *et al.* (1997) and Namkung and Kim (2000) also support the finding of increase in the radial dispersion coefficient with solids volume fraction at relatively dense conditions (app. when $\alpha_s > 0.01$) but the physical explanation is not very clear. First of all, the turbulence modulation theories of Gore and Crowe (1989) and Hestroni (1989) depend on data from relatively dilute two-phase flows, including gas-liquid flows. Secondly, these theories emphasize the transition from single phase to two-phase flow, rather than the variation of the turbulence intensity with the volume fraction of the discrete phase. Thirdly, the nature of gas turbulence and particle interactions in dense gas-solid flows is not really well known as in case of dilute flows (Elgobashi, 1994). Therefore, it would be more appropriate to state that in case of dense CFB risers, the solids alter the gas phase flow and turbulence in such a way that, the radial gas mixing increases with increasing solids loading.

Before proceeding to the next section, some of the studies which somewhat contradict the above general trends will be cited. For instance, Werther *et al.* (1992a) found no difference in radial dispersion coefficients at a superficial gas velocity of 3 m/s and the solids circulation rate changing between 0-70 kg/m²s, although the solids concentration at the measurement location changed between 0-1%. Recently, Sterneus *et al.* (2000) published the results of their gas mixing experiments carried out in a rectangular cross-section riser. They stated that a very dilute flow gives about the same dispersion as the single phase flow. Increasing the solids holdup at constant velocity increased the

dispersion coefficient to a plateau value after which no change in dispersion coefficient was observed. As they indicated, the increase in the dispersion coefficient with loading was possibly due to the large scale motions and fluctuations caused by the bubbles at the bottom of the bed, which is not usually observed in lab scale risers with high values of height-to-diameter ratio.

As a conclusion, in the range of experimental conditions of this study ($U_o = 3,5$ m/s and $G_s = 0-25$ kg/m²s), the radial dispersion coefficient was found to decrease sharply from its maximum single phase value to a minimum and then remain constant up to a solids volume fraction of 0.004. Next section presents the results of the experiments with SA injection which can be a promising tool to enhance the observed poor gas dispersion.

3.4. Measurements with Secondary Air Injection

Figures 4.23, 4.24 and 4.25 show the radial variation of the tracer concentration at three different measurement heights (0.44 m, 1.19 m and 2.34 m above the tracer gas injection plane) for tangential, radial and mixed injection cases for SA/PA = 0.4 ($U_o = 5$ m/s, $G_s=8$ kg/m²s). The curves obtained with tangential injection is similar to the curves obtained without the SA, whereas the data representing the radial and mixed injection cases are more scattered and non-uniform. This is consistent with the visual observations made throughout the experimental study; in case of tangential injection, more uniform fluidization was observed although the solids holdup in the riser was higher compared to radial and mixed injection cases at the same superficial gas velocity and solids circulation rate. When the secondary air was introduced via radial or mixed injectors, the solids motion around the SA injection zone showed some kind of intermittent behavior possibly due to the blockage effect of the SA jets.

When the bed was staged, regardless of the mode of injection, maintaining a stable operation was more difficult compared to non-SA operation. At constant superficial gas velocity, the variation of the external solids circulation during an experimental run varied more than the case without SA injection especially for the radial injection case. Thus,

longer gas sampling times had to be utilized in order to get meaningful averages of tracer gas concentration at any location. Similar to non-SA operation, when the SA is injected tangentially, the tracer gas concentration curves flatten with the distance from the tracer injection as can be seen from Figure 4.23. In case of radial and mixed injection, on the other hand, the tracer concentration curves do not flatten significantly between the measurement locations of 1.19 m and 2.34 m compared to the change observed between the measurement heights of 0.44 m and 1.19 m (Figures 4.24-4.25). This indicates that the effect of SA jets are more pronounced near the SA injection zone and their effects diminish with height, at least for radial and mixed injection cases. It should be noted that, with the secondary air injection, due to the design of the SA injectors (2 point injection, Figure 3.7 of Chapter 3), the flow pattern above the injection plane is no longer axisymmetric as in the case of non-SA operation. Thus, as stated in Chapter 3, the measurement line is only assumed to represent the radial distribution of the tracer gas on the riser cross section. The next section compares the three modes of injection with non-SA operation at three measurement levels.

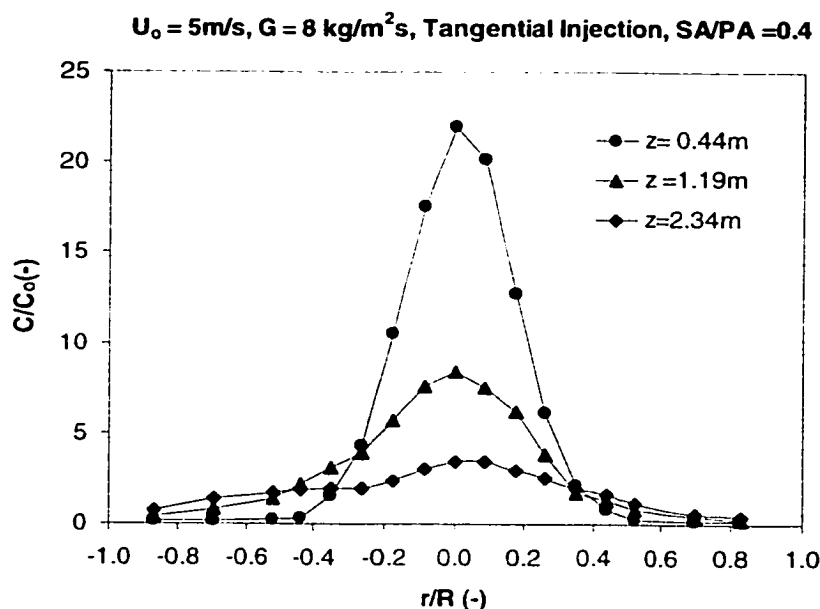


Figure 4.23. Radial distribution of the tracer gas at different heights above the tracer injection plane, tangential SA injection, $C_0 = 0.25\%$.

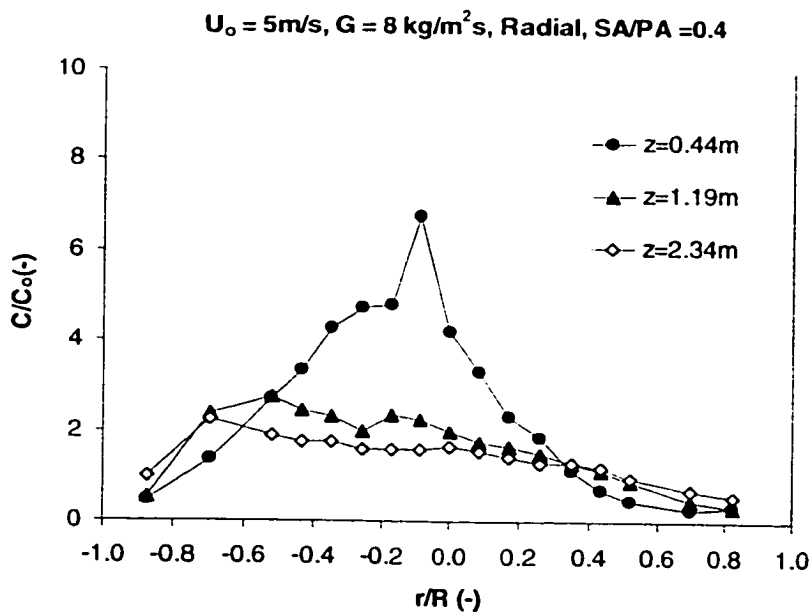


Figure 4.24. Radial distribution of the tracer gas at different heights above the tracer injection plane, radial SA injection, $C_0 = 0.25\%$.

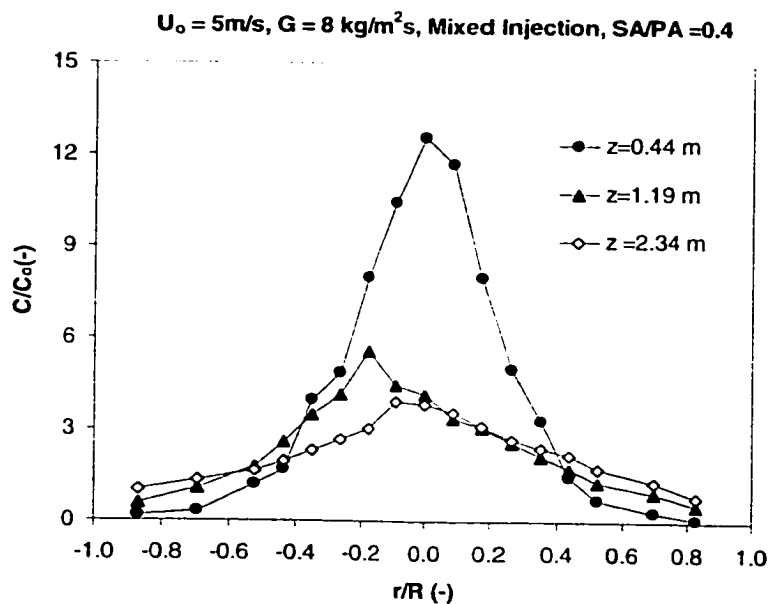


Figure 4.25. Radial distribution of the tracer gas at different heights above the tracer injection plane, mixed SA injection, $C_0 = 0.25\%$.

3.4.1. Effects of SA Injection Design on Radial Gas Mixing

Figures 4.26-4.28 present the variation of the radial distribution of the tracer gas for different cases at three measurement levels for $U_o = 5$ m/s and $G_s = 8$ kg/m²s. Compared to non-SA operation with solids at the same conditions, the effect of the SA injection on radial gas mixing is quite profound. Regardless of the mode of injection, the SA injection produces better mixing than the non-SA operation. The best mixing is achieved with radial injector; its effect on gas mixing at $z_i = 0.44$ m is immense (Figure 4.26). The maximum C/C_o obtained around the riser axis in this case is 6.7 compared to 33 of non-SA operation. The mixed injection comes in second in terms of the quality of radial mixing and then comes the tangential injection. At $z_i = 2.34$ m, the mixed and tangential injection curves are almost identical and the mixing with radial injector is still slightly better than the other two modes of injection (Figure 4.28).

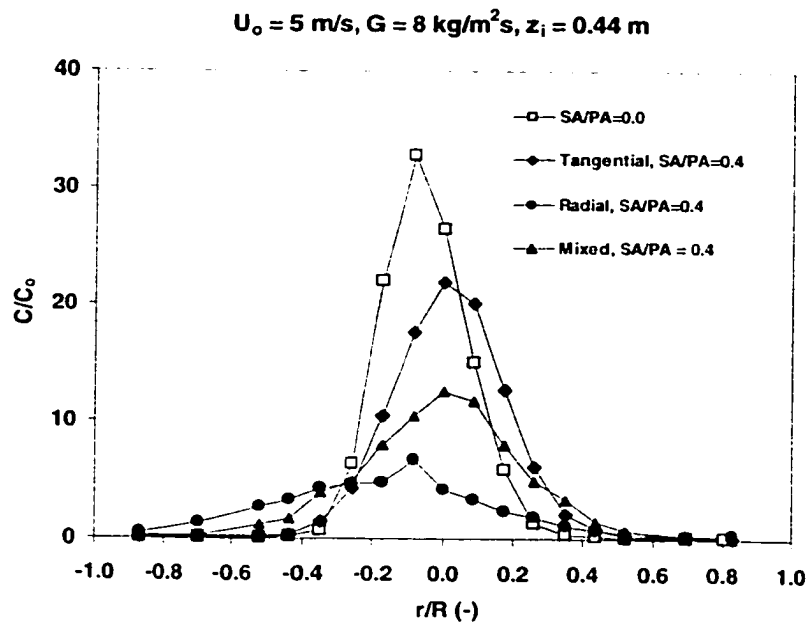


Figure 4.26. Effect of SA injector design on radial gas mixing at 0.44 m above the tracer gas injection plane, $U_o = 5$ m/s, $G_s = 8$ kg/m²s, $C_o = 0.25$ %.

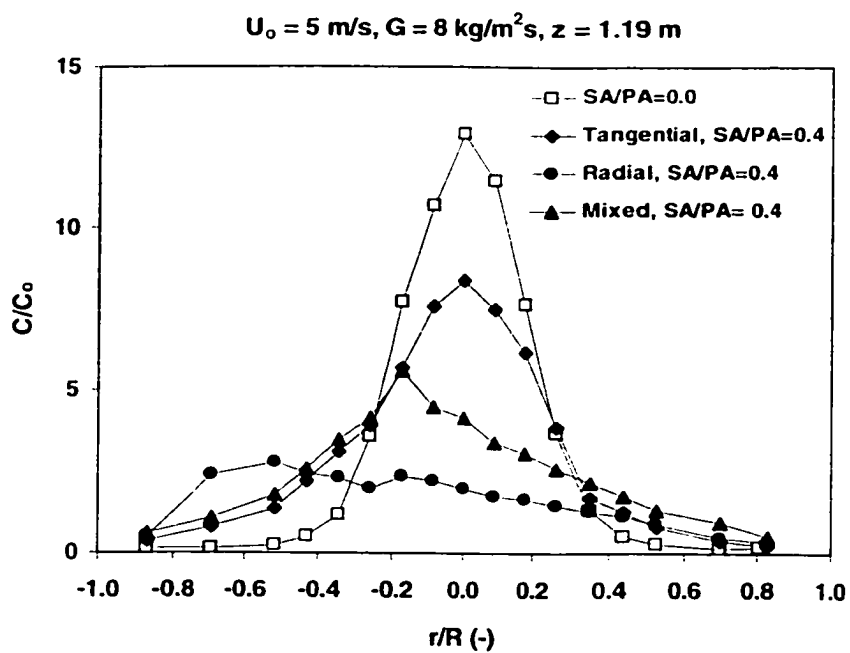


Figure 4.27. Effect of SA injector design on radial gas mixing at 1.19 m above the tracer gas injection plane, $U_o = 5 \text{ m/s}$, $G_s = 8 \text{ kg/m}^2\text{s}$, $C_0 = 0.25 \%$.

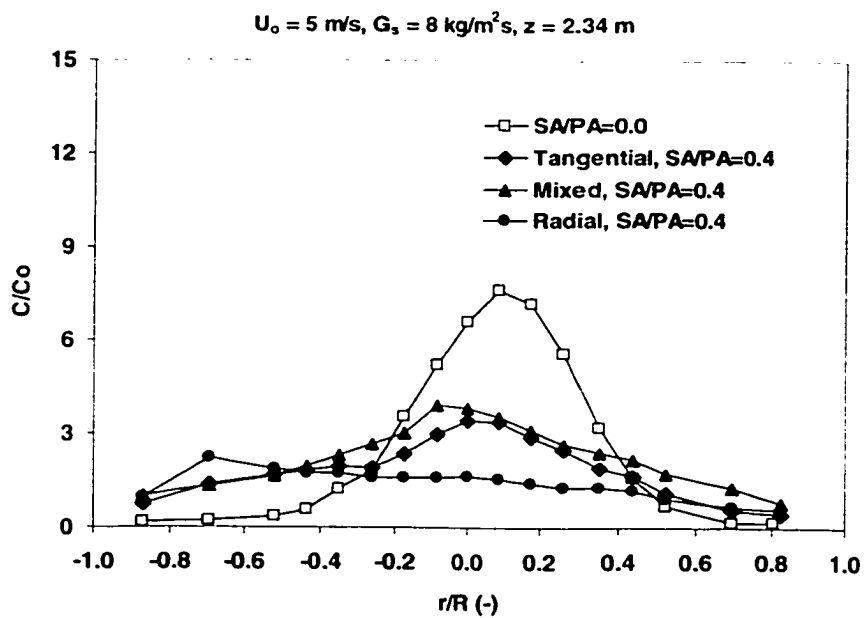


Figure 4.28. Effect of SA injector design on radial gas mixing at 2.34 m above the tracer gas injection plane, $U_o = 5 \text{ m/s}$, $G_s = 8 \text{ kg/m}^2\text{s}$, $C_0 = 0.25 \%$.

The average radial dispersion coefficients are calculated using MSDM as outlined in Chapter 2. Figure 4.29 gives the variation of the radial dispersion coefficients with distance from the SA injection port for five cases; non-SA operation with solids, single phase case, radial SA injection, tangential SA injection and mixed SA injection, at $U_0 = 5$ m/s and $G_s = 8$ kg/m²s. At 0.76 m above the SA injection port, the radial dispersion coefficient for the radial SA injection case reaches up to 83 cm²/s which is almost 7 times the value obtained in non-SA operation at the same conditions.

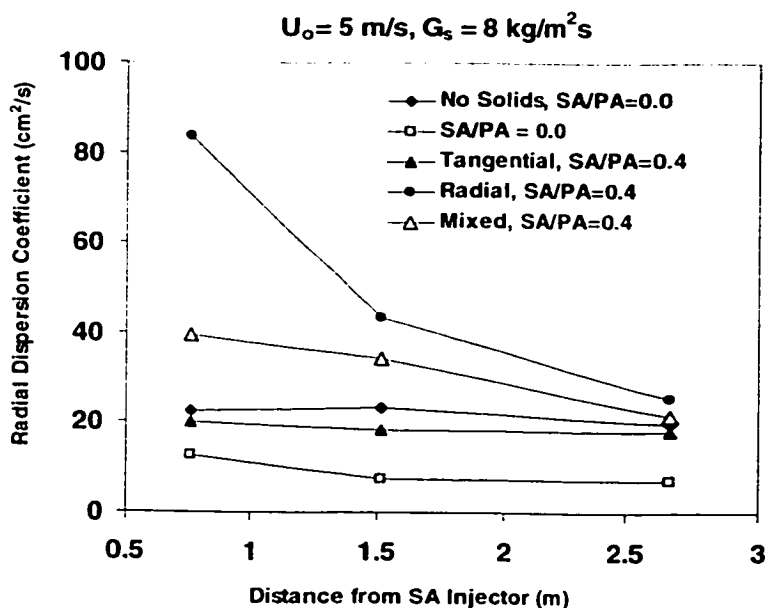


Figure 4.29. The variation of the radial dispersion coefficients with the distance from SA injector, $U_0=5$ m/s, $G_s = 8$ kg/m²s.

For radial and mixed SA injection cases, the radial dispersion coefficient is very sensitive to the distance from the SA injection port as can be seen from the figure. The value of the radial dispersion coefficient drops quickly with the distance for both cases; approaching the single phase radial dispersion coefficient value obtained at the third measurement level (2.66 m above the SA injection port). For the case of tangential injection on the other hand, the radial dispersion coefficient decreases slightly with distance from the SA injection port unlike the cases with radial and mixed SA injectors. The tangential SA injection results in a radial mixing which is comparable to that of the single phase flow.

Generally, the SA jets are expected to increase the intensity of the gas phase turbulence by shearing the mean gas flow, which will in turn increase the dispersion of the gas normal to the mean flow. However, the undue increase in the radial dispersion with the radial SA injector can not be only attributed to the increase in the turbulent intensity of the gas phase turbulence.

Based on the visual observations made during the experiments and from the analysis of experimental results, it is suggested that the impinging SA jets and the uprising gas solid suspension produces large scale gas fluctuations, most probably larger than the scale of the large scale eddies, forcing the gas to move in the radial direction. In case of radial injection, due to the design of the injector, the centerline of the SA jets are aligned with each other producing a striking effect. The rising gas solid suspension on the other hand has to flow past this obstacle or barrier produced by the SA jets. Although the exact physics are not known, this resembles a situation of flow past a solid body and similar wake effects could be produced downstream the SA jets. These wake effects or large scale fluctuations are responsible for this high level of enhancement in gas dispersion for the radial SA injection. This view is also supported by the fact that the effect of the SA injection is very localized close to the SA injection port and quickly diminishes at locations away from it. Recently, such an effect is also noted by Nadeau *et al.* (2001) for two opposed impinging jets perpendicular to main stream of gas in a reactor producing ultra-fine ceramic particles. Figure 4.30 shows the results of the experiments carried out without the solids in the riser at a superficial gas velocity of 5 m/s for SA/PA = 0.2. The same type of enhancement in the radial gas dispersion is also obtained for the single phase flow.

In order to investigate the flow structure with radial SA injection further, two-dimensional CFD simulations were performed without solids present in the riser using Fluent V4.5, the commercial CFD package. It is assumed that two-dimensional simulations approximate the flow at least at the SA injection plane. The time-averaged Navier-Stokes equations were solved with standard $k-\varepsilon$ eddy viscosity model for which the corresponding equations are given in Chapter 5. A total of 13554 cells were utilized in

the simulations and a second order interpolation scheme, quadratic upwind interpolation (QUICK), was used to solve the steep velocity gradients around the SA injection region⁵.

Figures 4.31 and 4.32 show the variation of the axial gas velocity and gas turbulent kinetic energy in the riser around the SA injection region. The superficial gas velocity was set as 5 m/s and SA/PA was 0.5 for this simulation. In both figures, $r = 0$ represents the symmetry line (center of the riser) whereas $r = 0.115$ m is the solid wall. As can be seen from figure 4.31, the SA jet is tilted upwards by both the momentum of the primary gas flow and the striking effect of the opposing jet. The physical dimension of the jet extends almost to 0.4 m above the SA injection level. The axial velocity inside the jet reaches to 18 m/s. Since the tracer gas was injected at a height of 1.52 m above the distributor plate on the riser axis, the injection point falls in the region directly affected by the SA jet. On the other hand, the highest value of the turbulent kinetic energy is obtained at midway between the riser wall and axis just near the SA jet itself with its value reaching $20 \text{ m}^2/\text{s}^2$ (Figure 4.32). This is a significant increase compared to its primary region (below the SA ports) counterpart which is about $1 \text{ m}^2/\text{s}^2$. Therefore, an alternative explanation for the increase of the dispersion in case of radial SA injector is suggested as follows; first the SA jet directly hits on the tracer gas injection point. Second, as the tracer gas is dispersed, the created turbulence further transports the gas towards the wall. The large scale fluctuations mentioned previously could not be captured in the simulations possibly due to time averaged nature of the equations.

In case of mixed injection, the SA jets are not aligned with each other, they just cover a wider proportion of the riser compared to radial injection acting like a plane that hinders the motion of the rising suspension. Thus, two jets will not strike with each other. The expected wake effects will be less than the radial injection case.

⁵ Appendix E gives detailed information on the interpolation schemes.

In case of tangential SA injection, the flow area is reduced due to the tangentially introduced SA jets, and the rising gas solid flow is expected to accelerate smoothly while passing through the SA injection ports. Ersoy *et al.* (1999) captured this acceleration effect by measuring the axial velocity component of the particle velocity using an optical probe. The tangential injection does not block or cut the up flowing suspension as the radial injector, hence, no large scale fluctuations are produced; the increase in the radial dispersion is solely due to the shearing effect of the tangential SA jets that leads to turbulence generation.

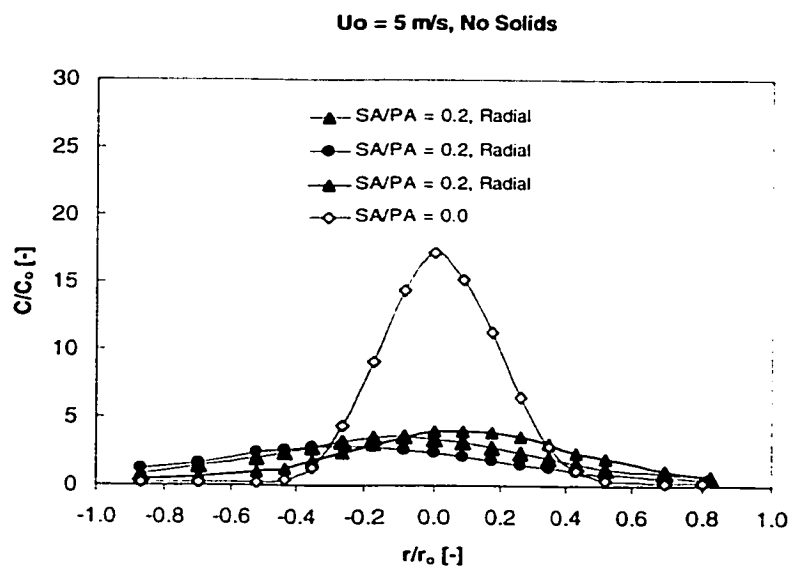


Figure 4.30. The effect of the radial SA injection on radial tracer dispersion for single phase flow, $U_o = 5 \text{ m/s}$, $z_i = 0.44 \text{ m}$, $C_o = 0.25\%$.

In light of the above arguments, it can be suggested that, the radial dispersion coefficient calculated using MSDM does not only reflect the intensity of the gas phase turbulence although it is originally derived from turbulent dispersion theory. It also bears the cumulative effect of the transport mechanisms aiding the gas to disperse in the radial direction whether it is the gas phase turbulence, gas bulk flow, large scale fluctuations or molecular diffusion. At this point, laser doppler velocimeter (LDV) measurements of the local gas and solids fluctuations above the SA injection ports might shed more light on the actual interactions.

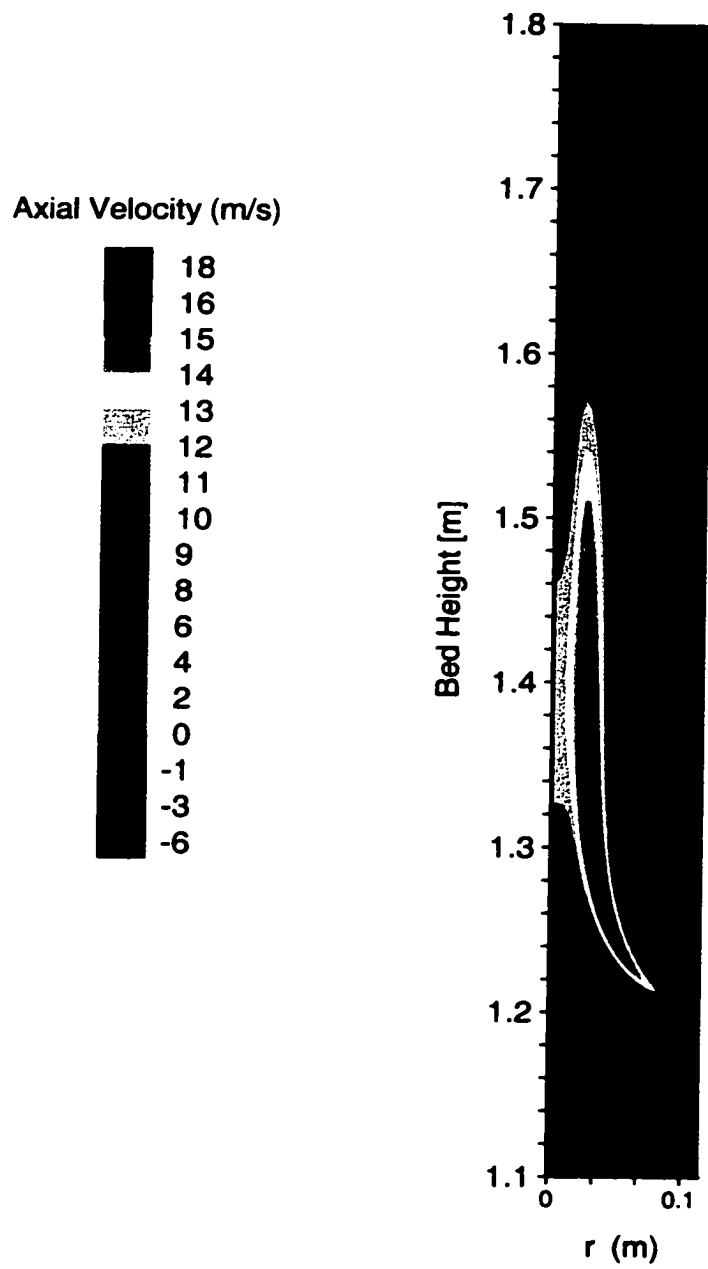


Figure 4.31. The variation of the axial gas velocity in the riser, two-dimensional single phase simulation with Fluent V4.5.

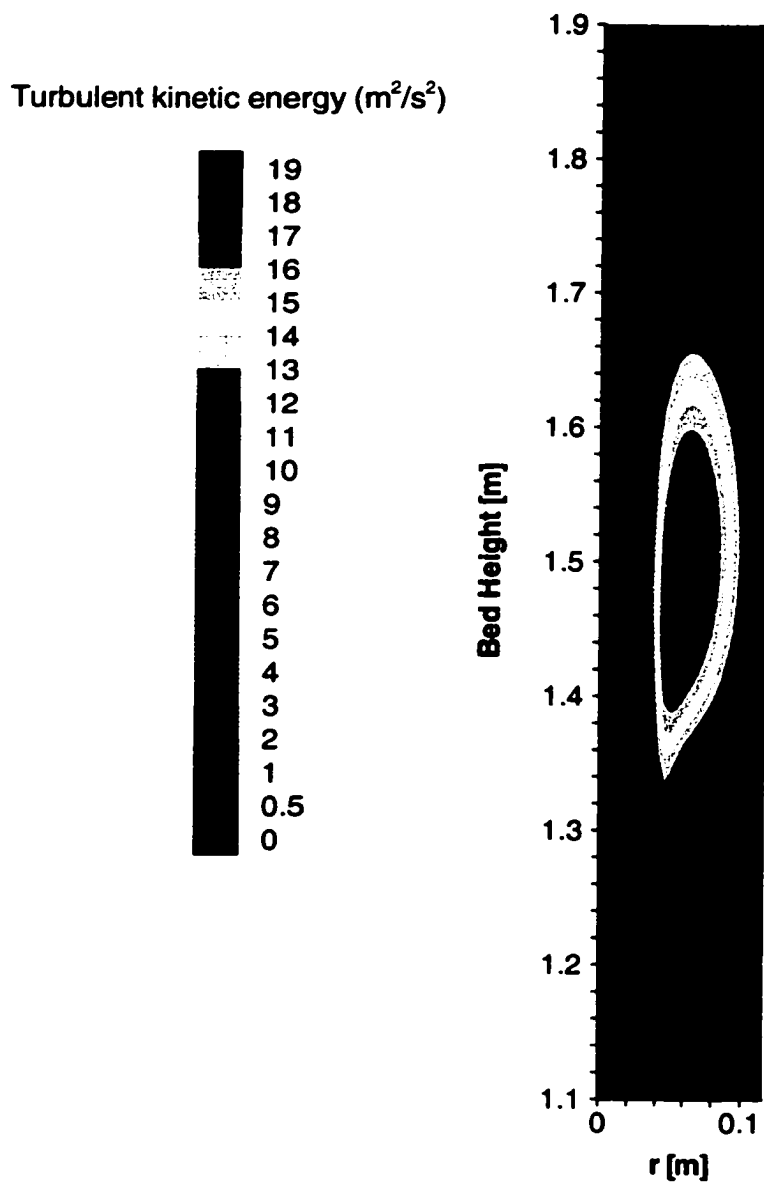


Figure 4.32 The variation of the turbulent kinetic energy in the riser, two-dimensional single phase simulation with Fluent V4.5.

3.4.2. Effects of the Solids Circulation Rate on Radial Gas Mixing with SA Injection

In the last section, referring to Figure 4.29, it was stated that the radial dispersion coefficients for the case of tangential SA injection were almost constant along the bed height above the SA injection ports unlike the radial and mixed injection cases. This can be explained by considering the axial solids suspension profiles obtained at $U_o = 5$ m/s and $G_s = 8$ kg/m²s (Figure 4.7). For radial and mixed injectors, the solids suspension density above the SA injection port is almost constant with a value equal to that of non-SA operation. For the tangential SA injection on the other hand, there is a gradual decrease in the suspension density above the SA injection port. Closer to the SA injection port, the effect of the tangential SA jets might be more profound but the higher solids volume fraction counter balance this effect by dissipating the generated turbulence.

The effects of the solids hold up are further investigated by carrying out experiments at varying solids circulation rates at a superficial gas velocity of 5 m/s. Figures 4.33-4.35 show the effects of the solids circulation rate on the dispersion of the tracer gas for the case of radial, tangential and mixed SA injection at SA/PA=0.2. When the bed was staged, for a single phase run, the maximum attainable value of SA/PA was 0.2 since a higher value was causing the solids to enter the riser through the return leg. Figures 4.33-4.35 clearly indicate that the radial gas dispersion deteriorates with increasing solids circulation rate at a constant superficial gas velocity; similar to non-SA operation (in the range of $0 < G_s < 15$ kg/m²s). Thus, roughly, there are two competing mechanisms; while the SA jets tend to increase the radial gas dispersion, solids tend to dissipate the fluctuations produced by the SA jets.

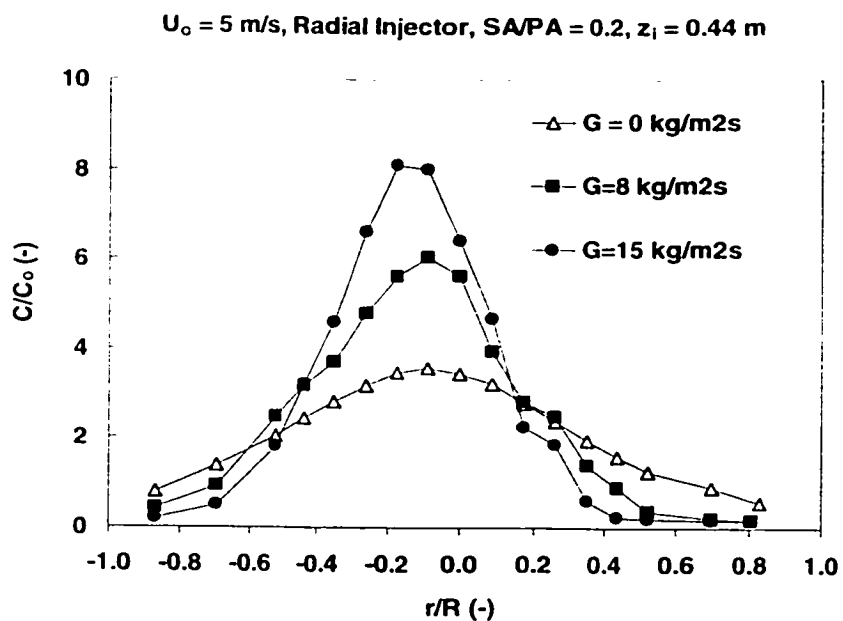


Figure 4.33. The effect of solids circulation rate on radial gas dispersion for radial SA injection, $U_o = 5 \text{ m/s}$, SA/PA=0.2, $z_i = 0.44\text{m}$, $C_o = 0.25\%$

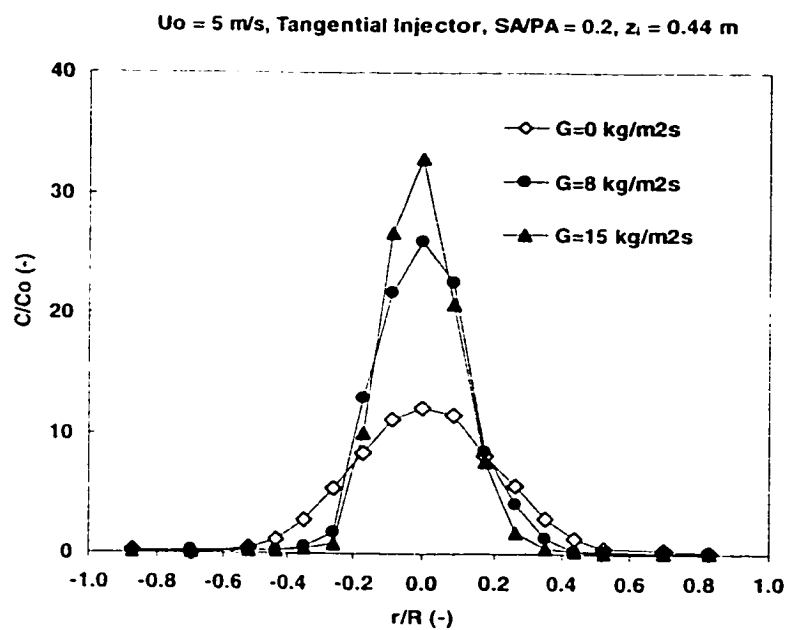


Figure 4.34. The effect of solids circulation rate on radial gas dispersion for tangential SA injection, $U_o = 5 \text{ m/s}$, SA/PA=0.2, $z_i = 0.44\text{m}$, $C_o = 0.25\%$

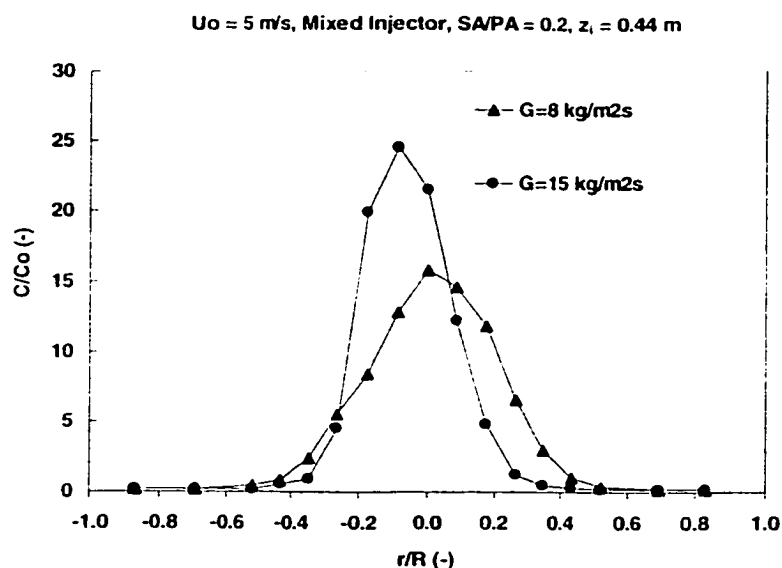


Figure 4.35. The effect of solids circulation rate on radial gas dispersion for mixed SA injection, $U_o = 5 \text{ m/s}$, SA/PA=0.2, $z_i = 0.44 \text{ m}$, $C_o = 0.25\%$

3.4.3. Effects of the SA/PA Ratio on Radial Gas Mixing with SA Injection

Figures 4.36-4.38 show the effects of the SA/PA ratio for all the three SA injection modes. As can be seen from the figures, except for the case of radial injection, the radial gas dispersion increases with increasing SA/PA ratio. Unfortunately, it was very difficult to maintain a steady state operation at higher values of SA/PA ratios, thus the obtained result could not be checked with another experiment for the case of radial injection. For tangential and mixed injection cases, the amount of shearing depends on the relative momentum of the SA jets, thus a higher SA/PA ratio leads to a larger turbulence production increasing the radial dispersion as can be seen from the figure.

Figure 4.39 summarizes the results presented in Figures 4.33-4.38. This figure shows the variation of the radial dispersion coefficient calculated using MSDM for different SA injector designs and non-SA operation at the first measurement level (0.76 m above SA injection port, 0.44 m above the tracer gas injection probe). The figure includes the dispersion coefficients for both SA/PA=0.2 and SA/PA=0.4 at $G_s = 8 \text{ kg/m}^2\text{s}$ for each of the secondary injection modes. The higher value represents the dispersion coefficient at

SA/PA=0.4. As can be seen from the figure, regardless of the mode of injection, SA results in higher dispersion coefficients compared non-SA operation. The SA operation is also sensitive to the solids holdup in the riser at same degree as the non-SA operation; the radial dispersion coefficients decrease with increasing solid hold-up. However, the relative effectiveness of the SA injection, especially that of the radial injector, still prevails at higher solids circulation rates, i.e., $G_s = 15 \text{ kg/m}^2\text{s}$. The calculated dispersion coefficient for radial SA injection case is $52 \text{ cm}^2/\text{s}$ compared to $4.3 \text{ cm}^2/\text{s}$ of the non-SA operation

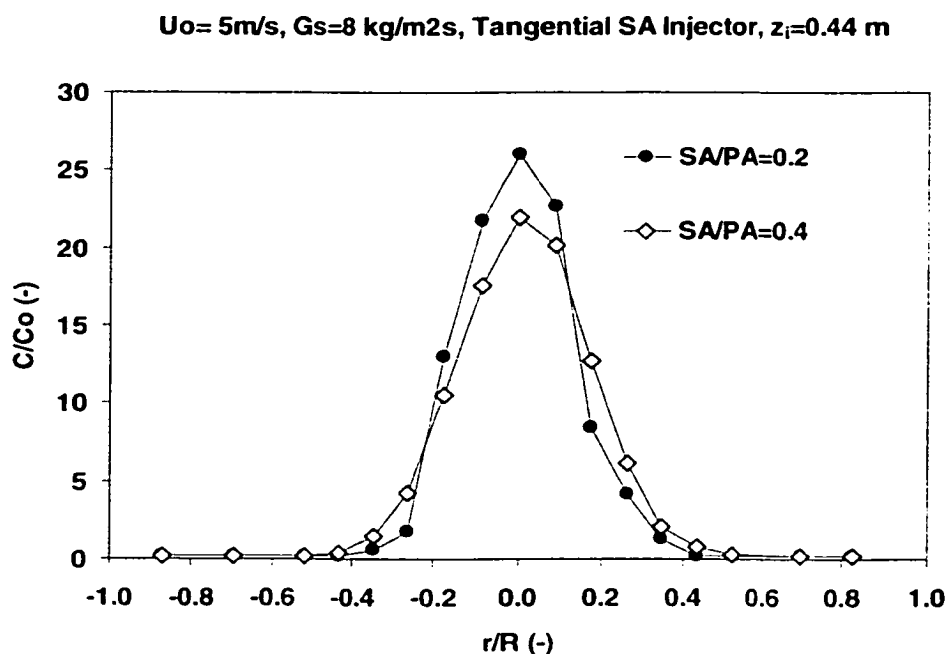


Figure 4.36. The effect of SA/PA ratio on radial gas dispersion for tangential SA injection, $U_o = 5 \text{ m/s}$, $G_s = 8 \text{ kg/m}^2\text{s}$, $z_i = 0.44\text{m}$, $C_o = 0.25\%$

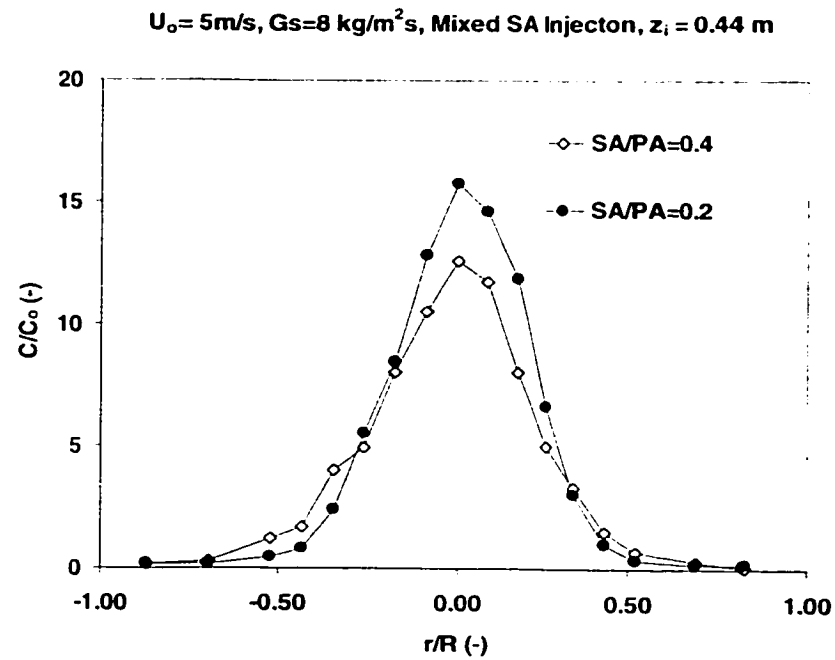


Figure 4.37. The effect of SA/PA ratio on radial gas dispersion for mixed SA injection, $U_o = 5 \text{ m/s}$, $G_s = 8 \text{ kg/m}^2\text{s}$, $z_i = 0.44 \text{ m}$, $C_o = 0.25\%$

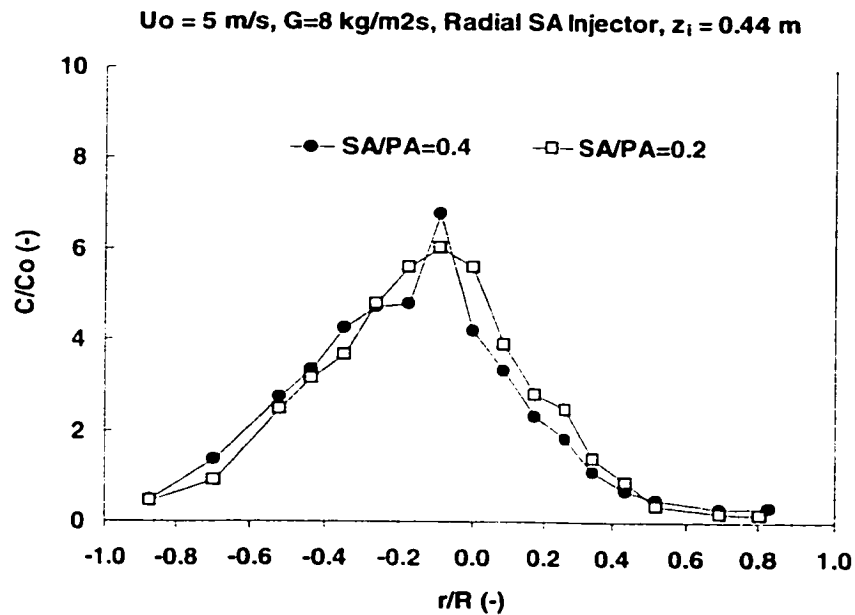


Figure 4.38. The effect of SA/PA ratio on radial gas dispersion for radial SA injection, $U_o = 5 \text{ m/s}$, $G_s = 8 \text{ kg/m}^2\text{s}$, $z_i = 0.44 \text{ m}$, $C_o = 0.25\%$

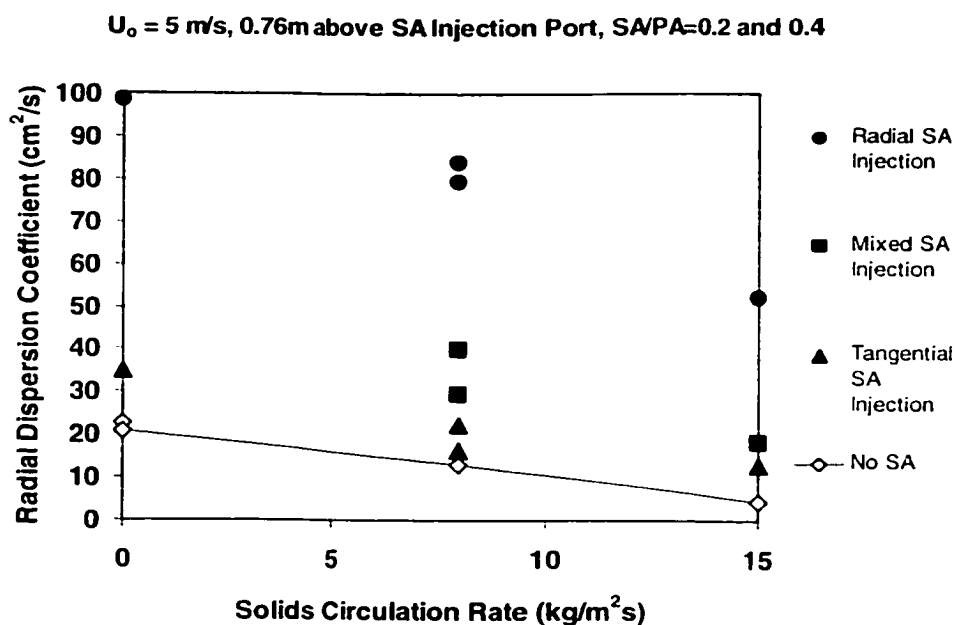


Figure 4.39. The effect of solids circulation rate on radial gas dispersion coefficient, $U_o = 5 \text{ m/s}$, $z_i = 0.44\text{m}$, $C_o = 0.25\%$

3.4.4. Comparison of the Results of this Study with Zheng *et al.* (1992) and Namkung and Kim (2000).

To the author's knowledge, there are two studies in the literature which investigate the effects of the SA injection on radial gas dispersion. Zheng *et al.* (1992) carried out experiments in a bed of 0.102 m ID and 5.25 m height. The experimental conditions of their study are given in Table 1.5. The secondary air was injected at a height of 1.65 m above the distributor plate. The tracer injection probe on the other hand, was located at 0.65 m above the SA injection port. Using a SA/PA ratio of 2.33 (they haven't reported the mode of injection), they obtained radial dispersion coefficient values between 20-38 cm²/s at a height of 0.6 m above the tracer injection probe. Similar to the results of this work, their dispersion coefficients tended to decrease with solids concentration.

Recently, Namkung and Kim (2000) reported some data which show the effects of SA injection on radial gas dispersion. They used a tangential injector, T3 and a radial injector, R3 (T3 and R3 are one-point injectors. See Figure 1.3 of Chapter 1) in their

experiments. The secondary air was injected at a height of 2 m above the distributor plate and the tracer gas was injected 1 m above the SA injection port. They have only carried out measurements at 0.25 m above the tracer injection probe. They obtained radial dispersion coefficients in the range of 10-25 cm²/s, lower than the values obtained in this study. This is most probably due to the fact that their riser was operated at a denser mode compared to this study, i.e., average solids volume fraction was higher than 0.01 in their experiments. They also obtained higher dispersion coefficients with increasing solids holdup which is typical to dense risers as discussed in detail in section 3.3.1. Interestingly, they found out higher radial dispersion coefficients with tangential SA injection compared to radial injection due to the increase in solids hold up when the SA air was injected tangentially.

3.5. Radial Gas Mixing Predictions with (DPFM)

As explained in Chapter 2, the dispersion coefficients quantify the degree of radial gas mixing. The common procedure is to use the dispersion coefficients in the models in which they are calculated from to model the radial gas dispersion (Werther *et al.*, 1992). Another practice is to develop a more sophisticated gas mixing model and use the radial dispersion coefficients found from simpler models as the dispersion coefficient data (Kruse *et al.*, 1995).

In this section, the dispersion coefficients found from MSDM are used in DPFM (Equation 2.7), to predict the radial variation of the tracer gas concentration with distance above the tracer injection port. Thus, all the assumptions behind the DPFM are assumed to be satisfied.

Figures 4.40 and 4.41 show two examples of such predictions using DPFM with the calculated dispersion coefficients from MSDM. As can be seen from the figures, DPFM predictions agree reasonably with the results of the tracer gas experiments for both SA and non-SA operation. The agreement is slightly worse for the SA injection, especially for mixed and radial injection. However, for quick engineering calculations, once the

dispersion coefficients are known, DPFM can also be used for radial mixing modeling with SA injection.

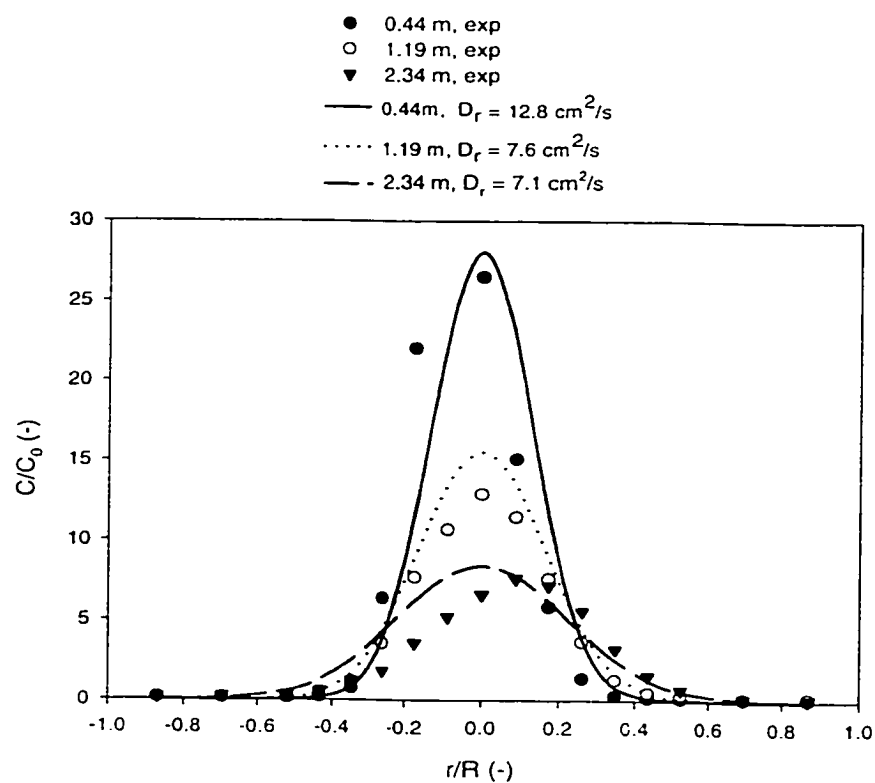


Figure 4.40. Prediction of the radial distribution of the tracer gas at different heights above the tracer injection probe, $U_0=5 \text{ m/s}$, $G_s=8 \text{ kg/m}^2\text{s}$, $SA/PA=0.0$, $C_0 = 0.25\%$

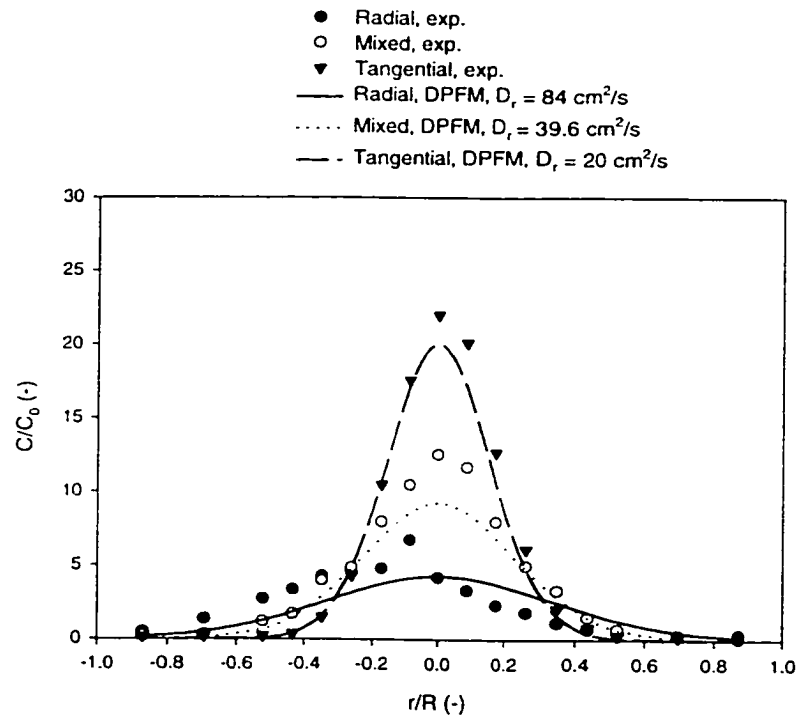


Figure 4.41. Prediction of the radial distribution of the tracer gas for different SA injection modes at $z = 0.44\text{m}$, $U_0 = 5\text{ m/s}$, $G_s = 8\text{ kg/m}^2\text{s}$, $SA/PA = 0.4$, $C_0 = 0.25\%$.

4. Backmixing Experiments

The gas backmixing experiments were carried out by injecting the tracer gas near the wall ($r/R = 0.9$) and taking measurements at 0.05 m below the injection plane as outlined in Chapter 3. Figure 4.42 shows the radial variation of the tracer gas for $U_0 = 5\text{ m/s}$, $G_s = 15\text{ kg/m}^2\text{s}$ and $SA/PA = 0.2$. For this secondary-to-primary air ratio, the primary air velocity and the SA jet velocity are 4.2 m/s and 13.8 m/s , respectively. The figure shows that regardless of the mode of injection, the SA decreases the gas backmixing near the wall compared to non-SA operation. The decrease in the gas backmixing is more pronounced for the tangential injection; the near wall concentration is almost half of the case without SA injection. The radial injector on the other hand does not cut the gas backmixing as

much as the tangential and mixed injectors but disperses the backmixed gas towards the center of the riser. This is most probably due to the significant enhancement in radial gas dispersion with radial injector as shown in previous sections. One of the interesting points about the figure is the higher tracer gas concentration measured near the opposite wall of the riser for the tangential SA injection compared to mixed and radial injectors. The increase in the tracer gas concentration near the wall is most probably due to the circumferential mixing imposed by the tangential SA jets.

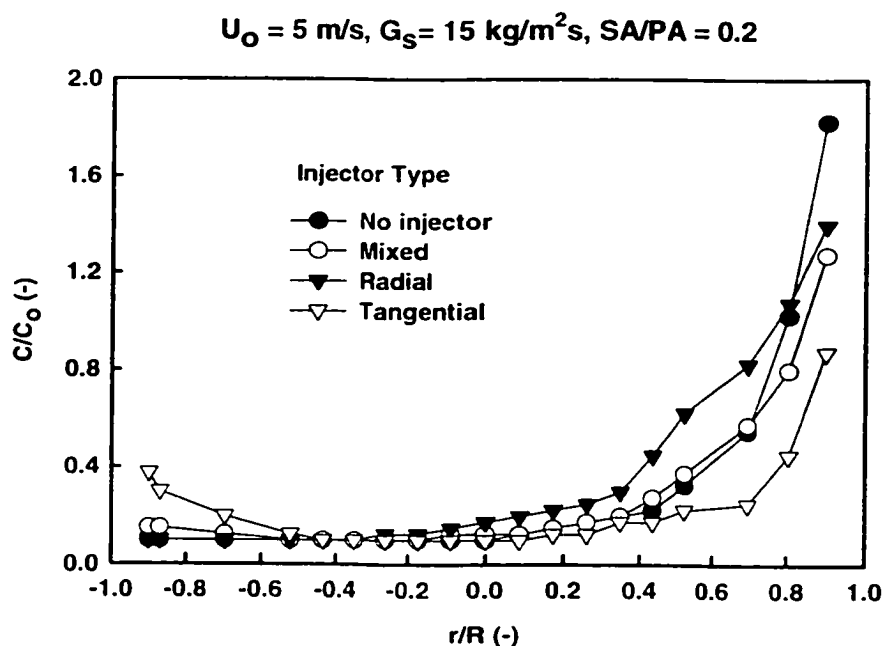


Figure 4.42. Radial distribution of the tracer gas at 5 cm below the tracer gas injection plane, $U_o = 5 \text{ m/s}$, $G_s = 15 \text{ kg/m}^2\text{s}$, $SA/PA = 0.2$, $C_0 = 0.4 \%$.

5. Mixing of SA with Rising Gas-Solid Suspension

The purpose of this set of experiments is to investigate and compare the mixing characteristics of the SA itself with the gas-solid flow in the riser for the tangential, radial and mixed injectors. As explained in Chapter 3, experiments are performed premixing the tracer gas with the SA and then feeding it into the riser (only from one side). The

measurements are taken 0.15 and 0.76 m above the SA injection ports. Figures 4.43 and 4.44 show the results of the experiments performed for $U_o = 5$ m/s, $G_s = 8$ kg/m²s and $SA/PA = 0.2$. The figures clearly indicate that the mixing mechanisms of the SA with the rising gas-solid suspension are different for the different injectors used. With the radial injector, the SA penetrates more through the gas-solid suspension towards the center of the riser. The motion of the SA towards the riser is mostly due to convective motion of the gas due to high momentum SA jets. When the tangential SA is used, however, the penetration of the SA towards the riser relies on the gas phase turbulence rather than the convective flow leading to a more gradual dispersion of the tracer gas towards the riser center. As can be seen from Figure 4.44, with radial SA injector, the radial dispersion of the tracer gas goes to completion at a shorter axial distance compared to tangential and mixed injectors.

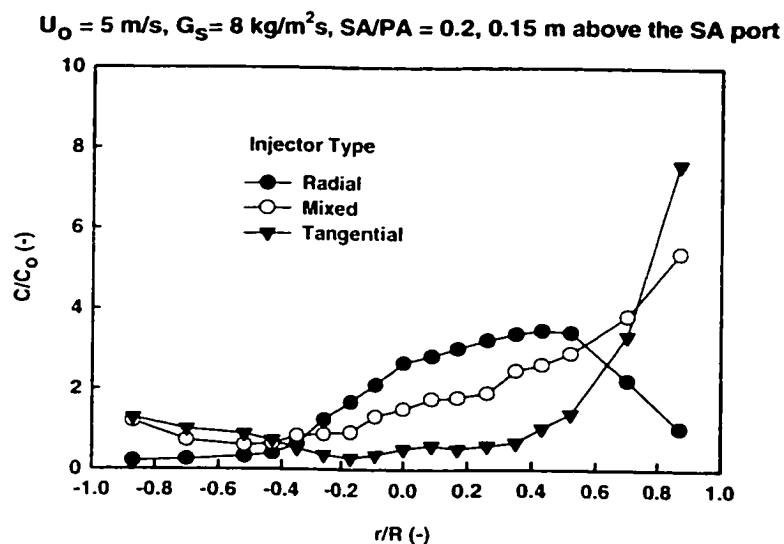


Figure 4.43. Radial distribution of the tracer gas at 0.15 m above the SA injection port, $U_o = 5$ m/s, $G_s = 8$ kg/m²s, $SA/PA = 0.2$, $C_0 = 0.25$ %

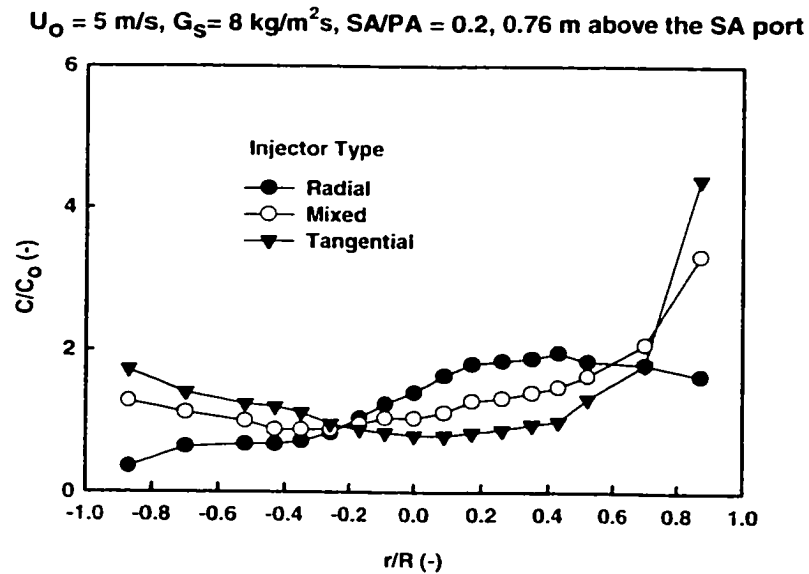


Figure 4.44. Radial distribution of the tracer gas at 0.76 m above the SA injection port, $U_o = 5 \text{ m/s}$, $G_s = 8 \text{ kg/m}^2\text{s}$, $SA/PA = 0.2$, $C_0 = 0.25 \%$.

6. Uncertainty in Experimental Results

The uncertainty and error in the experiments were tried to be minimized by repeating the corresponding measurements. The axial pressure measurements were carried out several times in a single run during the tracer gas measurements and mean values were used to represent the corresponding run. Such an approach is illustrated in Figure 4.45 for the case of the tangential SA injection at $U_o = 5 \text{ m/s}$, $G_s = 8 \text{ kg/m}^2\text{s}$ and $SA/PA = 0.4$.

The same approach was also taken in the tracer gas experiments. Generally, for the SA injection, the reproducibility of the tracer gas measurements was worse than that of the non-SA operation, especially for the radial SA injector. As explained in Chapter 3, longer sampling times were utilized to overcome this deficiency. As a result, the maximum

discrepancy between two dispersion coefficients obtained from two different measurements never exceeded 10%.

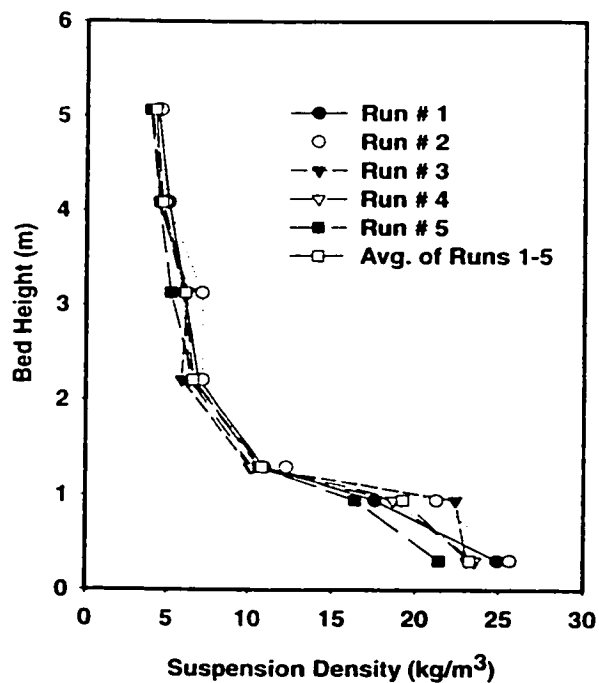


Figure 4.45. The repeatability in axial pressure measurements, $U_o = 5$ m/s, $G_s = 8$ kg/m²s and SA/PA = 0.4, tangential SA injector.

7. Conclusions

This chapter presents the results of the axial pressure measurements and gas mixing experiments carried out in this study. The detailed information on the experimental set-up and procedure is given in Chapter 3. In order to study the effects of the SA injection on

gas mixing and axial solids distribution, three different types of injectors are tested, the so-called radial, tangential and mixed injectors for which the detailed information is given in Chapter 3. The superficial gas velocity and the solids circulation rate are changed between 3-5 m/s and 0 - 25 kg/m²s during the experiments.

First, the effects of the SA injection on the axial solids distribution are investigated based on the time averaged axial static pressure measurements. The following conclusions are reached for the axial solids distribution in the riser with SA injection.

Regardless of the mode of injection, the suspension density in the primary zone (the region below the SA injection ports) increases with SA injection due to cumulative effect of two phenomena; decrease in the total gas flow in the primary zone and the blockage effect of the SA jets. The increase in the suspension density in the primary zone increases with increasing SA/PA. The tangential SA injector results in the highest increase in the suspension density in this zone followed by the mixed injector.

In the secondary zone (above the SA injection ports), the suspension density almost remains the same for the radial and mixed injectors when compared to that of non-SA operation. With tangential injection, however, there is a considerable increase in the suspension density also in this zone. This is mostly due to the helical motion of the suspension imposed by the tangential SA jets which in turn increases the net solids residence time in the riser leading to an increased suspension density.

The total solids hold up in the riser increases considerably at the same superficial gas velocity and the solids circulation rate especially for the tangential injection. Thus, tangential secondary air injection can be used as a tool to increase the total internal solids circulation in a CFB combustor.

Second, gas mixing in CFB risers with SA injection is studied using tracer gas technique. Three types of experiments are performed: radial, gas backmixing and mixing of SA with gas-solid suspension. The emphasis is placed on the radial mixing experiments. The intensity of the mixing in the radial direction is quantified by a radial dispersion

coefficient calculated from the tracer concentration measurements based the mean square displacement model (MSDM) presented in Chapter 2.

Following conclusions are reached in radial gas mixing experiments:

The radial gas dispersion coefficient in the empty (no solids) riser increases with superficial gas velocity. A constant radial Peclet number of 520 is found to characterize the radial mixing in the empty riser.

Within the limits of the operational conditions of this study, the radial dispersion coefficient in the dilute upper zone of the riser varies between 4.1- 23.2 cm^2/s for the case without secondary air injection. This corresponds a Peclet number range of 496-2778 when the Peclet number is defined based on the superficial gas velocity and the riser diameter. This includes the empty riser data. Excluding the empty riser data, the radial dispersion coefficient and the Peclet number are found to be between 4.1-12.9 cm^2/s and 893-2778, respectively.

The best mixing is achieved without the solids in the riser. Increasing the solids loading (by increasing the solids circulation rate at constant superficial gas velocity) decreases the radial dispersion sharply from its empty riser value. However, the decrease in radial dispersion levels off quickly. The decrease in the radial mixing with solids loading is explained in the light of the turbulence modulation theory. With the particles used and operating conditions employed in this study, the solids tend to dissipate the gas phase turbulence which is the main mechanism for the dispersion of the gas in the radial direction.

The secondary air injection increases the radial gas dispersion considerably. The highest increase in the radial dispersion coefficient is obtained with the radial SA injector with the dispersion coefficient values ranging between 52-99 cm^2/s . It is suggested that the immense effect of the radial SA injector is not only due to the extra turbulence generated by the shear of the SA jets but also due to the possible unsteady large scale gas motion produced by the impinging SA jets. The tangential SA injection produces the least

increase in the radial gas dispersion due to the increase in solids holdup which dissipates the generated turbulence. The performance of the mixed injector lies in between the tangential and radial injector. Thus, it can be concluded that with SA injection, two mechanisms are competing with each other: the dissipation of the gas turbulence due to solids and its augmentation with SA jets.

The effect of the SA injection on radial gas dispersion increases with SA/PA and decreases with height above the SA injection ports. For radial SA injector, however, even 2.66 m above the SA injector, the value of the radial dispersion coefficient is more than threefold of its non-SA operation counterpart.

The gas backmixing and mixing of SA injection with the rising gas-solid suspension experiments reveal the following conclusions.

Regardless of the mode of injection, SA jets decrease the gas backmixing just above the SA injection ports near the wall possibly by cutting the solids downflow. This decrease is more pronounced for the tangential injection case. Tangential injection also promotes the circumferential gas backmixing.

The mixing mechanisms of the SA with the rising gas-solid suspension depend strongly on the design of the injector. With the radial injector, the SA jets penetrates more towards the center of the riser and the radial mixing is accomplished at a shorter axial distance. With tangential injector on the other hand, the mixing of SA with the rising suspension takes place more gradually along the riser height.

Chapter 5

Two-Fluid Modeling of CFBs

1 Introduction

This chapter presents a gas-solid flow model proposed to describe the gas-solid hydrodynamics in the riser section of a CFB with SA injection. The model is based on solving the fundamental equations of fluid mechanics and is implemented using, FLUENT V4.5, the commercial computational fluid dynamics (CFD) package. The gas-solid model presented is essentially an isothermal two-fluid (Eulerian-Eulerian) model where both gas and solid phases are treated as two interpenetrating continua. The model has the capability of handling the complex nature of the gas-solid flows encountered in CFB risers regardless of geometry and flow configuration, making it suitable for problems such as secondary air injection. However, modeling of the closure schemes, gas-particle interactions and the computational time are the major drawbacks for which further improvements are needed.

The chapter starts with a classification of gas-solid two-phase flows based on the commonly used time scales in gas-solid flows. Following that, a brief review of CFB hydrodynamic models available in the literature is given. The emphasis is placed on the models based on solving the fundamental equations of fluid mechanics. The two-fluid

model used in this study is described with the underlying assumptions. The chapter ends with general conclusions.

In the next chapter, the application of the model to several riser flow problems is presented.

2 A Simple Classification of Gas-Solid Two Phase Flows

Gas-solid flow modeling is a challenging task. According to Crowe (1996), an ideal gas-solid flow model should:

- resolve all scales of gas turbulence,
- include all particles and influences of all surfaces on gas,
- provide of all forces and moments on particles,
- account for all particle collisions and interactions.

Even with today's rapidly developing computational technology, an ideal model defined above can not be fully applied to practical gas-solid flow problems. In order to simplify the problem without losing the essential physics and, to be computationally tractable at the same time, very often simplifying assumptions must be made. Figure 5.1 shows a simple process for the classification of gas-solid flows based on the current state of the art from which such simplified assumptions can be inferred.

One of the ways to classify gas-solid flows is to use some of the time scales associated with the flow. Usually, three time scales are utilized for this purpose. These time scales are the interparticle collision time, τ_c , the particle relaxation time, τ_{pr} (or aerodynamic response time) and the fluid integral turbulent time scale (or time scale of the most energetic eddies or eddy turnover time), τ_f (Elgobashi, 1994; Shirolkar *et al.*, 1996; Peirano and Leckner, 1998).

The interparticle collision time represents the time experienced by a particle between a binary particle collision in a gas-solid flow. It can be estimated using the kinetic theory of granular solids as shown by Gidaspow (1994).

The particle relaxation time is defined as the response of the particle to the relative velocity changes between itself and the surrounding gas. The mathematical expression for the particle relaxation time can be expressed as (Shirolkar *et al.*, 1996):

$$\tau_{pr} = \frac{24\rho_s d_p^2}{18\mu_g C_D Re_p} \quad (5.1)$$

where ρ_s is the particle density, d_p is particle diameter, μ_g is the gas absolute viscosity, C_D is the single particle drag coefficient and Re_p is the particle Reynolds number. The particle Reynolds number is defined based on the relative velocity between gas and particles.

$$Re_p = \frac{\rho_g d_p |\mathbf{u} - \mathbf{v}|}{\mu_g} \quad (5.2)$$

In equation (5.2), \mathbf{u} and \mathbf{v} represent the gas and particle velocity vectors, respectively. As can be seen from equation (5.1), the particle relaxation time increases with particle density and diameter. If $Re_p < 0.2$, Equation (5.1) can be further simplified with the assumption of Stokes flow around the particles (Geldart, 1986).

The fluid characteristic integral time scale, τ_f , represents the time scale of the most energetic eddies in a turbulent flow. It is also called as the eddy turnover time. In a turbulent flow, these most energetic eddies do most of the transport of the momentum and contaminants as well as the particle dispersion (Tennekes and Lumley, 1972). Thus, it is a relevant time scale in the analysis of the interaction of the particles with the gas flow. The integral time scale or the eddy turnover time can be estimated from:

$$\tau_f = \frac{u_{rms}}{L} \quad (5.3)$$

where u_{rms} is the gas fluctuating velocity and L is the characteristic length of the most energetic eddies. The length scale of the most energetic eddies in a turbulent flow can be comparable to the size of the vessel.

The first classification of gas-solid flows can be made depending on the volume fraction of solids as “dense” or “dilute”. If $\tau_{pr}/\tau_c \ll 1$, a particle has sufficient time to respond to the local gas velocity field before the next collision so its motion is controlled by the aerodynamic viscous forces rather than particle collisions. This is a dilute gas-solid flow. On the other hand, if $\tau_{pr}/\tau_c \gg 1$, the particle does not have enough time to respond to the aerodynamic forces before the next collision, so its motion is controlled by particle collisions leading to the definition of dense gas-solid flow. The practical limits are difficult to propose; but for instance, Elgobashi (1994) suggests a transition from a dilute flow to dense flow taking place at a particle volume fraction of 0.001.

In dense flows, modeling the particle-particle interactions is essential since it is the dominant mechanism of momentum transfer between the particles, and between the particles and the gas (Hrenya and Sinclair, 1997). The particles can shear the gas motion considerably and the solid phase fluctuations due to particle collisions can be greater than the fluctuations of the gas phase. In dilute flows, on the other hand, the gas turbulence determines the fluctuations of the particles (Balzer *et al.*, 1995; Simonin and Viollet, 1990). The particle velocity fluctuations can be smaller than those of the gas.

The effect of the particles on the gas or the gas on the particles is called coupling. In dilute flows, usually two-way coupling is assumed to be occurring; the gas affects the dispersion of the particles. The particles, on the other hand, can either dampen or augment the gas phase turbulence. The latter effect is known as the turbulence modulation. In the limit, for very dilute flows, the turbulence modulation can be neglected, hence, only one-way coupling can be considered. For dense flows, interactions are quite complicated and the information is very scarce since non-intrusive measuring techniques such as LDV cannot be used in such flows. To complicate the flow further, apart from the two-way coupling between the gas turbulence and the particles, a four-way coupling is assumed to exist due to particle/particle collisions (Elgobashi, 1994).

The second classification for gas-solid two-phase flows can be made based on the relation between the particle relaxation time and eddy turnover time. Based on the above

definitions, if $\tau_{pr} \ll \tau_f$, the particles follow the gas turbulent motion very closely. This is called as the scalar or the small particle limit. For very dilute flows with small particles, for instance, the particle dispersion will be limited to the dispersion of the gas itself as the particles will behave like a passive scalar. On the other hand, if $\tau_{pr} \gg \tau_f$, the particles are not affected by the gas phase turbulence and carried by the mean gas motion. This is called as the coarse particle limit. The turbulence modulation shows opposite trends at these limits; the small particles tend to decrease the gas phase turbulence whereas large particles tend to increase it due to wake effects (Gore and Crowe, 1989; Hestroni, 1989).

Peirano and Leckner (1998) presented the estimates of the characteristic time scale ratios described above in the core region of the transport zone of a CFB boiler evaluated from algebraic models for a simple shear flow. For a representative case of a hot bed at 850°C with a particle volume fraction of 0.005, $\rho_s/\rho_g = 2600$ and a fluidization velocity of 5 m/s, they showed that the ratio τ_{pr}/τ_c was always smaller than one for a particle diameter range of 80 μm to 1 mm. This shows that the path of the particle is at least equally influenced by the presence of the gas (viscous forces) and the particle collisions. On the other hand, the ratio τ_{pr}/τ_f is smaller than one for particle diameters less than 100 μm showing that the gas phase turbulence governs the motion of the particles. For particles larger than 100 μm , the effect of the gas phase turbulence diminishes as the diameter increases.

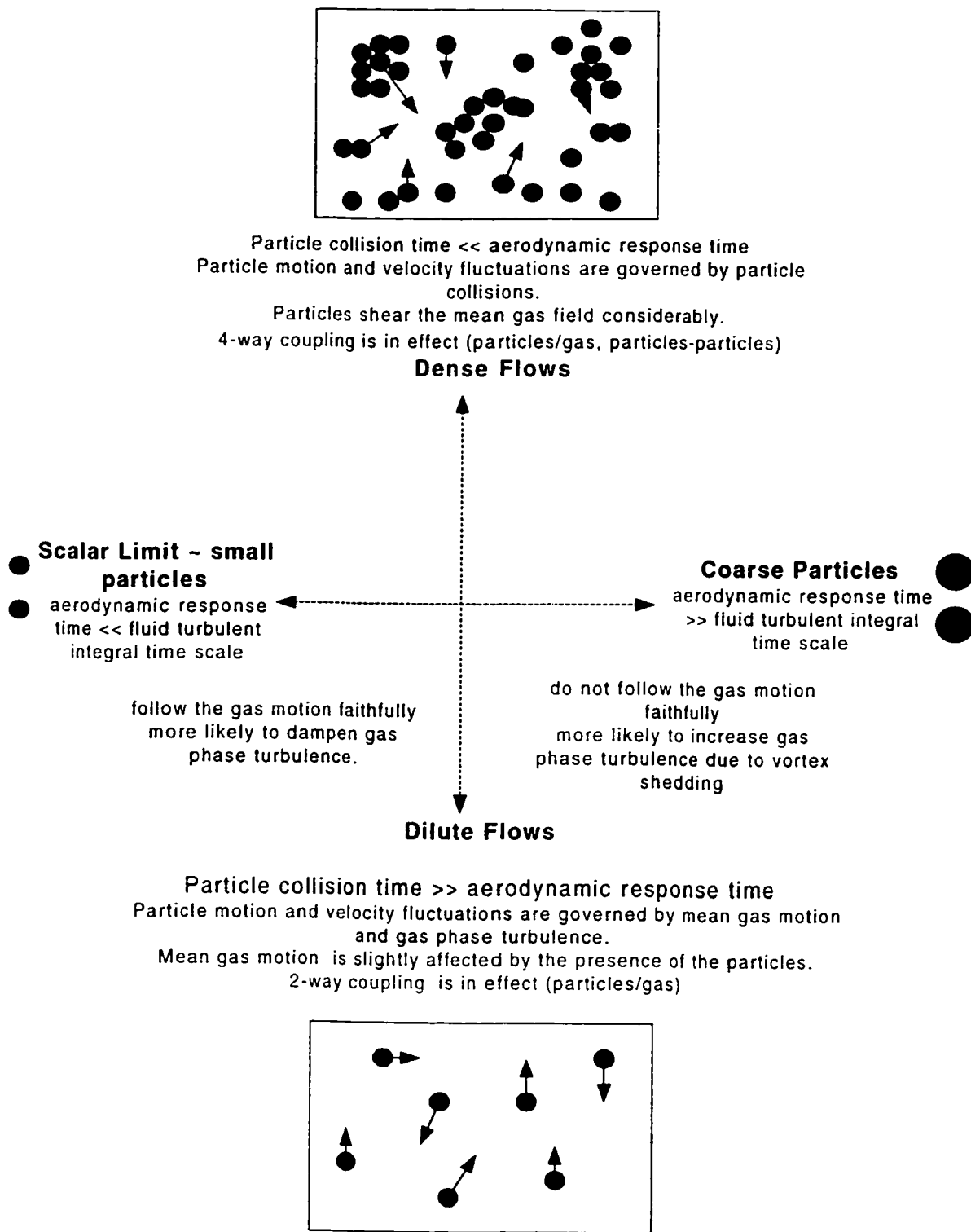


Figure 5.1. A classification of gas-solid two phase flows

3 CFB Hydrodynamic Models

Based on the original classification of Harris and Davidson (1994), the CFB hydrodynamic models can be classified in three groups:

- Those that predict the axial variation of the solids suspension density, but not the radial variation (Li and Kwauk, 1980; Kunii and Levenspiel, 1991).
- Those that predict the radial variation by assuming two or more regions, such as core-annulus or clustering annular flow models (Berruti and Kalogerakis, 1989; Rhodes, 1996; Pugsley and Berruti, 1996).
- Those that employ the fundamental equations of fluid dynamics to predict two-phase gas-solid flow (Sinclair and Jackson, 1989; Gidaspow, 1994; Balzer and Simonin, 1993; Samuelsberg and Hjertager, 1996a,b; Hrenya and Sinclair, 1997; Neri and Gidaspow, 2000).

The type I and II models involve the use of available correlations based on the experimental data. They are relatively simple, easy to use and can be used effectively as design tools to investigate the effects of operating conditions and riser dimensions on the flow structure (Pugsley and Berruti, 1996). It was also cited that type II models give very good agreement with the experimental data when compared to type III models (Berruti *et al.*, 1995). On the other hand, it can be argued that, the assumptions of the flow structure associated with such models oversimplify the complex experimentally observed patterns such as cluster formation and large scale turbulent fluctuations.

In type III models, a system of fundamental fluid dynamics equations for the gas phase and particles and relevant constitutive relations are solved using numerical methods. Thus, the attractiveness of the type III models lies in their generality and ability to deal with complex geometries, local flow phenomena such as inlet/exit effects and secondary reactant injection. However, their main difficulty is modeling and developing the appropriate constitutive relations and interaction terms between the gas and the particles.

In this study, a type III model is used to simulate the effects of SA injection on riser

hydrodynamics. In the following sections, the applied model and the underlying assumptions are discussed in detail.

4 Numerical Models (Type III models) for Gas-Solid Two-Phase Flows

The numerical approaches which employ the use of general fluid mechanics equations can be categorized in four main groups based on the modeling of the carrier (gas) phase (Crowe *et al.*, 1996):

- Two-equation models (Two-Fluid or Eulerian-Eulerian, Eulerian-Lagrangian)
- Large Eddy Simulation (LES)
- Discrete Vortex Simulation
- Direct Numerical Simulation (DNS)

The two-equation models are commonly employed in gas-solid flows since they are computationally cheap compared to the other three. In large eddy simulation (LES), the large eddies are computed directly whereas smaller scale turbulence is modeled. In direct numerical simulation (DNS), the instantaneous Navier-Stokes equations are solved on a grid whose spacing is smaller than the smallest length scale of turbulence and at a time step which can capture even the highest frequency turbulent fluctuations. In even single phase flows, DNS can only be applied to low Reynolds number flows with very simple geometries due to very large computational power requirement (Le *et al.*, 1997). Discrete vortex methods have been used to model particle transport in two-dimensional flows that are dominated by large-scale organized structures. This technique captures the essential features of the two-dimensional gas-solid flows without the complexity and time requirements of DNS (Eaton and Fessler, 1994).

The two-equation models are classified as Eulerian-Eulerian and Eulerian-Lagrangian depending on the treatment of the particulate phase. In Eulerian-Lagrangian models, the particles are treated as discrete entities and are tracked as they move through the computational domain. In other words, for each particle or group (parcel) of particles, the

rigid body equation of motion is integrated and the corresponding paths are found. For the integration of the particle equation of motion, the details of the gas motion including turbulence parameters are essential. The traditional Eulerian-Lagrangian approach has been used successfully in dilute gas-solid flows where particles collisions are not important such as those in pulverized coal combustors, cyclone separators and spray dryers (Stock, 1996).

For gas-solid systems in which the particle paths are determined by collisions such as fluidized beds, the Discrete Element Method (DEM), is another type of Lagrangian approach used by several researchers (Tsuji 2001; Hoomans *et al.*, 1996,1999). In DEM, the Lagrangian approach is used for the particles, however, different from the traditional approach, binary particle collisions are taken into account. Using DEM, Hoomans *et al.* (1999) was able to show the formation of the clusters in a CFB riser. It should also be noted that the model is limited to very low number of particles (in the order of 100000) due to computational requirements.

In Eulerian-Eulerian (two-fluid) models, the particles are treated as a continuum as the gas phase. Thus, there are two interpenetrating phases (gas and solid) and each phase is characterized by its own continuum equation of motion. The two-fluid approach becomes especially convenient when the particle loading is high and can be applied to flows of practical interest with a relatively small computational effort. However, the interaction terms between the phases need extensive modeling and can be specific to each type of application.

5 The Two-Fluid (Eulerian-Eulerian) Model

5.1 Continuum Assumption for Solids Phase

It can be argued that for very dilute flows, the assumption of solid phase continuum is questionable. Kuipers (1990) suggested that there should be at least 10^4 particles per unit volume for a statistical variation of not less than 1 %. This leads to a minimum volume

fraction of:

$$\alpha_{s,min} = \frac{10^4 \pi d_p^3}{6V} \quad (5.4)$$

where V can be taken as the volume of a typical cell used in the simulations. In another approach, Gidaspow (1994) proposed a formula to calculate the mean free path of the particles, l :

$$l = \frac{l}{6\sqrt{2}} \frac{d_p}{\alpha_s} \quad (5.5)$$

Assuming that the maximum mean free path of the particles is limited by the dimension of the system in question, i.e., $l \sim d_t$, one can estimate the minimum allowable particle phase volume fraction as:

$$\alpha_{s,min} = \frac{l}{6\sqrt{2}} \frac{d_p}{d_t} \quad (5.6)$$

where d_t is the riser diameter. Thus, Equations (5.4) and (5.6) can be used as rough estimates of the minimum values of the solids volume fraction below which the continuum assumption ceases to be valid.

5.2 Governing Conservation Equations

5.2.1 Introduction

Currently, there are two main approaches in formulating the two-fluid equations depending on the transport equations of the dispersed phase; deterministic and statistical. In the statistical approach, the dispersed phase is still assumed to behave like a continuum but the governing equations are derived from the transport equation of the probability density function. The reader is referred to Elgobashi (1994), Reeks (1991) and Buyevich (1972) for this type of derivation.

The conservation equations presented in this section are based on the deterministic formulation. In this approach, local instantaneous conservation equations of the gas phase (Navier-Stokes Equations) and the equation of motion for a solid particle are averaged over a region which is significantly larger than the particle diameter (or interparticle distance) but considerably smaller than the characteristic length of the bounding vessel. The reader is referred to Anderson and Jackson (1967) for the original derivation of the two-fluid model and to Enwald *et al.* (1996) for an excellent review of the two-fluid model formulation applied to fluidization.

The idea behind the two-fluid approach is summarized in Figure 5.2. As can be seen from the figure, before the relevant averaging procedure, there exists a gas phase described by the instantaneous continuum conservation equations (continuity and Navier-Stokes) and discrete solid particles described by Newtonian equation of motion. As mentioned before, theoretically, the instantaneous gas phase conservation equations and the equation of motion of each particle can be solved using direct numerical simulation provided that a numerical mesh smaller than the smallest length scale of the flow and a time step smaller than the time scale of the fastest fluctuation of the flow are used. Since this is not possible with the current computer or even supercomputer technology, averaging is one of the options available. Figure 5.2 shows the typical procedure for volume averaging.

In Eulerian approach, a given parameter which can be a scalar, vector or a tensor, is defined by the equation, $f = f(r,t)$, where r is a fixed point in space and t is time. The volume averaging is performed around a fixed point r at time t and defined as:

$$\langle f(r,t) \rangle_v = \frac{1}{V} \int_V f(r,t) dx dy dz \quad (5.7)$$

The volume averaging results in two interpenetrating phases (gas and solid); each phase being described by its own average properties in the averaging volume such as the mean velocity, pressure and volume fraction (Figure 5.2). There are two inevitable outcomes of the averaging procedure. One is the so-called closure problem which includes the modeling of the interactions between the phases and the constitutive relations for each

phase. The other one is the loss of information due to averaging. As the volume dimension used in averaging is much larger than the particle size and the interparticle spacing, the volume averaged equations will not yield detailed information at the scale of the particle diameter (Crowe *et al.*, 1996). This concept is very similar to the time averaging of the instantaneous Navier-Stokes equations for turbulence modeling. The time averaging (or Reynolds averaging) leads to an unknown tensor, Reynolds stress tensor, which will need modeling. Besides, the solution of the resulting set of equations can not produce information on the turbulent fluctuations faster than the averaging time interval.

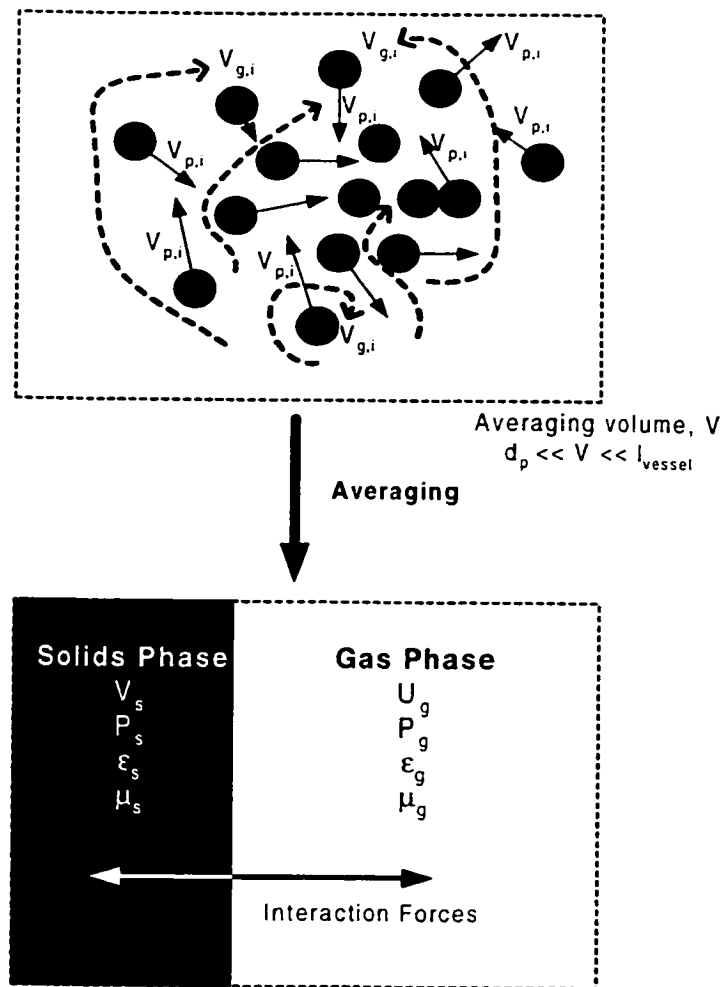


Figure 5. 2. Concept of two-fluid approach in gas-solid flows

5.2.2 Conservation Equations

The general assumptions of the following gas-solid flow model are:

1. The flow is isothermal.
2. There is no mass transfer between the phases.
3. Particles are perfectly spherical and mono-sized.

Based on the above assumptions, the averaged continuum equations for both phases are presented below.

Conservation of mass for gas and solid phases:

$$\frac{\partial}{\partial t}(\alpha_g \rho_g) + \nabla \cdot (\alpha_g \rho_g \mathbf{u}) = 0 \quad (5.8)$$

$$\frac{\partial}{\partial t}(\alpha_s \rho_s) + \nabla \cdot (\alpha_s \rho_s \mathbf{v}) = 0 \quad (5.9)$$

and the volume fractions comply with:

$$\alpha_g + \alpha_s = 1 \quad (5.10)$$

Conservation of momentum for gas and solid phases:

$$\frac{\partial}{\partial t}(\alpha_g \rho_g \mathbf{u}) + \nabla \cdot (\alpha_g \rho_g \mathbf{u} \mathbf{u}) = -\alpha_g \nabla p + \nabla \cdot (\alpha_g \boldsymbol{\tau}_g) + \alpha_g \rho_g \mathbf{g} + I_{gs} \quad (5.11)$$

$$\frac{\partial}{\partial t}(\alpha_s \rho_s \mathbf{v}) + \nabla \cdot (\alpha_s \rho_s \mathbf{v} \mathbf{v}) = -\alpha_s \nabla p - \nabla p_s + \nabla \cdot (\alpha_s \boldsymbol{\tau}_s) + \alpha_s \rho_s \mathbf{g} - I_{gs} \quad (5.12)$$

In equations 5.8-5.12, α is volume fraction, ρ is density, $\boldsymbol{\tau}$ is stress tensor, p is gas pressure, p_s is solid pressure, \mathbf{u} and \mathbf{v} are mean gas and solids phase velocities. The indices g and s are used to denote the gas and solid phases, respectively. The last term, I_{gs} represents the average interphase force per unit volume.

The first two terms on both sides of each momentum equation represent the force per unit

volume due to the acceleration of each phase. These forces are balanced by the corresponding pressure forces, viscous forces including the laminar and turbulent contributions, body forces and interphase forces per unit volume. The interphase force term in its most general form may include the stationary drag force, lift force, added mass force and Basset force.

5.3 Closure Laws

In order to solve the equations presented in the last section, several unknown terms require modeling. The models required for these “unknown terms” are called the closure laws. Thus, appropriate closure laws are required for the corresponding stress tensors for each phase, solids phase pressure and the interphase force. This section presents the model equations for each of these terms.

5.3.1 Gas and Solid Phase Stress Tensors, τ_g and τ_s

The gas phase is a continuum by nature, and the gas stress tensor is obtained from the classical Newtonian stress-strain relation:

$$\tau_g = \left(\xi_g - \frac{2}{3} \mu_{eff.g} \right) \nabla \cdot \bar{\mathbf{u}} + \mu_{eff.g} \left(\nabla \mathbf{u} + (\nabla \mathbf{u})^T \right) \quad (5.13)$$

where $\mu_{eff.g}$ and ξ_g are gas phase effective shear and bulk viscosity, respectively. The effective shear viscosity is taken as the sum of the gas phase laminar shear viscosity and an eddy viscosity to account for the turbulent momentum transport. If the flow is assumed to be incompressible, the first term vanishes and the gas phase stress tensor becomes:

$$\tau_g = \mu_{eff.g} \left(\nabla \mathbf{u} + (\nabla \mathbf{u})^T \right) \quad (5.14)$$

For the solids phase, the continuum assumption is assumed to be valid based on the discussions presented in the previous sections, and similar to the gas phase, Newtonian stress-strain relation is used to describe the solids phase stress tensor:

$$\tau_s = \left(\xi_s - \frac{2}{3} \mu_{eff,s} \right) \nabla \cdot \mathbf{v} \bar{\mathbf{I}} + \mu_{eff,s} \left(\nabla \mathbf{v} + (\nabla \mathbf{v})^T \right) \quad (5.15)$$

with $\mu_{eff,s}$ and ξ_s representing the solids phase effective shear and bulk viscosity, respectively. The fundamental assumption of Equation 5.15 is that the solids phase momentum flux (or shear stress) is a function of solids phase velocity gradient as in the case of gas phase. Unlike the gas phase laminar shear viscosity, however, the solids laminar shear viscosity is not the property of the fluid (solids phase) but is a function of the flow. Thus, expressions are needed for the solids phase shear and bulk viscosity to close Equation 5.15. In this study, these expressions are obtained from kinetic theory of granular flows.

5.3.2 Gas and Solids Phase Pressures, p and p_s

For the gas phase, the gas pressure term, p , takes a value to balance all the forces in Equations 5.11 and 5.12. For a fully developed flow, the acceleration terms vanish, and in the absence of the viscous stress terms, the gas phase pressure is balanced by the weight of each phase. The solids phase pressure is described in the context of kinetic theory of granular solids as shown in the following sections.

5.3.3 Gas-Solid Interphase Exchange Coefficient, β

In Eulerian-Eulerian approach, it is customary to express the average interphase force per unit volume (or momentum exchange) by an exchange coefficient, β , multiplied by the relative velocity between the phases (Enwald *et al.*, 1996; Peirano and Leckner, 1998):

$$I_{gs} = \beta [\mathbf{u} - \mathbf{v} - \mathbf{v}_{dr}] \quad (5.16)$$

where \mathbf{u} and \mathbf{v} are the mean velocity vectors of the gas and solid phases, respectively and \mathbf{v}_{dr} is the particle drift velocity. In a turbulent gas-solid flow, the drift velocity represents the net mean velocity gained by a particle due to gas turbulence as it travels through an eddy. The drift velocity depends on the particle relaxation time and the actual time the

particle interacts with the eddy (Senior and Grace, 1998). The modeling of drift velocity is quite challenging since the actual physical interactions between the particles and the gas phase are not known completely. Simonin and Viollet (1990) and Deutsch and Simonin (1991) proposed a model for the drift velocity based on Tchen's theory of dispersion for a dilute gas-solid flow in a homogenous turbulence field. However, the applicability of this model to the gas-solid flow in a CFB riser is questionable due to underlying assumptions. In this study, the drift velocity is not taken into account.

The exchange coefficient may include the contributions from stationary drag force, lift force, added mass force and history (Basset) force. The lift force (force in the direction perpendicular to the relative velocity between the phases) arises in the presence of a non-uniform velocity field (shear in the mean flow) and if the particle is rotating (Drew and Lahey, 1993). The added mass force is the inertial response to the displacement of the surrounding fluid by the particle since the accelerating particle must overcome the inertia that lies in its path. The history force (or the Basset force) arises from the diffusion of vorticity away from the particle as the particle changes its velocity. For gas-particle flows with $\rho_s/\rho_f \approx 1000$, the added mass force and the history force can be neglected (Stock, 1994). On the other hand, the magnitude of the lift force depends on the diameter of the dispersed phase (for instance in bubble columns, the lift force can be quite important) (Oesterle, 1994). For fluidized beds, due to the particle size range and particle loading, the stationary drag force is usually much larger than the lift force, hence the latter is usually neglected.

In the light of the above arguments, the gas-solid momentum exchange coefficient, β , is assumed to have only the stationary drag contribution and modeled using Wen and Yu's (1966) drag correlation:

$$\beta = \frac{3}{4} C_d \frac{\rho_g \alpha_s}{d_p} |\mathbf{u} - \mathbf{v}| \alpha_g^{-1.7} \quad (5.17)$$

where

$$C_d = \frac{24}{\alpha_g Re_p} \left[1 + 0.15(\alpha_g Re_p)^{0.687} \right] \quad (5.18)$$

and the particle Reynolds number is defined as:

$$Re_p = \frac{\rho_g d_p |\mathbf{u} - \mathbf{v}|}{\mu_g} \quad (5.19)$$

There are several other drag correlations applicable to gas-solid flows in the literature (Arastoopour *et al.*, 1990; Schuh *et al.*, 1989; Sylamlal and O'Brien, 1989; Di Felice, 1994; O'Brien and Sylamlal, 1993). Figure 5.3 gives a comparison of the exchange coefficient, β , calculated from different drag relations for a typical FCC particle with a particle diameter of $75\mu\text{m}$ and a density of 1600 kg/m^3 . The average relative velocity is assumed to be 1 m/s in the calculations. Excluding that of O'Brien and Sylamlal (1993), the exchange coefficient is almost the same for other drag laws considered within solids volume fraction range of 0-0.1. The correlation of O'Brien and Sylamlal (1993) significantly deviating from the others is the only relation in the literature which takes the cluster formation into account. The relation based on the coefficients obtained from the experiments carried out at two mass fluxes ($G_s = 98\text{ kg/m}^2\text{s}$ and $147\text{ kg/m}^2\text{s}$) is the corrected form of the original relation of Sylamlal and O'Brien (1989). In an earlier two-fluid simulation study, it was observed that the cluster correction of O'Brien and Sylamlal (1993) significantly underpredicts the drag force exerted on the particles resulting in an excessive downflow near the riser wall compared to experimental data (Koksal *et al.*, 1998). More experimental work is needed to obtain a reliable drag relation for the cluster formation.

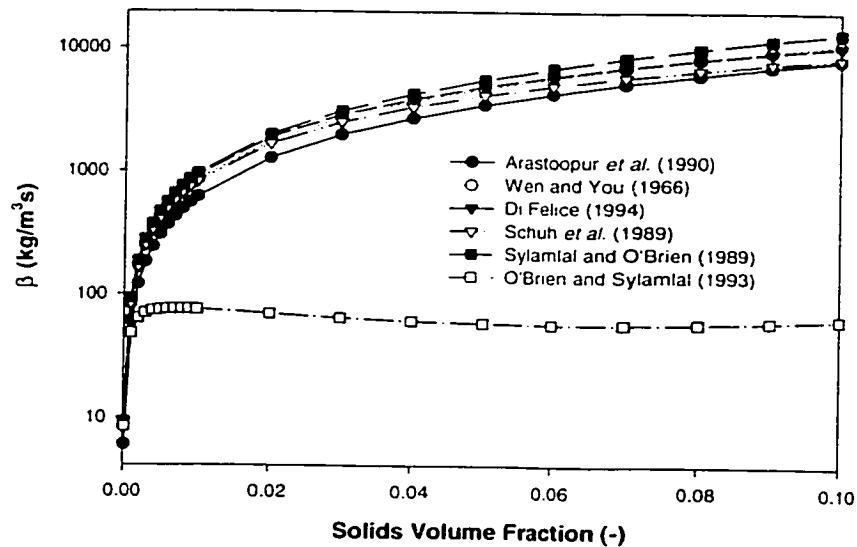


Figure 5.3. Comparison of the drag laws for gas-solid flows

5.3.4 Solid Phase Closures: Solids Phase Viscosity and Pressure

In this section, the solid phase closures based on the kinetic theory of granular solids are presented. First, a brief description of the physical understanding of the solids phase viscosity and pressure is discussed. Then, their formulations are given.

5.3.4.1 The Physical Significance of the Solids Phase Viscosity and Pressure

As mentioned in the previous sections, closure laws are needed for the solids phase viscosity and pressure to describe the corresponding stresses in the particulate phase. The fundamental principles used to describe the solids phase viscosity and pressure are based on the kinetic theory of gases (Chapman and Cowling, 1961).

At the molecular scale, the gas molecules fluctuate randomly, interact and collide with each other. According to the well established kinetic theory of gases, the microscopic momentum transfer across a plane, which is the source of shear stress, originates from two physical mechanisms associated with the motion of the gas molecules; random molecular motion known as the kinetic effect and the inter-molecular interactions known as the collisional effect (Chapman and Cowling, 1961). Thus, the gas phase shear viscosity is defined as the proportionality constant between the shear stress across a plane and the mean velocity gradient (Enwald *et al.*, 1996).

The motion of the particles forming the solid phase resembles the motion of the gas molecules forming the gas phase, albeit at a much larger scale. Therefore, it can be suggested that the solids phase shear viscosity be produced from similar mechanisms and interactions as the gas phase shear viscosity; the random particle motion (kinetic effect) and the particle collisions (collisional effect) (Gidaspow, 1994). At this point, in the context of the two-fluid model, the simplest approach would be to use a constant solids shear viscosity as opposed to a model based on the above mechanisms as previously done by Tsuo and Gidaspow (1990) and Benyahia *et al.* (1998).

The solids shear viscosity can also be expressed as a function of the mixture viscosity for which several correlations are available in the literature (Einstein 1906; Roscoe, 1952; Frankel and Acrivos, 1967). Although the exact relation between the viscosities of the gas and solid phases and the mixture viscosity is not known, a volume fraction weighted linear approximation can be used to define the solids viscosity (Enwald *et al.*, 1996) as:

$$\mu_s = \frac{\mu_{mix} - \mu_g \alpha_g}{1 - \alpha_g} \quad (5.20)$$

Einstein (1905) was the first to propose a model for the viscosity of a gas-solid mixture with a solids volume fraction less than 0.03:

$$\mu_{mix} = \mu_g (1 + 2.5\alpha_s) \quad (5.21)$$

Thus, using Equations 5.20 and 5.21, the solids shear viscosity can be calculated to be included in the two-fluid model.

As the solids shear viscosity and the associated shear stress represent the tangential forces per unit area in the particle assembly, the particle pressure may be thought as the normal force per unit area exerted on a surface by the particulate phase of a multiphase mixture (Campbell and Wang, 1991). The utilization of the particle pressure concept is not limited to the context of the two-fluid model; it has been used and derived in several fluidized bed stability theories (Murray, 1965). Analogous to the kinetic theory of gases, the particle pressure originates as a result of the impact of individual particles. As explained by Campbell and Wang (1991), the solid particles transmit force via both short-duration collisional impacts and long duration contacts; the latter not being present in the gas phase. Figure 5.4 shows the sketch of the particle pressure measurements carried out by Campbell and Wang (1991) in a bubbling fluidized bed. As can be seen from the figure, when the bed is not fluidized, the particle pressure decreases from a maximum to a minimum value with superficial gas velocity; the minimum value being observed at minimum fluidization conditions. The decrease is due to the increasing drag force exerted on the particles which leads to a decrease in long duration contacts. Thus, as the velocity increases the bed is supported more and more by fluid forces rather than particle contacts. As the bed is fluidized beyond the minimum fluidization conditions, the particle pressure increases again with increasing velocity due to the increase in short-duration collisional impacts. This increase is attributed to the agitation of the gas bubbles (Campbell and Wang, 1991).

In the next section, a universal theory is presented to describe the solid phase viscosity and pressure. With the help of this theory, the viscosity (bulk and shear) and the pressure of the particulate phase can be expressed as a function of time and position. This theory provides a general description of the observed phenomenon

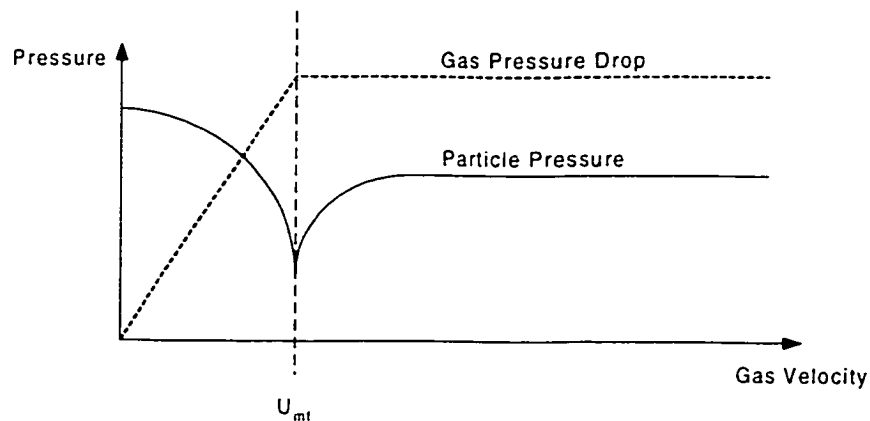


Figure 5.4. Sketch of the particle measurements of Campbell and Wang (1991).

5.3.4.2 Kinetic Theory of Granular Solids

For a detailed treatment, the reader is referred to the classical book of Gidaspow (1994) and the excellent review of Enwald *et al.* (1996) on the subject. In this section, only the model equations are presented with underlying assumptions.

The analogy between the motion of the gas molecules at molecular scale and the motion of solids particles are already presented in the previous section. The kinetic theory of granular flow is based on this analogy and follows the kinetic theory of dense gases (Chapman and Cowling, 1961). The development of kinetic theory of granular solids started with the work of Savage and Jeffrey (1981). Jenkins and Savage (1983), Lun *et al.* (1984) and Johnson and Jackson (1987) continued the development of this approach. Sinclair and Jackson (1989) first applied the kinetic theory of granular solids to a fully-developed gas solid flow in a pipe. Ding and Gidaspow (1990) developed the expressions for solids phase shear viscosity and the pressure for dense gas-solid flows based on kinetic theory and applied the model to simulate a bubbling fluidized bed. Balzer *et al.* (1995) extended the model and considered the effects of the interstitial gas on kinetic theory expressions.

The theory draws an analogy between the random motion of the particles and the thermal motion of the gas molecules in the kinetic theory of gases introducing a term called granular temperature, which represents kinetic energy of the random particle motion. The granular temperature is conceptually similar to thermal temperature which represents the kinetic energy of the random molecular motion in kinetic theory of gases. Figure 5.5 demonstrates the energy path in solids phase in a typical gas-solid flow using the concept of granular temperature. With the presence of all the forces in the particle assembly (drag force by the fluid, gas pressure, gravity and other possible external forces), a shearing motion is induced which continuously converts some of the kinetic energy associated with mean motion into granular temperature, i.e., particle velocity fluctuations. These particle fluctuations then generate an effective pressure and an effective viscosity in the particle phase (Sinclair and Jackson, 1989). Thus, the effective particle pressure and viscosity will be a strong function of granular temperature or fluctuating energy of the particles for which a separate transport equation can be written. The fluctuation energy of the particles is then dissipated by inelastic particle collisions and fluid friction. So, the value of the granular temperature which determines the particle phase pressure and viscosity depends on the balance between the production of the fluctuating energy due to shear work and its dissipation at any time.

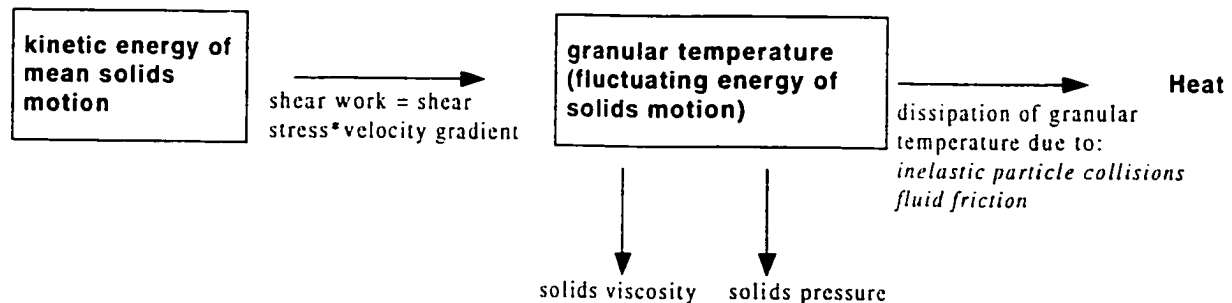


Figure 5.5. The concept of granular temperature in gas-solid flows based on kinetic theory of granular flow (based on Campbell, 1990)

Before presenting the model equations, the general assumptions of the kinetic theory model are given below:

- a) The particles are assumed to have binary collisions.
- b) The effects of the interstitial gas on the kinetic theory expressions are not considered.
- c) The friction between the particles and the rotational energy of the particles are neglected.
- d) The model is restricted to spherical, smooth and nearly elastic identical particles.

Following the definition of granular temperature, the actual (instantaneous) solids velocity is decomposed into a mean and a fluctuating component as:

$$\mathbf{v}_i = \mathbf{v} + \mathbf{v}' \quad (5.22)$$

and the pseudo or granular temperature, Θ_s (m^2/s^2) which represents the fluctuating energy of the solid phase is defined as:

$$\frac{3}{2}\Theta_s = \frac{1}{2}\langle \mathbf{v}'_s \cdot \mathbf{v}'_s \rangle \quad (5.23)$$

where $\langle \rangle$ denotes the appropriate averaging scheme. The fluctuating kinetic energy associated with random motion of particles is also called granular energy or pseudo-thermal energy.

The pseudo-thermal energy balance for the solids is obtained by subtracting the mechanical energy equation from the total energy balance with a similar procedure carried out to obtain the turbulent energy balance equation in single phase flows (Sinclair, 1997):

$$\frac{3}{2} \left[\frac{\partial}{\partial t} (\alpha_s \rho_s \Theta_s) + \nabla \cdot (\alpha_s \rho_s \mathbf{v} \Theta) \right] = \left(-p_s \bar{\bar{I}} + \bar{\bar{\tau}}_s \right) : \nabla \mathbf{v} + \nabla \cdot (k_\Theta \nabla \Theta_s) - \gamma_\Theta + \phi_{gs} \quad (5.24)$$

The first two terms on the left hand side of Equation 5.24 represent the time rate of change of granular energy and its change due to convective motion of the solids,

respectively. The first term on the right hand side of Equation 5.24 is the production of the pseudo-thermal energy (granular energy) due to shear work. The second term is the diffusion term due to the gradients of the granular temperature with k_{θ} representing the diffusion coefficient. The last two terms represent the dissipation of the pseudo-thermal energy due to inelastic collisions and the fluctuating energy exchange term with the gas phase, respectively. Equation 5.24 is the original form presented in Gidaspow (1994). It should be noted that FLUENT V4.5 has three different kinetic theory models based on the works of Gidaspow (1994), Sylamlal *et al.* (1993) and Hrenya and Sinclair (1997). In this study, the kinetic theory model of Hrenya and Sinclair (1997) is used.

The kinetic theory model of Hrenya and Sinclair (1997) is based on the time-averaged form of the pseudo-thermal energy balance equation which contains several extra terms due to time averaging. In their model, they considered the effects of the particle phase turbulence on the pseudo-thermal energy of the solids phase which considerably helped to increase the prediction capability of the kinetic theory model when tested against experimental data of Bader *et al.* (1988), Harris *et al.* (1994) and Weinstein *et al.* (1986).

Before presenting the terms associated with Equation 5.24 based on Hrenya and Sinclair (1997), it will be useful to give a brief explanation on the particle phase turbulence in gas-solid flows. In dense gas-solid flows, it is known that large scale fluctuations exist in suspension density due to the collective motion of particles (Horio, 1997). These particles form solid congregations such as clusters, particle sheets and swarms. These solid congregations continuously form and disintegrate producing turbulent-like fluctuations in the particle phase.

At this point, the difference between the particle velocity fluctuations associated with granular temperature and the large scale fluctuations mentioned in the previous paragraph should be clearly identified. The granular temperature or the associated particle velocity fluctuation in Equation 5.23, represents the random motion of the *individual* particles, so does the pseudo-thermal energy. However, the turbulence in the particle phase occurs due to the random motion of *groups* of particles at a scale much larger than the scale of the

individual particle motion and hence represent the kinetic energy of the random collective motion (Hrenya and Sinclair, 1997). The large scale fluctuations due to the collective motion of particles are first accounted by Dasgupta *et al.* (1994) by a two-equation eddy viscosity turbulence model. In the present study, the same modeling approach is followed for the particle phase turbulence as explained in the next section.

The time-averaged form of the pseudo-thermal energy balance equation of Hrenya and Sinclair (1997) has the following modifications to Equation 5.24: The dissipation rate of the particle-phase turbulent kinetic energy appears as a source term in the pseudo-thermal energy balance equation as:

$$\rho_s \alpha_s \varepsilon_s \quad (5.25)$$

where ε_s is the dissipation rate of the solids turbulent kinetic energy (m^2/s^3). A correlation between the solids volume fraction and velocity fluctuations appears as the second additional source term and is modeled by a conventional gradient model:

$$\Theta_s \langle v'_s \alpha'_s \rangle = -\Theta_s \left(\frac{\mu_{s,t}}{\rho_s} \right) \nabla \alpha_s \quad (5.26)$$

where $\mu_{s,t}$ represents the turbulent eddy viscosity of the particle phase.

The dissipation of the pseudo-thermal energy in Equation 5.24 is modeled with the following equation (Hrenya and Sinclair, 1997; Fluent 4.5 Update Manual, 1998):

$$\gamma_\Theta = \frac{48 \rho_s \eta (1-\eta)}{\sqrt{\pi} d_p} \left[\alpha_s^3 g_o \Theta_s^{1.5} + 1.5 \alpha_s^2 g_o \left(2 + \frac{g_o}{3} \right) \Theta_s^{0.5} \langle \alpha'_s \Theta'_s \rangle \right] \quad (5.27)$$

where g_o is the radial distribution function and can be interpreted as the probability of a single particle touching another particle in the solids phase. Its value increases with increasing solids volume fraction and is usually derived from statistical mechanics (Boomer *et al.*, 1994). Appendix D gives a listing of the radial distribution functions

available in the literature. In this study, the following expression by Lun *et al.* (1984) is used as in the original model of Hrenya and Sinclair (1997):

$$g_o = \frac{\alpha_{s,max}^{1/3}}{\alpha_{s,max}^{1/3} - \alpha_s^{1/3}} \quad (5.28)$$

where $\alpha_{s,max}$ represents the maximum packing limit of the solids phase. The term, η , in Equation 5.27 is defined as:

$$\eta = \frac{1}{2}(1 + e) \quad (5.29)$$

where e is the so-called coefficient of restitution. The coefficient of restitution describes the energy loss in a binary particle collision, it has a value of 1 for a perfect elastic collision. Thus, for elastic collisions ($e = 1.0$), the dissipation term (Equation 5.27) vanishes indicating the absence of the granular energy loss due to particle collisions. In Equation 5.27, the correlation term between the solids volume fraction fluctuation and the fluctuation of the granular temperature arises due to time averaging. Hrenya and Sinclair (1997) has proposed the following expression for this correlation along the riser radius:

$$\langle \alpha'_s \Theta'_s \rangle = m \alpha_{s,avg} k_{s,avg} \left[(\alpha_{s,max} - \alpha_{s,wall} - 1) \left(\frac{r}{R} \right)^n + 1 \right] \quad (5.30)$$

where $\alpha_{s,avg}$ is the average value of the solids volume fraction across a cross section, $k_{s,avg}$ is the average value of the solids fluctuating kinetic energy (the energy associated with the collective motion of the particles) across the riser and $\alpha_{s,wall}$ is the value of the solids volume fraction at the wall. The constants m and n are set to be -5 and 8 , respectively in the original model of Hrenya and Sinclair (1997). The correlation given in Equation 5.30 makes a significant contribution to total dissipation of granular energy (Equation 5.27) which in turn affects the prediction of both mean and fluctuating quantities as shown in the coming sections. A further discussion is presented when the model is applied to

simulate the experimental data of Ersoy (1998).

Referring to Equation 5.24, the following diffusion coefficient for granular temperature is used in this study (Lun *et al.*, 1984; Louge *et al.*, 1991) as in the original model of Hrenya and Sinclair (1997).

$$k_{\Theta} = \frac{25\sqrt{\pi}}{128} \rho_s d_p \left[\left(\frac{1}{1 + \frac{l}{L}} \frac{8}{\eta g_o} + \frac{96\alpha_s}{5} \right) \left(\frac{1 + \frac{12}{5}\eta^2(4\eta - 3)\alpha_s g_o}{41 - 33\eta} \right) + \frac{512}{25\pi} \eta \alpha_s^2 g_o \right] \sqrt{\Theta_s}$$

where l is the mean free path of the particles given in Equation (5.5) and L is the characteristic length of the system, i.e., the radius of the pipe in a cylindrical riser. Other expressions for the diffusion coefficient available in the literature by different researchers are presented in Appendix D.

The last term of Equation 5.24 is given by Gidaspow (1994) as:

$$\phi_{gs} = \beta(\langle \mathbf{u}' \cdot \mathbf{v}' \rangle - 3\Theta) \quad (5.32)$$

where β is the gas-solid momentum exchange coefficient given by Equation 5.17. Equation 5.32 represents the energy transfer between the gas and solid phases. The first term on the right hand side is the correlation between the fluctuating components of gas and solid phase velocity fields and describes the rate of production of kinetic fluctuating energy due to gas-phase turbulence. Unfortunately, there is not a reliable model for this term in the literature for dense gas-solid flows (Nieuwland *et al.*, 1996a). Neglecting the correlation term means to assume that the correlation between them is negligibly small; this is the case when the particle response time is much larger than the characteristic time scale of the gas phase turbulence (course particle case; Figure 5.2). Thus, the particles must be heavy and large. In this study, this term is neglected. The second term represents the dissipation of the granular energy due to fluid friction and is retained in the model.

Once the solution of Equation 5.24 is carried out numerically and the granular

temperature is found as a function of time and position, the solids phase laminar shear viscosity, solids phase bulk viscosity and solids pressure can be expressed as a function of granular temperature based on kinetic theory (Gidaspow, 1994). In the literature, there are several forms of kinetic theory expressions for solids viscosity and pressure as can be seen in Appendix D (Sylamlal *et al.*, 1993; Gidaspow *et al.*, 1992; Balzer and Simonin, 1993; Lun *et al.*, 1984; Louge *et al.*, 1991). Essentially, all the kinetic theory viscosity models follow the basic relation below (Gidaspow, 1994):

$$\text{Viscosity} = \text{CONSTANT} \times \text{Bulk Density} \times \text{Mean Free Path} \times \text{Fluctuating Velocity}$$

which is analogous to the description of gas viscosity in kinetic theory of gases. Similarly, the particle pressure expressions have the form:

$$\text{Pressure} = \text{CONSTANT} \times \text{Bulk Density} \times \text{Granular Temperature}$$

which is the analogous form of ideal gas relation with thermal temperature.

The expressions for solids laminar shear viscosity, bulk viscosity and pressure in Hrenya and Sinclair (1997) model are used based on the works of Lun *et al.* (1984) and Louge *et al.* (1991):

Solids Phase Laminar Shear Viscosity:

The kinetic part:

$$\mu_{s,kin} = \frac{5\rho_s d_p (\Theta_s \pi)^{1/2}}{96\alpha_s \eta (2-\eta) g_o} \left(\frac{1}{1+l/L} \right) \left[1 + \frac{8}{5} \eta (3\eta - 2) \alpha_s g_o \right] \quad (5.33)$$

The collisional part:

$$\mu_{s,col} = \frac{5\rho_s d_p (\Theta_s \pi)^{1/2}}{96} \left[\left(\frac{8\alpha_s}{5(2-\eta)} \right) \left(1 + \frac{8}{5} \eta (3\eta - 2) \alpha_s g_o \right) + \frac{768}{25\pi} \eta \alpha_s^2 g_o \right] \quad (5.34)$$

The solids total laminar shear viscosity is obtained by summing the kinetic and collisional

contributions.

Solids Bulk Viscosity:

$$\xi_s = \frac{4}{3} \alpha_s \rho_s d_p g_o (1 + e) \sqrt{\frac{\Theta_s}{\pi}} \quad (5.35)$$

It describes the resistance of the solids phase to compression.

Solids Pressure:

$$p_s = \rho_s \left(\frac{\alpha_s}{1 + (l/L)} + 4\eta\alpha_s^2 g_o \right) \Theta_s \quad (5.36)$$

Thus, with the aid of the equations presented in this section, the solids laminar stress tensor is fully specified. In the next section, closures for the Reynolds stresses are given for both phases.

5.3.5 Gas and Solid Phase Turbulence

5.3.5.1 The k - ε Eddy Viscosity Turbulence Model

A brief introduction about the physics of turbulence in gas phase is given in Chapter 2. In the previous section, it was presented that the large scale fluctuations associated with the random motion of group of particles (clusters, swarms, streamers, sheets etc...) creates the so-called particle phase turbulence. In this section the mathematical modeling of gas and solids turbulence is presented. The two-equation k - ε turbulence model is used for this purpose for both phases. For single-phase flows, the standard k - ε model is a robust, reliable, computationally efficient turbulence model and is well tested in pipe flows with high Reynolds numbers (Wilcox, 1998). For the particle phase, to describe the turbulence in this phase using the single phase k - ε model is a major assumption. However, the lack of either a well tested model or sufficient information on the characteristics turbulence in dense gas-solid flows justifies the approach taken here.

The effective shear viscosity for both gas and solid phases are described as:

$$\begin{aligned}\mu_{eff,g} &= \mu_g + \mu_{g,t} \\ \mu_{eff,s} &= \mu_{s,kin} + \mu_{s,coll} + \mu_{s,t}\end{aligned}\quad (5.37)$$

where $\mu_{g,t}$ and $\mu_{s,t}$ are the turbulent eddy viscosity for gas and solids phase, respectively. In a standard two-equation turbulence model, the turbulent eddy viscosity ($i = \text{gas or solid}$; $\omega = u \text{ or } v$) is evaluated assuming that it is proportional to the product of a turbulent velocity scale and a length scale based on the mixing length concept of Prandtl (Schlichting, 1996):

$$\mu_{i,t} = \rho_i C_{\mu,i} \frac{k_i^2}{\varepsilon_i} \quad (5.38)$$

where k_i (m^2/s^2) is turbulent kinetic energy defined as:

$$k_i = \frac{1}{2} \langle \omega \cdot \omega \rangle \quad (5.39)$$

and ε_i is the dissipation rate of turbulent kinetic energy (m^2/s^3).

The turbulent kinetic energy and its dissipation rate are obtained from the solutions of two transport equations:

$$\begin{aligned}\frac{\partial}{\partial t}(\alpha_i \rho_i k_i) + \nabla \cdot (\alpha_i \rho_i \omega k_i) &= \alpha_i \left[\left(\mu_{i,t} (\nabla \omega + (\nabla \omega)^T) \right) : \nabla \omega \right] + \\ &\quad \nabla \cdot \left(\alpha_i \frac{\mu_{i,t}}{\sigma_{i,g}} \nabla k_i \right) - \alpha_i \rho_i \varepsilon_i\end{aligned}\quad (5.40)$$

$$\begin{aligned}\frac{\partial}{\partial t}(\alpha_i \rho_i \varepsilon_i) + \nabla \cdot (\alpha_i \rho_i \omega \varepsilon_i) &= \alpha_i \frac{\varepsilon_i}{k_i} C_{\varepsilon 1,i} \left[\left(\mu_{i,t} (\nabla \omega + (\nabla \omega)^T) \right) : \omega \right] \\ &\quad + \nabla \cdot \left(\alpha_i \frac{\mu_{g,t}}{\sigma_{\varepsilon,i}} \nabla \varepsilon_i \right) - \alpha_i \rho_i C_{\varepsilon 2,i} \frac{\varepsilon_i^2}{k_i}\end{aligned}\quad (5.41)$$

In Equations 5.40 and 5.41, the first term on the left hand side of the equation represents the time rate of change of turbulent kinetic energy and its dissipation rate. The second term represents the transport of the turbulent kinetic energy and its dissipation rate due to the convective motion. The right hand side consists of the production, diffusion and the dissipation terms. In the current model, the turbulence generation due to buoyancy and rotation is neglected. However, these terms can be easily included using FLUENT V4.5's interface.

The empirical constants used in the model are not modified and are set as the same as standard single phase k - ϵ model, i.e., $C_{\mu,i} = 0.09$, $\sigma_{k,i} = 1.0$, $\sigma_{\epsilon,i} = 1.3$, $C_{\epsilon 1,i} = 1.44$, $C_{\epsilon 2,i} = 1.92$ for both gas and solid phases.

5.3.5.2 Near Wall Turbulence Modeling

In mathematical modeling of turbulence, most of the available two-equation models (k - ϵ , *RNG* k - ϵ or k - w) cease to be valid near the solid boundaries because of the assumptions made in developing the particular model. Thus, usually, the regions near the solid boundaries or walls are modeled using special empirical correlations known as wall functions. In this study, the standard equilibrium wall function approach of Launder and Spalding (1972) is used. This approach assumes an equal production and dissipation of turbulence in the boundary layer. FLUENT V4.5 also offers a non-equilibrium wall function approach and a two-layer zonal model which abandons the use of wall functions (Fluent's User Guide, 1996).

Koksal (1998) compared the standard wall function, non-equilibrium wall function and the two layer zonal model in a 2-D gas-solid flow simulation in a vertical channel (Figures 5.6 and 5.7). The kinetic theory model employed was that of Sylamlal *et al.* (1993) for which the relevant expressions are given in Appendix D. The details of the simulation can be found in Koksal (1998). As can be seen from the figures, the standard and non-equilibrium wall function approaches give almost identical curves for solids volume fraction and axial velocity in the channel whereas the two layer zonal model fails

to predict the expected core annular behavior. It should be noted that the wall function model is a purely empirical approach valid for single phase flows. Its extrapolation to gas-solid flows has not yet been tested.

In the standard wall function approach, the following relations are used based on a fully developed boundary layer over a stationary wall:

$$\begin{aligned}
 u^* &= y^* && \text{when } 0 < y^* < 11 \\
 u^* &= \frac{1}{\kappa} \ln[9.81y^*] && \text{when } y^* > 11
 \end{aligned}$$

where

$$u^* = \frac{u_p C_\mu^{1/4} k_p^{1/2}}{\sqrt{\frac{\tau_{wall}}{\rho}}} \quad y^* = \frac{\rho C_\mu^{1/4} k_p^{1/2} y_p}{\mu} \tag{5.42}$$

κ : von Karman's constant (= 0.42)

u_p : mean velocity at point p.

k_p : turbulent kinetic energy at point p

y_p : distance from point p to the wall.

μ : dynamic viscosity

τ_w : shear stress at the wall

The calculation procedure works as follows:

Near the wall region in the boundary layer, the complete transport equation for turbulent kinetic energy is solved (Equation 5.40) with the wall shear stress included in the production term assuming zero normal gradient for kinetic energy at the wall coupled with Equation 5.42. Once a solution which satisfies both Equation 5.40 and 5.42 is found, the value of the dissipation rate, ε , in this region is then found assuming the equality of the production and dissipation of turbulence as:

$$\varepsilon = \frac{C_\mu^{1/4} k_p^{3/2}}{\kappa y_p} \tag{5.43}$$

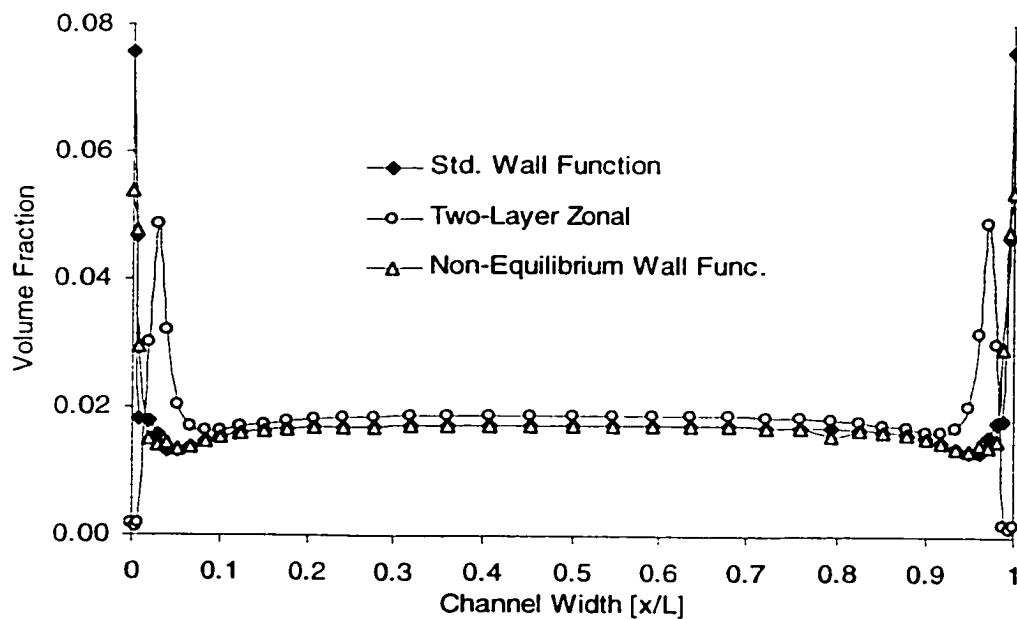


Figure 5.6. Effect of near wall turbulence modeling on solids volume fraction in a 2-D gas-solid flow in a vertical channel (Koksal, 1998)

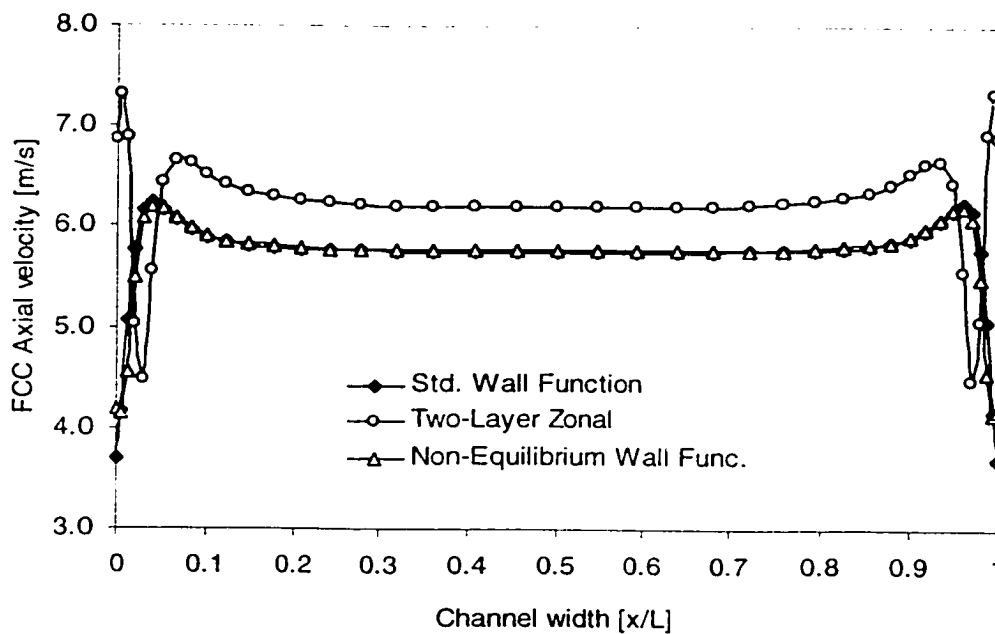


Figure 5.7. Effect of near wall turbulence modeling on solids axial velocity in a 2-D gas-solid flow in a vertical channel (Koksal, 1998)

5.4 Numerical Solution of the Model Equations

The model equations presented in section 5 of this chapter are solved numerically using FLUENT V4.5, a commercial CFD software package of FLUENT Inc. Fluent V4.5's numerical solution methods, basics of the solution algorithms, discretization and interpolation schemes used are presented in Appendix E.

5.5 Wall Boundary Conditions

To solve the equations presented in the previous sections, the appropriate boundary conditions for gas and solid velocities, granular temperature and turbulence quantities (k and ϵ) are needed. The near wall and wall treatments of the turbulence quantities are already discussed in section 5.3.5.2. The flow inlet, exit and other specific boundary conditions are discussed in Chapter 6 when each simulation is discussed separately. In this section, the wall boundary conditions are presented for gas and solid phase velocities and granular temperature.

Gas Phase Velocity:

The classical no-slip boundary condition is applied for gas phase at the wall. Thus, both the normal and the tangential component of the gas velocity are set to zero at the solid wall.

Solid Phase Velocity:

The normal component of the solid phase velocity is set to zero as that of the gas phase. However, since the particle diameter is usually larger than the length scale of surface roughness of the rigid wall, the particles may partially slip at the wall leading to a finite value of solid phase tangential velocity (Ding and Gidaspow, 1990). According to the assumption of Eldighidy *et al.* (1977), the tangential solid velocity at the wall is proportional to its gradient at the wall with the inter-particle spacing being the proportionality constant:

$$v_t = -\lambda_p \frac{\partial v_t}{\partial n} \quad (5.44)$$

where n is the direction normal to the wall and λ_p is the mean distance between the particles and can be estimated as:

$$\lambda_p = \frac{l}{\alpha_s^{1/3}} d_p \quad (5.45)$$

Thus, as the particle diameter gets smaller, the solid phase velocity boundary conditions approaches to no-slip condition.

In the context of kinetic theory, another correlation for the solid phase tangential velocity at the wall was proposed by Hui *et al.* (1984) and Johnson and Jackson (1987). It is based on a microscopic model which assumes that the lateral momentum flux transmitted to the wall by particle collisions is equal to the tangential stress exerted by the particles adjacent to the wall. It is given by the following expression:

$$-\alpha_s \mu_s \frac{\partial v_t}{\partial n} = \frac{\rho_s \pi v S \sqrt{\Theta}}{2\sqrt{3} \left[\frac{\alpha_{s,max}}{\alpha_s} - \left(\frac{\alpha_{s,max}}{\alpha_s} \right)^{2/3} \right]} \quad (5.46)$$

where S is the specularity coefficient (Pita and Sundaresan, 1991). All the other parameters in Equation 5.46 have been described in previous sections. While the left hand side of the equation describes the lateral momentum flux, the right hand side gives the tangential stress which can be expressed as the product of the change of momentum per particle collision, the collision frequency and the number of particles per unit area next to the wall. The specularity coefficient, S , which ranges between zero and unity is essentially a measure of the roughness or the friction of the wall. If S is zero, the right hand side of Equation 5.56 vanishes; the particle will slip freely at the wall. For large values S , the amount of slip is minimized; in the limit, the particle attains a no-slip condition when $S = 1$.

Solid Phase Granular Temperature:

For the granular temperature boundary condition at the wall, the zero flux condition can be applied (Koksal *et al.*, 1998; Koksal and Hamdullahpur, 1999). Hui *et al.* (1984) and Johnson and Jackson (1987) proposed a boundary condition also for the granular temperature at the wall using kinetic theory of granular solids. Similar to Equation 5.46, their boundary condition depends on a microscopic energy balance at the wall. They suggested that the flux of pseudo-thermal energy to the wall plus the generation of pseudo-thermal energy by particle slip at the wall is balanced by the dissipation of the pseudo-thermal energy at the wall due to inelastic particle collisions. This energy balance can be expressed as:

$$-k_{\Theta} \frac{\partial \Theta}{\partial n} = \frac{-\rho_s \pi v^2 S \sqrt{\Theta}}{2\sqrt{3} \left[\frac{\alpha_{s,max}}{\alpha_s} - \left(\frac{\alpha_{s,max}}{\alpha_s} \right)^{2/3} \right]} + \frac{\sqrt{3} \rho_s \pi (1 - e_w^2) \beta \sqrt{\Theta}}{4 \left[\frac{\alpha_{s,max}}{\alpha_s} - \left(\frac{\alpha_{s,max}}{\alpha_s} \right)^{2/3} \right]} \quad (5.47)$$

where e_w is the coefficient of restitution for particle-wall collisions describing the elasticity of the particle-wall collision. When $e_w = 1$, the particle will rebound from the wall without any momentum loss. When $S = 0$ and $e_w = 1$, the zero flux condition for granular temperature is obtained as the right hand side of Equation 5.47 vanishes. In this study, Equations 5.46 and 5.47 are used as the wall boundary conditions for the solid phase tangential velocity and granular temperature.

6 Conclusion

In this chapter, a two-fluid gas solid flow model is presented for application to a riser flow in a CFB with SA injection. In the model, the solid phase is considered as a continuum, and the two phases (gas and solid) are coupled by an interphase drag force described by Wen and Yu (1966). The individual fluctuations of particles in the solid phase which create the solid phase laminar shear viscosity, bulk viscosity and pressure are modeled by the kinetic theory model of Hrenya and Sinclair (1997). The large scale

fluctuations in the particle phase due to particle congregations typical to a riser flow are taken into account by a two-equation eddy viscosity k - ϵ model. The gas phase turbulence is also modeled by the standard k - ϵ model with standard wall function approach near the wall. The implementation of the model with FLUENT V4.5 is presented in Chapter 6.

Chapter 6

Simulation Results and Discussion

1 Introduction

In this chapter, the results of the simulations using the two-fluid approach are presented. Fluent V4.5, a commercial CFD package of Fluent Inc., is used for implementing the model. First, the model is applied to the CFB riser data of Miller and Gidaspow (1992) to test and investigate the results of the model without SA injection. The CFB data of Miller and Gidaspow (1992) are taken as a benchmark study since it provides a comprehensive set of data on CFB riser flow. It is also used by several other researchers in two-fluid model application and testing (Neri and Gidaspow, 2000; Fan *et al.*, 1999). Then, the model is tested against the experimental data of Ersoy (1998) for the simulation of a laboratory scale CFB riser with SA injection. Finally, the gas mixing phenomena in CFB risers is modeled in the context of the two-fluid model. Each of these cases is discussed separately in this chapter.

2 Riser Flow Simulation without SA Injection

Miller and Gidaspow (1992) carried out an experimental study in a laboratory scale CFB riser (ID = 7.5 cm, Height = 6.6 m) at Illinois Institute of Technology (IIT). They used

FCC particles with an average particle diameter, d_p , of 75 μm and a particle density, ρ_s , of 1654 kg/m^3 , in their experiments. They measured the local solids volume fraction in the riser with an X-ray densitometer and used an extraction probe to measure the local solids flux. The local solids velocity was then calculated from the measurements of the local solids flux and the solids volume fraction. In this section, the results of the simulation of their experimental run with a superficial gas velocity of 2.89 m/s and a solids circulation rate of 12 $\text{kg/m}^2\text{s}$ are presented.

IIT riser is simulated in a 2-D axisymmetric grid as shown in Figure 6.1. The dimensions of the grid in radial and axial direction are 0.0375 m and 6.6 m, same as the dimensions of the actual riser. In the actual riser, the exit is a smooth 90° bend having an ID of 0.075m. In the 2-D axisymmetric representation, the size of the outlet plane is set such that it gives the same exit area as that of the actual riser. The total number of internal cells used to construct the grid is set as 3081 excluding the boundary cells (39 cells in the radial direction, 79 cells in the axial direction). Thus, the average cell size becomes 0.096 cm and 8.35 cm in the radial and the axial directions, respectively. In the radial direction, the grid spacing is distributed non-uniformly; more cells are placed closer to the wall to capture the complex flow behavior around the wall region. In the axial direction, uniform grid spacing is used except the outlet region where the grid spacing is decreased to accommodate the sharp exit.

The inlet section is modeled similar to the actual geometrical configuration of the riser inlet where the solids and the gas enter the riser as a two-phase mixture (Miller and Gidaspow, 1992). In this study, uniform plug flow is assumed for both phases at the inlet. The average solids velocity at the inlet is calculated from the following relation based on the given solids mass flux:

$$v_{inlet} = \frac{G_s}{\alpha_s \rho_s} \quad (6.1)$$

This gives an average solids velocity of 0.0726 m/s at the inlet for a specific solids

volume fraction of 0.1 and a flux of 12 kg/m²s. The value of solids volume fraction at the inlet, i.e., 0.1, is taken the same as the value used in the experiments. The value of the granular temperature at the inlet is set to be equal to the value of the solids velocity (Nieuwland *et al.*, 1996a). The values of the turbulent kinetic energy and its dissipation rate for both phases at the inlet are calculated from the following relations based on the inputs of the turbulent intensity and the characteristic length of the flow as ($i = \text{gas or solid}$, $\omega = u$ or v where u and v are the average gas and solids velocity, respectively):

$$k_i = \frac{3}{2} (\omega_{av} I_i)^2 \quad (6.2)$$

where I is the turbulent intensity and ω_{av} is the average velocity at the inlet. The inlet boundary condition for the dissipation rate of the turbulent kinetic energy is calculated from:

$$\varepsilon_i = C_\mu^{3/4} \frac{k_i^{3/2}}{0.07L} \quad (6.3)$$

where L is the characteristic length of the flow and C_μ is the empirical constant used in the k- ε turbulence model having a value of 0.09. In the simulations, the turbulence intensity and the characteristic length are set as 5% and 0.075 m (ID of the riser) for both phases. The properties of the gas and solid phases used in the simulations are given in Table 6.1

Table 6.1. Properties of the gas and solid phase for the simulation of riser data Miller and Gidaspow (1992)

Gas Phase	Air
Operating pressure, P	1 atm
Temperature, T	20 °C
Shear viscosity, μ_g	1.8×10^{-5} kg/m.s
Solid Phase	FCC
Mean diameter, d_p	75 μm
Particle density, ρ_s	1654 kg/m ³
Coefficient of restitution, e	0.9
Wall coefficient of restitution, e_w	0.9
Specularity coefficient at the wall, S	0.5

A time step of 0.0005 sec is used in the simulations to ensure numerical stability. It has been observed that the time step is one of the critical parameters to reach a converged solution. The simulations last until the steady state solution is reached. The typical computational time for a 2-D simulation with approximately 4000 cells is 3-4 days on a Dec Alpha 500 MHz workstation. The numerical procedure and schemes are already discussed and presented in Appendix E. The convective transport terms are evaluated by the power law interpolation scheme as given in Appendix E.

Figure 6.2 shows the variation of the solids volume fraction in the riser based on the model equations presented in Chapter 5. The figure is not drawn to actual scale of the riser, the radial direction is magnified to provide a larger plot area. The center line in the figure represents the symmetry line on the grid given in Figure 6.1 As can be seen from Figure 6.2, a core-annular type of flow structure, typical to a riser flow, is successfully obtained with solids concentrated near the walls. A relatively dense region at the bottom and the top of the riser beneath the so-called splash plate is also obtained.

The quantitative comparisons of the solid axial velocity and volume fraction with measurements at a height of 5.52 m above the distributor plate in the riser are given in Figures 6.3 and 6.4. In Figure 6.3, the radial variation of the air velocity is also presented. In case of axial solids velocity, both the magnitude of the solids velocity and the shape of the profile agree well with those of the experimental measurements. The solids volume fraction, on the other hand, is slightly underpredicted. The discrepancy between the simulated and the experimental solids volume fraction values is highest near the wall. It is also interesting to note that the air velocity profile is not as flat as one would normally obtain in the case of single phase turbulent duct flow. This result can be explained by the fact that due to the non-uniformity in particle distribution, the suspension experiences less resistance to flow near the tube axis compared to the wall region. This leads to the calculated parabolic gas and solids velocity profiles.

The integration of the solids and air velocity profiles gave averaged cross-sectional axial velocity values of 1.85 m/s and 2.9 m/s, respectively, leading to an average slip velocity

of 1.05 m/s. Furthermore, the simulated profiles of solids velocity and volume fraction gave a solids flux of $12 \text{ kg/m}^2\text{s}$ which is the prescribed value at the inlet representing a satisfactory internal check for the mass conservation.

The profiles presented in Figures 6.3 and 6.4 represent the flow behavior both qualitatively and quantitatively almost all through the riser height excluding the inlet and exit regions. However, in the experiments carried out in the current study a more distinct bottom dense bed region was reported (Miller and Gidaspow, 1992). Thus, in the simulations the fully developed flow is reached at a shorter axial distance compared to the measurements.

Figures 6.5 and 6.6 show the effects of the different kinetic theory expressions/formulations on the riser hydrodynamics at the same superficial gas velocity and solids circulation rate. The first simulation, for which the variation of the solids volume fraction is given in Figure 6.5, uses a volume averaged granular energy balance equation (Equation 5.24) as opposed to the time averaged one as described in Chapter 5. The kinetic theory expressions of Hrenya and Sinclair (1997) for the particle viscosity and the pressure are utilized as in the case of the original model. Figure 6.5 shows that the expected core-annular structure is not obtained in the riser in this case even the same relations for solids phase viscosity and pressure are used. The profile of solids volume fraction for this case is presented in Figure 6.4 for comparison. It clearly shows an increase in solids volume fraction at the center of the riser contrary to the measurements.

The second simulation carried out uses the kinetic theory expressions of Sylamlal *et al.* (1993) as presented in Appendix D with the volume averaged granular temperature equation. Figure 6.6 shows the variation of the solids volume fraction in the riser for this case. The evolution of the simulation in time shows an accumulation of solids at the riser axis similar to the previous case. Different from Figure 6.5, a thin strip of dense solids is obtained also near the wall. However, without the time averaged granular energy balance equation, it was not possible to obtain the expected distribution of solids.

The different solutions obtained in the simulations can be explained comparing the

variation of the granular temperature in the riser obtained for the cases discussed above (Figure 6.7). Figure 6.7 shows the radial variation of the non-dimensional solids granular temperature in the riser at a height of 5.52 m above the distributor plate. For each case, the maximum value of the granular temperature is used to produce the corresponding non-dimensional profile. As described in Chapter 6, the granular temperature represents the fluctuating kinetic energy of the individual particles. It is produced mainly due to the shear in the solids phase and dissipated due to inelastic binary particle collisions. Thus, the granular temperature is expected to be high in the riser in the regions of high shear and low solids concentration which are the regions of high production and low dissipation. Therefore the granular temperature reaches a maximum in the center of the riser where the solids volume fraction is minimum (minimum dissipation) and attains a minimum value near the wall where the solids volume fraction is maximum (maximum dissipation). As can be seen from Figure 6.7, the expected granular temperature profile is obtained only when the time averaged transport equation is used as in the case of original model. The other two cases fail to predict the expected core-annular flow structure as they do not produce a correct profile for granular temperature. It can be suggested that the time averaging provides more physical structure to the problem formulation leading to a more realistic granular temperature distribution.

It should also be pointed out that when the kinetic theory expressions of Hrenya and Sinclair (1997) are used, whether with time averaged granular temperature equation or not, a steady-state solution is reached in a shorter computational time. However, with Sylamlal *et al.* (1993) kinetic theory model, as can be seen from Figure 6.6, even after 35 seconds of simulation¹ time, a steady state solution is not obtained.

The above discussions show that although the kinetic theory expressions of different researchers stem from the same principles, each set of equation may not only lead to a different solution but also may show different characteristics as far as numerical stability

1. It almost corresponds to a computational time of 2-3 weeks on a Dec Alpha workstation

and solution convergence are considered. For instance, the two-phase eddy viscosity particle phase turbulence model with the kinetic theory expressions of Sylamlal *et al.* (1993) has always resulted in a diverged solution throughout all the simulation attempts.

Figure 6.8 presents the variations of the granular temperature, air and solids turbulent kinetic energy at the same cross-section obtained from the original model described in Chapter 5. The granular temperature reaches a maximum value of $40 \text{ m}^2/\text{s}^2$ at the center. Neri and Gidaspow (2000) also obtained the same type of profile for the granular temperature in the simulation of the data of Miller and Gidaspow (1992) with a maximum value of $1.6 \text{ m}^2/\text{s}^2$ on the riser axis which is almost one order of magnitude less than the maximum value obtained in this study. The air turbulent kinetic energy shows a typical profile for a turbulent pipe flow with a maximum value near the wall due to turbulence production, decreasing to a value of $1.25 \text{ m}^2/\text{s}^2$ at the center. The CFD model of Fan *et al.* (1999) applied to the same data also gave similar values for the air turbulent kinetic energy. It is interesting to note that the particles fluctuate with larger energy than the fluid itself which is a typical feature of dense gas-solid flows attributed to particle-particle interactions. On the other hand, the fluctuating energy of the large scale motion which produces the particle eddy viscosity lies in the range of $0.02 \text{ m}^2/\text{s}^2$. This value can be seen as the average fluctuating energy of the clusters in the riser. Unfortunately, the lack of experimental data for air and solids turbulent kinetic energy in dense gas-solid flows makes it difficult to fully verify the accuracy of these parameters.

Figure 6.9 shows the radial variation of the laminar and turbulent shear viscosity for the solids phase in the riser at a height of 5.52 m above the distributor plate. The solids laminar viscosity is calculated from the kinetic theory whereas the solids turbulent eddy viscosity comes from the two-equation turbulence model. The total effective viscosity of the solids phase is also shown on the same plot. It is interesting to note that the magnitudes of the solids laminar and turbulent eddy viscosity are in the same order of magnitude, unlike the gas phase where the laminar shear viscosity is often neglected when the flow is fully turbulent. The average value of the effective total solids shear viscosity is in the range of 0.2 Pa.s as can be seen from the figure. Neri and Gidaspow

(2000) simulated the same data using kinetic theory of expressions of Gidaspow (1994) and obtained an average laminar shear viscosity value of 0.01 Pa.s, a value which is almost one order of magnitude smaller than the one calculated in this study. The discrepancy comes from the predicted values of the granular temperature as discussed previously. Their simulation did not include a turbulence model for the solids phase so a value of turbulent eddy viscosity was not reported.

The radial variation of the solids pressure at the same cross-section ($h = 5.52$ m) is given in Figure 6.10. As can be seen from figure, the solids pressure is almost constant along the riser cross-section with an average value of 175-180 Pa. Neri and Gidaspow (2000) obtained a value of solids pressure in the range of 40-60 Pa in their simulations whereas solid pressures in the range 100 Pa were reported by Gidaspow and Huilin (1996) for operating conditions similar to Gidaspow and Miller (1992).

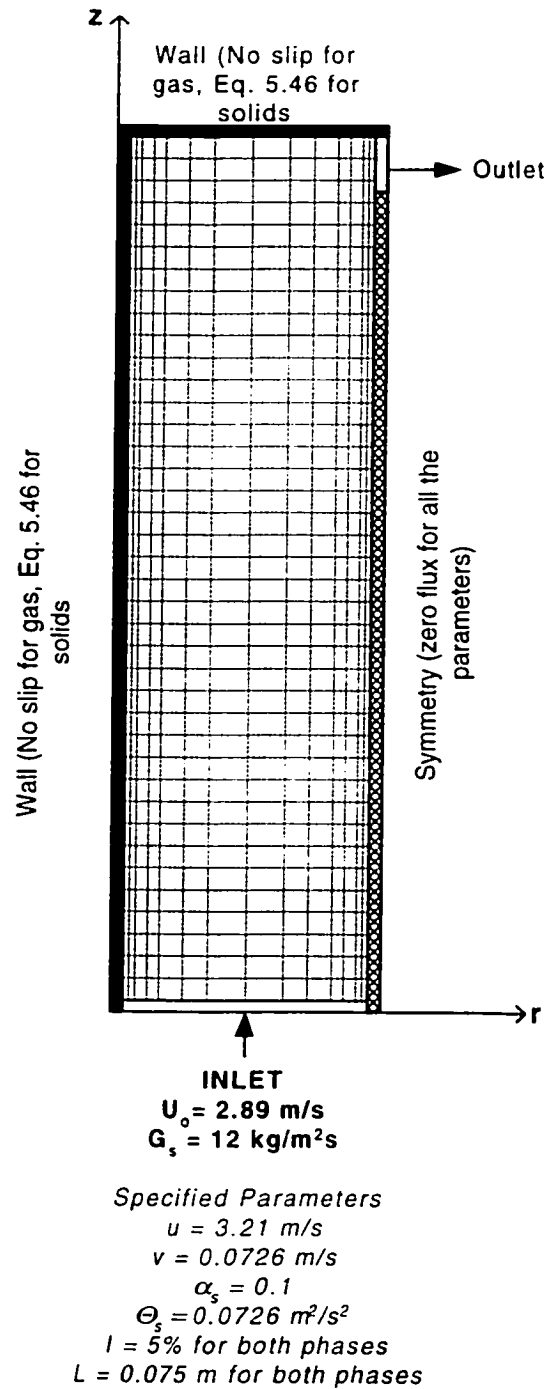


Figure 6.1. 2-D grid for riser simulation of Miller and Gidaspow (1992)

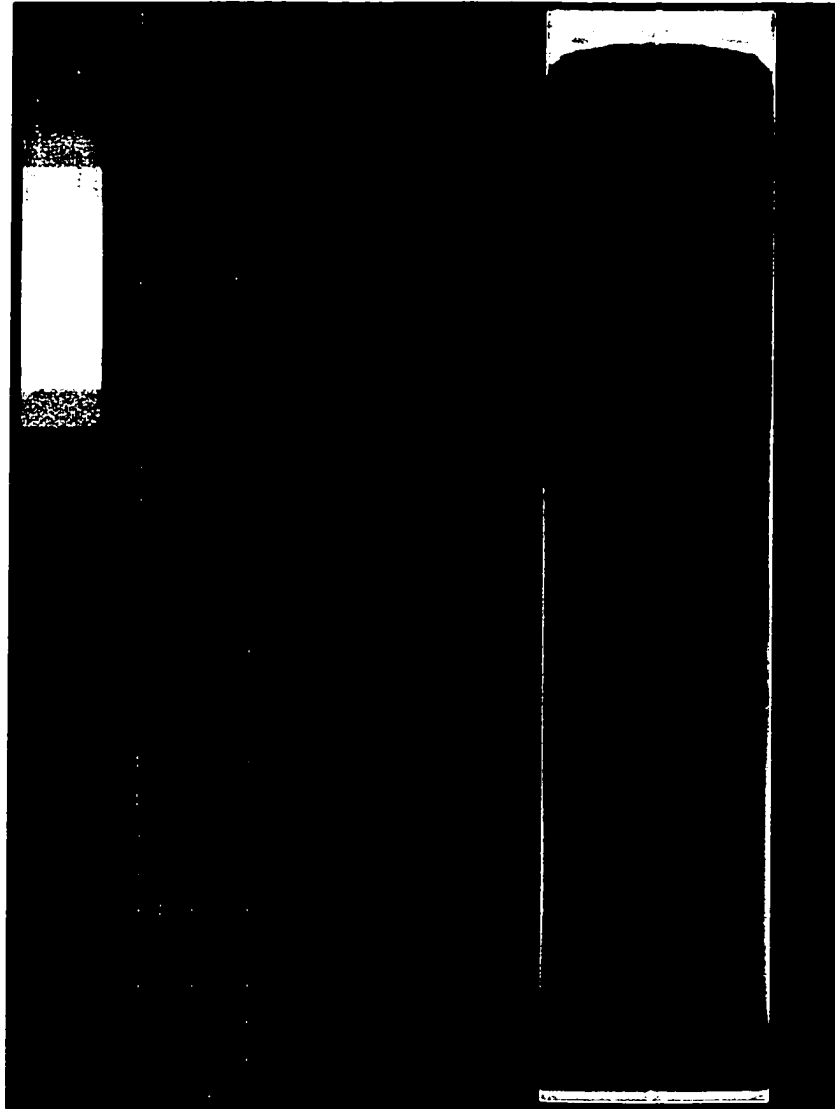


Figure 6.2. The contours of solids volume fraction for the riser simulation of Miller and Gidaspow (1992). Kinetic theory model: Hrenya and Sinclair (1997) with time averaged granular energy balance equation and two-equation $k-\varepsilon$ particle phase turbulence model (colors on scale: blue: $\alpha_s = 0$, red: $\alpha_s = 0.1$)

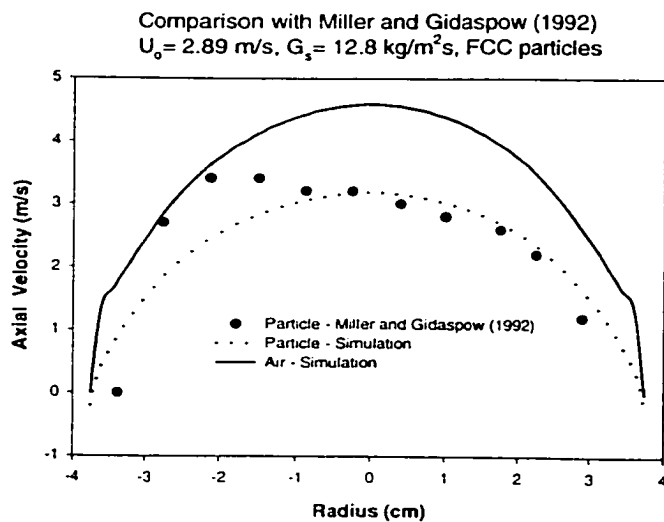


Figure 6.3. Comparison of the simulation and the experimental results at a height of 5.52 m above the distributor plate for solids axial velocity. The simulated radial variation of the air velocity is also presented.

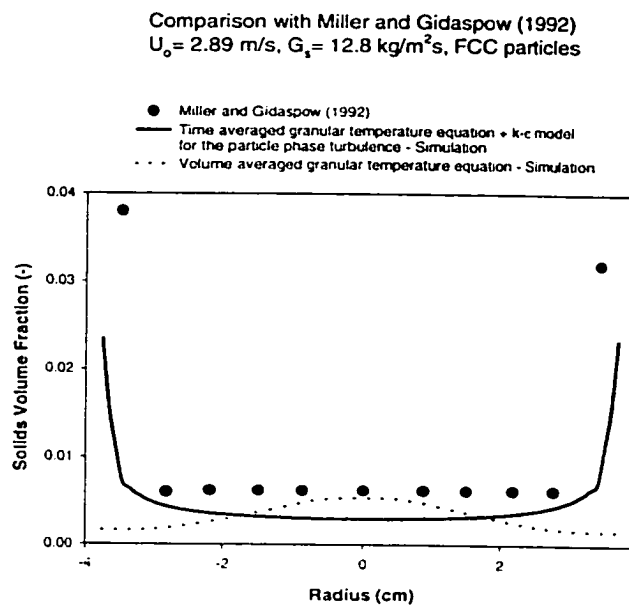


Figure 6.4. Comparison of the simulation and the experimental results at a height of 5.52 m above the distributor plate for solids volume fraction.

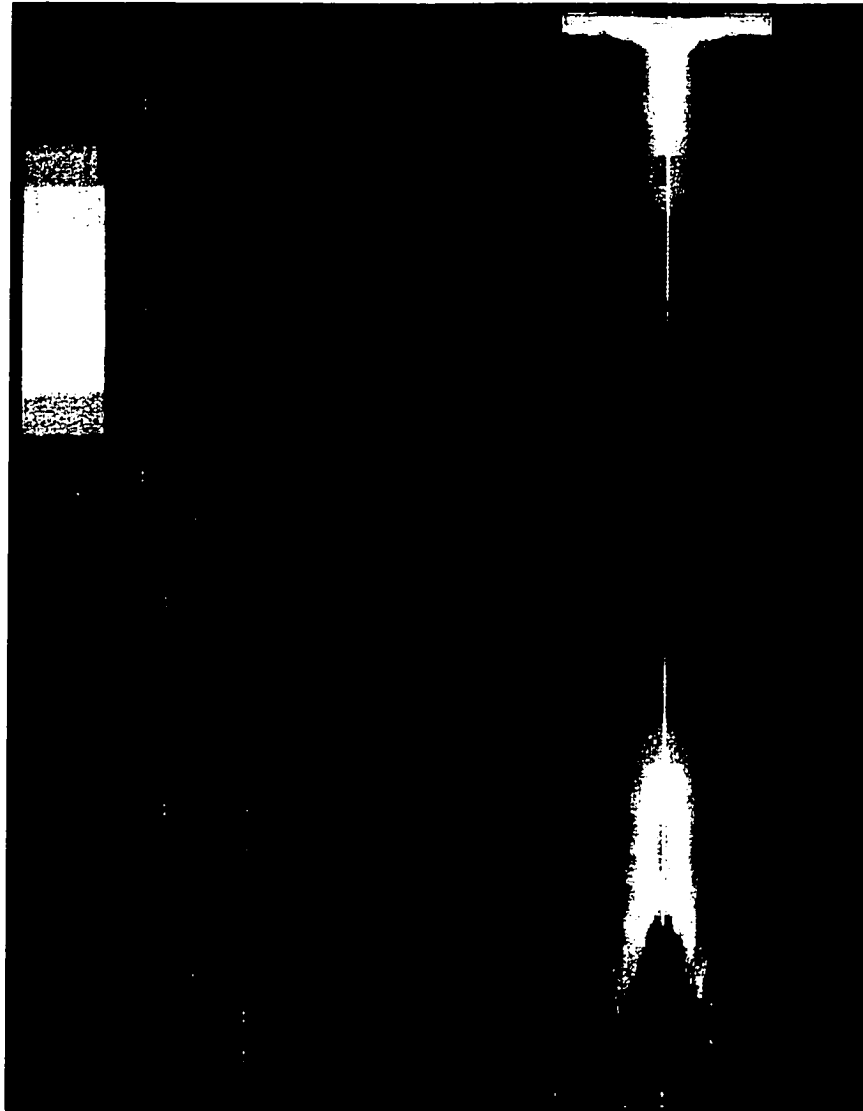


Figure 6.5. The contours of solids volume fraction for the riser simulation of Miller and Gidaspow (1992). Kinetic theory model: Hrenya and Sinclair (1997) with volume averaged granular energy balance equation, no solids phase $k-\epsilon$ turbulence model (colors on scale: blue: $\alpha_s = 0$, red: $\alpha_s = 0.1$)

a) $t = 5.5$ s b) $t = 12$ s c) $t = 18.5$ s d) $t = 28$ s e) $t = 35$ s

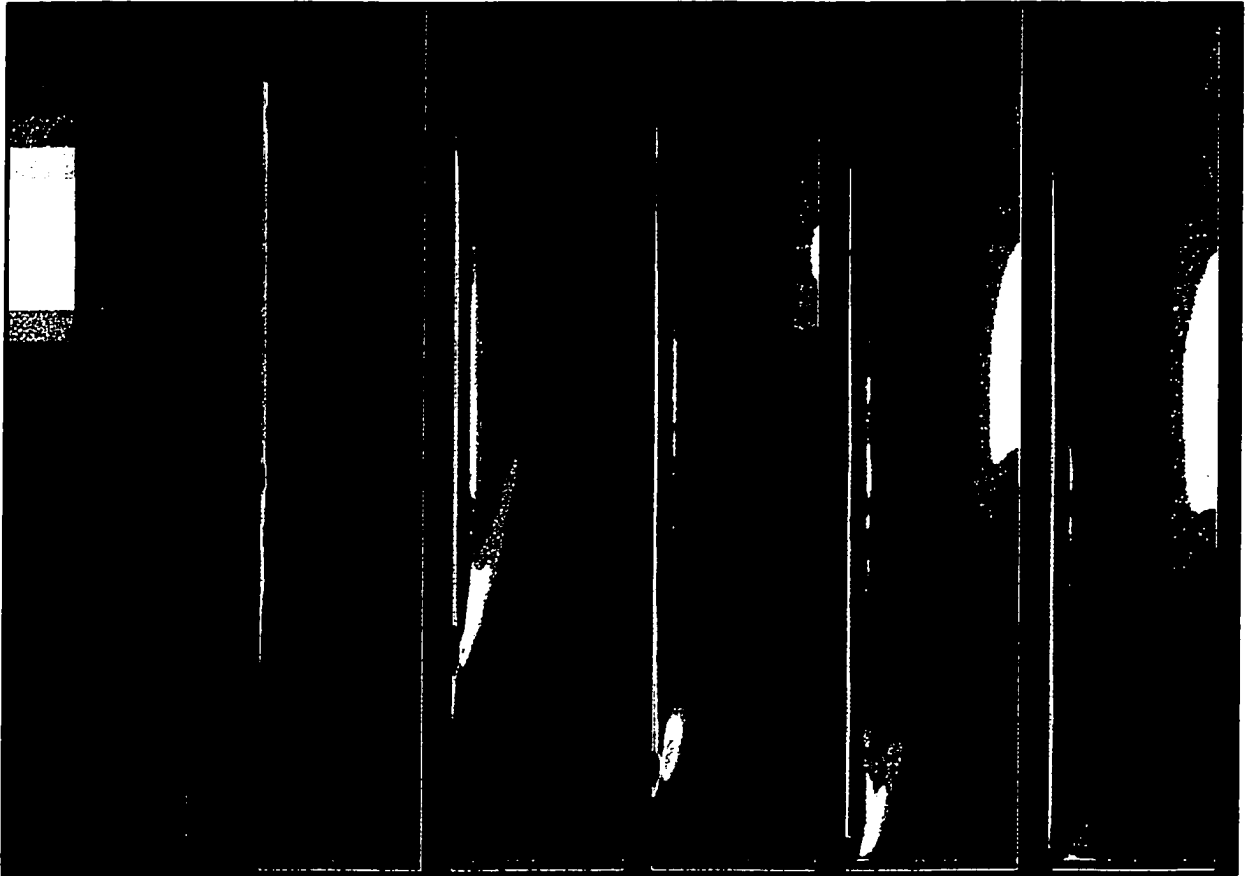


Figure 6.6. The contours of solids volume fraction for the riser simulation of Miller and Gidaspow (1992) at $t = 5.5$ s, 12 s, 18.5 s, 28 s and 35 s based on the kinetic theory expressions of Sylamlal *et al.* (1993), volume averaged granular energy balance equation, no solids phase $k-\varepsilon$ turbulence model. (colors on scale: blue: $\alpha_s = 0$, red: $\alpha_s = 0.1$. (The right plane is the symmetry plane (center line)))

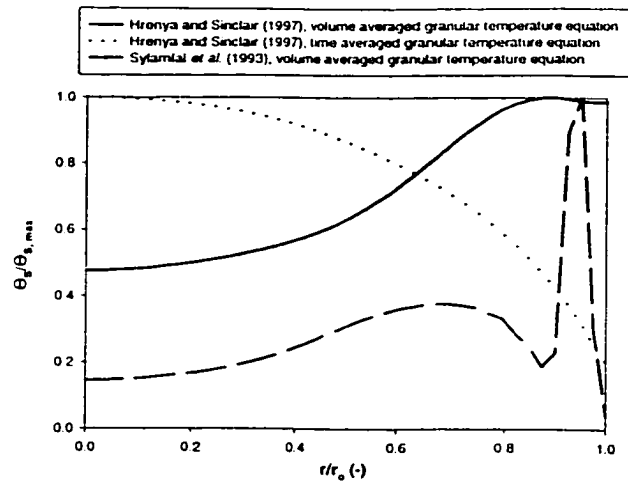


Figure 6.7. Comparison of the granular temperature profiles at a height of 5.52 m above the distributor plate for different kinetic theory formulations.

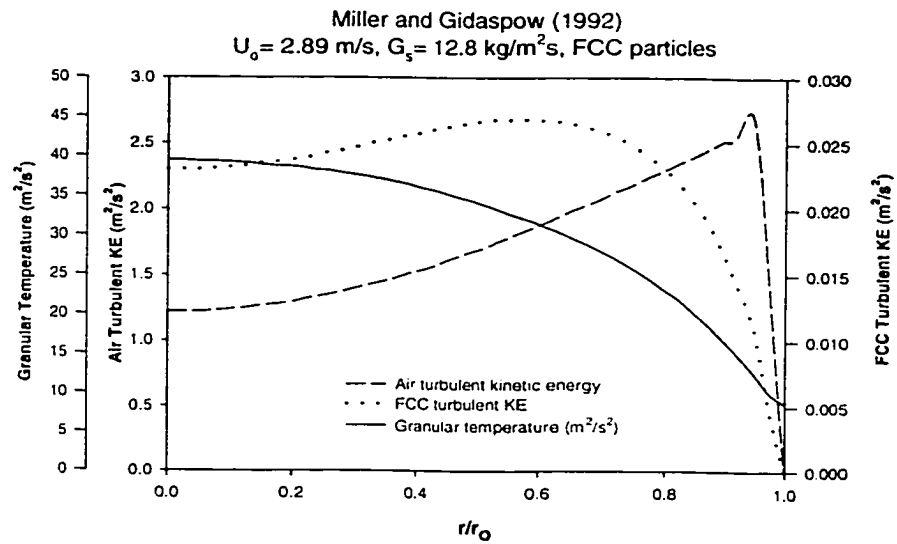


Figure 6.8. The variation of the granular temperature, solids turbulent kinetic energy and air turbulent kinetic energy in the riser at a height of 5.52 m.

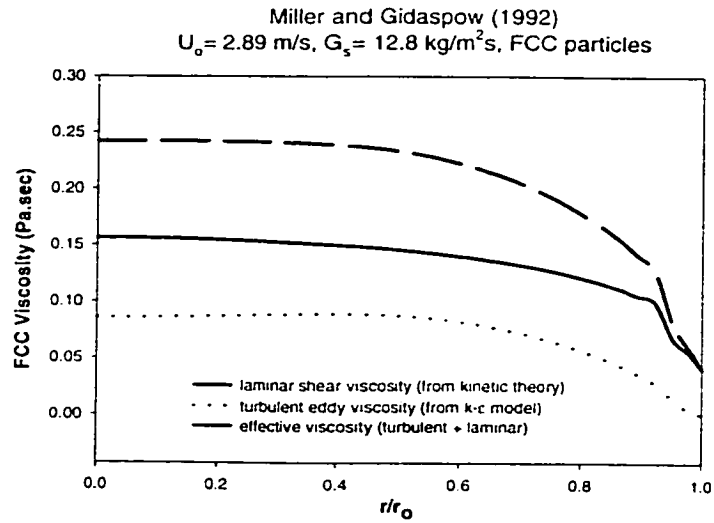


Figure 6.9. The solids phase laminar and turbulent shear viscosity at a height of 5.52 m above the distributor plate.

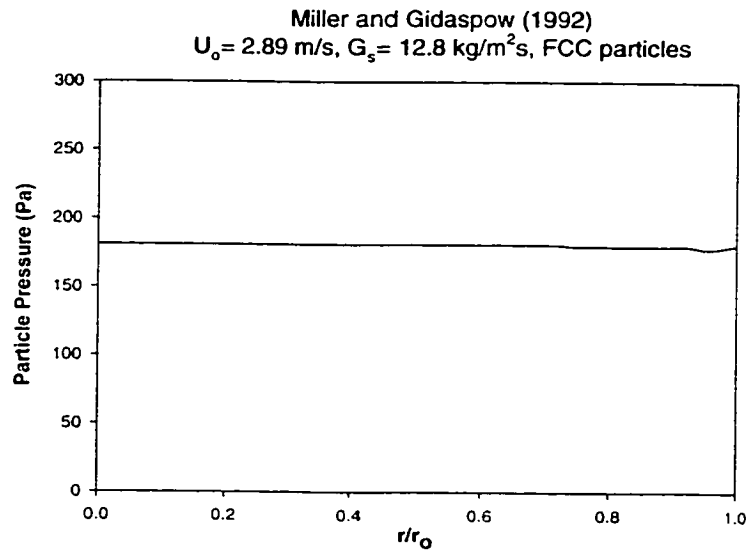


Figure 6.10. The solids phase pressure at a height of 5.52 m above the distributor plate.

3 Riser Flow Simulation with SA Injection

Ersoy (1998) carried out particle velocity and pressure drop measurements in a laboratory scale riser described in Chapter 3 to investigate the effects of the secondary air injection on riser hydrodynamics. For particle velocity measurements, an optical probe (Vector VSI - 2000) which is composed of two 1 mm diameter bundles of optical fiber spaced 4 mm apart was used. The secondary air was injected at a height of 1.2 m above the distributor plate with three different types of injectors; radial, tangential and mixed, which were already described in Chapter 3. The particle velocity was measured at four different heights 0.52 m, 0.93 m, 1.26 m and 1.83 m above the distributor plate. The bed material used in the experiments was FCC particles with a mean particle diameter of 60 μm and a particle density of 1600 kg/m^3 .

Table 6.2. Properties of the gas and solids phase for the simulation of data of Ersoy (1998)

Gas Phase	Air
Operating pressure, P	1 atm
Temperature, T	20 °C
Shear viscosity, μ_r	1.8×10^{-5} kg/m.s
Solid Phase	FCC
Mean diameter, d_p	60 μm
Particle density, ρ_s	1600 kg/m^3
Coefficient of restitution, e	0.9
Wall coefficient of restitution, e_w	0.9
Specularity coefficient at the wall, S	0.5

The simulations are carried out on a 2-D Cartesian grid as shown in Figure 6.11. The total number of internal cells used are set as 3381 (49 cells in the x direction, 69 cells in the z direction) excluding the boundary cells. The grid is constructed by considering the actual dimensions and geometry of the riser. The primary air enters the riser through an inlet which has a width of 0.23 m (ID of the actual riser). The solids enter the riser laterally through a second inlet of 0.15 m width (ID of the return leg in the actual riser). The height

of the riser is set as 7.6 m similar to the height of the actual riser. The width of the riser outlet is set as 0.2 m. The dimensions of the two secondary air inlets which are located 1.2 m above the primary air inlet are determined such that the SA jet velocity is matched to its actual experimental value for a specified SA/PA ratio. With these dimensions, the average cell sizes in x and z directions become 0.47 cm and 11 cm, respectively. More computational cells are placed near the walls, outlet region, solids and secondary air inlets to resolve the flow better in these regions.

At the primary air inlet, a parabolic profile for air velocity based on the SA/PA air ratio is specified. No solids are allowed to enter the riser through this inlet. The air turbulence intensity and the characteristic length are set as 5% and 0.23 m from which the inlet cell values of air turbulent kinetic energy and its dissipation rate are calculated based on Equations 6.2 and 6.3. At the solids inlet, a uniform solids velocity and volume fraction are specified to give the prescribed mass flux based on Equation 6.1. The solids granular temperature is set as the same value as the solids velocity. The turbulent intensity of the solids and its characteristic length are specified as 5% and 0.15 m, respectively.

The time step used in the simulations is set as 0.0005 sec. The power law interpolation scheme is used for the calculation of the convective transport terms at the cell centers as described in Appendix E.

Figures 6.12 and 6.13 show the variation of the solids volume fraction in the riser for two operating conditions, $U_o = 3$ m/s, $G_s = 18$ kg/m²s and $U_o = 5$ m/s, $G_s = 33$ kg/m²s for SA/PA = 0 and SA/PA = 0.5. It should be pointed that, in the figures the actual height to diameter ratio is not conserved, the x direction is magnified. As can be seen, a core-annular structure is obtained in the simulations depending on whether the total fluidization air is staged or not. When the secondary air is utilized, the region below the SA injection plane (the so-called primary region) becomes denser compared to the case without SA injection due to the decrease in the air flow rate in the primary region and cut-off effect of the SA jets. This is consistent with the bed suspension density data presented in Chapter 4. Another distinct difference between the staged and non-staged operation is

the thickness of the annulus region in the figures. With the secondary air injection, a thicker annulus is obtained in the region above the SA injection plane (the so-called secondary region) for both operating conditions.

Figures 6.12 and 6.13 also show a very interesting characteristic of the SA injection. As seen in both of the figures, the SA jets push the rising solids towards the center of the riser creating solids accumulation around the center region just above the SA injection plane. However, the solids quickly disperse with height and the core-annular structure is again established in the riser. This type of flow structure around the SA injection zone is also observed by Marzochella *et al.* (1996b) as shown in Figure 6.14. The photograph presented in Figure 6.14 shows an instantaneous view of the gas and solids in a 2-D lab scale CFB with ballatoni as the bed material. The gas-solid flow structure around the SA injection region is similar to those presented in Figures 6.12 and 6.13. Figure 6.14 also shows the solids distribution obtained from the two-fluid model simulation² using the experimental data of Marzochella *et al.* (1996b). Thus, it confirms that the model gives a very realistic picture of the gas-solid flow behavior in CFB risers with SA injection.

Figure 6.15 shows the comparison of the pressure drop along the riser obtained from the simulations and the experiments for $U_o = 3$ m/s, $G_s = 18$ kg/m²s, SA/PA = 0 and $U_o = 5$ m/s, $G_s = 33$ kg/m²s, SA/PA = 0 (Ersoy, 1998). The pressure drop curves presented are produced finding the pressure drop between two consecutive pressure ports whose axial distances from the distributor plate are set according to those used in the experiments. The agreement between the simulated and the experimental pressure drop is fairly good in the fully developed region whereas it deteriorates closer to the bottom of the riser. The discrepancy near the bottom of the riser can be attributed to several points regarding the simulation. These points are:

1. 2-D flow assumption ,

² The kinetic theory expressions of Sylamlal *et al.* (1993) are used in this simulation with volume averaged granular temperature equation.

2. Neglecting the distributor plate in the simulations,
3. The input values of the solids velocity and volume fraction used to give the prescribed solids flux. (since the solids velocity and the solids volume fraction values at the exit of the return leg are not known experimentally)

Figure 6.16 and 6.17 show the comparison of the simulation and the experimental results for the pressure drop along the riser when the fluidization air is staged ($SA/PA = 0.5$) at two different operating conditions ($U_o = 3$ m/s, $G_s = 18$ kg/m²s, and $U_o = 5$ m/s, $G_s = 33$ kg/m²s). The experimental values are presented for both tangential and radial injection cases. Similar to the cases without SA injection, the discrepancy between the simulation and the experiments increases near the bottom of the riser. In the experiments, a more gradual increase in the pressure drop is measured approaching to the bottom of the riser whereas the simulation results show a sudden increase in the pressure drop just at the riser bottom. Thus, in the simulations, the flow development seems to be completed at a shorter axial distance compared to the experiments.

Figures 6.18-6.21 show the comparison of the simulation and the experimental results for the axial particle velocity in the riser at four different axial locations above the distributor plate ($U_o = 3$ m/s, $G_s = 18$ kg/m²s). The experimental axial particle velocity profiles for the cases with both the tangential and the radial injection are given for comparison. As can be seen from the figures, similar to the pressure drop predictions, the discrepancy between the simulation and the experimental results increases near the bottom of the bed.

At 0.52 m above the distributor plate (0.68 m below the SA injection ports), both the measurements and the simulations show a decrease in the axial particle velocity, as expected, due to the decrease in the gas flow through the primary region when the total fluidization air is staged (Figure 6.18). For the non-staged operation ($SA/PA = 0$), the experimental value of the axial solid velocity reaches a maximum value of 3.65 m/s at the center ($x/L = 0.5$). The solids downflow velocity was measured to be approximately 0.4 m/s near the wall. The simulation for this case predicts a maximum velocity of 6.4 m/s at $x/L = 0.8$. When the fluidization air is staged ($SA/PA=0.5$), the maximum values of the

measured and predicted particle velocity drop to 2.6 m/s and 5.5 m/s, respectively, the latter occurring at $x/L = 0.88$. As can be inferred from Figure 6.18, although the value of the maximum velocity obtained from the simulation and experiment differs significantly, the average velocity at the same cross-section is almost the same for both cases. The unsymmetrical profiles obtained in the simulations arise from the acceleration of the gas-solid flow towards the opposite side of the riser away from the solids inlet. As seen from the distribution of the solids in the riser (Figures 6.12 and 6.13), the solids entering the riser through the return leg blocks the flow area of the rising gas-solid flow, pushing it towards the opposite wall. The same acceleration effect is not observed in the measurements, since in the actual riser, the blockage effect may not be as strong as would be in a 2-D channel due to the 3-D geometry. However, it is still interesting to mark that the decrease in the maximum velocity is approximately 1 m/s for both the simulation and the experiment when the fluidization air is staged.

Figure 6.19 shows the radial variation of the axial particle velocity obtained from the simulations and the experiments for $SA/PA = 0$ and 0.5 at a height of 0.93 m above the distributor plate (0.27 m below the SA injection port). The acceleration of the gas-solid flow has largely diminished and the solids velocity profiles have become more symmetrical compared to the simulated profiles given in Figure 6.18. For $SA/PA = 0$, the agreement between the experimental measurements and the simulations is satisfactory, the maximum velocity on the riser axis and the solids down flow velocity near the wall are accurately predicted. For $SA/PA = 0.5$, the simulated velocity profile is still not perfectly symmetrical, however the value of the downflow velocity near the wall is well replicated.

Figure 6.20 shows the radial variation of the axial particle velocity obtained from the simulations and the experiments for $SA/PA = 0$ and 0.5 at a height of 1.26 m above the distributor plate (0.06 m below the SA injection port). When the SA injected, no solids downflow were observed near the wall just above the SA injection port in the experiments. This unique characteristic of SA injection is also captured in the simulations with almost identical upward solids velocity near the wall having an approximate value of

1 m/s. This is also consistent with the results of the gas backmixing experiments (Chapter 4) which showed a decrease in gas backmixing due to SA injection since the gas backmixing phenomena is usually attributed to the solids down flow near the wall.

Figure 6.21 shows the radial variation of the axial particle velocity obtained from the simulations and the experiments for SA/PA = 0 and 0.5 at a height of 1.83 m above the distributor plate (0.63 m below the SA injection port). The profiles for the staged and non-staged operation (SA/PA = 0 and 0.5) overlap with each other for both the simulations and the experiments. This shows that the effect of the SA injection on the particle motion diminishes very quickly along the riser height. The maximum gas velocity at the center and the solids down flow near the wall are predicted satisfactorily for both SA/PA = 0 and SA/PA = 0.5 cases.

The simulated particle velocity profiles are more parabolic in shape compared to the experimental measurements especially above the SA injection port as seen in Figures 6.20 and 6.21. A parametric study shows that the constant “**m**” of Equation 5.30 (Chapter 5) affects the mean particle and gas velocity profiles significantly. Equation 5.30 is repeated here for convenience:

$$\langle \alpha'_s \Theta'_s \rangle = m \alpha_{s,avg} k_{s,avg} \left[(\alpha_{s,max} - \alpha_{s,wall} - 1) \left(\frac{r}{R} \right)^n + 1 \right] \quad (6.4)$$

This equation was suggested by Hrenya and Sinclair (1997) to model the correlation between the fluctuating components of the solids volume fraction and the granular temperature. As can be seen from the equation, the magnitude of this correlation is directly proportional to the value of the constant, **m**, for which a value of -5 was initially proposed by Hrenya and Sinclair (1997) based on a comparison of their model predictions with experimental data. This correlation term (Equation 6.4) appears in the dissipation term of the granular temperature equation (Equation 5.27) which is also repeated below:

$$\gamma_{\Theta} = \frac{48\rho_s\eta(1-\eta)}{\sqrt{\pi}d_p} \left[\alpha_s^3 g_o \Theta_s^{1.5} + 1.5\alpha_s^2 g_o \left(2 + \frac{g_o}{3} \right) \Theta_s^{0.5} \langle \alpha'_s \Theta'_s \rangle \right] \quad (6.5)$$

Equation 6.4 which is a negative quantity³ decreases the magnitude of the dissipation of the granular temperature given in Equation 6.5, i.e., it acts like a source term for granular energy. Thus, lowering the absolute value of constant “**m**” leads to a decrease in the granular temperature as shown in Figure 6.22. In this figure, the granular temperature profiles are given at a height of 1.82 m above the distributor plate for three different values of **m** = -1, -5 and -8 at a superficial gas velocity of 3 m/s and a solids circulation rate of 18 kg/m²s. As expected, the granular temperature decreases as the magnitude of **m** decreases. The decrease in the granular temperature also affects the suspension density as shown in Figure 6.23. This figure shows the variation of the solids suspension density at the same cross-section for the same case. As can be inferred from the figure, the cross-sectional average of the suspension density increases as the magnitude of **m** is decreased. It is also interesting to note that the solids concentration remains almost the same for the core region whereas it changes significantly near the wall as **m** is changed.

Finally, in Figure 6.24, the axial solids velocity profiles are presented for **m** = -1, -5 and -8. The most parabolic velocity profile is obtained for **m** = -1 and it becomes flatter as the magnitude of **m** is increased. The case **m** = -1 gives the best prediction for the experimentally measured velocity at the center of the riser and near the wall. In fact, it is the only case which shows a negative velocity (downflow) near the wall similar to the experimental measurements. Downflow near the wall is not obtained for **m** = -5 and -8. Thus, lowering the magnitude of constant **m**, decreases the granular temperature which in turn increases the suspension density such that the experimentally observed down flow occurs near the wall. As the suspension density increases near the wall increasing the resistance to the flow, the particle velocity in the core increases to produce a higher

³ The correlation between the solids volume fraction and the granular temperature is a negative quantity since the granular energy of the particles tends to be dissipated more due to particle collisions as the solids concentration increases.

maximum velocity at the center leading to a more parabolic profile. Prior to this discussion, the simulation results presented in this section are all based on the case of $m = -1$ since it has resulted in the least discrepancy between the simulation results and the experimental measurements.

The above discussion shows the importance of the reliability of the closure models in two-fluid approach. One of the ways to increase the prediction capability of the two-fluid approach is to develop more reliable expressions for the correlations such as the one given in Equation 6.4, especially under dense flow conditions.

The particle-particle coefficient of restitution which measures the elasticity of the collisions between the particles is also another important parameter in the model as discussed in Chapter 5. Figure 6.25 shows the effect of the coefficient of restitution on the solids distribution in the riser at superficial gas velocity of 3 m/s and a solids circulation rate of 18 kg/m²s. When the coefficient of restitution is set as 1 in the model (indicating pure elastic collision between two particles without a kinetic energy loss), the granular temperature is no further dissipated in collisions between the particles. Hence, the average value of the granular temperature increases leading to a decrease in the average solids volume fraction or the solids hold up in the riser as seen in Figure 6.25.

Figures 6.26 and 6.27 show the variation of the solids fluctuating kinetic energy (granular temperature) and the air turbulent kinetic energy in the riser for SA/PA = 0 and SA/PA = 0.5 at $U_o = 3$ m/s and $G_s = 18$ kg/m²s. Both figures clearly indicate that SA injection increases the fluctuating kinetic energy of the solids and the gas above the SA ports considerably. This is consistent with the results of the gas mixing experiments presented in Chapter 5. Unlike the experiments, however, the effect of the SA injection does not seem to go down with height towards the bed exit above the SA injection plane. It should be mentioned that the gas phase turbulence model formulation does not include the so-called turbulence modulation effects, i.e., the dissipation of gas phase turbulence due to presence of the particles or its possible increase due to the wakes behind the particles.

Figure 6.28 shows the effect of the numerical discretization scheme on the solids distribution in the riser. The power and the second order upwind schemes are presented in Appendix E. As can be seen from the figure, a higher order interpolation scheme results in a slight increase in the solids holdup in the riser. It should be noted that the computational time in the simulation with second order upwind scheme was much higher compared to power law scheme. The upwind scheme is also found to be not as stable as the power law scheme as far as the solution convergence is concerned.

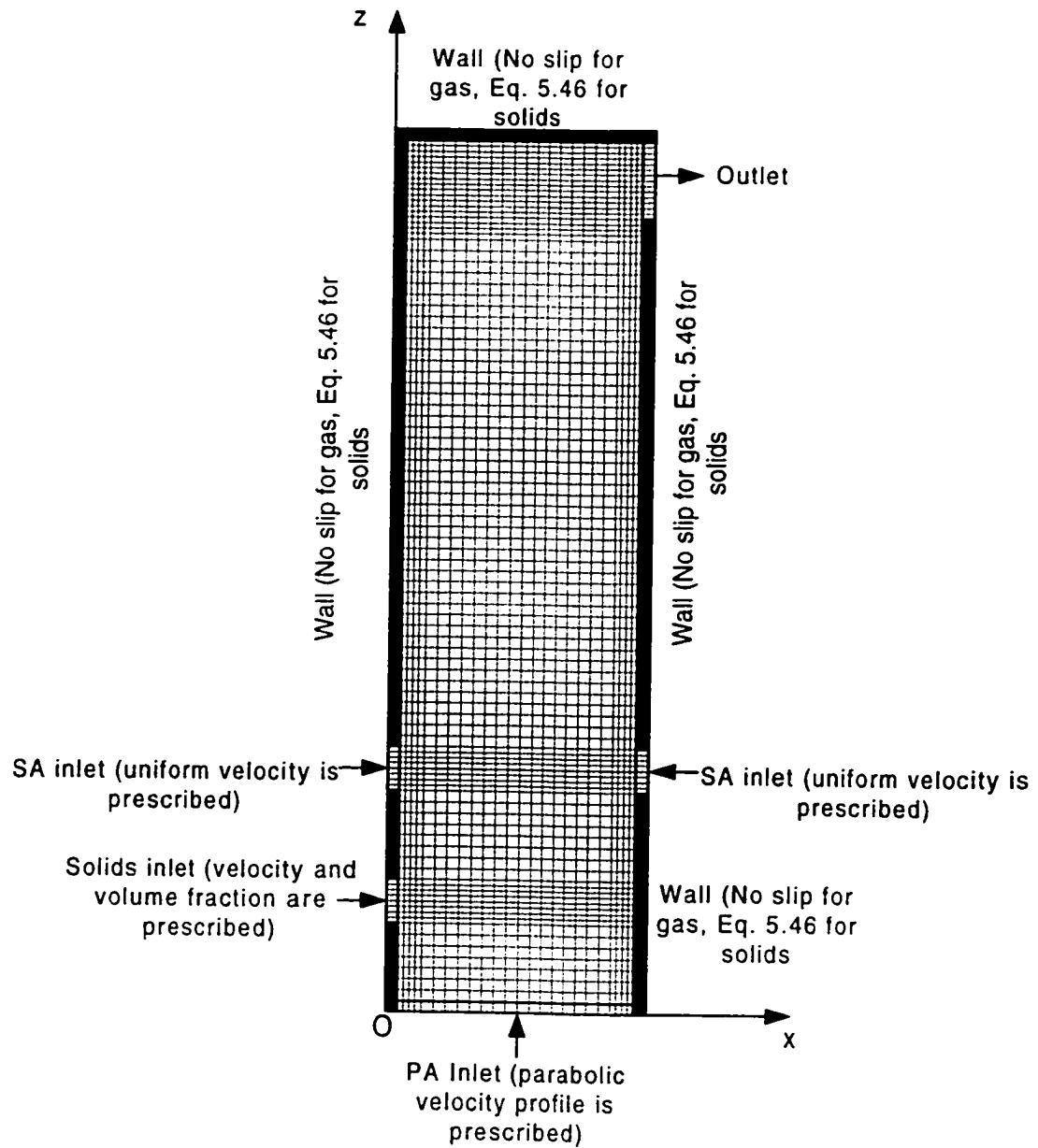


Figure 6.11. 2-D Cartesian grid for the riser simulation with SA injection.

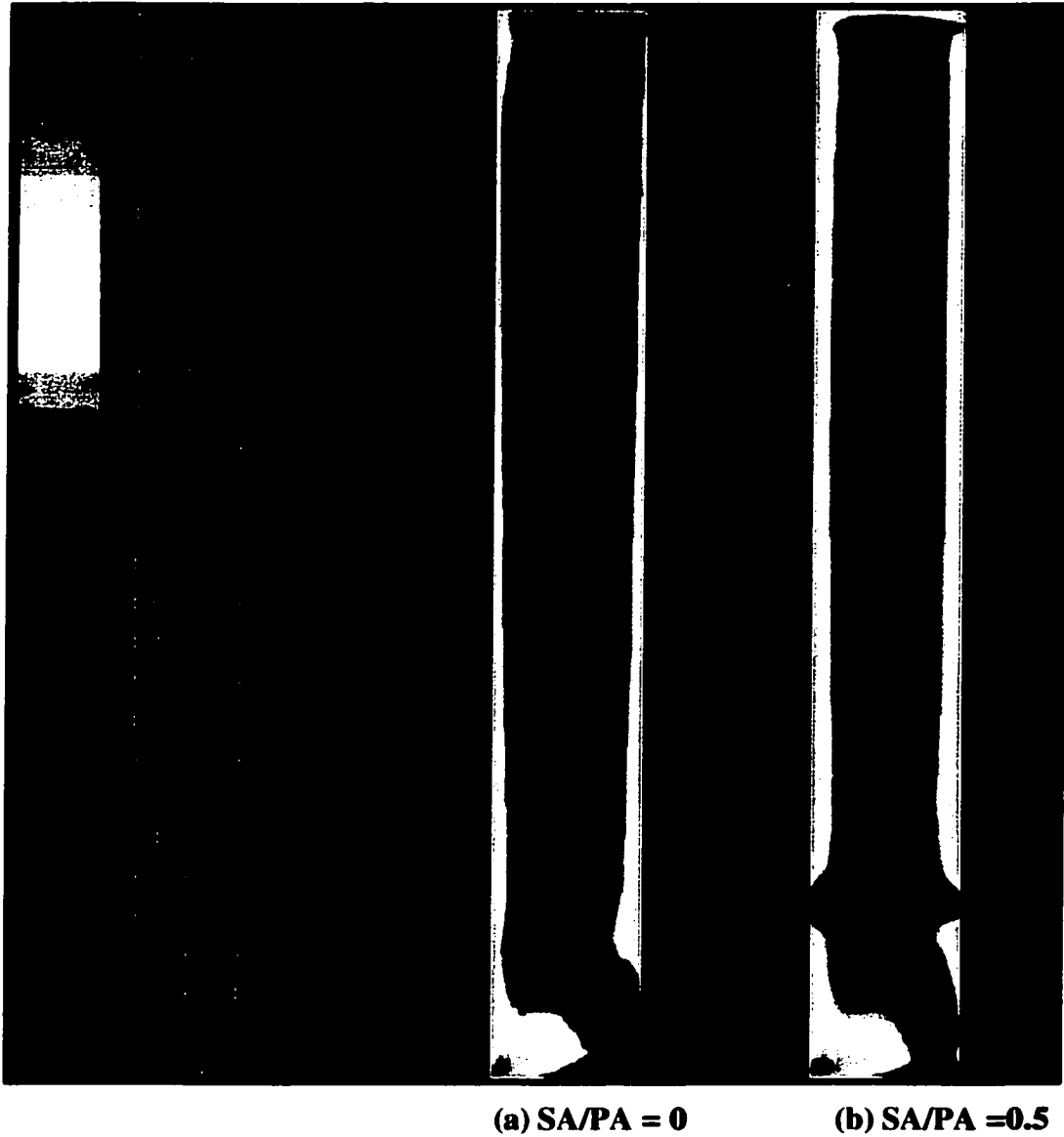


Figure 6.12. Solids volume fraction contours in the riser for two cases, $SA/PA = 0$ and $SA/PA = 0.5$, $U_o = 3$ m/s, $G_s = 18$ kg/m²s (colors: blue, $\alpha_s = 0$, red $\alpha_s = 0.4$)

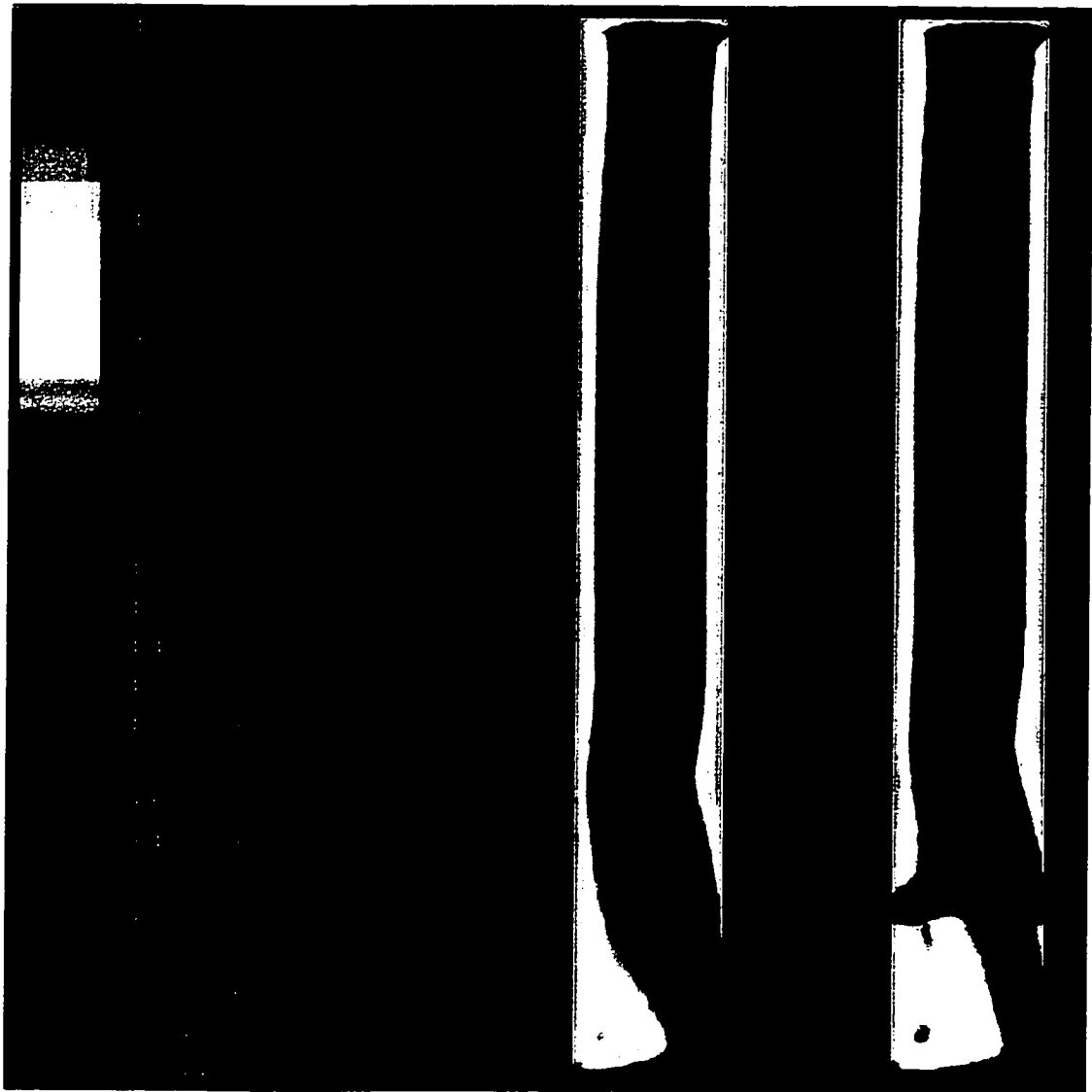
(a) $SA/PA = 0$ (b) $SA/PA = 0.5$

Figure 6.13. Solids volume fraction contours in the riser for two cases, $SA/PA = 0$ and $SA/PA = 0.5$, $U_0 = 5$ m/s, $G_s = 33$ kg/m²s (colors: blue, $\alpha_s = 0$, red $\alpha_s = 0.4$)

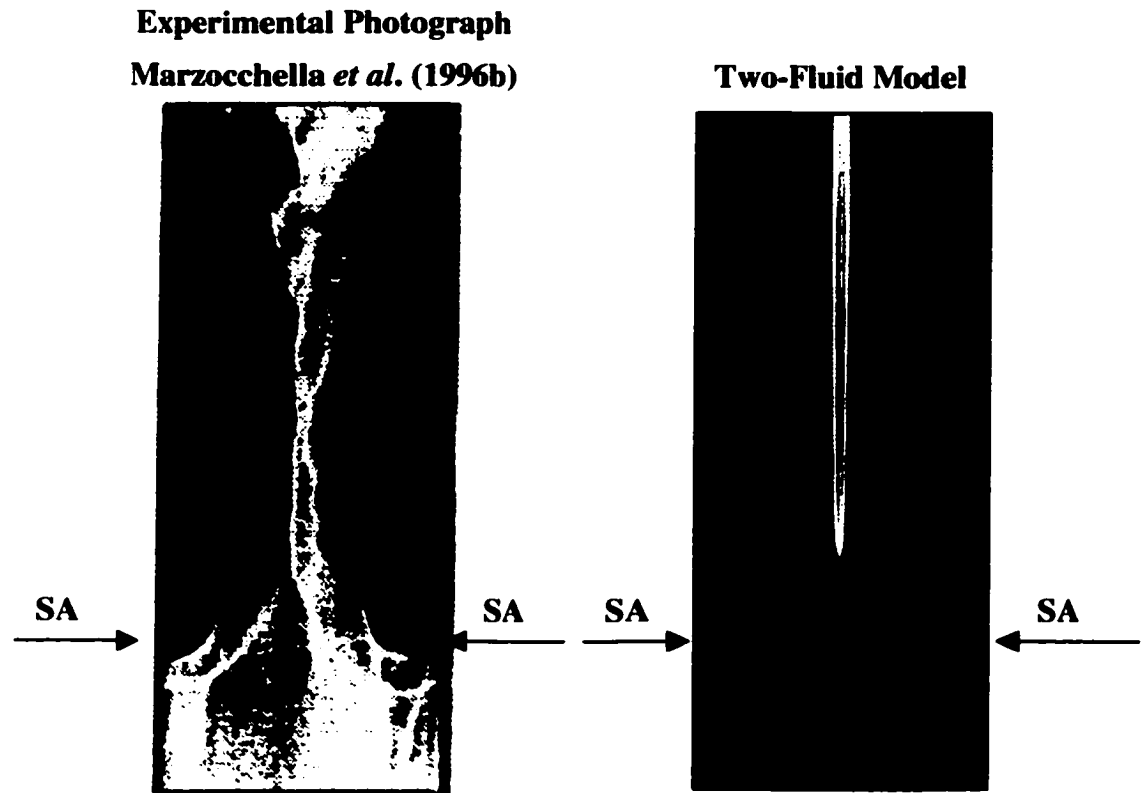


Figure 6.14. Solids distribution in a 2-D riser with SA injection, $U_o = 6$ m/s, $G_s = 35$ kg/m²s, SA jet velocity = 30 m/s, bed material: ballatoni ($d_p = 89$ μ m, $\rho_s = 2540$ kg/m³), photograph from Marzocchella *et al.*, 1996b, white: solids, black: gas.

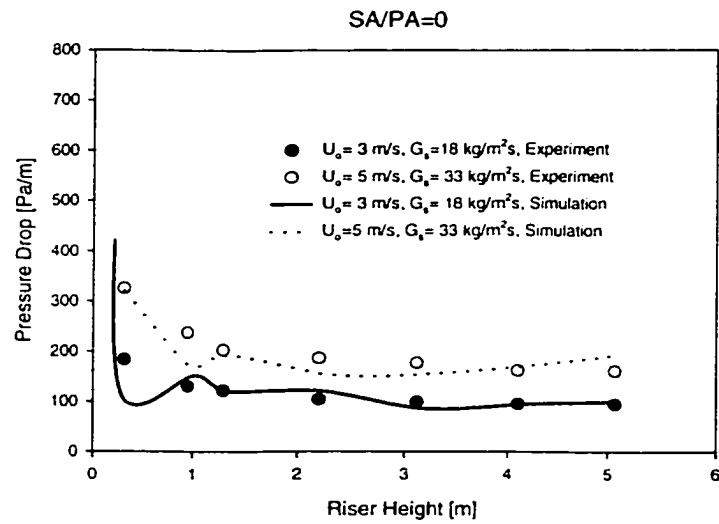


Figure 6.15. Riser pressure drop, simulation vs experiment, $U_o = 3$ m/s, $G_s = 18$ kg/m²s and $U_o = 5$ m/s, $G_s = 33$ kg/m²s, SA/PA = 0

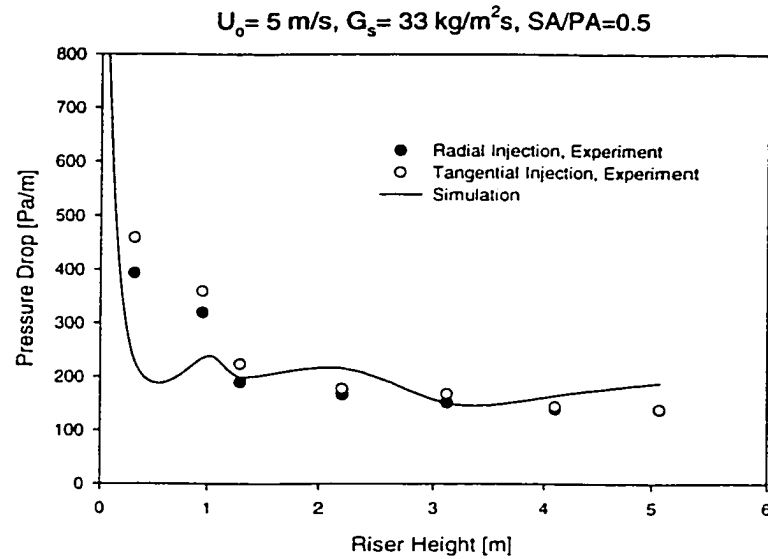


Figure 6.16. Riser pressure drop, simulation vs experiment, $U_o = 5$ m/s, $G_s = 33$ kg/m²s, SA/PA = 0.5

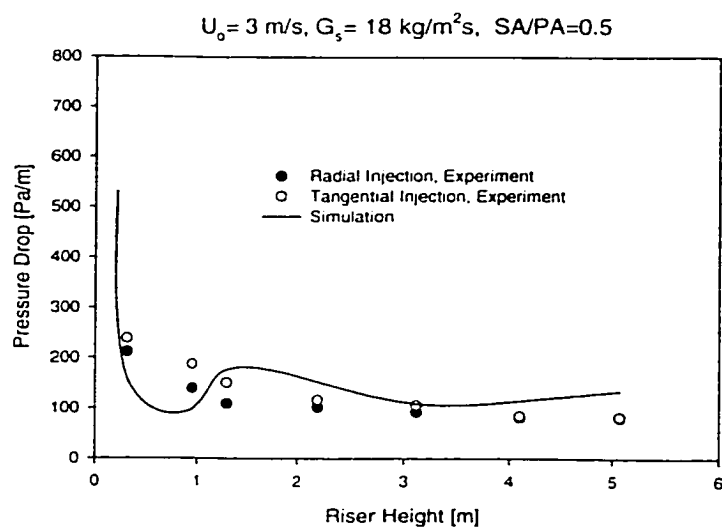


Figure 6.17. Riser pressure drop, simulation vs experiment, $U_o = 3 \text{ m/s}$, $G_s = 18 \text{ kg/m}^2\text{s}$, $SA/PA = 0.5$

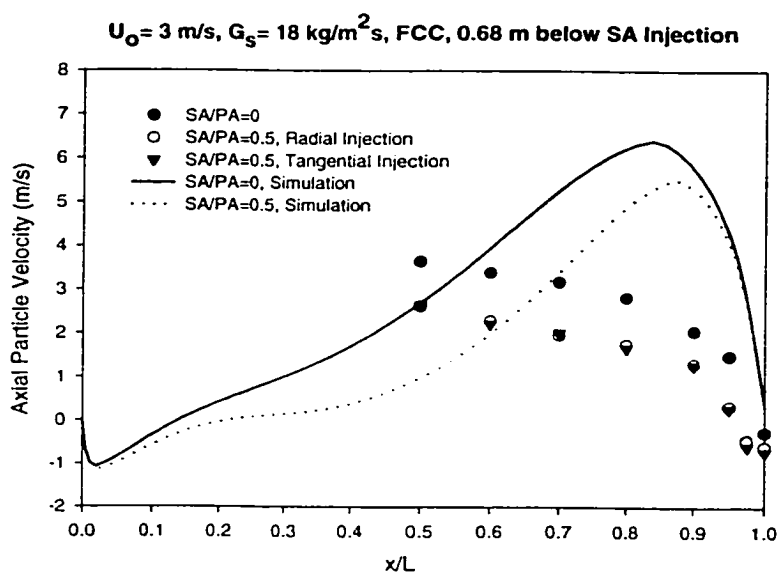


Figure 6.18. Axial Particle Velocity, Simulation vs Experiment, $U_o = 3 \text{ m/s}$, $G_s = 18 \text{ kg/m}^2\text{s}$, 0.52 m above the distributor plate.

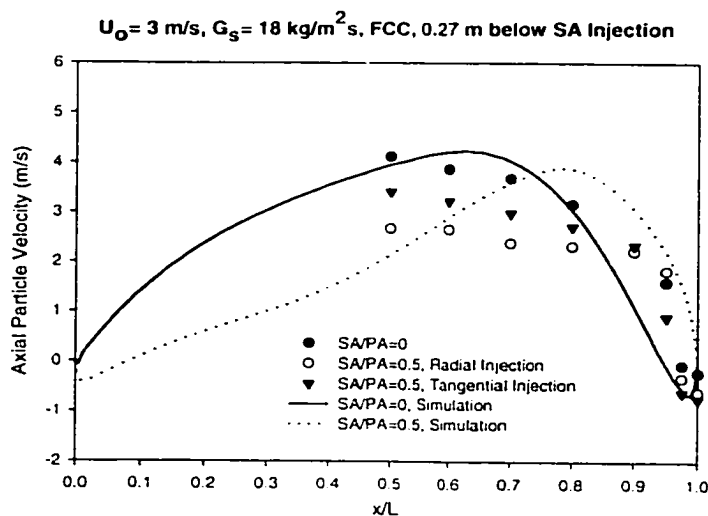


Figure 6.19. Axial Particle Velocity, Simulation vs Experiment, $U_o = 3 \text{ m/s}$, $G_s = 18 \text{ kg/m}^2\text{s}$, 0.93 m above the distributor plate.

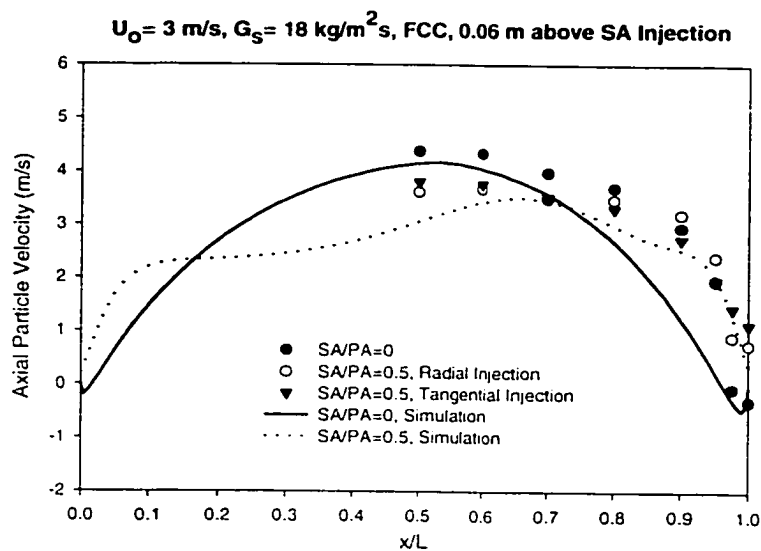


Figure 6.20. Axial Particle Velocity, Simulation vs Experiment, $U_o = 3 \text{ m/s}$, $G_s = 18 \text{ kg/m}^2\text{s}$, 1.26 m above the distributor plate.

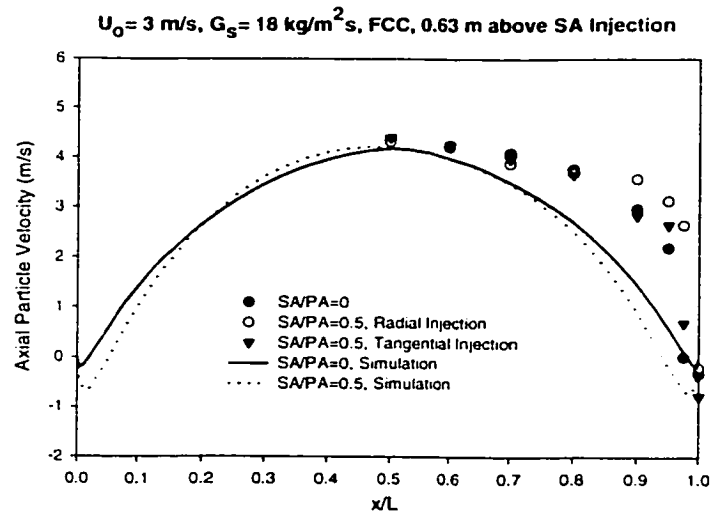


Figure 6.21. Axial Particle Velocity, Simulation vs Experiment, $U_0 = 3 \text{ m/s}$, $G_s = 18 \text{ kg/m}^2\text{s}$, 1.82 m above the distributor plate.

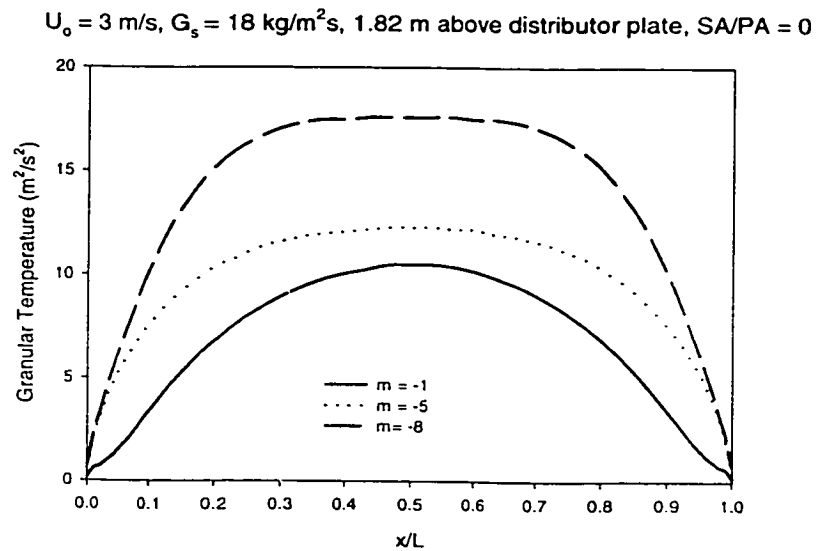


Figure 6.22. The effect of constant, m , defined in Equation 6.4 on the granular temperature, $U_0 = 3 \text{ m/s}$, $G_s = 18 \text{ kg/m}^2\text{s}$, SA/PA = 0.

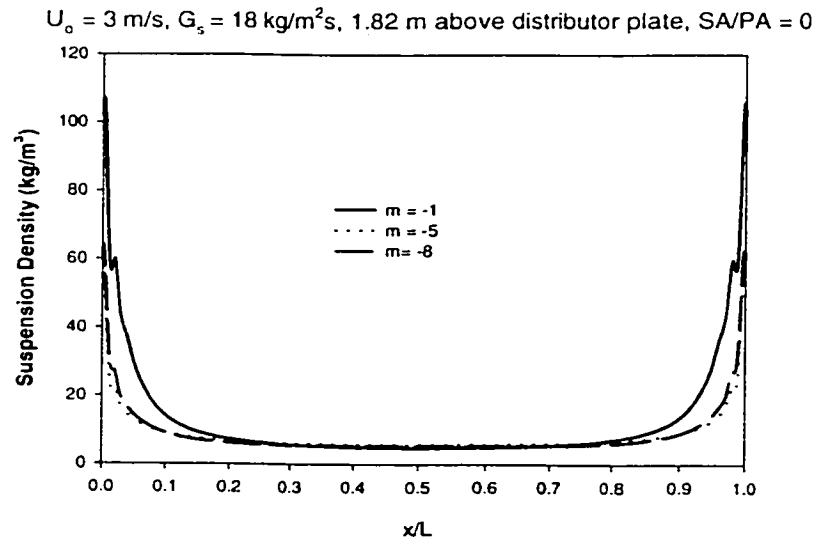


Figure 6.23. The effect of constant, m , defined in Equation 6.4 on the suspension density, $U_o = 3 \text{ m/s}$, $G_s = 18 \text{ kg/m}^2\text{s}$, SA/PA = 0.

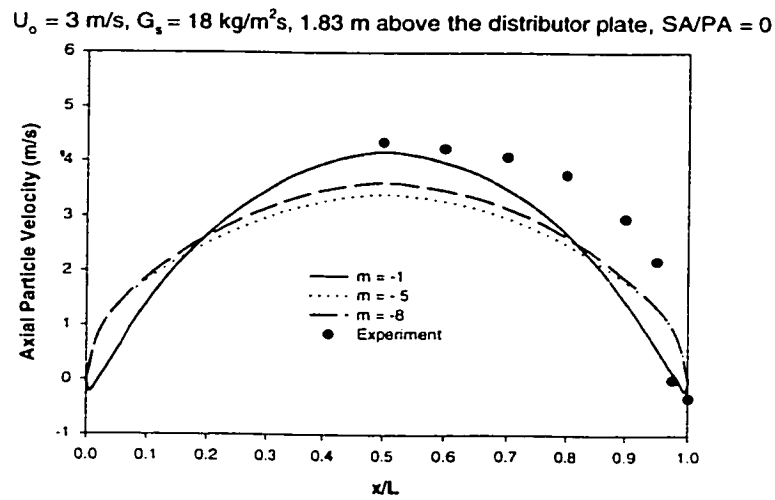


Figure 6.24. The effect of constant, m , defined in Equation 6.4 on the solids axial velocity, $U_o = 3 \text{ m/s}$, $G_s = 18 \text{ kg/m}^2\text{s}$, SA/PA = 0.

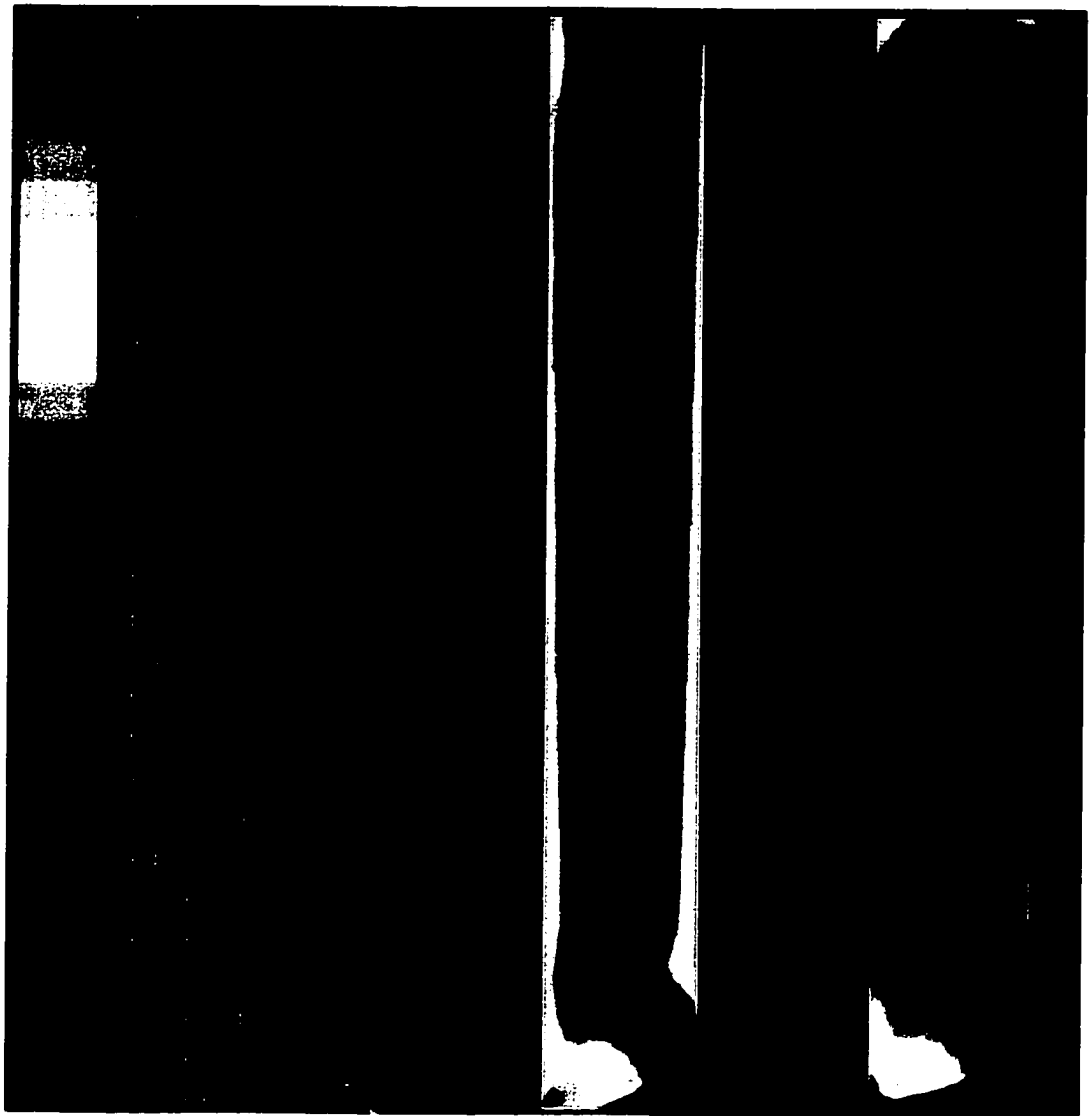
a) $e = 0.9$ b) $e = 1.0$

Figure 6.25. The effect of the particle-particle coefficient of restitution on the solids distribution in the riser, $U_o = 3$ m/s, $G_s = 18$ kg/m²s, SA/PA = 0 (colors: blue, $\alpha_s = 0$, red $\alpha_s = 0.4$)

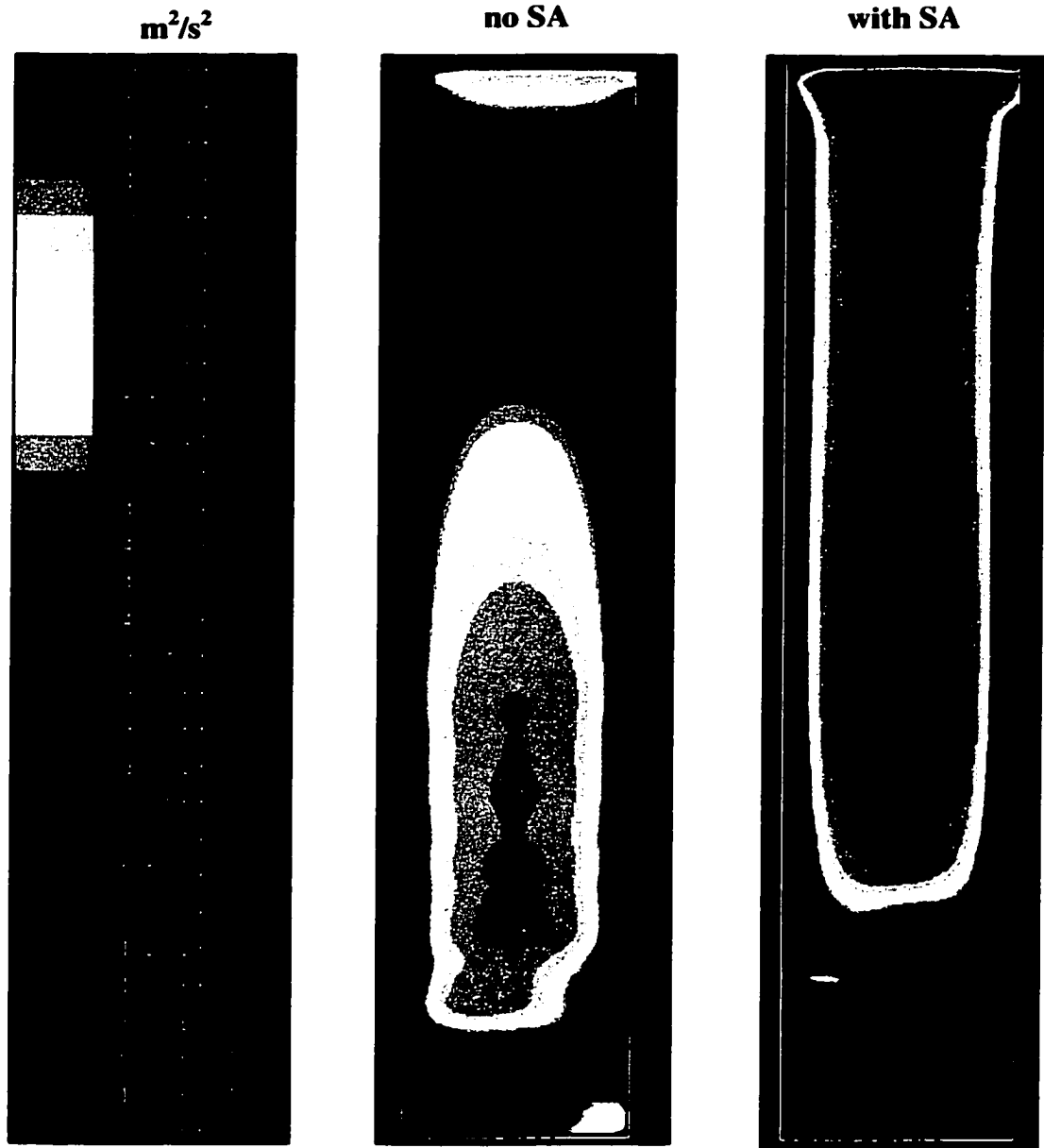


Figure 6.26. The effect of SA injection on granular temperature, $U_o = 3$ m/s, $G_s = 18$ kg/m²s, SA/PA = 0 and 0.5.

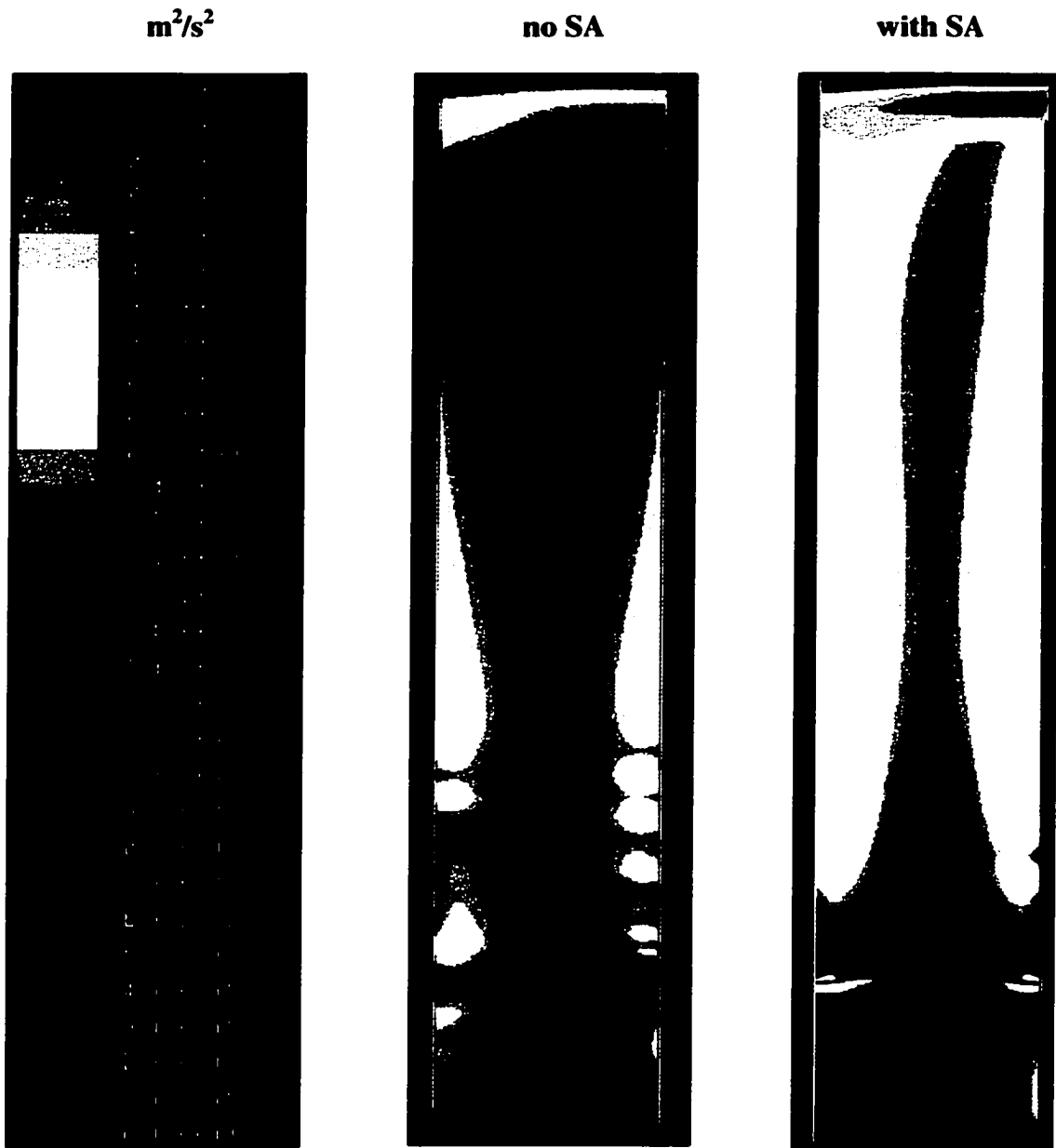


Figure 6. 27. The effect of SA injection on air turbulent kinetic energy, $U_o = 3 \text{ m/s}$, $G_s = 18 \text{ kg/m}^2\text{s}$, $SA/PA = 0$ and 0.5 .

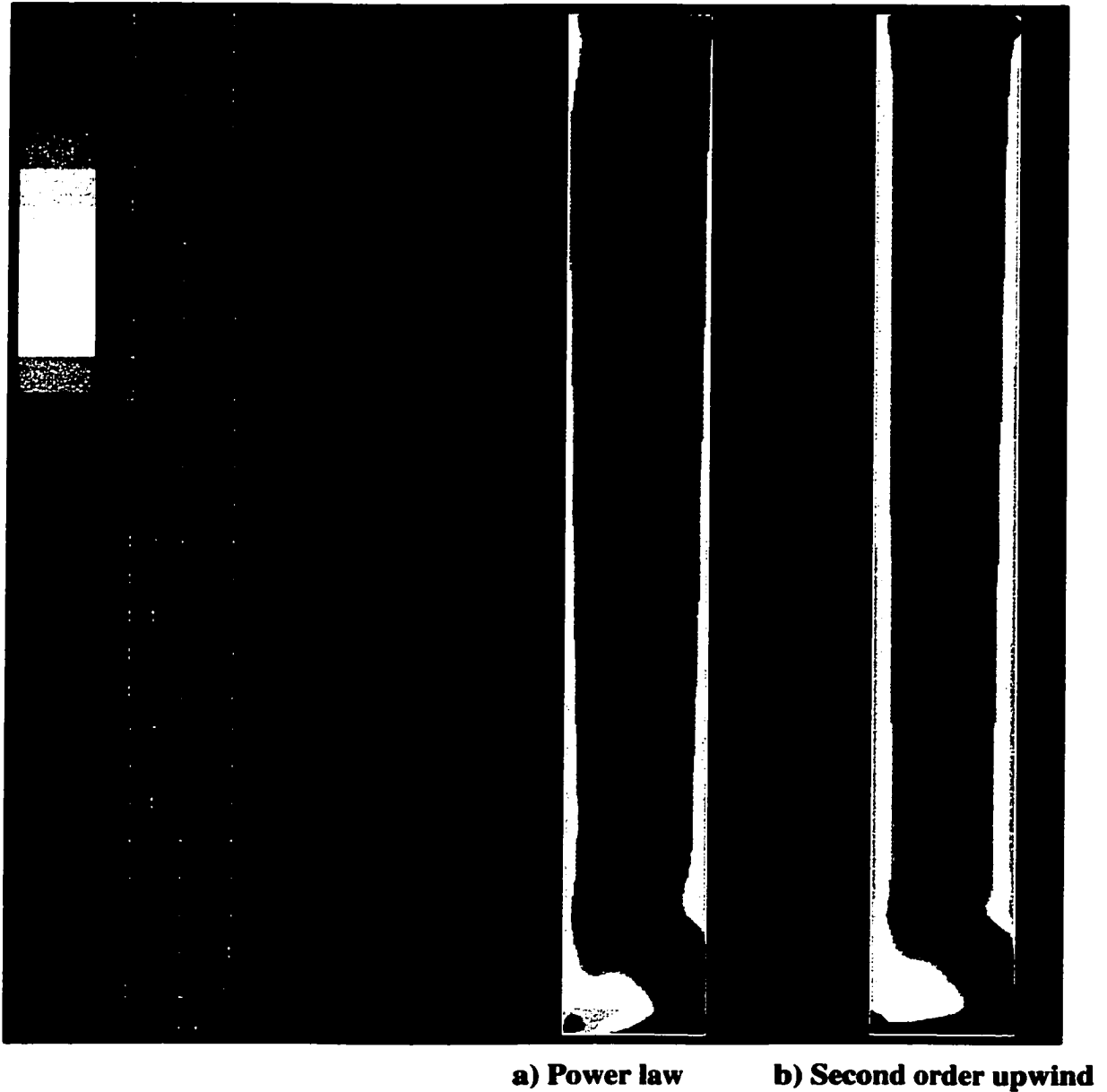


Figure 6.28. The effect of the discretization scheme on the solids distribution in the riser, $U_o = 3 \text{ m/s}$, $G_s = 18 \text{ kg/m}^2\text{s}$, $SA/PA = 0$ (colors: blue, $\alpha_s = 0$, red $\alpha_s = 0.4$).

4 Modeling of Mixing of SA with Rising Gas-Solid Suspension

This section closely follows the paper published in the proceedings of 7th Annual Conference of the Computational Fluid Dynamics Society of Canada (Koksal and Hamdullahpur, 1999).

The modeling of gas mixing in the context of two-fluid approach requires the solution of one extra scalar equation: species (tracer gas) transport equation given below.

$$\frac{\partial}{\partial t}(\rho_g Y_i) + \nabla \cdot (\rho_g \bar{U}_g Y_i) = \nabla \cdot (\Gamma_{eff} \nabla Y_i) \quad (6.6)$$

where Y_i is the mass fraction of the tracer gas (CO_2) and Γ_{eff} is the effective dispersion coefficient of CO_2 in air given by:

$$\Gamma_{eff} = \rho_g D_{CO_2} + \frac{\mu_{g,t}}{Sc} \quad (6.7)$$

D_{CO_2} is the binary molecular diffusion coefficient of CO_2 in air ($1.65 \times 10^{-5} \text{ m}^2/\text{s}$ at STP) and Sc is turbulent Schmidt number defined as:

$$Sc_t = \frac{\mu_{g,t}}{\rho_g D_t} \quad (6.8)$$

where D_t is the turbulent dispersion coefficient of CO_2 in air. As can be seen from Equation 6.7, for a constant Schmidt number, the total dispersion of the tracer gas depends on the turbulent eddy viscosity which in turn is a function of the gas phase turbulent kinetic energy (Equation 5.38, Chapter 5). Therefore, the key aspect is the determination of the gas phase turbulence under two-phase flow conditions.

In order to consider the effects of the particles on gas phase turbulence, the turbulence modulation model of Simonin and Viollet (1990) is utilized with the standard $k-\epsilon$ eddy viscosity turbulence model. The model of Simonin and Viollet (1990) is available as a

built-in model for the user in Fluent V4.5. The model adds two extra terms to the transport equations of turbulent kinetic energy and dissipation rate. The latter is based on Elgobashi and Abou-Arab (1983). The reader is referred to corresponding papers for the detailed derivation and explanation of the corresponding terms.

The simulations were carried out with the kinetic theory model of Sylamlal *et al.* (1993) The geometry of the grid was designed according to the dimensions of CFB pilot plant at Dalhousie University (7.6 m high, 0.23 m ID). The simulations were performed on a 2D Cartesian grid (50×40) for 10 seconds with sand particles ($\rho_s = 2650 \text{ kg/m}^3$, $d_p = 130 \text{ }\mu\text{m}$). The superficial gas velocity was kept constant at 5 m/s. Two different solid mass flux and SA/TA values were simulated; $G_s = 10 \text{ kg/m}^2\text{s}$ and $50 \text{ kg/m}^2\text{s}$, $SA/TA = 0.25$ and $SA/TA = 0.5$. Uniform, plug flow was assumed for both phases at the inlet with sand volume fraction being 0.02. The turbulent intensity of the air at both inlets were set as 5 %. Carbon dioxide, CO_2 , was used as a tracer gas and mixed with SA. The flow rate of CO_2 was set to be 1 % of the total flow rate in the simulations.

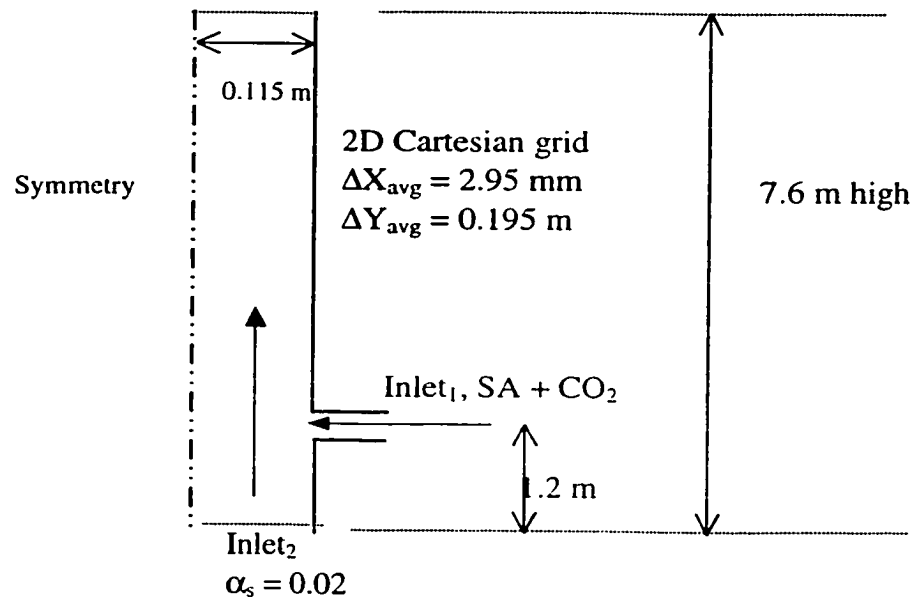


Figure 6.29. Grid geometry for SA mixing study

The tracer concentration in the following figures was non-dimensionalized by dividing it by the mean mixed concentration, C_o . In all of the simulations performed in this study, the coefficient of restitution was taken to be 1. Hence, particle collisions are assumed to be perfectly elastic. No slip boundary condition was applied for gas phase velocity whereas the solid phase was allowed to slip on the walls. The flux of the fluctuating kinetic energy of solid phase was set to be equal to zero at the wall. The inlet value of the granular temperature was taken to be same as the inlet velocity of the solid phase. At the near-wall region, standard wall function approach was used for gas phase turbulence. The particle phase turbulence was not considered.

Figure 6.30 shows the effects of solids loading on mixing of SA with gas-solid suspension for $SA/TA = 0.5$ at two different elevations above the SA injection port. As can be inferred from these two plots, mixing is retarded as the loading increases in the range of solids mass flux investigated. Thus, the quickest mixing along the riser is achieved in the case of empty pipe which complies with the experimental measurements presented in Chapter 4. Contrary to the experiments, the gas dispersion in the radial direction continues to decrease as the flux is increased to $50 \text{ kg/m}^2\text{s}$. In the experiments, the decreasing trend of the radial dispersion was found to diminish as the flux was increased to $25 \text{ kg/m}^2\text{s}$. The discrepancy can be due to the fact that the present formulation does not take the turbulence production in the wakes behind the particles which can also decrease the level of attenuation or even augment the gas phase turbulence in dense flow conditions.

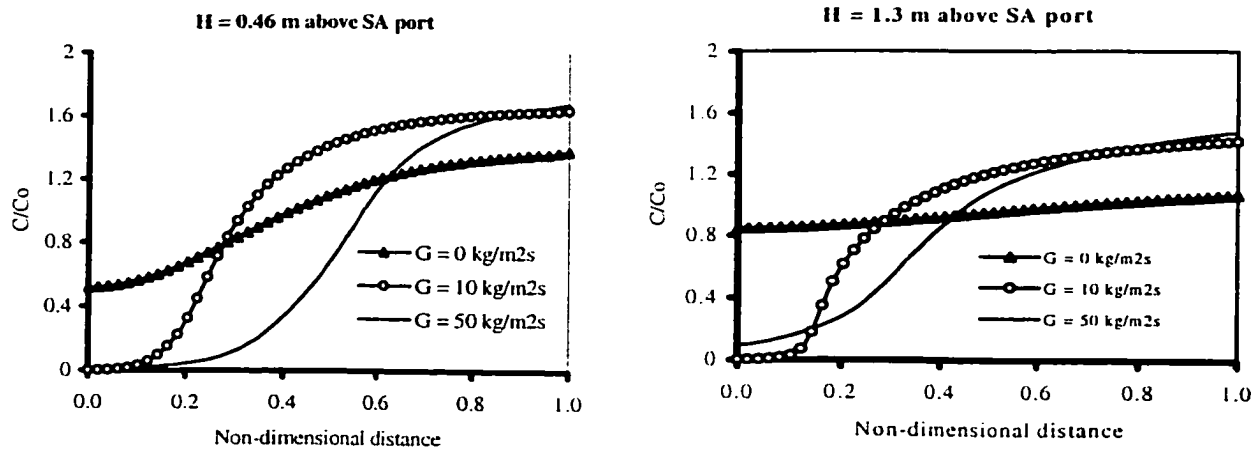


Figure 6.30. Non-dimensional tracer concentration for $SA/TA = 0.5$ (0.46 m and 1.3 above SA port)

Figure 6.31 presents the effects of SA/TA on mixing for $G = 10 \text{ kg/m}^2\text{s}$. The trends of the curves are consistent with the fact that increasing SA/TA increases the mixing quality. As momentum of the SA increases with increasing SA/TA , the gas can penetrate more through the gas-solid suspension in the lateral direction increasing mixing. Also, the shear induced by the SA jet generates turbulence increasing its kinetic energy which in turn increases the net turbulent dispersion of gas in the lateral direction as shown in Figure 6.32. The gas phase turbulent kinetic energy for SA injection case is predicted an order of magnitude larger than that for non-SA injection case just above SA injection port as can be seen in Figure 6.32. Both results are in qualitative agreement with the trends of the experimental results.

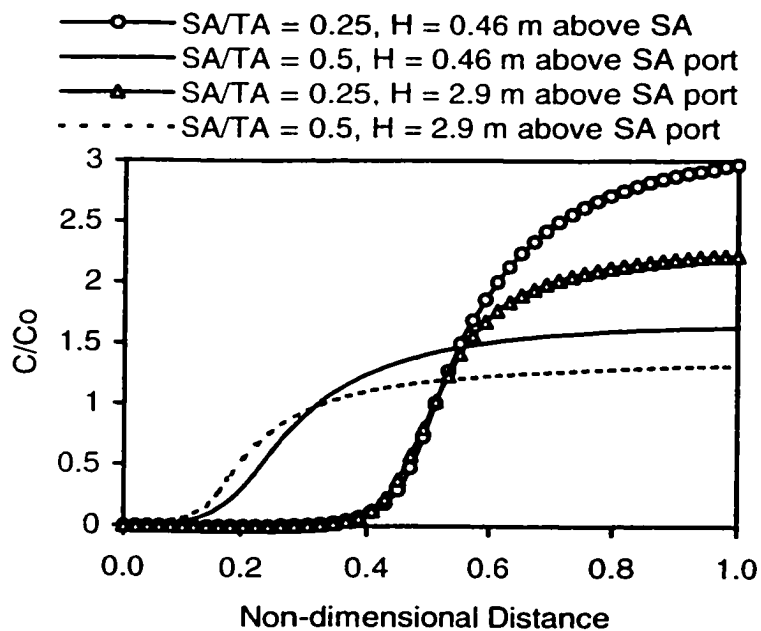


Figure 6.31. Effect of SA/TA on radial gas mixing ($G = 10 \text{ kg/m}^2\text{s}$)

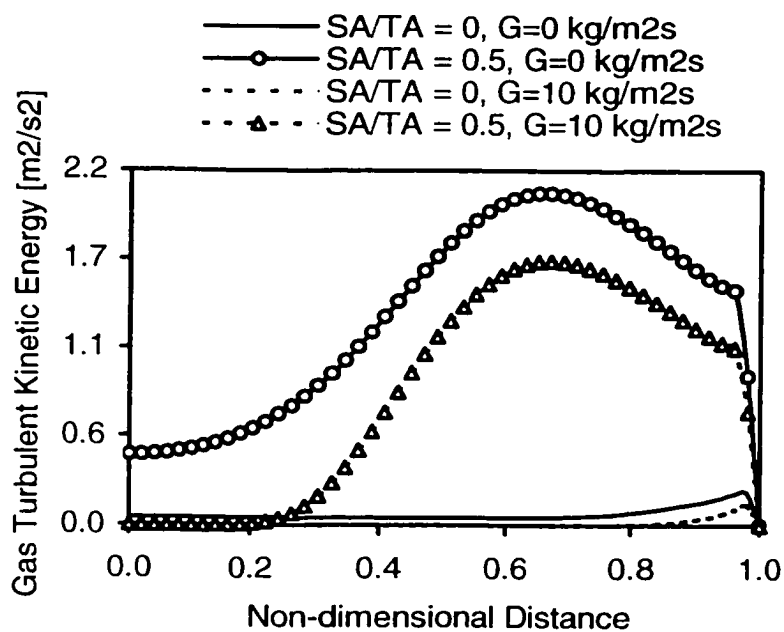


Figure 6.32. Effect of SA injection on gas phase turbulent kinetic energy.

5 Conclusions

In this chapter, the application of the two-fluid gas-solid flow model given in Chapter 5 is presented. The simulations are carried out using Fluent V4.5, Fluent Inc. The two-fluid model is first applied to the riser data of Miller and Gidaspow (1992). A good agreement is obtained between the computed and the experimental values of the solids axial velocity and the solids volume fraction. It is shown that the expected core annular behavior in the riser is obtained only when the transport equation for the solids fluctuating energy is time averaged and a two-equation eddy viscosity model for the particle phase is utilized. The computed profiles of the solids fluctuating energy, solids pressure and air turbulent kinetic energy are presented for the riser flow. The fluctuating energy of the solids is found to be larger than the air turbulent kinetic energy due to intense particle-particle collisions. The particle pressure and the effective particle viscosity in the riser are computed to be around 175 Pa and 0.18 Pa.sec, respectively.

Second, the two-fluid model presented in Chapter 5 is applied to the riser data of Ersoy (1998) to investigate the prediction capability of the model for SA injection conditions. It is shown that the model captures the most essential aspects of the riser flow with SA injection with a reasonable accuracy. The characteristics captured in the simulations which are similar to experimental measurements and observations can be summarized as:

- a) The increase in the solids volume fraction (suspension density) with SA injection below the SA injection ports,
- b) The accumulation of the solids around the center of the riser due to the momentum of the SA jets above the injection zone,
- c) The absence of the solids downflow near the wall above the SA injection ports,
- d) The increase in the air and solids fluctuating kinetic energies with SA injection above the SA injection ports which leads to higher gas dispersion coefficients as shown in Chapter 4.

Quantitatively, the measured and computed solids axial velocity and the pressure gradient in the riser agree well with each other away from the distributor plate. The predicted values of the axial solids velocity at the center of the riser and near the wall are found to be very close to the experimental values. The prediction capability of the model deteriorates at the bottom of the riser close to the solid inlet. However, this deterioration is mostly attributed to the 2-D approximation of the flow and the omitting the distributor plate in the simulations.

Finally, the mixing of SA with the rising gas-solid suspension is modeled in the context of the two-fluid model considering the turbulence modulation effects. The simulation results qualitatively agree with the results of the tracer gas measurements presented in Chapter 4.

Chapter 7

Overall Conclusions and Recommendations

1. Overall Conclusions

This study investigates the flow dynamics and gas mixing in CFB risers with SA injection. The experimental part of this study involves axial static pressure measurements to obtain information on the axial distribution of solids in the riser and tracer gas experiments for gas mixing using three different SA injector designs. On the numerical side, this study proposes a computational fluid dynamics (CFD) model that can be applied to CFB risers with SA injection.

The axial pressure measurements show that the SA injection significantly alters the axial solids distribution in the riser compared to the case without SA injection at the same superficial gas velocity and solids circulation rate. Especially with tangential SA injection the total solids hold up in the riser increases considerably compared to non-SA operation at the same conditions. Therefore, the tangential SA injector can be used as an effective tool to increase the internal circulation of solids in a CFB combustor especially when burning coal with high carbon content for which the combustion efficiency can be a critical parameter.

The radial gas mixing experiments show that for CFB combustor operating conditions, the radial gas mixing in the riser is poor and the mixing quality deteriorates sharply with solids loading. However, the experimental results also indicate that SA injection can be a promising tool to enhance the observed poor radial gas mixing in CFB risers. Especially, the radial SA injector increases gas dispersion almost an order of magnitude compared to non-SA operation.

Based on the results of the experiments, it is suggested that in order to increase the gas dispersion in CFB combustors, the SA ports should be designed to cover the whole width of the riser. Also, the gas velocity through each port should be adjusted such that the corresponding SA jet can penetrate into the riser to strike its counterpart coming from the opposite wall.

The mixing mechanisms of the SA with the rising gas solid suspension are found to be different especially for tangential and radial injectors. With the radial injector, the mixing is achieved at a shorter axial distance compared to other modes of injections. When the tangential injector is utilized, on the other hand, a more gradual mixing with the rising gas-solid suspension is obtained.

In the numerical part of this study, a 2-D Eulerian-Eulerian gas-solid flow model is used to simulate the gas-solid flow in the riser section of a CFB with SA injection using Fluent V4.5. The simulation results show that the model can satisfactorily simulate the riser experimental data with SA injection and can capture some of the characteristic aspects of the SA injection successfully. With sufficient computational resources, the model can be used to design and optimize the SA injector ports in CFB combustors.

2. Recommendations for Future Work

The recommendations for future work are as follows:

- a) Since the application of SA injection is more related to CFB combustors, it is important to carry out experiments in a model riser which is geometrically more

similar to an actual CFB combustor with low height/diameter ratio. Apparently, the flow mechanisms induced by the SA jets are local and apparatus dependent.

- b) This study has focused on the effects of the SA on gas mixing above the SA injection ports. The gas mixing phenomena with SA injection in the bottom dense region below the SA injection ports should also be investigated.
- c) The co-current and counter current SA injector designs can also have interesting effects on gas-solids hydrodynamics.
- d) The effect of the SA on solids mixing is an important aspect of SA injection problem and has not yet been investigated.
- e) The existing CFB riser needs some modifications in order to provide a more stable operation over a wide variety of solids circulation rates. The radial gas mixing experiments are difficult to perform and meaningful averages are not obtained unless the fluctuation in the solids circulation rate is minimized.
- f) The SA injection is actually a 3-D optimization problem based on the design requirements and is very suitable to be investigated by means of computational fluid dynamics. Once the sufficient computational resources are available, a 3-D gas-solid flow simulation can produce better predictions.

Literature Cited

- Abrahamsen, A.R., Geldart, D., Powder Technology, vol. 26, p. 35, 1980.
- Adams, C.K., "Gas Mixing in Fast Fluidized Bed", in Circulating Fluidized Bed Technology II, ed., Basu, P., Large, J.F., Pergamon Press, Toronto, pp. 299-306, 1988.
- Amos, G., Rhodes, M.J., Mineo, H., "Gas Mixing in Gas-Solid Risers", Chemical Engineering Science, vol. 48, No. 5, pp. 943-949, 1993.
- Anderson, T.B., Jackson, R., "A Fluid Mechanical Description of Fluidized Beds", Ind. Eng. Chem. Fund., vol. 6, 527, 1967.
- Arastoopour, H., Pakdel, P., Adewumi, M., "Hydrodynamic Analysis of Dilute Gas-Solid Flow in a Vertical Pipe", Powder Technology, vol. 62, pp. 163-170, 1990.
- Arena, U., "Gas Mixing" in Circulating Fluidized Beds, eds., Grace, J.R., Avidan, A.A., Knowlton, T.M., chp. 3, pp. 86-118, Chapman & Hall, London, 1997.
- Arena, U., Cammarato, L., Massimilla, L., Pirozzi, D., Circulating Fluidized Bed Technology II, ed., Basu, P., Large, J.F., Pergamon Press, Toronto, pp. 223-230, 1988.
- Arena, U., Marzocchella, A., Massimilla, L., Malandrino, A., "Hydrodynamics of Circulating Fluidized Beds with Risers of Different Shape and Size", Powder Technology, 70, 237-247, 1992.
- Bader, R., Findlay, J., Knowlton, T.M., "Gas/Solid Flow Patterns in a 30.5-cm-Diameter Circulating Fluidized Bed", in Circulating Fluidized Bed Technology II, ed., Basu, P., Large, J.F., Pergamon Press, Toronto, pp. 123-137, 1988.
- Bai, D., Yi, J., Jin, Y., Yu, Z., "Residence Time Distributions of Gas and Solids in a Circulating Fluidized Bed", in Fluidization VII, eds., Potter, O.E., Nicklin, D.J., Engineering Foundation, pp. 195-202, 1992.
- Balzer, G., Boelle, A., Simonin, O., "Eulerian Gas-Solid Flow Modeling of Dense Fluidized Bed", Fluidization VIII, Engineering Foundation, Tours, pp. 1125-1134, 1995.
- Balzer, G., Simonin, O., "Extension of Eulerian Gas-Solid Flow Modelling to Dense Fluidized Bed", EDF, Report HE-44/93.13, 1993.
- Baskakov, A.P., Maskaev, V.K., Usoltsev, A.G., Ivanov, I.V., Zubkov, V.A., "Influence of Secondary Air on Convective Heat Transfer Between Walls of Riser and Circulating Fluidized Bed (CFB)", in Preprints of CFB IV, ed., Avidan, A.A., pp. 324-327, 1993.
- Basu, P., Fraser, S.A., Circulating Fluidized Bed Bolier. Design and Operation, Butterworths-Heinemann-Reed Publishing Inc., Stoneham, MA., p. 182, 1991.

- Benyahia, S., Arastoopour, H., Knowlton, T., "Prediction of Solid and Gas Behavior in a Riser Using a Computational Multiphase Approach", Fluidization IX, Eds., Fan, L.S., Knowlton, T., 1998.
- Berruti, F., Chaouki, J., Pugsley, T.S., Patience, G.S., "Hydrodynamics of Circulating Fluidized Bed Risers: A Review", *The Canadian Journal of Chemical Engineering*, vol. 73, p. 579-602, 1995.
- Berruti, F., Kalogerakis, N., *Can. J. Chem. Eng.*, vol. 67., p. 1010, 1989.
- Bi, T.H., Ellis, N., Abba, I.A., Grace, J.R., "A state-of-the-art review of gas-solid turbulent fluidization", *Chem. Eng. Sci.*, vol. 55., pp. 4789-4825, 2000.
- Bischoff, K.B., Levenspiel, O., "Fluid Dispersion-Generalization and Comparison of Mathematical Models-I", *Chemical Engineering Science*, vol. 17, pp. 245-255, 1962.
- Boemer, A., Qi, H., Renz, U., "Modeling of Bubble Eruption in a Fluidized Bed with the Eulerian Approach", 28th IEA-FBC Meeting, Kitakyushu, Japan, 1994.
- Boemer, A., Qi, H., Renz, U., Vasquez, S., Boysan, F., "Eulerian Computation of Fluidized Bed Hydrodynamics- A Comparison of Physical Models", *Int. Conf. FBC, ASME*, vol. 2, p. 775-787, 1995.
- Brereton, C., "Combustion Performance" in Circulating Fluidized Beds, eds., Grace, J.R., Avidan, A.A., Knowlton, T.M., chp. 10, pp. 369-416, Chapman & Hall, London, 1997.
- Brereton, C., Grace, J.R., "End Effects in Circulating Fluidized Bed Hydrodynamics", in Preprints of CFB IV, ed., Avidan, A.A., pp. 169-174, 1993.
- Brereton, C.M.H., Grace, J.R., Yu, J., "Axial Gas Mixing in a Circulating Fluidized Bed", in Circulating Fluidized Bed Technology II, ed., Basu, P., Large, J.F., Pergamon Press, Toronto, pp. 307-314, 1988.
- Brodkey, R.S., The Phenomena of Fluid Motions, Addison-Wesley, 1967.
- Buyevich, Yu., "Statistical Hydromechanics of Disperse Particles, Part 2: Solution of the Kinetic Equation for Suspended Particles", *J. Fluid Mechanics*, vol. 52, pp. 345-355, 1972.
- Campbell, C.S., Wang, D.G., "Particle Pressure in Gas-Fluidized Beds", *J. Fluid Mechanics*, vol. 227, pp. 571-573, 1991.
- Cankurt, N.T., Yerushalmi, J., "Gas Backmixing in High Velocity Fluidized Beds", in Fluidization, eds., Davidson, J.F., Keairns, D.L., Cambridge University Press, Cambridge, 1978.
- Chapman, S., Cowling, T.G., The Mathematical Theory of Non-Uniform Gases, 2nd Edition, Cambridge University Press, 1961.

- Cho, J.Y., Namkung, W., Kim, S.D., Park, S., Kim, P.T., "Effect of Secondary Air Injection On Bed-To-Wall Heat Transfer in A Circulating Fluidized Bed", *Journal of Chemical Engineering of Japan*, vol. 29, no. 1, 1996.
- Cho, Y.J., Namkung, W., Kim, S.D., Park, S., "Effect of Secondary Air Injection on Axial Solid Holdup Distribution in a Circulating Fluidized Bed", *J. Chem. Eng. Japan*, 27, no.2, 158-164, 1994.
- Couturier, M., Doucette, B., Stevens, D., Poolpol, S., Razbin, V., "Temperature, Gas Concentration and Solid Mass Flux Profiles Within a Large Circulating Fluidized Bed Combustor", in Proceedings of 11th Int. Conference on Fluidized Bed Combustion, vol. 1, pp. 107-114, 1991.
- Crowe, C., Chung, J.N., Troutt, T.R., "Particle Dispersion By Organized Turbulent Structures", chp. 18, in Particulate Two-Phase Flow, pp. 626-669, ed., Roco, M.C., Butterworth-Heinemann, 1993.
- Crowe, C.T., "Review-Numerical Models for Dilute Gas-Particle Flows", *Journal of Fluids Engineering*, vol. 104, p. 297-303, 1982.
- Crowe, C.T., Troutt, T.R., Chung, J.N., "Numerical Models For Two-Phase Turbulent Flows", *Annu. Rev. Fluid. Mech.*, vol. 28, p. 11-33, 1996.
- Dasgupta, S., Jackson, R., Sundaresan, S., "Turbulent Gas-Particle Flow in Vertical Risers", *AIChE J*, vol. 40, p. 215, 1994.
- Davies, J.T., Turbulence Phenomena. Academic Press, New York, 1972.
- Deutsch, E., Simonin, O., "Large Eddy Simulation Applied to the Motion of Particles in Stationary Homogeneous Turbulence", *Turbulence Modification in Multiphase Flows*, ASME FED, vol. 110, pp. 34-42, 1991.
- Di Felice, R., " The Voidage Function for Fluid-Particle Interaction Systems", *Int. J. Multiphase Flow*, vol. 20, pp. 153-159, 1994.
- Diego, L.F., Londono, C.A., Wang, S.X., Gibbs, B.M., "Influence of Operating Parameters on NO_x and N₂O axial profiles in a Circulating Fluidized Bed Combustor", *Fuel*, vol. 75, pp. 971-978, 1996.
- Ding, J., Gidaspow, D., "A Bubbling Fluidization Model Using Kinetic Theory of Granular Flow", *AIChE J*, vol. 36, no. 4, p. 523-538, 1990.
- Drew, "Mathematical Modeling of Two-Phase Flow", *Ann. Rev. Fluid Mechanics*, vol. 15, pp. 261-291, 1983.
- Drew, D.A., Lahey, R.T., in Particulate Two-Phase Flow, Ch.16, p. 509-566, Butterworth-Heinemann, Boston, 1993.

- Dry, R.J., White, C.C., "Gas Residence Time in a High-Velocity Circulating Fluidized Bed of FCC Catalyst", *Powder Technology*, vol. 58, pp. 17-23, 1989.
- Eaton, J.K., Fessler, J.R., "Preferential Concentration of Particles by Turbulence", *Int. J. Multiphase Flow*, vol. 20, p. 169-209, 1994.
- Einstein, A., "Eine Neue Bestimmung der Molekuldimensionen", *Ann. Phys. Vol. 19*, pp. 289-306, 1906.
- Elgihidy, S.M., Chen, R.Y., Comparin, R.A., "Deposition of Suspensions in the Entrance of a Channel", *J. Fluid. Eng., ASME*, pp. 365, 1977.
- Elgobashi, S., "On Predicting Particle-Laden Turbulent Flows", *Applied Scientific Research*, vol. 52, p. 309-329, 1994.
- Elgobashi, S.E., Abou-Arab, T.W., "A Two-Equation Turbulence Model for Two-Phase Flows", *Physics of Fluids*, vol. 26(4), p. 931-938, 1983.
- Enwald, H., Peirano, E., Almstedt, A.E., "Eulerian Two-Phase Flow Theory Applied to Fluidization", *Int. J. Multiphase Flow*, vol. 22, Suppl., p. 21-66, 1996.
- Ersoy, E.L., Militzer, J., Hamdullahpur, F., "Effect of Secondary Air Injection On the Hydrodynamics of Circulating Fluidized Beds", in Proceedings of 14th Conference on FBC, vol. 2, p. 1247, 1997.
- Ersoy, L.E., "Effect of Secondary Air Injection on the Hydrodynamics of CFBs", PhD Thesis, Dalhousie University, 1998.
- Ersoy, L.E., Koksai, M., Hamdullahpur, F., "Effects of Mode of Secondary Air Injection on Gas and Solid Velocity Profiles in a CFB Riser", *Circulating Fluidized Bed Technology VI*, ed., Werther, J., pp. 417-422, DECHAMA, Germany, 1999.
- Fan, J., Sun, P., Ma, Y., Cen, K., "On a Eulerian and Lagrangian Combined Model in Dense Particle-Laden Riser Flow", *The Canadian Journal of Chemical Engineering*, vol. 77, pp. 1113-1120, vol. 77, 1999.
- Flint, D.L., Kada, H., Hanratty, T.J., "Point Source Turbulent Diffusion in a Pipe", vol. 6., no.2., 325-331, 1960.
- Fluent 4.5 Update Manual, Fluent Inc, 1998.
- Fluent User's Guide, vol. 4, Chapter 19, Theory, Fluent Incorporated, 1996.
- Frankel, N.A., Acrivos, A., "On the Viscosity of a Concentrated Suspension of Solid Spheres", *Chem. Eng. Sci.* vol. 22, pp. 847-853, 1967.
- Gayan, P., Diego, L.F., Adanez, D.J., "Radial Gas Mixing in a Fast Fluidized Bed", *Powder Technology*, vol. 94, pp. 163-171, 1997.

- Geldart, D., "Particle Entrainment and Carryover" in Gas Fluidization Technology, Wiley and Sons, 1986.
- Gibilaro, L.G., Di Felice, R., Waldram, S.P., "Generalized friction Factor and Drag Coefficient Correlations for Fluid-Particle Interactions", Chem. Eng. Sci., vol. 40, pp. 1817-1823.
- Gidaspow, D., Bezbaruah, R., B., Ding, J., "Hydrodynamics of Circulating Fluidized Beds: Kinetic Theory Approach", eds., Potter, O.E., Nicklin, D.J., in Fluidization VII, Engineering Foundation, p. 75-82, 1992.
- Gidaspow, D., Huilin, L., "Collisional Viscosity of FCC Particles in a CFB", AIChE J, vol. 42, no. 9, p. 2503-2510, 1996.
- Gidaspow, D., Multiphase Flow and Fluidization, Academic Press, 1994.
- Gore, R.A., Crowe, C.T., "Effect of Particle Size on Modulating Turbulent Intensity", Int. J. Multiphase Flow, vol. 15, no. 2, p. 279-285, 1989.
- Grace, J.R., Bi, H.T., "Fundamentals of Circulating Fluidized Beds", in Circulating Fluidized Beds, eds., Grace, J.R., Avidan, A.A., Knowlton, T.M., chp. 1, Chapman & Hall, London, 1997.
- Grace, J.R., in Handbook of Multiphase Systems, ed. Hestroni, G., p 8-1, Hemisphere, 1982.
- Grace, J.R., Issangya, A.S., Bai, D., Bi, H., Zhu, J., "Situating the High-Density Circulating Fluidized Bed", AIChE J, vol. 45, pp. 2108-2116, 1999.
- Guilin, Y., Zhe, H., Lianzhong, Z., "Radial Gas Dispersion in a Fast Fluidized Bed", in Fluidization IV, eds., Kunii, D., Toei, R., Engineering Foundation, pp. 145-152, 1984.
- Haider, A., Levenspiel, O., Powder Technology, vol. 58, p.63, 1989.
- Harris, B.J., Davidson, J.F., Circulating Fluidized Bed Technology IV, AIChE, New York, p. 32-39, 1994.
- Hestroni, G., "Particles-Turbulence Interaction", Int. J. Multiphase Flow, vol. 15, No. 5, pp. 735-746, 1989.
- Hinze, J.C., Turbulence - An introduction to its Mechanism and Theory, McGraw-Hill, 1975.
- Hoomans, B P B; Kuipers, J A M; Briels, W J; Swaaij, W P M van, "Discrete particle simulation of bubble and slug formation in a two-dimensional gas-fluidised bed: A hard-sphere approach", Chemical Engineering Science, v.51, n.1, pp.99, 1996.

- Horio, M., "Hydrodynamics", in Circulating Fluidized Beds, eds., Grace, J.R., Avidan, A.A., Knowlton, T.M., chp. 2, Chapman & Hall, London, 1997.
- Horio, M., Ishii, H., Nishimuro, M., "On the Nature of Turbulent and Fast Fluidized Beds", *Powder technology*, vol. 70, p. 229-236, 1992.
- Hrenya, C.M., Sinclair, J.L., "Effects of Particle-Phase Turbulence in Gas-Solid Flows", *AIChE J*, vol. 43, no. 4., pp. 853-869, 1997.
- Hui, K., Haff, P.K., Ungar, J.E., Jackson, R., "Boundary Conditions for High Shear Grain Flows", *J. Fluid Mechanics*, vol. 145, pp. 223-233, 1984.
- Hutchinson, P., Hewitt, G.F., Dukler, A.E., *Chemical Engineering Science*, vol. 26, pp. 419, 1971.
- Ilias, S., Ying, S., Mathur, G.D., Govind, R., "Studies on a Swirling Circulating Fluidized Bed", in CFB Technology II, ed., Basu, P., Large, J.F., Pergamon Press, Toronto, pp. 537-546, 1988.
- Ishii, M., Zuber, N., "Drag Coefficient and Relative Velocity in Bubbly, Droplet or Particulate Flows", *AIChE J*, vol. 25, pp. 107-126, 1979.
- Jenkins, J.T., Savage, S.B., "A Theory for Rapid Flow of Identical, Smooth, Nearly Elastic Spherical Particles", *J. Fluid Mechanics*, vol. 130, p. 187, 1983.
- Johnson, P.C., Jackson, R., "Frictional-Collisional Constitutive Relations of Granular Materials with Application to Plane Shearing", *Journal of Fluid Mechanics*, vol. 176, p. 67, 1987.
- Jovanovic, G.N., Catipovic, N.M., Fritzgerald, T.J., Levenspiel, O., "The Mixing of Tracer Gas in Fluidized Bed of Large Particles", *Fluidization III*, 325-332, 1980.
- Kang, Y., Song, P.S., Yun, S.J., Jeong, Y.Y., Kim, S.D., "Effects of Secondary Air Injection on Gas-Solid Flow Behavior in Circulating Fluidized Beds", *Chem. Eng. Comm.*, vol. 177, pp. 31-47, 2000.
- Klinkenberg, A., Krajenbrink, H.J., Lauwerier, A.H., *Ind. Eng. Chem.*, vol. 6, 1202, 1953.
- Koksal, M., "Eulerian-Eulerian (Two-Fluid) Modeling of Circulating Fluidized Beds", Directed Study Report, Dalhousie University, .1998.
- Koksal, M., Ersoy, L.E., Hamdullahpur, F., "2-D Hydrodynamic Modeling of a Circulating Fluidized Bed Riser with Secondary Air Injection-A Two-Fluid Approach", 3rd Int. Conf. On Multiphase Flows, Lyon, France, 1998.

- Koksal, M., Hamdullahpur, F., "Modeling of Mixing of Secondary Air with Gas-Solid Suspension in CFB Risers", Proceedings of 7th Annual Conference of the Computational Fluid Dynamics Society of Canada, pp. 7.27-7.33, Halifax, Canada, 1999.
- Kruse, M., Schoenfelder, H., Werther, J., "A Two-Dimensional Model for Gas Mixing in the Upper Dilute Zone of a Circulating Fluidized Bed ", The Canadian Journal of Chemical Engineering , vol. 73, pp. 620-634,1995.
- Kuipers, J.A.M., A Two-Fluid Micro Balance Model of Fluidized Beds, P.hD. Thesis, University of Twente, 1990.
- Kulick, J.D., Fessler, J.R., Eaton, J.K., "Particle Response and Turbulence Modification in Fully Developed Channel Flow", J. Fluid Mechanics, vol. 227, pp. 109-134, 1994.
- Kunii, D., Levenspiel, O., "Circulating Fluidized Bed-Reactors", Chemical Engineering Science, vol. 52, No. 15, p. 2471-2482, 1997.
- Kunii, D., Levenspiel, O., "Effect of Exit Geometry on the Vertical Distribution of Solids in Circulating Fluidized Beds. Part I: Solution of Fundamental Equations; Part II: Analysis of Reported Data and Prediction", Powder Technology, 84, 83-90, (1995).
- Kunii, D., Levenspiel, O., Fluidization Engineering, Butterworth-Heinemann, 1991.
- Lauder, B.E., Spalding, D.B., Lectures in Mathematical Models of Turbulence, Academic Press, London, 1972.
- Le, H., Moin, P., Kim, J., "Direct Numerical Simulation of Turbulent Flow over a Backward Facing Step", J. Fluid Mechanics, vol. 330, pp. 349-374, 1997.
- Leckner, B., "Fluidized Bed Combustion: Mixing and Pollutant Limitation", Progress in Energy and Combustion Science, vol. 24, pp. 31-61, 1998.
- Levenspiel. O., Chemical Reaction Engineering, Wiley&Sons, 2nd Edition, 1964.
- Li, J., Weinstein, H., "An Experimental Comparison of Gas Backmixing in Fluidized Beds Across the Regime Spectrum", Chemical Engineering Science, vol. 44, No. 8, pp. 1697-1705, 1989.
- Li, Y., Kwauk, M., "The Dynamics of Fast Fluidization", Fluidization, eds., Grace, J.R., Matsen, J.M., pp. 537-544, Plenum Press, New York, 1980.
- Li, Y., Wu, P., "A Study on Axial Gas Mixing in a Fast Fluidized Bed", in Circulating Fluidized Bed Technology III, eds., Basu, P., Horio, M., Hasatani, M., Pergamon Press, Toronto, pp. 581-586, 1991.

- Lim, K.S., Zhu, J.X., Grace, J.R., "Hydrodynamics of Gas-Solid Fluidization", *Int. J. Multiphase Flow*, vol. 21, Suppl., pp. 141-193, 1995.
- Liu, J., Grace, J.R., Bi, H., Morikawa, H., Zhu, J., "Gas dispersion in fast fluidization and dense suspension upflow", *Chem. Eng. Sci.*, vol. 54, pp. 5441-5449, 1999.
- Louge, M., Chang, H., "Pressure and Voidage Gradients in Vertical Gas-Solid Risers", *Powder Technology*, vol. 60, p. 197-201, 1990.
- Louge, M., in Circulating Fluidized Beds, eds., Grace, J.R., Avidan, A.A., Knowlton, T.M., chp. 1, Chapman & Hall, London, 1997.
- Louge, M.Y., Mastorakos, E., Jenkins, J.T., "The Role of Particle Collisions in Pneumatic Transport", *J. Fluid Mechanics*, vol. 231, pp. 345-359, 1991.
- Lun, C.K.K., Savage, S.B., Jeffrey, D.J., Chepuruiy, N., "Kinetic Theories for Granular Flow: Inelastic Particles in Couette Flow and Slightly Inelastic Particles in a General Flow-Field", *J. Fluid Mechanics*, vol. 140, p. 223-256, 1984.
- Lyngfelt, A., Amand, L.E., Leckner, B., "Reversed air staging-a method for reduction of N₂O emissions from fluidized bed combustion of coal", *Fuel*, vol. 77, pp. 953-959, 1998.
- Lyngfelt, A; Leckner, B., "SO₂ capture and N₂O reduction in a circulating fluidized-bed boiler: influence of temperature and air staging", *Fuel*, vol. 73, no. 11, pp. 1553-1652, 1993.
- Martin, M.P., Turlier, P., Bernard, J.R., Wild, G., "Gas and Solid Behavior in Cracking Circulating Fluidized Beds", *Powder Technology*, vol. 70, p. 249-258, 1992.
- Marzocchella, A., Arena, U., "Hydrodynamics of a Circulating Fluidized Bed Operated with Different Secondary Air Injection Devices", *Powder Technology*, vol. 87, p. 185-191, 1996a.
- Marzocchella, A., Arena, U., "Mixing of a Lateral Gas-Stream in a Two-dimensional Riser of a Circulating Fluidized Bed", *The Canadian Journal of Chemical Engineering*, vol. 74, pp. 195-202, 1996b.
- Mastellone, M.L., Arena, U., "The Influence of Particle Size and Density on the Radial Gas Mixing in the Dilute Region of the Circulating Fluidized Bed", *The Canadian Journal of Chemical Engineering*, vol. 77, 231-237, 1999.
- Miller, A., Gidaspow, D., "Dense, Vertical Gas-Solid Flow in a Pipe", *AIChE J.*, vol., 38(11), 1801-1815, (1992).
- Murray, J.D., "On the Mathematics of Fluidization, Part 1, Fundamental Equations and Wave Propagation", *J. Fluid Mechanics*, vol. 21, 465-493, 1965.

- Nadeau, P., Berk, D., Munz, R., "Mixing in a Cross-Flow-Impinging Jet Reactor", *AIChE J*, vol. 47, no. 3, pp. 536-544, 2001.
- Namkung, W., Kim, S.D., "Radial Gas Mixing in a Circulating Fluidized Bed", *Powder Technology*, vol. 113, 23-29, 2000.
- Namkung, W., Kim, S.D., "Gas Backmixing in a Circulating Fluidized Bed", *Powder Technology*, vol. 99, pp. 70-78, 1998.
- Naumann, E.B., Buffham, B.A., Mixing in Continuous Flow Systems, John Wiley and Sons, pp. 112, 1983.
- Neri, A., Gidaspow, D., "Riser Hydrodynamics: Simulations Using Kinetic Theory", *AIChE J*, vol. 46, no. 1, pp. 52-67, 2000.
- Nieuwland, J.J., Annaland, M.S., Kuipers, J.A.M., Swaaij, W.P.M., "Hydrodynamic Modeling of Gas/Particle Flows in Riser Reactors", *AIChE J*, vol. 42, no. 6, p. 1569-1582, 1996a.
- Nieuwland, J.J., Meijer, R., Kuipers, J.A.M., Swaaij, W.P.M., "Measurements of Solids Concentration and Axial Solids Velocity in Gas-Solid Two-Phase Flows", *Powder Technology*, vol. 87, p. 127-139, 1996b.
- O'Brien, T.J., Sylamlal, M., "Particle Cluster Effects in the Numerical Simulation of a Circulating Fluidized Bed", 4th int. Conference on CFB, Preprint Volume, pp. 430-435, 1993.
- Oesterle, B., "Une etude de l'influence des forces transversales agissant sur les particules dans les ecoulements gaz-solide", *Powder Technology*, vol. 79, pp. 81-93, 1994.
- Palchonok, G.I., Johnsson, F., Leckner, B., "Estimate of Turbulence Effects in CFB Boilers", in Preprints of Circulating Fluidized Bed Technology V, part.MSD7, pp. 1-6, 1996.
- Patankar, S.V., *Numerical Heat Transfer and Fluid Flow*, Hemisphere Publishing, Washington, DC, 1980.
- Patience, G.S., Chaouki, J., "Gas Phase Hydrodynamics in the Riser of a Circulating Fluidized Bed", *Chemical Engineering Science*, vol. 48, No. 18, pp. 3195-3205, 1993.
- Pecora, A.A.B., Goldstein, L.J., "A Fluid Dynamics Study of a Circulating Fluidized Bed with Secondary Air Injection", *Proceedings of ASME Heat Transfer Division*, HTD-334, vol. 3, pp. 287- 292, 1996.
- Peirano, E., Leckner, B., "Fundamentals of Turbulent Gas-Solid Flows Applied to Circulating Fluidized Bed Combustion", *Progress in Energy and Combustion Science*, vol. 24, pp. 259-296, 1998.

- Peirano, E., Palchonok, G.I., Johnsson, F., Leckner, B., "Estimates of Turbulence Mechanisms in Circulating Fluidized Bed Combustors" Powder Technology, vol. 96, pp. 90-105, 1998.
- Peric, M., Kessler, R., Scheurerer, G., "Comparison of Finite-Volume Numerical Methods with Staggered and Collocated Grids", Computational Fluids, V. 16(4), pp. 389-403, 1988.
- Pita, J., Sundaresan, S., "Gas-Solid Flow in Vertical Tubes", AIChE J, vol. 37, no.7, pp.1009-1018, 1991.
- Pugsley, T., Lapointe, D., Hirschberg, B., Werther, J., "Exit Effects in Circulating Fluidized Bed Risers", Can. J. Chem. Eng., 75, 1001-1010, 1997.
- Pugsley, T.S., Berruti., "A Predictive Hydrodynamic Model For Circulating Fluidized Bed Risers", Powder Technology, vol. 89, p. 57-69, 1996.
- Rage, T., Studies of Tracer Dispersion and Fluid Flow in Porous Media, Ph.D. Thesis, Department of Physics, University of Oslo, 1996.
<http://www.uio.no/~trage/thesis/thesis/thesis.html>, 2001.
- Reeks, M.W., "On a Kinetic Equation for the Transport of Particles in Turbulent Flows", Physics of Fluids A3, pp. 446-456, 1991.
- Rhodes, M., "What is Turbulent Fluidization?", Powder Technology, vol. 88, pp. 3-14, 1996.
- Rhodes, M.J., Powder Technology, vol. 60., p. 27., 1990.
- Roscoe, "The Viscosity of Suspensions of Rigid Spheres", Brit. J. Appl. Phys., vol. 3, pp. 267-269, 1952.
- Samuelsberg, A., Hjertager, B.H., "An Experimental and Numerical Study of Flow Patterns in a Circulating Fluidized Bed Reactor", Int. J. Multiphase Flow, vol. 22, no. 3, p. 575-591, 1996a.
- Samuelsberg, A., Hjertager, B.H., "Computational Modeling of Gas/Particle Flow in a Riser", AIChE J, vol. 42, no. 6, p. 1536-1546, 1996b.
- Savage, S.B., "Granular Flows at High Shear Rates", Theory of Dispersed Multiphase Flow, ed., Meyer, R.E., pp. 339-358, Academic Press, 1983.
- Savage, S.B., Jeffrey, D.J., "The Stress Tensor in a Granular Flow at High Shear Rates", J. Fluid Mechanics, vol. 110, pp. 255-272, pp. 1981.
- Schlichting, H., Boundary Layer Theory, McGraw Hill, 1996.

- Schlichting, H., Boundary Layer Theory, McGraw-Hill, 7th Edition, 1979.
- Schreck, S., Kleis, S.J., "Modification of Grid-Generated Turbulence by Solid Particles", *J. Fluid Mechanics*, vol. 249, pp. 665-688, 1993.
- Schugerl, K., "Experimental Comparison of Mixing Processes in Two- And Three-Phase Fluidized Beds", in Proceedings of Int. Symposium on Fluidization, ed., Drinkeburg, A.A.H., pp. 782-796, Netherlands University Press, Amsterdam, 1967.
- Schuh, M.J., Schuler, C.A., Humphrey, J.A.C., "Numerical Calculation of Particle-Laden Gas Flows Past Tubes", *AIChE J*, vol. 35, p. 466-480, 1989.
- Senior, R.C., Grace, J.R., "Integrated Particle Collision and Turbulent Diffusion Model For Dilute Gas-Solid Suspensions", *Powder Technology*, vol. 96, p. 48-78, 1998.
- Sherwood, T.K., Pigford, R.L., Wilke, C.R., Mass Transfer, McGraw-Hill, 1975.
- Shirolkar, J.S., Coimbra, C.F.M., McQuay, M.Q., "Fundamental Aspects of Modeling Turbulent Particle Dispersion in Dilute Flows", *Prog. Energy Combust. Sci.*, vol. 22, p. 363-399, 1996.
- Simonin, O., Viollet, P.L., "Prediction of an Oxygen Droplet Pulverization in a Compressible Subsonic Coflowing Hydrogen Flow", *ASME FED*, vol. 91, pp. 65-82, 1990.
- Sinclair, J.L., Jackson, R., "Gas-Particle Flow in a Vertical Pipe with Particle-Particle Interactions", *AIChE Journal*, vol. 35, no. 9, pp.1473-1486, 1989.
- Sterneus, J., Johnsson, F., Leckner, B., "Gas Mixing in Circulating Fluidised-Bed Risers", *Chem. Eng. Science*, vol. 55, pp. 129-148, 2000.
- Sterneus, J., Johnsson, F., Leckner, B., Palchonok, G.I., "Gas and Solids Flow in Circulating Beds – Discussion on Turbulence", *Chem. Eng. Science*, vol. 54, pp. 5377-5382, 1999.
- Stock, D.E., "Particle Dispersion in Flowing Gases-1994 Freeman Scholar Lecture", *Journal of Fluids Engineering*, vol. 118, p. 4-17, 1996.
- Svensson, A., Johnsson, F., Leckner, B., "Bottom Bed Regimes in a Circulating Fluidized Bed Boiler", *International Journal of Multiphase Flow*, vol. 22, no. 6, pp. 1187-1204, 1996.
- Syamlal, M., Rogers, W., O'Brian, T.J., "MFIx Documentation, Theory Guide", technical note DOE/METC-94/10004, 1993.
- Syamlal, M., "High Order Discretization Methods for the Numerical Simulation of Fluidized Beds", *AIChE Annual Meeting*, 1997.

- Sylamlal, M., O'Brien, T.J., "Computer Simulation of Bubbles in a Fluidized Bed", *AIChE Symp. Ser.*, vol. 85, pp. 22-31, 1989.
- Talukdar, J., "Coal Combustion in a Circulating Fluidized Bed", PhD Thesis, Technical University of Nova Scotia, 1996.
- Taylor, G.I., "Diffusion by Continuous Movements", *Proc. Lond. Math. Soc.*, A 20, pp. 196-211, 1921.
- Taylor, G.I., in The Scientific Papers of Sir Geoffrey Ingram Taylor, ed., Batchelor, F.R.S., vol. 2., Cambridge University Press, 1960.
- Tennekes, H., Lumley, J.L., *A First Course in Turbulence*, MIT Press, 1972.
- Thermax Babcock&Wilcox Limited, "<http://www.tbwindia.com/cfb.htm>", 2001.
- Towle, W.L., Sherwood, T.K., *Ind. Eng. Chem.*, vol. 31, 457, 1939.
- Tsuji, Y., "Activities in Discrete Particle Simulation in Japan", *Powder Technology*, vol. 113, no.3, pp. 278-287, 2001.
- Tsuji, Y., Morikawa, Y., "LDV Measurements of an Air-Solid Two-Phase Flow in a Horizontal Pipe", *J. Fluid Mechanics*, vol. 120, pp. 385-409, 1982.
- Tsuji, Y., Morikawa, Y., Shiomi, H., "LDV Measurements of an Air-Solid Two-Phase Flow in a Vertical Pipe", *J. Fluid Mechanics*, vol. 139, pp. 417-434, 1984.
- Tsuo, Y., Gidaspow, D., "Computation of Flow Patterns in Circulating Fluidized Beds", *AIChE J*, vol. 36, no. 6, p. 885-896, 1990
- van Deemter, J.J., "Mixing Patterns in Large-Scale Fluidized Beds", in Fluidization, eds., Grace, J.R. and Matsen, J.M., Plenum Press, New York, 1980.
- van Deemter, J.J., "Mixing" in Fluidization, eds., Davidson, J.F., Clift, R., Harrison, D., 2nd Edition, Academic Press, 1985.
- van Zoonen, D., "Measurements of Diffusional Phenomena and Velocity Profiles in a Vertical Riser", in Proc. Symp. on the Interaction Between Fluids and Particles, *Instn. Chem. Engrs.*, London, pp. 64-71, 1962.
- Wang, X.S., Gibbs, B.M., "Hydrodynamics of a Circulating Fluidized Bed with Secondary Air Injection", in Circulating Fluidized Bed Technology III, ed., Basu, P., Horio, M., Hasatani, M., Pergamon Press, Toronto, pp. 225-230, 1991
- Weinell, C.E., Dam-Johansen, K., Johnson, E.J., "Single Particle Behavior in Circulating Fluidized Beds", *Powder Technology*, vol.92, p.241-252, 1997.

- Weinstein, H., Li, J., "An Evaluation of the Actual Density in the Acceleration Section of Vertical Risers", *Powder Technology*, vol. 57, p. 77-79, 1989.
- Weinstein, H., Li, J., Badlamudi, E., Feindt, H.J., Graff, R.A., "Gas Backmixing of Fluidized Beds in Different Regimes and Different Regions", in *Fluidization VI*, eds., Grace, J.R., Shemilt, L.W., Bergougnou, M., Engineering Foundation, pp. 57-64, 1989.
- Weinstein, H., Shao, M., Wasserzug, L., "Radial Solid Density Variation in a Fast Fluidized Bed", *AIChE Symp. Ser.*, vol. 117, 1984.
- Wen, C.Y., Yu, Y.H., "Mechanics of Fluidization", *Chem. Eng. Prog. Symp. Series*, vol. 62, p. 100-111, 1966.
- Werther, J., "Fluid Mechanics of Large-Scale CFB Units", *Circulating Fluidized Bed Technology IV*, Ed., Avidan, A.A., pp. 1-14, AIChE, New York, 1994.
- Werther, J., Hartge, E.U., Kruse, M., "Radial Gas Mixing in the Upper Dilute Core of a Circulating Fluidized Bed", *Powder Technology*, vol. 70, p. 293-301, 1992a.
- Werther, J., Hartge, E.U., Kruse, M., Nowak, W., "Radial Gas Mixing in Core Zone of a Pilot Scale CFB", in *Circulating Fluidized Bed Technology III*, ed., Basu, P., Horio, M., Hasatani, M., Pergamon Press, Toronto, pp. 593-598, 1991.
- Werther, J., Hartge, E.U., Kruse, M., "Gas Mixing and Interphase Mass Transfer in the Circulating Fluidized Bed", in *Fluidization VII*, eds., Potter, O.E., Nicklin, D.J., Engineering Foundation, pp. 257-264, 1992b.
- Werther, J., Hirschberg, B., "Factors Affecting Segregation in Circulating Fluidized-Bed Riser", *AIChE J*, vol. 44, no. 1, pp. 25-34, 1998.
- Wilcox, D., *Turbulence Modeling For CFD*, DCW Industries, 1998.
- Yates, J., Simons, S.J.R., "Experimental Methods in Fluidization Research", *Int. J. Multiphase Flow*, vol. 20, Suppl., p. 297-330, 1994.
- Yerushalmi, J., "High Velocity Fluidized Beds", in *Gas Fluidization Technology*, chp. 7, ed., Geldart, D., pp. 155-196, 1986.
- Yerushalmi, J., Turner, D.H., Squires, A.M., "The Fast Fluidized Bed", *Ind. Eng. Chem. Proc. Des. Dev.*, 15, 47-53, 1976.
- Yokuda, E., "Particle Dispersion in Particle Generated Turbulence", M.S Thesis, Washington State University, 1990.
- Yudine, M.I., "Physical Considerations on Heavy Particle Diffusion", *Adv. Geophys.* Vol. 6, pp. 185-191, 1959.

- Zheng, Q., Wei, X., Fei, L., "Experimental Study on Radial Gas Dispersion and Its Enhancement in Circulating Fluidized Beds", in Fluidization VII, eds., Potter, O.E., Nicklin, D.J., Engineering Foundation, pp. 285-293, 1992.
- Zhou, J., Grace, J.R., Brereton, C.H.M., Lim, C.J., "Influence of Wall Roughness on the Hydrodynamics in a Circulating Fluidized Bed", *AIChE J.*, 42, no.4, 1153-1156, 1996.
- Zhu, J.X., Bi, H.T., "Development of CFB and High Density Circulating Fluidized Beds", in Preprints of CFB IV, ed., Avidan, A.A., pp. 565-570, 1993.

Appendices

Appendix A

Gas-Solid Fluidization Regimes

Fluidization is the operation by which solid particles show fluidlike properties through suspension in a gas or liquid (Kunii and Levenspiel, 1991). Under the fluidized state, the gravitational force on granular particles is offset by the fluid drag on them. The fluidized beds have enhanced mixing, uniform temperature distribution and higher contact efficiency when compared to other conventional reactors.

Figure A.1 shows the fluidization regimes with increasing superficial gas velocity in fluidized beds (Grace and Bi, 1997). As the operational velocity is gradually increased in a bed filled with granular solids, the bed passes from the packed bed state to the fluidized state, once, the minimum fluidization velocity is exceeded. The *minimum fluidization velocity*, U_{mf} , is defined as the lowest gas velocity at which all the particles are suspended by gas. The onset of bubbling is indicated by the *minimum bubbling velocity*, U_{mb} , the gas velocity at which the bubbles first appear in the bed. For beds of coarse particles, the minimum fluidization and the minimum bubbling velocities are usually close to each other whereas for the beds of fine particles a homogeneous bubble-free fluidization is observed between the minimum fluidization and minimum bubbling velocities.

When the minimum bubbling velocity is exceeded, gas bubbles form above the distributor plate and they grow as they rise towards the surface of the bed mainly due to coalescence. The top surface of the bed is well defined with bubbles breaking through periodically. The bubble size and speed increases with increasing superficial gas velocity.

With further increase in the gas velocity, the size of the bubbles becomes even bigger

covering the cross section of the bed, causing a *slugging regime*. The top section of the bed rises and collapses periodically with a reasonable regular frequency.

A continued increase in the velocity may eventually show a change in the pattern in the bed expansion. At this stage, the bubble phase loses its identity, due to rapid coalescence and break up. This results in violently active and highly expanded bed. Particles are thrown into the freeboard above the bed. The bed surface is not very clear. Such beds are said to be operated in *turbulent regime*. The transition from bubbling/slugging regime to turbulent regime is gradual and spans a range of gas velocities which depend on the properties of gas and solids, also on equipment scale (Yerushalmi, 1986). Yerushalmi and his co-workers, measuring the pressure fluctuations, were the first to characterize the transition to turbulent fluidization by two velocities, U_c and U_k (Yerushalmi, 1986). They proposed that the former marks the onset of the transition with a peak in the amplitude of the pressure fluctuations and the latter one shows the end of the transition with a leveling off in the amplitude of the pressure fluctuations. There is now a general agreement on U_c , however, U_k , is the subject of continuing debate and discussions (Rhodes, 1996).

The turbulent regime extends to the so-called *transport velocity*, U_{tr} . As the transport velocity is approached there is a sharp increase in the rate of particle carryover, and in the absence of solids recycle, the bed would empty rapidly. Beyond the transport velocity, particles fed to the bottom of the column or vessel traverse it in fully entrained transport flow, and the concentration or density of the resulting suspension depends not only on the velocity of the gas but also on the flow rate of solids. If the solids are fed to the column to its bottom via external cyclones and a standpipe, then it is possible to maintain in the column a relatively large solids concentration typical of the *fast fluidization regime*. The fast bed condition is also marked by aggregation of the particles in clusters and strands which break apart and reform in rapid succession, extensive back-mixing of solids, and slip velocities that are in order of magnitude greater than the terminal velocities of the individual particles.

The transition from fast fluidization to *pneumatic transport regime* is marked by the

disappearance of a dense phase region of relatively high density and large amplitude pressure fluctuations at the bottom of the riser. In this regime, there is no axial variation of solids concentration except in the bottom acceleration section. However, some particle strands may still be identified near the wall (Grace, 1997).

Recently, new experimental evidences have shown the presence of a new flow regime occurring at high solids mass flux values ($G_s > 250 \text{ kg.m}^2\text{s}$) and high superficial gas velocities (Grace *et al.*, 1999). This new flow regime is named as *dense suspension upflow* (DSU) by Grace *et al.* (1999). In this new flow regime, the solids no longer flow downward near the wall but they move upward and a core-annular structure does not exist. Clearly, more research is needed in this area.

In the context of the description of the gas-solid fluidization regimes, in a circulating fluidized bed several regimes can co-exist together, simultaneously. For instance, the bottom dense region of industrial CFB combustors are usually in bubbling regime in contrast to laboratory scale circulating fluidized beds whose bottom parts operate mostly in turbulent regime (Svennsonn *et al.* 1996; Leckner, 1988) whereas the riser part is in fast fluidization or pneumatic transport regimes. Kunii and Levenspiel (1991) define the circulating fluidized bed as a fluid bed which has a steady recirculation of solids through a solid circulation device. This broad definition is consistent with many experimental observations reported in literature and accepted in this thesis.

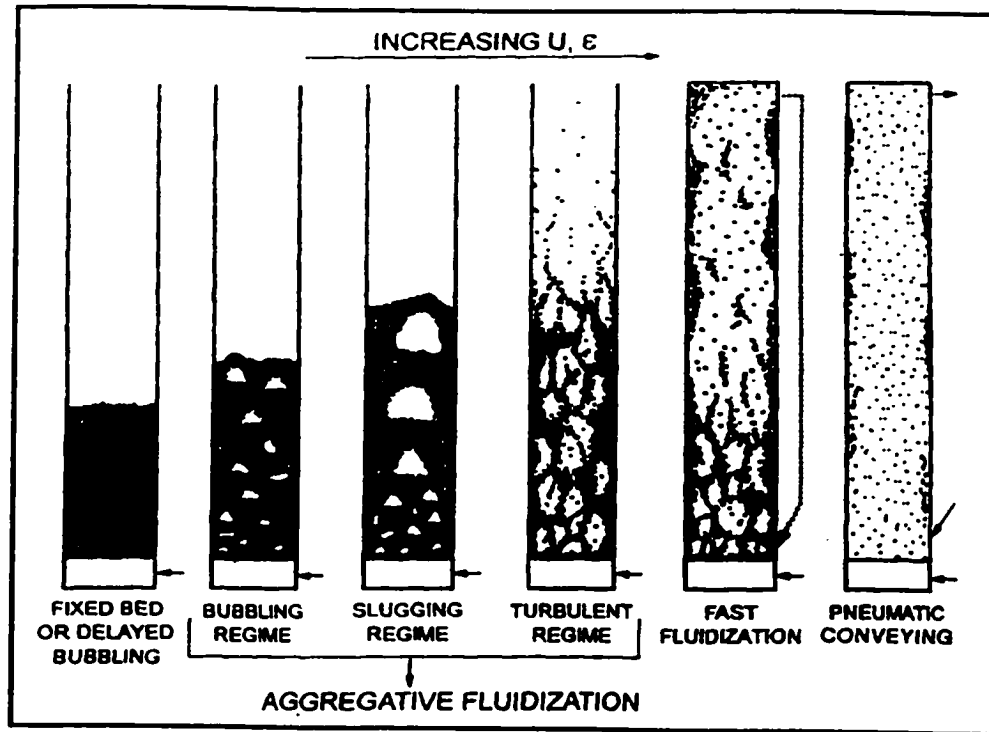


Figure A1. Gas-Solid Fluidization Regimes (Grace and Bi, 1997)

Appendix B

Properties of the Bed Material Used in the Experiments

If a powder contains a range of sizes which can be divided into narrow size fractions with mass fractions x_i of size $d_{sv,i}$, it can be shown that the surface/volume mean size is (Abrahamsen and Geldart, 1980):

$$d_{sv} = \frac{1}{\sum_{\text{all}} \left(\frac{x_i}{d_{sv,i}} \right)} \quad (\text{B.1})$$

The mean sieve diameter, d_p , which can be found using a standard sieve analysis based on equation (B.1), is equal to the surface/volume diameter if the particles are perfectly spherical. For near spherical particles such as the quartz sand used in the experiments, the following correlation was proposed by Abrahamsen and Geldart (1980):

$$d_{sv} = 0.871d_p \quad (\text{B.2})$$

In the experiments, OO grade Nova Scotia sand was used. Table B.1 shows the sieve analysis of the sampled silica sand. The mean sieve diameter of OO grade Nova Scotia sand was found to be 251 μm .

Table B.1. Size analysis of OO grade Nova Scotia sand used in the experiments.

Range (μm)	Sample Weight (g)	Weight fraction, x_i	$d_{p,i}$	$x_i/d_{p,i}$
1000-500	14.9	0.031	0.750	0.041
500-250	232.2	0.482	0.375	1.285
250-150	200.4	0.416	0.200	2.080
150-106	32.4	0.067	0.128	0.525
106-75	1.8	0.004	0.091	0.042
75-45	0.09	0.000	0.060	0.003
45-0	0.07	0.000	0.023	0.006
	$\Sigma = 481.8$			$\Sigma (x_i/d_{p,i}) = 3.98$ $d_p = 251 \mu\text{m}$

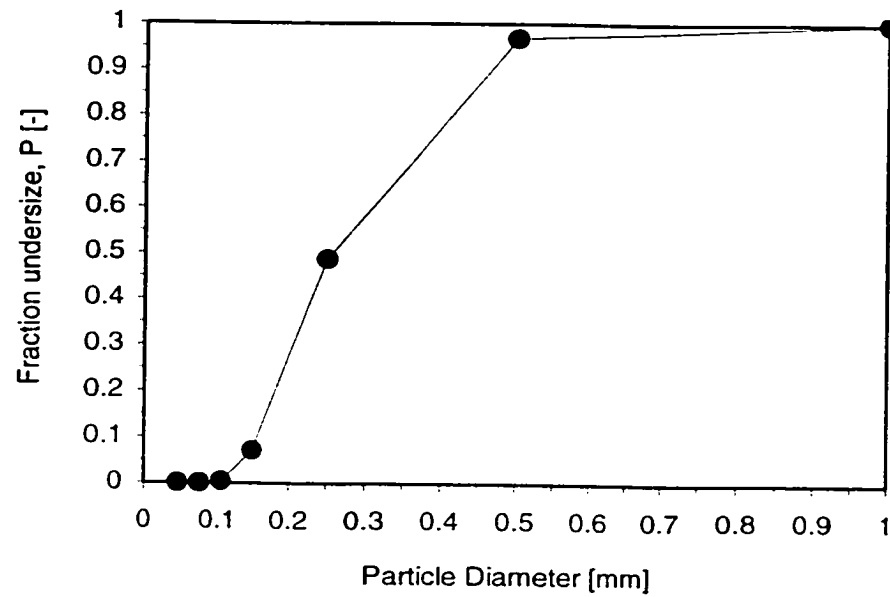


Figure B.1. Particle size distribution of OO grade Nova Scotia sand.

Table B.2 summarizes the values of some important parameters related with the particles used in the experiments.

Table B.2. Properties of the particles used in the experiments

Silica Sand (00 Grade)	
Geldart's classification	B
Mean sieve diameter, μm	251
Mean surface/volume diameter, μm	219
Particle density, kg/m^3	2664
Bulk density, kg/m^3	1498
Terminal velocity, m/s	1.4
Minimum fluidization velocity, m/s	0.05
Archimede's number	1016

In Table B.2, the single particle terminal velocity was calculated with the method as described in Haider and Levenspiel (1989). The minimum fluidization velocity was estimated using a correlation proposed by Grace (1982). All the correlations used are based on the surface/volume mean diameter.

Appendix C

Calibration of the Pressure Transducers and Flow Meters

Two identical pressure transducers (Omega PX164 – 005D5V) were used in the experiments. One of them was used to measure the primary and secondary air flow rates while the other one was used to measure the static pressure along the riser. The transducers used in the experiments are solid state piezoresistive devices. They are ideally suited to applications requiring exact measurement of pressure where the benefits of repeatability, low hysteresis and long term stability are important. The transducers have an accuracy of 0.1 % of the full scale measurement.

Both of the transducers were calibrated prior to experiments using a precise inclined manometer which had a resolution of 0.1 mm H₂O of by Dwyer Instruments, Inc. One of them was excited by 5 VDC whereas the other one was connected to a 10 VDC power supply. The calibration data, its plot and the linear fit to the measured data for both of the transducers are given below.

Table C.1. Calibration data for Omega transducers

5 VDC Excitation		10 VDC Excitation	
mm H ₂ O	Measured (volts)	mm H ₂ O	Measured (Volts)
0.0	0.5	0.0	1.26
40.9	1.1	15.1	1.68
35.8	1.0	17.9	1.76
29.3	0.9	21.4	1.86
21.0	0.8	24.9	1.95
13.4	0.7	30.3	2.10
8.7	0.6	35.8	2.25
95.9	1.8	41.0	2.38
		51.2	2.68
		60.3	2.93
		69.8	3.19
		82.6	3.55
		102.3	4.09
		123.3	4.64

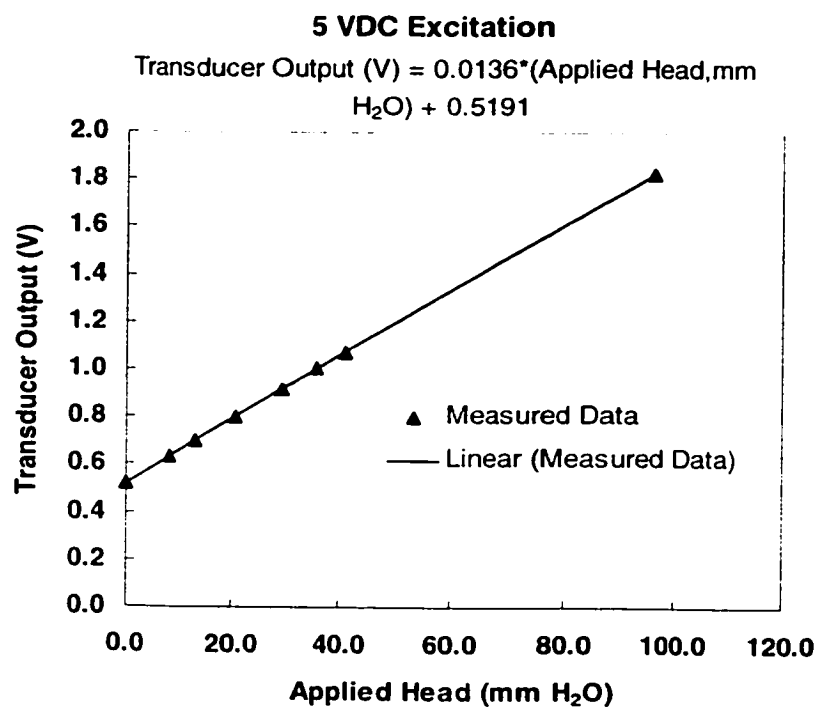


Figure C.1. Calibration curve of Omega transducer (5 VDC excitation)

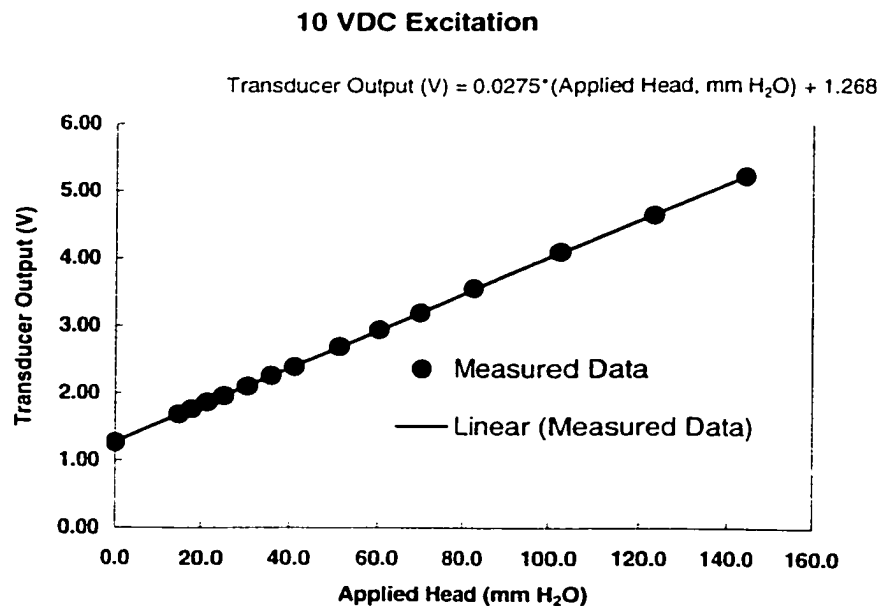


Figure C.2. Calibration curve of Omega transducer (10 VDC excitation)

The calibration of the flow meters used to measure the tracer gas flow rate and the sampled gas flow rate were done by the manufacturer (Cole and Parmer Inc.). The calibration curves and the linear fits to the data are presented on the next page.

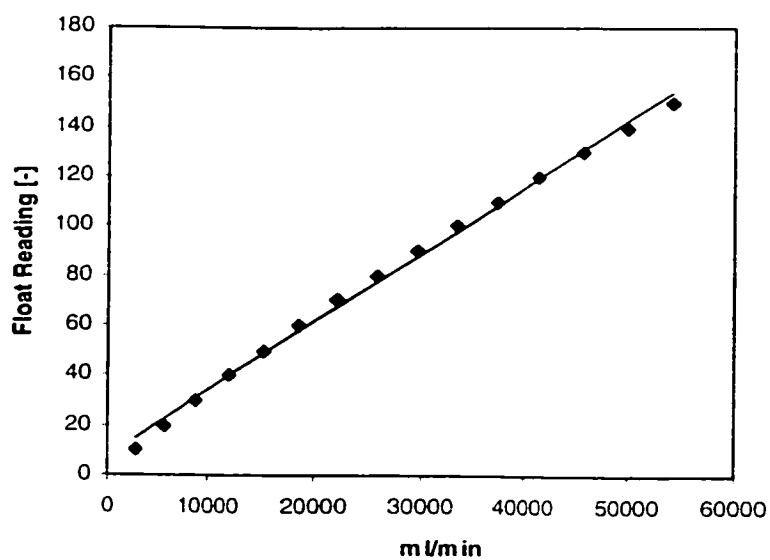


Figure C.3. Calibration curve of CO₂ flow meter

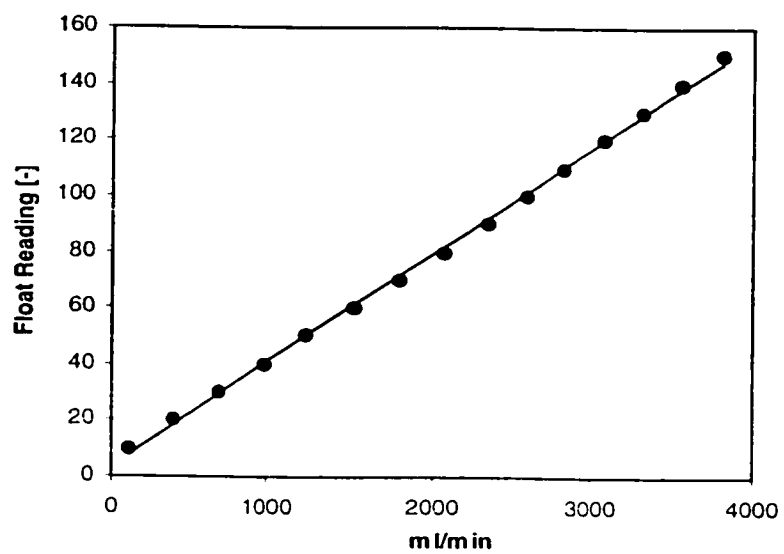


Figure C.4. Calibration curve of the sample gas (air) flow meter

Appendix D

Kinetic Theory Expressions in the Literature

All the parameters used in the following expressions are described in Chapter 5.

Table D1. Radial distribution function by different researchers

Researcher	Radial Distribution Function, g_n
Carnahan and Starling (1969)	$\frac{1}{1-\alpha_s} + \frac{3\alpha_s}{2(1-\alpha_s)^2} + \frac{\alpha_s^2}{2(1-\alpha_s)^3}$
Ogawa <i>et al.</i> (1980)	$\left[1 - \left(\frac{\alpha_s}{\alpha_{s,max}} \right)^{1/3} \right]^{-1}$
Lun and Savage (1986)	$\left(1 - \frac{\alpha_s}{\alpha_{s,max}} \right)^{-2.5\alpha_{s,max}}$
Ding and Gidaspow (1990)	$\frac{3}{5} \left[1 - \left(\frac{\alpha_s}{\alpha_{s,max}} \right)^{1/3} \right]^{-1}$
Sylamlal <i>et al.</i> (1993)	$\frac{1}{1-\alpha_s} + \frac{3\alpha_s}{2(1-\alpha_s)^2}$

Table D.2. Solids viscosity by different researchers

Researcher	Collisional Part, $\mu_{s,coll}$	Kinetic Part, $\mu_{s,kin}$
Gidaspow <i>et al.</i> (1992)	$\frac{4}{5}\alpha_s\rho_s d_p g_0 (1+e) \left(\frac{\Theta}{\pi}\right)^{1/2}$	$\frac{2\sqrt{5\pi}}{96}\rho_s d_p \sqrt{\Theta} \left[1 + \frac{4}{5}g_0\alpha_s(1+e)\right]^2$
Sylamlal <i>et al.</i> (1993)	$\frac{4}{5}\alpha_s\rho_s d_p g_0 (1+e) \left(\frac{\Theta}{\pi}\right)^{1/2}$	$\frac{d_p\rho_s\sqrt{\Theta\pi}}{6(3-\epsilon)} \left[1 + \frac{2}{5}(1+e)(3\epsilon-1)\alpha_s g_0\right]$
Balzer and Simonin (1993)	$\frac{4}{5}\alpha_s\rho_s d_p g_0 (1+e) \left(\frac{\Theta}{\pi}\right)^{1/2}$	$\frac{\Theta\alpha_s\rho_s^2}{2\beta + \rho_s\alpha_s^2 \cdot \frac{(1+e)(3-\epsilon)}{5} \frac{6}{d_p} \sqrt{\frac{16\Theta}{\pi}}}$

where β is the momentum exchange coefficient.

Table D.3. Diffusion coefficient for the granular temperature by different researchers

	Collisional Part, $k_{\Theta,coll}$	Kinetic Part, $k_{\Theta,kin}$
Gidaspow <i>et al.</i> (1992)	$2\alpha_s^2\rho_s g_0 d_p (1+e) \left(\frac{\Theta}{\pi}\right)^{1/2}$	$\frac{75}{192} \frac{\rho_s d_p \sqrt{\pi\Theta}}{(1+e)g_0} \left[1 + \frac{6}{5}(1+e)g_0\alpha_s\right]^2$
Sylamlal <i>et al.</i> (1993)	$\frac{15}{4} \frac{d_p\rho_s\alpha_s\sqrt{\pi\Theta}}{(41-33\eta)} \left[1 + \frac{12}{5}\eta^2(4\eta-3)\alpha_s g_0 + \frac{16}{15\pi}(41-33\eta)\eta\alpha_s g_0\right]$	Neglected
	where $\eta = \frac{1}{2}(1+e)$	
Balzer and Simonin (1993)	$2\alpha_s^2\rho_s g_0 d_p (1+e) \left(\frac{\Theta}{\pi}\right)^{1/2}$	$\frac{5}{9} \frac{\alpha_s^2\rho_s^2\theta}{\beta} \left[1 + \frac{5}{9} \frac{\alpha_s^2\rho_s(1+e)(49-33\epsilon)}{\beta d_p} \sqrt{\frac{\Theta}{\pi}}\right]^{-1}$

Appendix E

Fluent V4.5

Fluent V4.5 is a general purpose commercial software that can simulate a variety of single phase and multiphase flows. In this section, the general features of this software will be presented based on the information in user's manual.

Fluent uses a control volume based technique to solve the conservation equations for mass, momentum, energy, species and turbulence quantities (Patankar, 1980). This control volume based technique consists of:

- Division of the domain into discrete control volumes using a general curvilinear grid.
- Integration of the governing equations on the individual control volumes to construct the algebraic equations for discrete unknowns.
- Solution of the discretized equations.

Fluent defines the discrete volume using a non-staggered grid storage scheme as illustrated in Figure E.1. In this scheme, the same control volume is employed for integration of all the conservation equations and all variables (pressure, Cartesian velocity components, Reynolds stress components and all scalars) are stored at the control volume center. In order to avoid the oscillatory pressure or velocity fields, which is the major problem of the non-staggered grids (Patankar, 1980), the face pressures and the mass fluxes are calculated according to the procedures described in Peric *et al.* (1977).

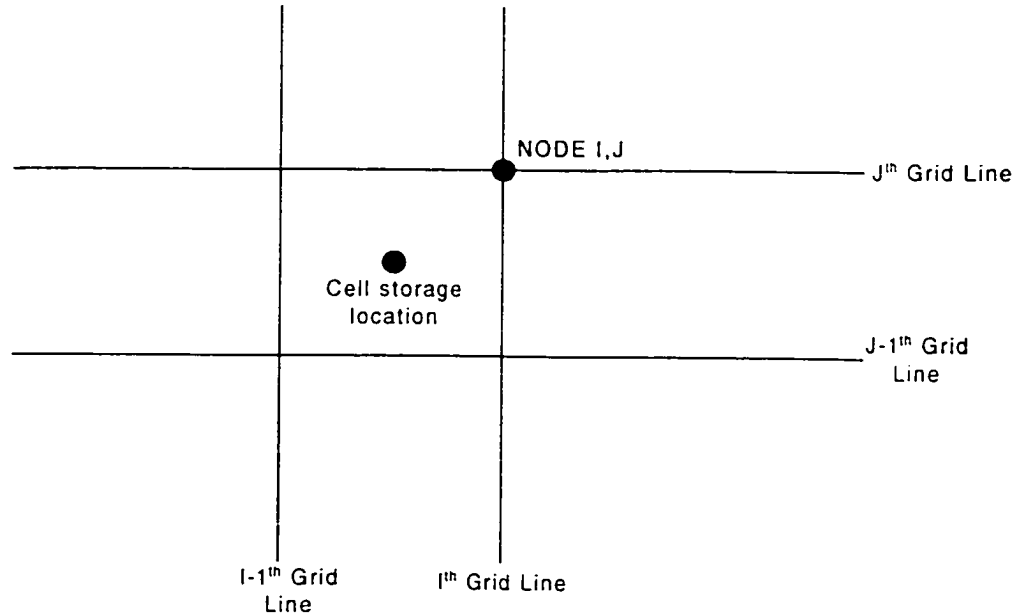


Figure E.1. Non-Staggered Control Volume Storage Scheme.

The interpolation to determine the face values of the unknowns is accomplished via either Power Law, blended Second Order Upwind/Central Difference or Quick interpolation schemes. Fluent uses the simple (SIMPLE or SIMPLEC) family algorithms which are based on using a relationship between velocity and pressure corrections in order to recast the continuity equation in terms of a pressure correction calculation (Patankar, 1980).

The integration of the differential equations based on a simple 1-D control volume (Figure E.2) can be shown as follows. In Figure E.2, W, P and E represent the cell values whereas w and e show the control volume face values to be found from one of the interpolating schemes mentioned above. When the 1-D differential equations for continuity, momentum are integrated about the control volume given in Figure E.2, the following algebraic relations are obtained:

$$(\rho u A)_e - (\rho u A)_w = 0 \text{ or } J_e - J_w = 0 \text{ for mass}$$

$$J_e u_e - J_w u_w = -(p_e - p_w)A + \left[\frac{\mu_e}{\Delta x_e} (u_E - u_P) - \frac{\mu_w}{\Delta x_w} (u_P - u_W) \right] A + F \Delta V \quad \text{for momentum}$$

where J_e and J_w are the mass fluxes at the cell face, F is the body force per unit volume, and ΔV is the cell volume.

For the solution of the mass and momentum conservation balances, the mass fluxes, pressure and velocity values at the cell faces (e and w) are needed. The Power law interpolation scheme interpolates the face value of a variable, ϕ , using the exact solution of a 1-D convection diffusion equation:

$$\frac{\phi(x) - \phi_o}{\phi_L - \phi_o} = \frac{\exp(Pe \frac{x}{L}) - 1}{\exp(Pe) - 1}$$

where Pe is the Peclet number defined as:

$$Pe = \frac{\rho u L}{\Gamma}$$

with Γ being the appropriate diffusion coefficient. Thus, a solution is obtained

for the variation of ϕ along x between the known values (cell center) of ϕ , i.e., ϕ_L and ϕ_o . The solution depends on the value of the Peclet number. For large values of Pe (convection dominates diffusion) the value of ϕ at $x = L/2$ is equal to the upstream value. For $Pe = 0$, the value of ϕ at $x = L/2$ becomes a simple average of the cell values. As can be seen, the power law scheme makes use of the cell center values of the adjacent cells.

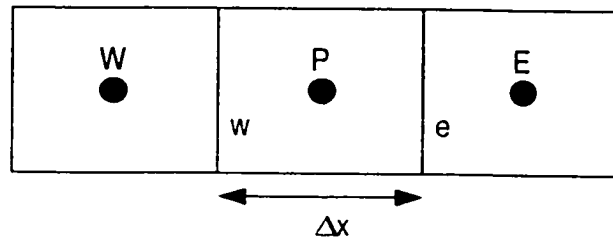


Figure E.2.1-D Control Volume Nomenclature

Fundamentally, higher order interpolation schemes such as second order upwind and QUICK make use of the cell center values of the parameters stored at two or more adjacent cells to perform the integration. This increases the accuracy for flows with sharp gradients. The major drawback, however, are the instabilities that might occur in the solution.

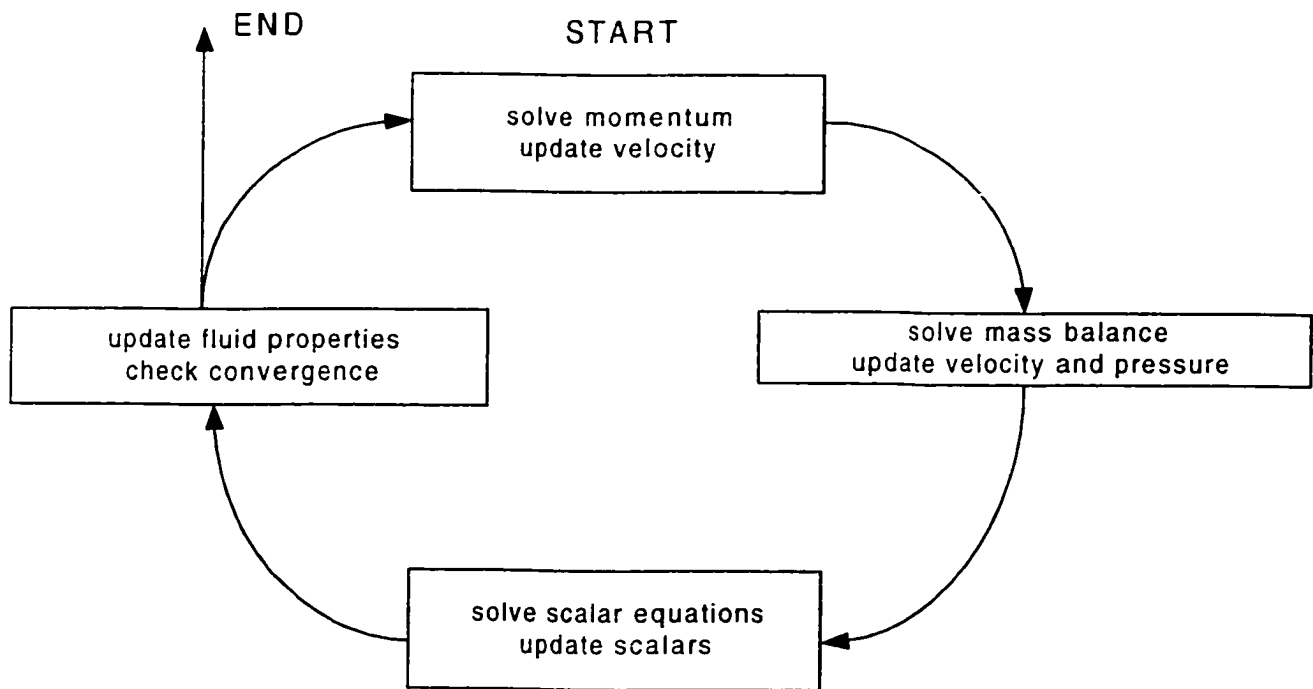


Figure E.3. Overview of the Solution Process in Fluent V4.5

The general solution procedure of Fluent V4.5 is given in Figure E.3. Specifically, the two-fluid model algorithm works as follows:

1. Get the initial and boundary conditions.
2. Perform time step iteration.
3. Calculate gas velocity.
4. Calculate the pressure correction from gas continuity equation and correct gas

velocity, pressure and fluxes (SIMPLE).

5. Calculate the phase volume fractions (gas and solids).
6. Calculate solids velocity.
7. Calculate the solids pressure corrections and correct solid velocities, fluxes and volume fractions. Update properties and calculate the granular temperature.
8. Calculate other scalar quantities such as solids phase viscosity, species concentration etc.. If not converged go to step 3.
9. Advance time step and go to step 2.

Fluent 4.5 uses two iterative techniques to obtain an approximate solution to the set of the discretized equations; Full Elimination Algorithm (FEA) and Coupled Tri-Diagonal Matrix Algorithm (TDMA). The detailed information on these solution techniques can be found in Fluent 4.5 Update Manual (1998).